CP 3359

Proceedings of the Eighth Annual Thermal and Fluids Analysis Workshop
Spacecraft Analysis and Design

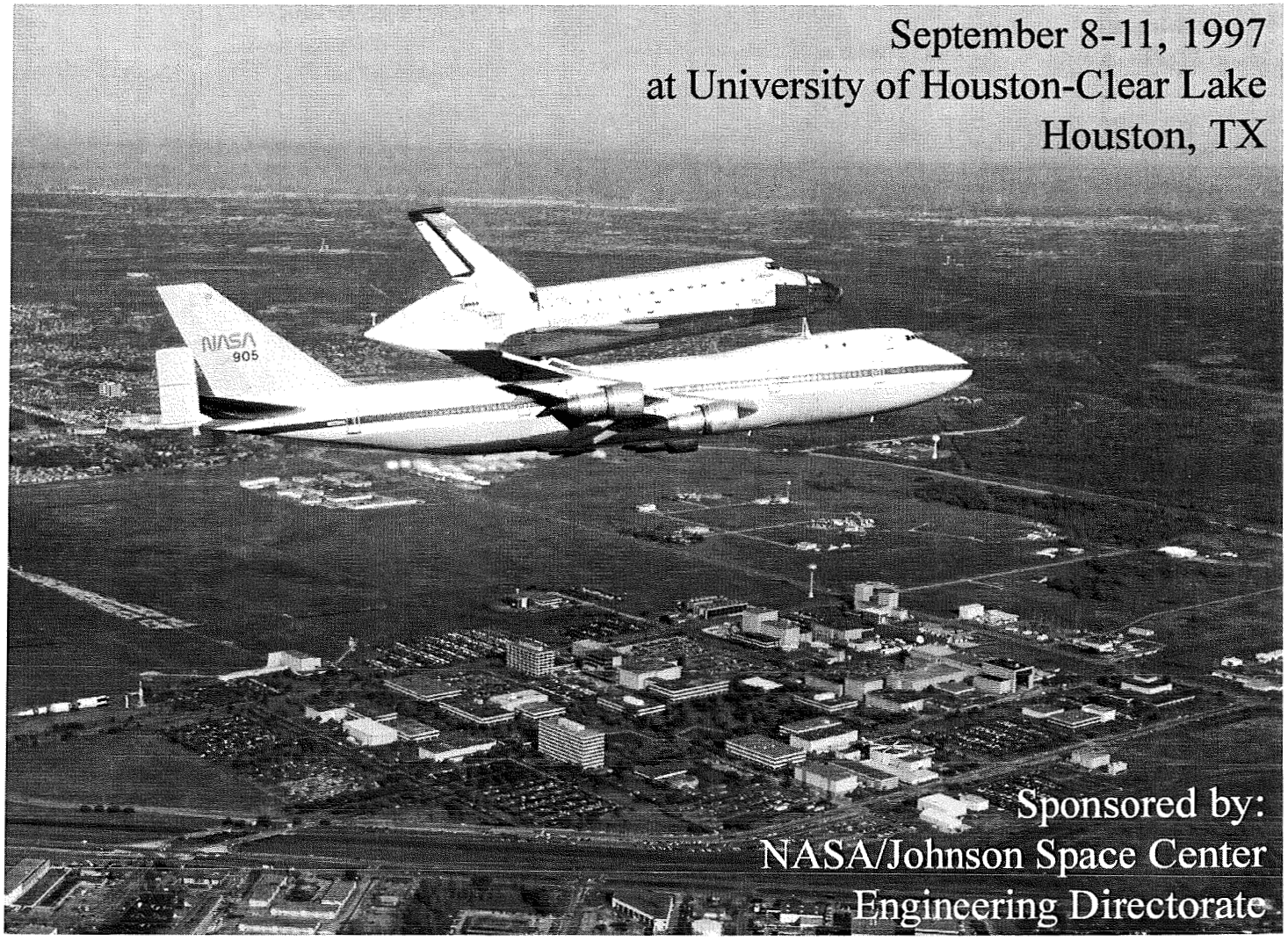

September 8-11, 1997
at University of Houston-Clear Lake
Houston, TX

Sponsored by:
NASA/Johnson Space Center
Engineering Directorate

Contents

General Papers:

VERIFICATION OF RadCAD: SPECULAR CAPABILITIES

Sam Lucas
Cullimore and Ring Technologies
Littleton, CO

Abstract

As part of the RadCAD's development process, it is necessary to compare RadCAD's results with other radiation tools and exact solutions when and where possible. Form factor algorithms have been previously verified with exact solutions. This paper will consider RadCAD's specular capabilities. First, radiation exchange factors will be compared against exact solutions and results from TRASYS for various geometries. Critical dimensions and optical properties are changed for each geometry. Second, a specular adjunct plate system will be used to verify absorbed heat fluxes. This particular geometric problem has had some attention in the literature. Previous authors have used this problem to validate software results with exact analytical solution. This paper will compare absorbed heat rates against the exact solution and other published results from other thermal radiation tools.

The agreement between RadCAD and the exact solutions is good. The maximum error for both specular and diffuse exchange factors for both geometries and all optical properties was 3%. The absorbed fluxes differed by a maximum of 4% for the adjunct plate problem.

Nomenclature

A	surface area	(m^2)
E	percent error	(-)
L	length	(m)
N_r	number of rays shot per surface	(-)
$Q_{e/ab}$	radiant energy rate leaving the cavity	(W)
$(Q_{e/ab})_b$	radiant energy rate leaving a black cavity	(W)
R	radius	(m^2)
R_A	result from an analytical solution	(W,-)
R_S	result from a simulation tool	(W,-)
α	absorptivity	(-)
$\bar{\varepsilon}$	radiating effectiveness	(-)
ε	emissivity	(-)
θ	cone half angle	(°)
ρ	reflectivity	(-)
τ	transmissivity	(-)
$\mathcal{F}_{i-j}$	exchange factor from surface i to j	(-)

Subscripts

1,2,3	surface number
d	diffuse component of reflectivity
e	exact analytical solution
s	specular component of reflectivity

Introduction

RadCAD™[†] is a Monte Carlo simulation designed for solving thermal radiation problems. RadCAD utilizes AutoCAD™[‡] as the underlying CAD engine. Panczak and Ring discussed the integration and advantages of a CAD engine.[1,2] RadCAD allows analysts to read in existing CAD data bases, but also to create models interactively. Analysts have the choice of creating a model using AutoCAD surfaces or to use RadCAD's custom surfaces. Optical properties, orbit definition, and analysis parameters, are defined using pull down menus and dialog boxes. RadCAD has been developed for personal computers, which brings the capability of Monte Carlo simulation to low cost platforms.

As part of RadCAD's development process, it is necessary to validate results produced by RadCAD with exact analytical solutions and other radiation simulation tools. A comparison of form factors produced by RadCAD to exact solutions has already been performed.[3] This paper compares radiation exchange factors (or Radks) to exact solutions and results from TRASYS. Specular and diffuse exchange factors will be calculated for the internal surfaces of a cylinder and cone. Optical properties and dimensions

[†] RadCAD is a registered trademark of Cullimore and Ring Technologies.

[‡] AutoCAD is a registered trademark of Autodesk.

were changed to create 98 cases. For each case the number of rays shot from each surface was increased from 1,000 to 100,000. RadCAD's results will be used to calculate an effective emissivity ($\bar{\varepsilon}$). An exact effective emissivity ($\bar{\varepsilon}_e$) for both a cone and cylinder was calculated by Lin and Sparrow[4]. Connolly and Lucas used this formulation to verify the specular exchange factors for TRASYS[5]. Comparisons to both TRASYS and the exact solution will be made.

In order to verify TRASYS's ray tracing algorithms, Connolly and Lucas used an adjunct plate system[5]. These authors compared TRASYS's results to both OPERA and NEVEADA results. Hering calculated the exact solution to adjunct plates[6]. Hering results were numerically integrated by Connolly and Lucas in order to make a comparison between TRASYS and OPERA , NEVADA and the exact solution. The current paper will compare RadCAD's results to the exact analytical solution, and results from TRASYS, OPERA and NEVADA. Optical properties and solar vector position will be changed to create 12 cases. The number of rays shot per surface will also be increased from 1,000 to 100,000 for each case.

Geometric Configurations

Three geometric configurations were considered to validate RadCAD's specular algorithms . Specular exchange factors were validated using the interior surfaces of a cone and cylinder. Specular solar fluxes were validated using the interior surfaces of a wedge. For all geometries, primary dimensions and optical properties were changed.

All surfaces are assumed to be opaque (τ=0). So, all radiant incident energy is either absorbed or reflected. Therefore, the sum of absorptivity (α) and reflectivity (ρ) is one, or

$$\alpha + \rho = 1 \qquad (1)$$

Also, Kirchoff's law applies to the surfaces. The emissivity and absorptivity are equal (ε=α). The reflectivity is defined in a typical manner as the sum of the specular (ρ_s) and diffuse (ρ_d) components, according to,

$$\rho = \rho_s + \rho_d \qquad (2)$$

The percent specularity of a surface is defined as the ratio of specular reflectivity to reflectivity, or

$$\frac{\rho_s}{\rho_s+\rho_d} \qquad (3)$$

Therefore, when a surface is 100% specular, the diffuse component of reflectivity is zero (ρ_d=0). From (3) it is concluded that the reflectivity is equal to the specular reflectivity ($\rho = \rho_s$).

The configurations and optical properties for each geometry will be discussed next.

Cone

The first geometric configuration considered consisted of a cone and a disk as shown in Figure 1. The cone has length L and a opening angle of 2θ. Surface 1 is defined as the cone and has an area, A_1. A disk is used to close out the geometry, and has an area A_2. Given L and θ the disk radius is easily calculated.

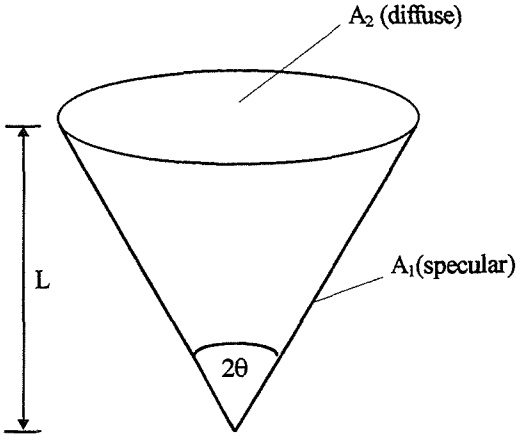

Figure 1 Cone Geometry

The disk radius, opening angle and optical properties were varied. The length remained fixed at a value of one (L=1) for all cases. The values for the half angle of the cone were: 10°, 20°, 30°, and 60°. Optical properties for surface 1 are given in Table 1. The disk had an emissivity of one and was considered diffuse for all cases. Surface 1 was considered to be 100% specular for all cases. As seen from Table 1, both ε and ρ (or ρ_s) varied from 0.1 to 0.9.

Table 1 Cone Optical Properties

$\varepsilon = \alpha$	$\rho=\rho_s$		$\varepsilon = \alpha$	$\rho=\rho_s$
0.1	0.9		0.5	0.5
0.2	0.8		0.7	0.3
0.3	0.7		0.9	0.1

Cylinder

The second geometric configuration consisted of a cylinder and two disks and is shown in Figure 2. As shown in this figure the cylinder had a radius R and length L. Surface 1 was defined as the cylinder, and has area, A_1. Surfaces 2 and 3 were defined as disks and had an area A_2 and A_3, respectively. Surfaces 1 and 2 were 100% specular for all specular cases. Surface 3 was diffuse and black for all cases.

Dimensions and optical properties of the cylinder were allowed to vary from case to case. Values for L/R were: 2, 4, 6, 8, and 10. Optical properties for surfaces 1 and 2 are defined in Table 2.

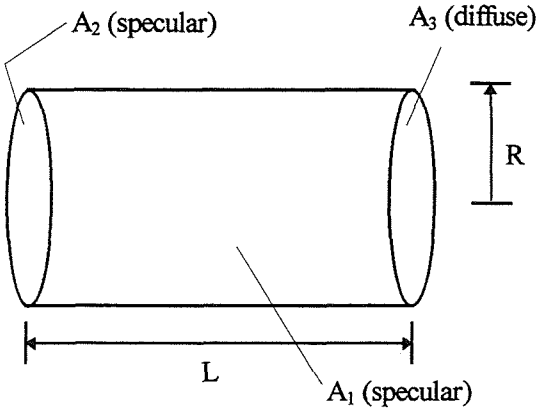

Figure 2 Cylinder Geometry

Table 2 Cylinder Optical Properties

$\varepsilon = \alpha$	$\rho = \rho_s$		$\varepsilon = \alpha$	$\rho = \rho_s$
0.1	0.9		0.7	0.3
0.3	0.7		0.9	0.1
0.5	0.5			

Wedge

A sketch of the wedge used to validate specular absorbed fluxes is shown in Figure 3. The nodal breakdown was chosen to "trap" rays in the wedge[5]. As shown in this figure two different solar angles were considered. Position 1 and 2 were 10° and 50°, respectively, from surface 1. The wedge was assumed to be 1 meter in length and 100% specular triangles were used at the ends.

Table 3 gives the optical properties used for the two solar positions. Values for ε were 0.1 and 0.5, and the wedge was assumed to be 0%, 50% and 100% specular. Values of ε, ρ_s and ρ_d are given in Table 3.

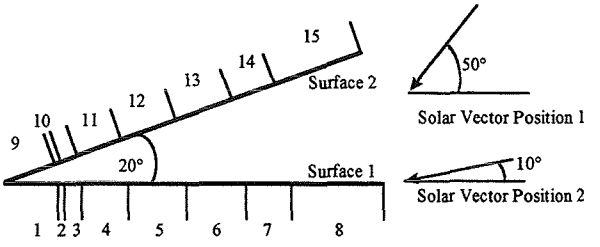

Nodal Break Down			
Surface 1		Surface 2	
Node	Location	Node	Location
1	0.1732	9	0.1732
2	0.1848	10	0.1848
3	0.2267	11	0.2267
4	0.3473	12	0.3473
5	0.5	13	0.5321
6	0.6527	14	0.8152
7	0.766	15	1.0
8	1.0		

Figure 3 Geometry for the Wedge

Table 3 Optical Properties for the Wedge

$\varepsilon = \alpha$	ρ_s	ρ_d
0.1	0.0	0.9
0.1	0.45	0.45
0.1	0.9	0.0
0.5	0.0	0.5
0.5	0.25	0.25
0.5	0.5	0.0

Exact Solutions

Exact solutions were found in the literature for all three geometries. Lin and Sparrow presented specular and diffuse exchange factors for the cone and cylinder geometries. Connolly and Lucas numerically integrated Hering's results for the wedge geometry.

Lin and Sparrow defined a radiating effectiveness ($\bar{\varepsilon}$) for cones and cylinders of various sizes and optical properties. The radiating effectiveness for a cavity is defined as,

$$\bar{\varepsilon} = \frac{Q_{e/ab}}{(Q_{e/ab})_b} \tag{4}$$

where, $Q_{e/ab}$ = radiant energy rate leaving the cavity

$(Q_{e/ab})_b$ = radiant energy rate leaving a black cavity.

Equation (4) is interpreted as the emissive performance of a non black cavity. A black cavity has the best

performance. As the emissivity of the cavity approaches one, then $\bar{\varepsilon}$ approaches one.

Cone

The analytical results for radiating emissivities for both a specular ($\bar{\varepsilon}_{e,s}$)and diffuse ($\bar{\varepsilon}_{e,d}$) cone were taken from Reference 5, and are presented here in Table 4. Lin and Sparrow showed the specular solution and diffuse solution converged at a cone half angle of approximately 50°.

Table 4 Exact Results for Cone

$\varepsilon = 0.1, \rho = \rho_s = 0.9$			$\varepsilon = 0.5, \rho = \rho_s = 0.5$		
θ	$\bar{\varepsilon}_{e,s}$	$\bar{\varepsilon}_{e,d}$	θ	$\bar{\varepsilon}_{e,s}$	$\bar{\varepsilon}_{e,d}$
10	0.418	0.332	10	0.922	0.775
20	0.25	0.232	20	0.795	0.709
30	0.182	0.177	30	0.69	0.65
60	0.114	0.11	60	0.536	0.53
$\varepsilon = 0.2, \rho = \rho_s = 0.8$			$\varepsilon = 0.7, \rho = \rho_s = 0.3$		
θ	$\bar{\varepsilon}_{e,s}$	$\bar{\varepsilon}_{e,d}$	θ	$\bar{\varepsilon}_{e,s}$	$\bar{\varepsilon}_{e,d}$
10	0.655	0.5	10	0.973	0.882
20	0.445	0.398	20	0.914	0.845
30	0.33	0.323	30	0.85	0.814
60	0.222	0.22	60	0.727	0.72
$\varepsilon = 0.3, \rho = \rho_s = 0.7$			$\varepsilon = 0.9, \rho = \rho_s = 0.3$		
θ	$\bar{\varepsilon}_{e,s}$	$\bar{\varepsilon}_{e,d}$	θ	$\bar{\varepsilon}_{e,s}$	$\bar{\varepsilon}_{e,d}$
10	0.795	0.618	10	0.99	0.968
20	0.595	0.523	20	0.982	0.955
30	0.477	0.449	30	0.96	0.945
60	0.33	0.33	60	0.91	0.91

Cylinder

Analytical results for radiating emissivities for a specular and diffuse cylinder were taken from Reference 5, and are presented here in Table 5. For this geometry, Lin and Sparrow showed that the effective emissivity for both specular and diffuse optical properties did not change as a function of L/R for L/R>6.

Wedge

Hering solved the adjunct plate geometry in a general form. Connolly and Lucas numerically integrated Hering's results for solar position 2.

Table 6 shows these results. The solar flux has been assumed to be 1 W/m^2. This was done to facilitate viewing the results.

Table 5 Exact Results for Cylinder

$\varepsilon = 0.1, \rho = \rho_s = 0.9$			$\varepsilon = 0.7, \rho = \rho_s = 0.3$		
L/R	$\bar{\varepsilon}_{e,s}$	$\bar{\varepsilon}_{e,d}$	L/R	$\bar{\varepsilon}_{e,s}$	$\bar{\varepsilon}_{e,d}$
2	0.9919	0.977	2	0.7024	0.664
4	0.9975	0.977	4	0.8305	0.7136
6	0.9988	0.977	6	0.8909	0.718
8	0.9993	0.977	8	0.9244	0.718
10	0.9996	0.977	10	0.9448	0.718
$\varepsilon = 0.3, \rho = \rho_s = 0.7$			$\varepsilon = 0.9, \rho = \rho_s = 0.1$		
L/R	$\bar{\varepsilon}_{e,s}$	$\bar{\varepsilon}_{e,d}$	L/R	$\bar{\varepsilon}_{e,s}$	$\bar{\varepsilon}_{e,d}$
2	0.9547	0.909	2	0.3486	0.3486
4	0.9833	0.918	4	0.4931	0.45
6	0.9916	0.918	6	0.5912	0.477
8	0.995	0.918	8	0.6624	0.489
10	0.9967	0.918	10	0.7161	0.495
$\varepsilon = 0.5, \rho = \rho_s = 0.5$					
L/R	$\bar{\varepsilon}_{e,s}$	$\bar{\varepsilon}_{e,d}$			
2	0.8717	0.809			
4	0.9422	0.836			
6	0.9677	0.836			
8	0.9797	0.836			
10	0.9861	0.836			

Table 6 Exact Solution Results for Wedge

	Flux [W/m^2]					
	α=0.1			α=0.5		
Node	ρ_s/ρ=0.0	ρ_s/ρ=0.5	ρ_s/ρ=1.0	ρ_s/ρ=0.0	ρ_s/ρ=0.5	ρ_s/ρ=1.0
1	0.02025	0.03535	0.06688	0.02899	0.04532	0.07283
2	0.00124	0.00192	0.00372	0.00192	0.00291	0.00452
3	0.00437	0.00613	0.00823	0.00691	0.01003	0.01323
4	0.01167	0.01299	0.01131	0.01963	0.02466	0.02582
5	0.01300	0.00950	0.00379	0.02410	0.01948	0.01331
6	0.01107	0.00760	0.00379	0.02300	0.01835	0.01331
7	0.00695	0.00482	0.00281	0.01606	0.01304	0.00988
8	0.01086	0.00808	0.00581	0.02944	0.02508	0.02040
9	0.02025	0.03535	0.06688	0.02899	0.04532	0.07283
10	0.00124	0.00192	0.00372	0.00192	0.00291	0.00452
11	0.00437	0.00613	0.00823	0.00691	0.01003	0.01323
12	0.01167	0.01299	0.01131	0.01963	0.02466	0.02582
13	0.01548	0.01118	0.00459	0.02905	0.02338	0.01611
14	0.01822	0.01255	0.00703	0.04088	0.03297	0.02468
15	0.00819	0.00619	0.00459	0.02278	0.01958	0.01611
sum	0.15883	0.1727	0.21269	0.30021	0.31772	0.3466

Computer Simulation Results

The aforementioned geometries have been analyzed using various radiation computer software tools. TRASYS was used to calculate specular

radiating effectiveness for both the cone and cylinder[5]. TRASYS, OPERA, and NEVADA have been used to analyze the wedge geometry[5].

In order to calculate the radiating effectiveness exchange factors ($\mathcal{F}_{i-j}$) were needed for the cone and cylinder. An exchange factor between surface i and j is defined as the fraction of energy that leaves i and is absorbed by j by all possible paths, including specular and diffuse reflections. The product of area and exchange factor is often referred to as a Radk.

Cone

Using equation (4) the effective emissivity for a cone is

$$\bar{\varepsilon} = \mathcal{F}_{1-2} / \sin\theta \qquad (5)$$

where, $\mathcal{F}_{1-2}$ is the exchange factor between the cone and disk.

Table 7 Specular Effective Emissivity for the Cone from TRASYS and RadCAD

Optical Properties	θ	Effective Emissivity			
			RadCAD Varying N_r		
		TRASYS	1000	10000	100000
ε=0.1 ρ=ρs=0.9	10	0.4238	0.4253	0.4217	0.4230
	20	0.2526	0.2527	0.2539	0.2540
	30	0.183	0.1847	0.1842	0.1843
	60	0.1129	0.1138	0.1135	0.1136
ε=0.2 ρ=ρs=0.8	10	0.6577	0.6612	0.6563	0.6574
	20	0.4444	0.4448	0.4467	0.4474
	30	0.3398	0.3426	0.3412	0.3422
	60	0.2224	0.2240	0.2242	0.2238
ε=0.3 ρ=ρs=0.7	10	0.7923	0.7864	0.7922	0.7923
	20	0.5903	0.6025	0.5949	0.5963
	30	0.4742	0.4773	0.4769	0.4777
	60	0.3287	0.3300	0.3310	0.3309
ε=0.5 ρ=ρs=0.5	10	0.9233	0.9213	0.9277	0.9212
	20	0.7856	0.8001	0.7966	0.7983
	30	0.6867	0.6890	0.6971	0.6940
	60	0.532	0.5365	0.5356	0.5353
ε=0.3 ρ=ρs=0.7	10	0.9749	0.9811	0.9681	0.9708
	20	0.898	0.9177	0.9127	0.9153
	30	0.839	0.8487	0.8496	0.8500
	60	0.7238	0.7340	0.7287	0.7301
ε=0.9 ρ=ρs=0.1	10	0.9959	1.0174	0.9924	0.9904
	20	0.9668	0.9794	0.9801	0.9812
	30	0.9454	0.9573	0.9577	0.9603
	60	0.9046	0.9114	0.9076	0.9125

The specular effective emissivities for the cone geometry were calculated using Radks produced by RadCAD. The cone half angle was varied as discussed above, and the optical properties varied according to Table 1. The number of rays shot per surfaces (N_r) was also allowed to vary. TRASYS has also been used to generate Radks and effective emissivities [5]. Both the RadCAD and TRASYS results are given in Table 7.

Diffuse effective emissivities were generated based upon diffuse Radks produced by RadCAD. These results are given in Table 8 for varying number of rays shot per surface. For these results the reflectivity was equal to the diffuse component ($\rho=\rho_d$).

Table 8 Diffuse Effective Emissivity for the Cone from RadCAD

Optical Properties	θ	Effective Emissivity RadCAD Varying N_r		
		1000	10000	100000
ε=0.1 ρ=ρd=0.9	10	0.3259	0.3344	0.3325
	20	0.2354	0.2335	0.2340
	30	0.1785	0.1791	0.1789
	60	0.1137	0.1136	0.1137
ε=0.2 ρ=ρd=0.8	10	0.4988	0.5000	0.4987
	20	0.3987	0.3970	0.3974
	30	0.3219	0.3258	0.3251
	60	0.2232	0.2240	0.2238
ε=0.3 ρ=ρd=0.7	10	0.6199	0.6140	0.6127
	20	0.5267	0.5205	0.5224
	30	0.4434	0.4525	0.4493
	60	0.3352	0.3301	0.3306
ε=0.5 ρ=ρd=0.5	10	0.7540	0.7684	0.7721
	20	0.7091	0.7099	0.7098
	30	0.6559	0.6485	0.6502
	60	0.5390	0.5354	0.5350
ε=0.3 ρ=ρd=0.7	10	0.8862	0.8789	0.8790
	20	0.8351	0.8459	0.8470
	30	0.8080	0.8105	0.8090
	60	0.7309	0.7300	0.7285
ε=0.9 ρ=ρd=0.1	10	0.9710	0.9633	0.9606
	20	0.9519	0.9501	0.9560
	30	0.9445	0.9424	0.9403
	60	0.9147	0.9123	0.9113

Cylinder

Using equation (4) the effective emissivity for a cylinder is

$$\bar{\varepsilon} = 2L\mathcal{F}_{1-3}/R + \mathcal{F}_{2-3} \qquad (6)$$

where, $\mathcal{F}_{1-2}$ is the exchange factor between the cylinder and the diffuse disk.

$\mathcal{F}_{2\text{-}3}$ is the exchange factor between the specular disk and the diffuse disk.

The specular effective emissivities for the cylinder geometry were calculated using Radks produced by RadCAD. The length to radius ratio was varied as discussed above, and the optical properties varied according to Table 1. The number of rays shot per surfaces was also allowed to vary. TRASYS was also was used to generate Radks and effective emissivities were then calculated[5]. Both the RadCAD and TRASYS results are given in Table 9.

Diffuse effective emissivities were generated based upon diffuse Radks produced by RadCAD. These results are given in Table 10 for varying number of rays shot per surface. For these results the reflectivity was equal to the diffuse component ($\rho=\rho_d$).

Table 9 Specular Effective Emissivity for the Cylinder from TRASY and RadCAD

Optical Properties	L/R	Effective Emissivity			
			RadCAD Varying N_r		
		TRASYS	1000	10000	100000
ε=0.1 $\rho=\rho_s$=0.9	2	0.336	0.3513	0.3483	0.3486
	4	0.475	0.4931	0.4965	0.4928
	6	0.5611	0.6021	0.5895	0.5908
	8	0.6127	0.6566	0.6603	0.6613
	10	0.6456	0.7189	0.7192	0.7158
ε=0.3 $\rho=\rho_s$=0.7	2	0.6677	0.7069	0.7003	0.7027
	4	0.7931	0.8258	0.8277	0.8318
	6	0.8318	0.8857	0.8888	0.8905
	8	0.8609	0.9179	0.9253	0.9253
	10	0.8483	0.9524	0.9468	0.9443
ε=0.5 $\rho=\rho_s$=0.5	2	0.8419	0.8728	0.8750	0.8704
	4	0.9227	0.9461	0.9477	0.9407
	6	0.9246	0.9696	0.9682	0.9695
	8	0.9362	0.9873	0.9813	0.9813
	10	0.9221	0.9875	0.9831	0.9855
ε=0.7 $\rho=\rho_s$=0.3	2	0.9341	0.9559	0.9581	0.9549
	4	0.9917	0.9969	0.9836	0.9836
	6	0.9644	0.9925	0.9911	0.9927
	8	0.9682	0.9823	0.9930	0.9951
	10	0.9589	1.0083	0.9956	0.9967
ε=0.9 $\rho=\rho_s$=0.1	2	0.9797	1.0053	0.9917	0.9921
	4	1.0002	0.9769	0.9986	0.9958
	6	0.9855	1.0029	1.0004	0.9980
	8	0.9879	0.9945	0.9990	0.9992
	10	0.984	0.9943	1.0006	0.9986

Table 10 Diffuse Effective Emissivity for the Cylinder from RadCAD

Optical Properties	L/R	Effective Emissivity		
		RadCAD Varying N_r		
		1000	10000	100000
ε=0.1 $\rho=\rho_d$=0.9	2	0.3503	0.3468	0.3474
	4	0.4472	0.4457	0.4463
	6	0.4860	0.4812	0.4788
	8	0.4810	0.4956	0.4920
	10	0.4959	0.4896	0.4976
ε=0.3 $\rho=\rho_d$=0.7	2	0.6666	0.6596	0.6574
	4	0.7086	0.7168	0.7097
	6	0.7152	0.7159	0.7192
	8	0.7166	0.7253	0.7194
	10	0.7128	0.7195	0.7215
ε=0.5 $\rho=\rho_d$=0.5	2	0.8119	0.8045	0.8090
	4	0.8482	0.8306	0.8307
	6	0.8432	0.8456	0.8370
	8	0.8349	0.8383	0.8356
	10	0.8454	0.8364	0.8371
ε=0.7 $\rho=\rho_d$=0.3	2	0.9117	0.9045	0.9033
	4	0.9098	0.9108	0.9144
	6	0.9245	0.9180	0.9139
	8	0.9193	0.9112	0.9156
	10	0.9136	0.9153	0.9144
ε=0.9 $\rho=\rho_d$=0.1	2	0.9740	0.9780	0.9707
	4	0.9673	0.9793	0.9743
	6	0.9734	0.9750	0.9751
	8	0.9821	0.9744	0.9766
	10	0.9773	0.9763	0.9755

Wedge

RadCAD was used to calculate absorbed fluxes for the wedge using solar position 1 and 2. Results for position 1 are given in Table 11 and Table 12. The first table gives the absorbed fluxes of α=0.1 and varying values of reflectivity. The second table gives similar information except for α=0.5. Due to the large amount of data only this solar angle will be presented here. This angle was chosen since exact solutions were given in Table 6. Results for both solar angles for OPERA, NEVADA and TRASYS can be found in Reference 5.

A comparison of effective emissivities and absorbed fluxes for all geometries will be presented next.

Table 11 Absorbed Fluxes from RadCAD ε=0.1

	Flux [W/m^2]								
	α=0.1 ρ_s/ρ=0.0			α=0.1 ρ_s/ρ=0.5			α=0.1 ρ_s/ρ=1.0		
Node	1000	10,000	100,000	1000	10,000	100,000	1000	10,000	100,000
1	0.02074	0.02061	0.02067	0.03620	0.03585	0.03575	0.06701	0.06687	0.06686
2	0.00128	0.00125	0.00125	0.00196	0.00190	0.00193	0.00362	0.00372	0.00376
3	0.00446	0.00440	0.00441	0.00618	0.00618	0.00616	0.00815	0.00825	0.00824
4	0.01201	0.01174	0.01177	0.01279	0.01315	0.01312	0.01138	0.01132	0.01130
5	0.01298	0.01318	0.01313	0.00964	0.00966	0.00965	0.00379	0.00379	0.00379
6	0.01106	0.01110	0.01115	0.00769	0.00767	0.00764	0.00379	0.00379	0.00379
7	0.00701	0.00699	0.00701	0.00487	0.00484	0.00485	0.00281	0.00281	0.00281
8	0.01114	0.01092	0.01096	0.00807	0.00808	0.00813	0.00581	0.00581	0.00581
9	0.02080	0.02057	0.02067	0.03591	0.03588	0.03576	0.06687	0.06683	0.06687
10	0.00121	0.00127	0.00126	0.00197	0.00192	0.00194	0.00375	0.00380	0.00375
11	0.00440	0.00444	0.00441	0.00618	0.00615	0.00617	0.00823	0.00823	0.00823
12	0.01183	0.01177	0.01178	0.01311	0.01309	0.01312	0.01131	0.01131	0.01131
13	0.01555	0.01563	0.01562	0.01142	0.01140	0.01138	0.00459	0.00459	0.00459
14	0.01842	0.01826	0.01836	0.01250	0.01264	0.01265	0.00703	0.00703	0.00703
15	0.00833	0.00824	0.00828	0.00635	0.00620	0.00622	0.00459	0.00459	0.00459
sum	0.16122	0.16037	0.16073	0.17484	0.17461	0.17447	0.21273	0.21274	0.21273

Table 12 Absorbed Fluxes from RadCAD ε=0.5

	Flux [W/m^2]								
	α=0.5 ρ_s/ρ=0.0			α=0.5 ρ_s/ρ=0.5			α=0.5 ρ_s/ρ=1.0		
Node	1000	10,000	100,000	1000	10,000	100,000	1000	10,000	100,000
1	0.02877	0.02904	0.02894	0.04521	0.04529	0.04524	0.07298	0.07287	0.07283
2	0.00204	0.00189	0.00192	0.00300	0.00290	0.00292	0.00441	0.00451	0.00452
3	0.00695	0.00683	0.00691	0.01025	0.00997	0.01006	0.01334	0.01321	0.01321
4	0.01957	0.01951	0.01957	0.02446	0.02471	0.02467	0.02569	0.02582	0.02585
5	0.02435	0.02416	0.02410	0.01961	0.01955	0.01958	0.01331	0.01331	0.01331
6	0.02258	0.02316	0.02299	0.01829	0.01848	0.01836	0.01331	0.01331	0.01331
7	0.01605	0.01611	0.01611	0.01298	0.01290	0.01304	0.00988	0.00988	0.00988
8	0.02967	0.02941	0.02950	0.02485	0.02506	0.02507	0.02040	0.02040	0.02040
9	0.02892	0.02900	0.02894	0.04545	0.04522	0.04526	0.07291	0.07285	0.07282
10	0.00186	0.00190	0.00192	0.00284	0.00293	0.00292	0.00452	0.00450	0.00454
11	0.00689	0.00691	0.00689	0.01007	0.01003	0.01006	0.01317	0.01324	0.01324
12	0.01972	0.01951	0.01958	0.02441	0.02477	0.02466	0.02582	0.02582	0.02582
13	0.02906	0.02912	0.02909	0.02364	0.02344	0.02348	0.01611	0.01611	0.01611
14	0.04045	0.04091	0.04076	0.03277	0.03290	0.03297	0.02468	0.02468	0.02468
15	0.02298	0.02275	0.02281	0.01976	0.01954	0.01959	0.01611	0.01611	0.01611
sum	0.29986	0.30021	0.30003	0.31759	0.31769	0.31788	0.34664	0.34662	0.34663

Comparison of Results

A comparison between RadCAD and the analytical solution and results from other radiation simulation software will be presented next. For all comparisons the percent error will be defined as,

$$E = (1 - \frac{R_A}{R_S}) \times 100 \qquad (7)$$

where, R_A is the analytical result whether radiating effectiveness or flux and

R_S is the simulation tool result whether radiating effectiveness or flux.

The percent error will be both positive and negative in value. A positive value implies that the simulation tool

over predicted the parameter in question. A negative value means the simulation tool under predicted.

Cone

Using equation (7), Table 4 and Table 7 comparisons between the analytical solution and calculated specular radiating effectiveness using both RadCAD and TRASYS results were made. These comparisons are shown in Figure 4 through Figure 9 where the percent errors as a function of half cone angle for the cone geometry with specular optical properties are presented. In each of the figures, the TRASYS results are presented first, followed by the RadCAD results. The number of rays shot as shown in the figures varied from 1,000 to 100,000, therefore there are three percent errors based upon RadCAD results for every TRASYS.

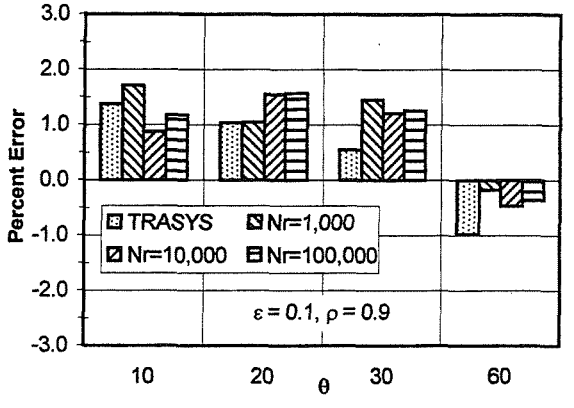

Figure 4 Cone Percent Error for Specular Radiating Effectiveness ε=0.1

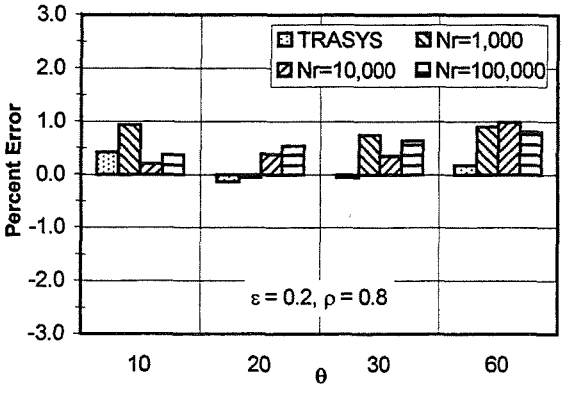

Figure 5 Cone Percent Error for Specular Radiating Effectiveness ε=0.2

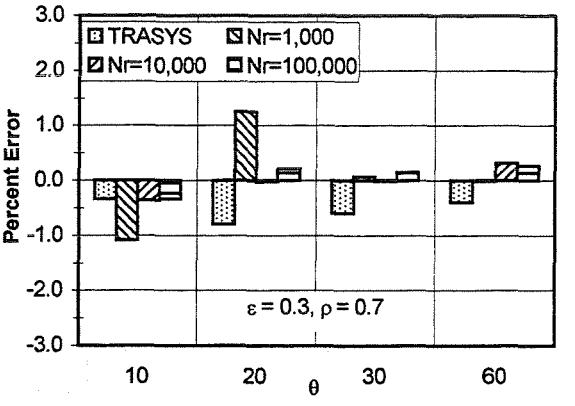

Figure 6 Cone Percent Error for Specular Radiating Effectiveness ε=0.3

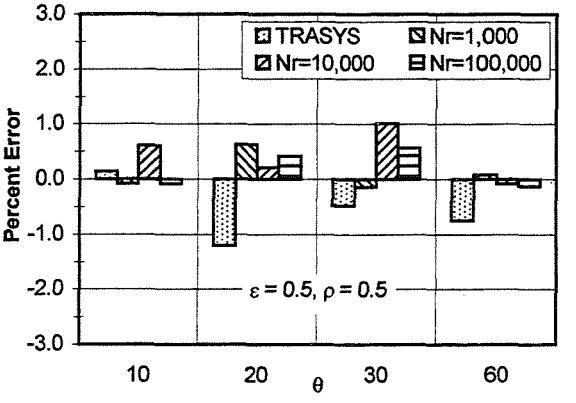

Figure 7 Cone Percent Error for Specular Radiating Effectiveness ε=0.5

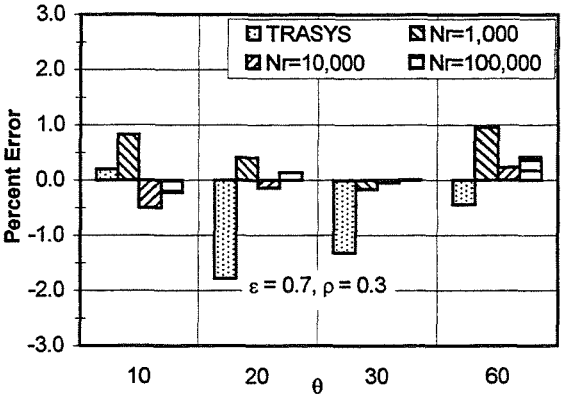

Figure 8 Cone Percent Error for Specular Radiating Effectiveness ε=0.7

Using equation (7), Table 4, and Table 8 comparisons between the analytical solution and calculated diffuse radiating effectiveness using RadCAD were made. These comparisons are shown in Table 13. The percent errors are listed for varying half

cone angle for the cone geometry with diffuse optical properties. The number of rays shot varied from 1,000 to 100,000.

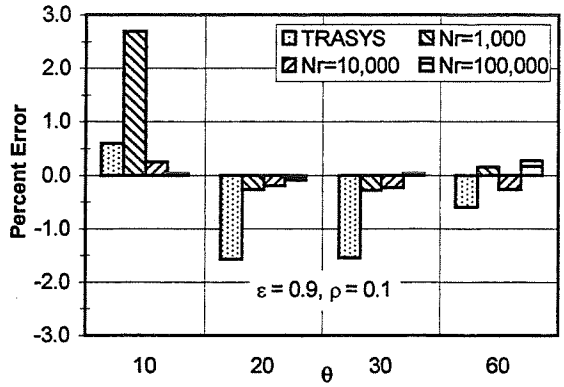

Figure 9 Cone Percent Error for Specular Radiating Effectiveness ε=0.9

Table 13 Cone Percent Error for Diffuse Radiating Effectiveness

Optical Properties	θ	Percent Error RadCAD Varying N_r 1000	10000	100000
	10	-1.83	0.72	0.14
ε=0.1	20	1.45	0.63	0.88
$\rho=\rho_d$=0.9	30	0.86	1.17	1.05
	60	-0.24	-0.31	-0.29
	10	-0.24	-0.00	-0.25
ε=0.2	20	0.18	-0.26	-0.16
$\rho=\rho_d$=0.8	30	-0.34	0.87	0.65
	60	0.53	0.80	1.72
	10	0.30	-0.65	-0.86
ε=0.3	20	0.71	-0.48	-0.11
$\rho=\rho_d$=0.7	30	-1.24	0.78	0.06
	60	1.58	0.03	0.20
	10	-2.71	-0.85	-0.38
ε=0.5	20	0.01	0.13	0.12
$\rho=\rho_d$=0.5	30	0.91	-0.23	0.04
	60	0.56	-0.12	-0.18
	10	0.47	-0.36	-0.34
ε=0.7	20	-1.17	0.10	0.24
$\rho=\rho_d$=0.3	30	-0.73	-0.43	-0.61
	60	0.56	0.42	0.20
	10	0.31	-0.48	-0.76
ε=0.9	20	-0.32	-0.52	0.10
$\rho=\rho_d$=0.1	30	-0.05	-0.27	-0.50
	60	0.51	0.26	0.14

Cylinder

Comparisons between the analytical solution and calculated specular radiating effectiveness using both RadCAD and TRASYS results were made. The results of these comparisons are shown in Figure 10 through Figure 14. Where the percent errors as a function of the length to radius ratio for the cylinder geometry with specular optical properties are presented. In each of the figures, the TRASYS results are presented first, followed the RadCAD results. The number of rays shot as shown in the figures varied from 1,000 to 100,000, therefore there are three percent errors based upon RadCAD results for every TRASYS.

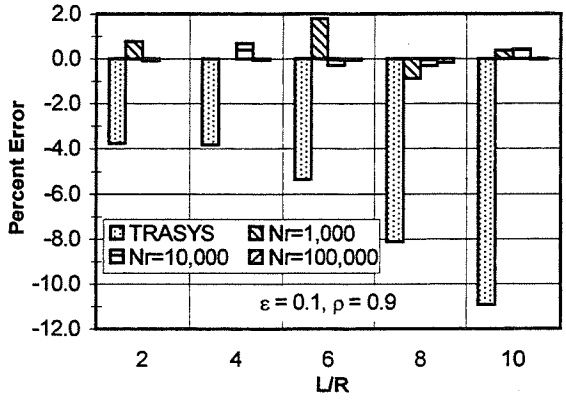

Figure 10 Cylinder Percent Error for Specular Radiating Effectiveness ε=0.1

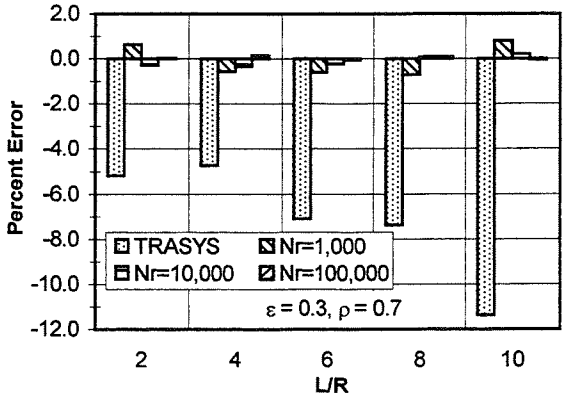

Figure 11 Cylinder Percent Error for Specular Radiating Effectiveness ε=0.3

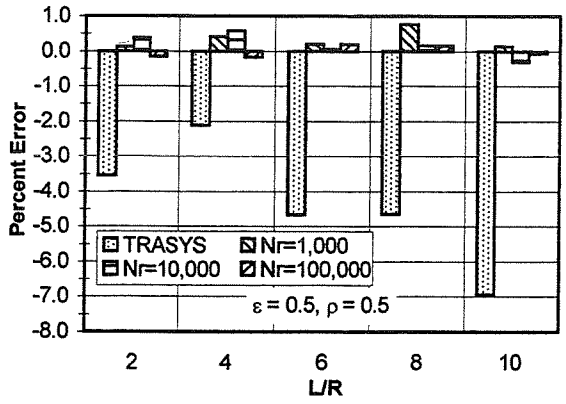

Figure 12 Cylinder Percent Error for Specular Radiating Effectiveness ε=0.5

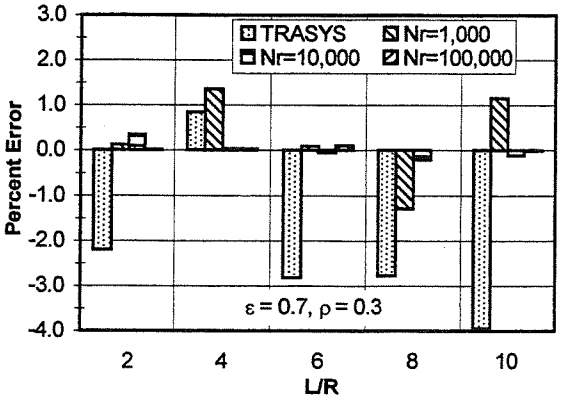

Figure 13 Cylinder Percent Error for Specular Radiating Effectiveness ε=0.7

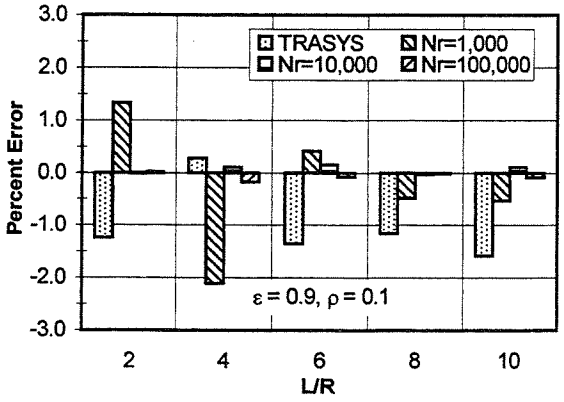

Figure 14 Cylinder Percent Error for Specular Radiating Effectiveness ε=0.9

Comparisons between the analytical solution and calculated diffuse radiating effectiveness using RadCAD were made. These comparisons are shown in Table 14 where the percent errors are listed for varying length to radius ratios for the cylinder geometry with diffuse optical properties. These comparisons were based on equation (7), Table 5, and Table 10. The number of rays shot varied from 1,000 to 100,000.

Table 14 Cylinder Percent Error for Diffuse Radiating Effectiveness

Optical Properties	L/R	Percent Error RadCAD Varying N_r 1000	10000	100000
	2	0.490	-0.532	-0.348
ε=0.1	4	-0.619	-0.959	-0.837
ρ=ρd=0.9	6	1.843	0.882	0.369
	8	-1.655	1.330	0.612
	10	0.188	-1.100	0.513
	2	0.387	-0.663	-0.999
ε=0.3	4	-0.712	0.441	-0.556
ρ=ρd=0.7	6	-0.392	-0.288	0.167
	8	-0.201	1.011	0.194
	10	-0.725	0.215	0.484
	2	0.356	-0.562	0.000
ε=0.5	4	1.443	-0.653	-0.644
ρ=ρd=0.5	6	0.850	1.137	0.115
	8	-0.134	0.277	-0.053
	10	1.113	0.050	0.133
	2	0.293	-0.495	-0.636
ε=0.7	4	-0.896	-0.788	-0.395
ρ=ρd=0.3	6	0.705	0.003	-0.449
	8	0.137	-0.744	-0.267
	10	-0.482	-0.298	-0.391
	2	-0.311	0.102	-0.645
ε=0.9	4	-0.998	0.233	-0.280
ρ=ρd=0.1	6	-0.365	-0.209	-0.200
	8	0.519	-0.267	-0.042
	10	0.031	-0.072	-0.154

Wedge

The percent error for the absorbed fluxes for solar position 1 as calculated by (7) are shown in Figure 15 through Figure 20. These figures give a comparison for RadCAD, OPERA, NEVADA, and TRASYS to the exact solution. The absorbed flux as calculated by each radiation simulation tool for solar position 2 is shown in Figure 21 through Figure 26. A comparison is made for each node. These figures are presented after the references.

Discussion

A comparison of RadCAD results to both exact analytical solutions and other radiation

simulation programs has been made. A discussion of the results will follow.

Cone

Overall the agreement between RadCAD and the analytical solution is quite good. The error from results produced by RadCAD ranged from -2.8% to 1.1% for a 1,000 rays. When 100,000 rays were shot the minimum and maximum error reduced to -1.6% and 0.36% respectively. While the minimum and maximum error produced by TRASYS was -1.39% and 1.8%. The values for the exact solution were taken from Figure 4 of Reference 4. There is some inherent uncertainty in reading this figure. The error for the diffuse results varied from -1.6% to 2.7% for 1,000 rays and -1.0% to 0.9% for 100,000 rays.

Cylinder

Overall the agreement between RadCAD and the analytical solution is quite good for the cylinder geometry. The error from results produced by RadCAD ranged from -2.0% to 2% for a 1,000 rays. When 100,000 rays were shot the minimum and maximum error reduced to -0.2% and 0.2% respectively. The TRASYS results were not quite as good the minimum and maximum error produced by TRASYS was -0.9% and 10.0%. The values for the exact solution were taken from equation (47) of Reference 4 and were evaluated by Reference 5. So, there is not the same uncertainty that existed in the cone results. The error for the diffuse results varied from -1.6% to 1.9% for 1,000 rays and -1.0% to 1.0% for 100,000 rays.

Wedge

The comparison for the absorbed fluxes was quite good. For solar position 1 RadCAD results differed by a maximum of -3.4% from the exact analytical solution for all nodes and optical properties considered. As can be seen by the data presented for the solar position 2, RadCAD results show good agreement with other radiation simulation software. This solar position offered an excellent case to verify RadCAD's ray tracing algorithms. In this case some nodes will not receive any of the incoming flux.

Conclusion

Both RadCAD's exchange factors and absorbed fluxes have been compared to exact analytical solutions and other existing radiation software tools. The agreement is good for all cases considered. RadCAD's specular capabilities can be used with confidence.

Acknowledgments

RadCAD development has been funded by the NASA Marshall Space Flight Center, with Mr. Bill Till serving as technical monitor.

References

1. Panczak, T. and Ring, S., "RadCAD: Integrating Radiation Analysis with Modern CAD Systems," SAE paper 961375, 26th ICES Conference, July 1996.

2. Panczak, T. and Ring, S., "RadCAD: Next Generation Thermal Radiation", SAE paper 972241, 27th ICES Conference, July 1997.

3. Lucas, S., "RadCAD: Validation of a New Thermal Radiation Analyzer," SAE paper 972242, 27th ICES Conference, July 1997.

4. Lin, S. H. and Sparrow, E. M., "Radiant Interchange Among Curved Specularly Reflecting Surfaces --- Application to Cylindrical and Conical Cavities," Journal of Heat Transfer, Transaction of ASME, May 1965, pp. 299-307.

5. Connolly, M. and Lucas, S., "Ray Tracing Capabilities in TRASYS," Interoffice Memorandum Martin Marietta, November 5, 1990.

6. Hering, R. G., "Radiative Heat Exchange and Equilibrium Surface Temperature in a Space Environment," Journal of Spacecraft, Vol. 5, January 1968, pp. 47-55.

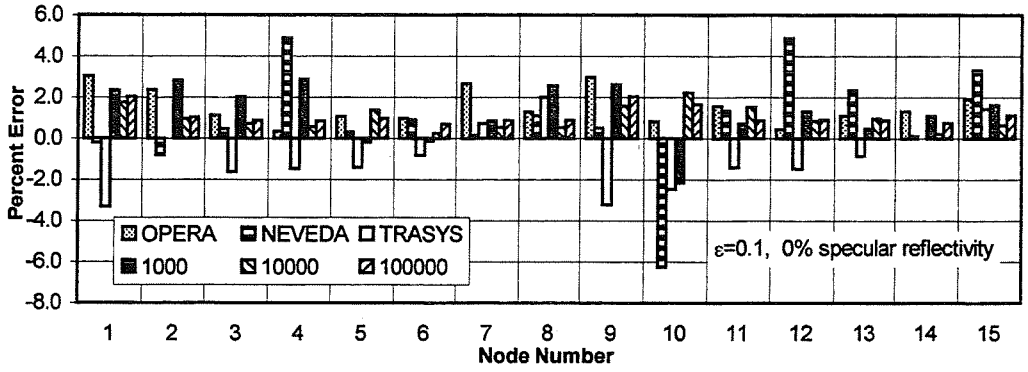

Figure 15 Wedge Percent Error for ε=0.1 and 0% Specular Reflectivity Solar Position 1

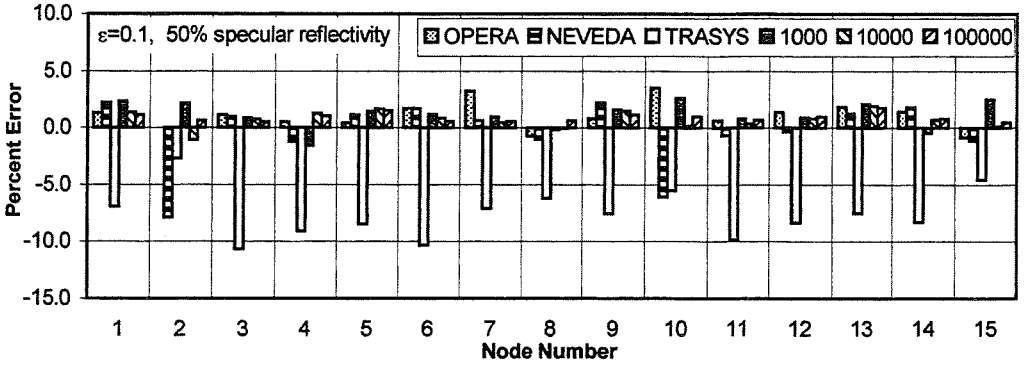

Figure 16 Wedge Percent Error for ε=0.1 and 50% Specular Reflectivity Solar Position 1

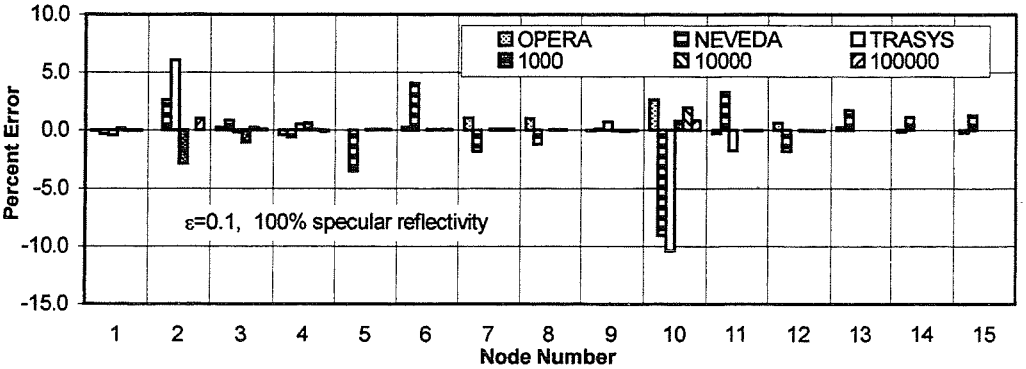

Figure 17 Wedge Percent Error for ε=0.1 and 100% Specular Reflectivity Solar Position 1

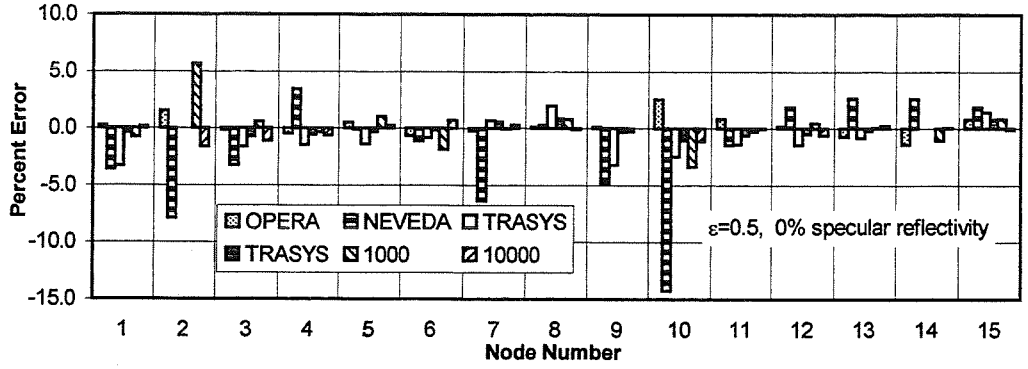

Figure 18 Wedge Percent Error for ε=0.5 and 0% Specular Reflectivity Solar Position 1

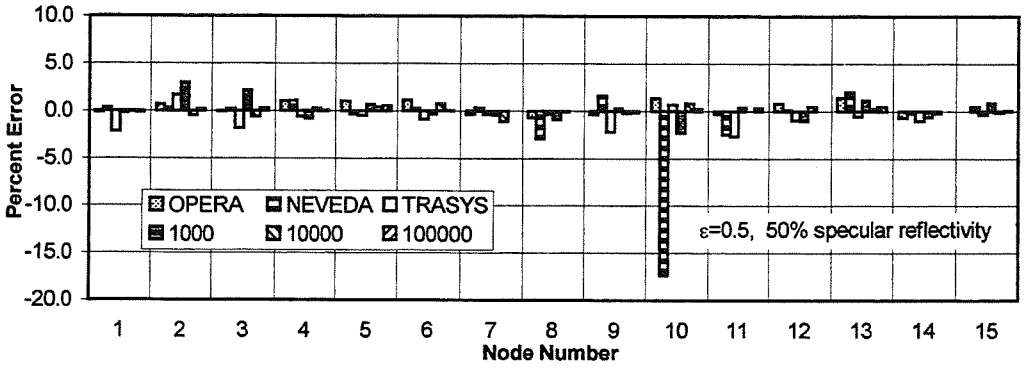

Figure 19 Wedge Percent Error for ε=0.5 and 50% Specular Reflectivity Solar Position 1

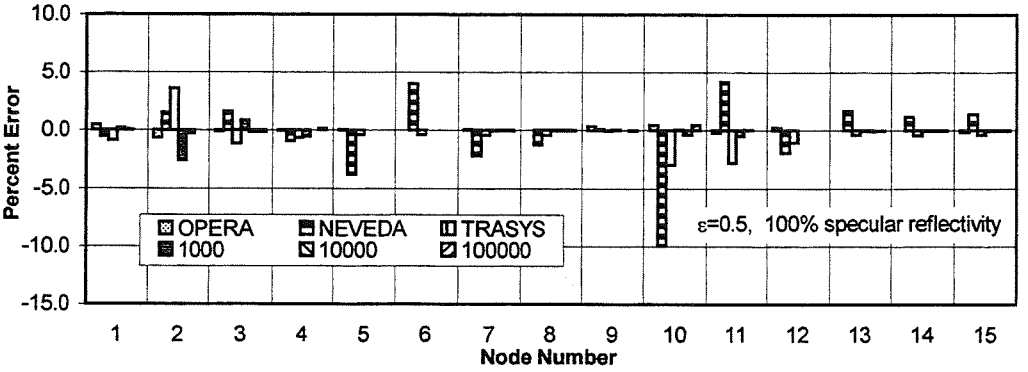

Figure 20 Wedge Percent Error for ε=0.5 and 100% Specular Reflectivity Solar Position 1

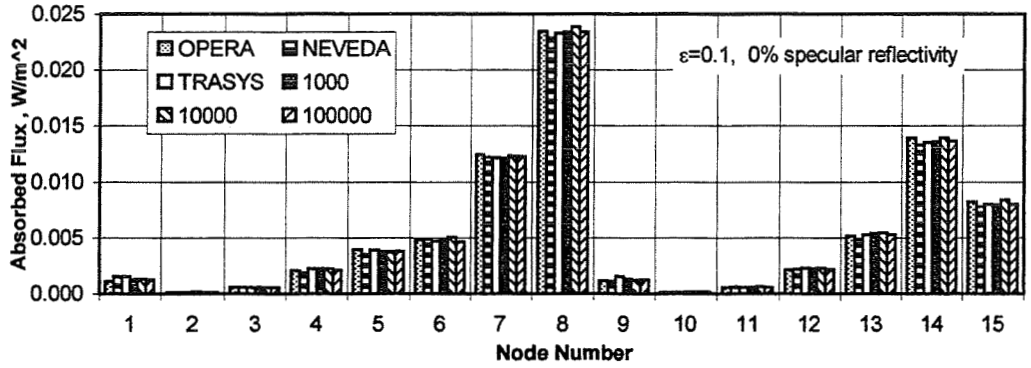

Figure 21 Wedge Absorbed Flux for ε=0.1 and 0% Specular Reflectivity Solar Position 2

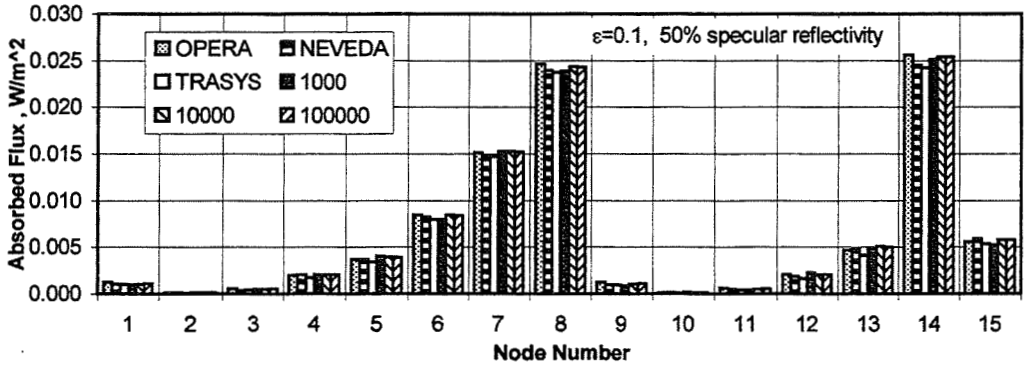

Figure 22 Wedge Absorbed Flux for ε=0.1 and 50% Specular Reflectivity Solar Position 2

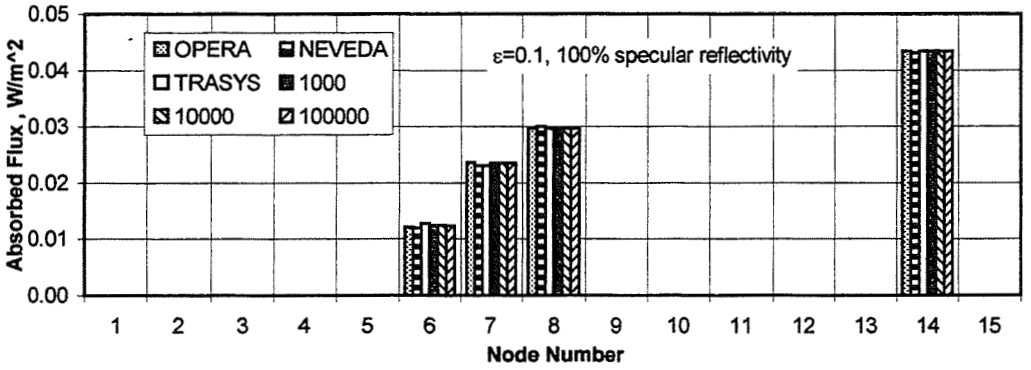

Figure 23 Wedge Absorbed Flux for ε=0.1 and 100% Specular Reflectivity Solar Position 2

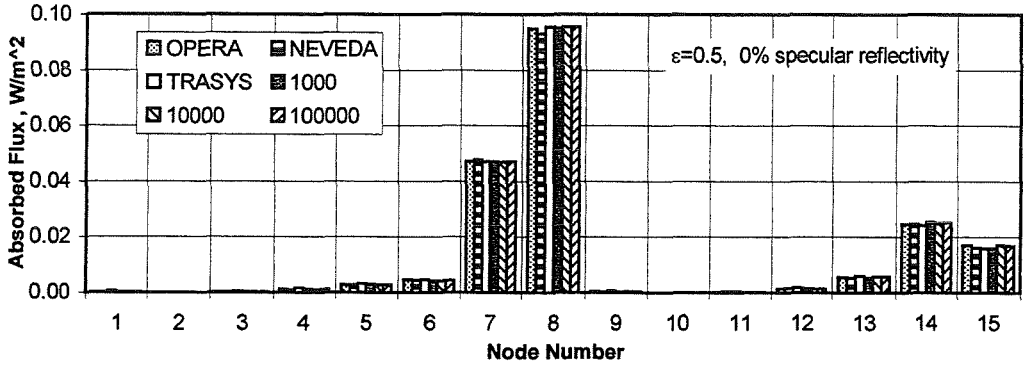

Figure 24 Wedge Absorbed Flux for ε=0.5 and 0% Specular Reflectivity Solar Position 2

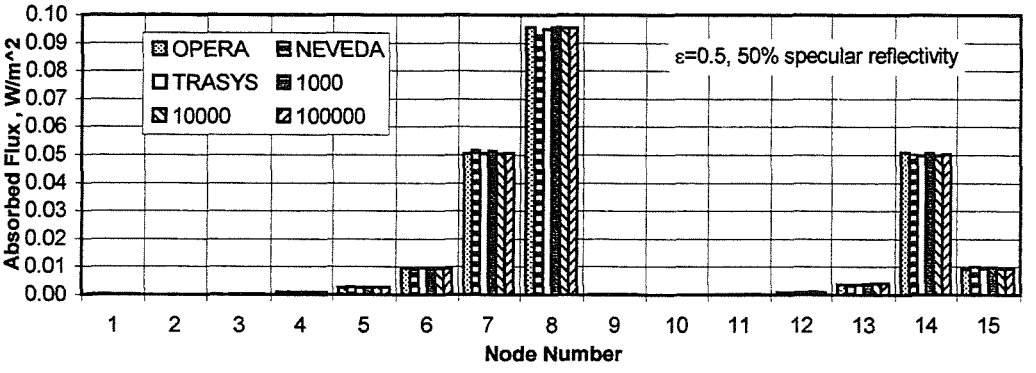

Figure 25 Wedge Absorbed Flux for ε=0.5 and 50% Specular Reflectivity Solar Position 2

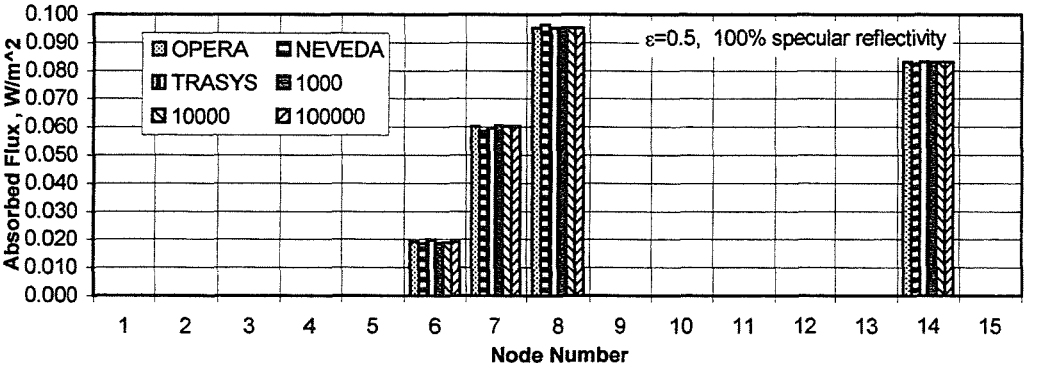

Figure 26 Wedge Absorbed Flux for ε=0.5 and 100% Specular Reflectivity Solar Position 2

THERMAL ANALYSIS WITH FINITE ELEMENTS

Perry G. Voyer
Development Engineer
Eastman Kodak Company
Rochester, NY

Abstract

Thermal analyses typically use the lumped mass approximation with a finite difference method solution technique. Lumped mass approximation applies all of the nodal mass to the center of the node. This is a good approximation and is easily formulated for finite difference method solution techniques. Finite difference methods produce an unnatural representation of irregular geometry. Finite element method solution technique accepts irregular geometry. Complex geometries can be modeled with finite elements by the application of several elemental shapes. This paper presents one-dimensional finite element and finite difference formulations. An example problem demonstrates the finite element and finite difference solution techniques for a one-dimensional transient heat transfer problem including conduction, convection, and radiation.

Nomenclature

a	Unknown Nodal Temperatures	(K)
A	Area	(m^2)
c	Specific Heat	(J/kg-K)
C	Capacitance Matrix	
CAP	Lumped Node Capacitance	(J/K)
d_1	Constant	
d_2	Constant	
dt	Differential Time	(s)
dx	Differential Length	(m)
f	Force Vector Matrix	
F	View Factor	(Dimensionless)
f(r)	Equation as a Function of r	
G^L	Linear Conductance Term	(W/K)
G^R	Radiation Conductance Term	(W/K)
h	Heat Transfer Coefficient	(W/m^2-K)
k	Thermal Conductivity	(W/m-K)
K	Element Stiffness Matrix	
L	Length	(m)
m	Number of Lumped Nodes	
n	Integer Value for Gaussian Quadrature	
N	Shape Function Matrix	
P	Perimeter	(m)
q	Heat Flux	(W/m^2)
Q	Heat Generation	(W)
r	Serendipity Coordinate System	
R	Galerkin Residual Term	
s	Local Coordinate System	
t	Time	(s)
T	Temperature	(K)
T'	Temperature at t+Δt	(K)
T_a	Ambient Fluid Temperature	(K)
T_r	Radiation Receiver Temperature	(K)
V	Volume	(m^3)
w	Gaussian Quadrature Weighting Factor	
W	Weighting Function Matrix	
x	Spacial Direction	(m)
Δt	Time Step	(s)
ε	Emissivity	(Dimensionless)
ρ	Density	(kg/m^3)
σ	Stefan-Boltzmann Constant	(W/m^2-K^4)
θ	Finite Difference Scheme Parameter	

General Superscripts and Subscripts

ai	Ambient Fluid at Element Node Location i
aj	Ambient Fluid at Element Node Location j
B	Represents Boundary Surface
cv	Convection Term
e	Represents an Element
i	Represents an Element or Lumped Node Location
j	Represents an Element or Lumped Node Location
kt	Capacitance Term
r	Radiation Term
ri	Radiation Receiver Temperature at Element Node Location i
rj	Radiation Receiver Temperature at Element Node Location j
s	Term Towards a Surface
t+1	Next Time Step
T	Transpose
x	Spacial Direction

Introduction

Thermal analyses most often use the finite difference method (FDM) solution technique. FDM solution solvers typically have limited, if any, pre- and post-graphical processing. The number of nodes are kept to a minimum for less interactive interpretation of

the results with a limited pre- and post-graphical processor. Thermal radiation interchange solution programs generally have a limited number of nodes because of the computational time they require.

Finite element method (FEM) solution techniques have powerful pre- and post-graphical processors for structural engineering applications. Pre- and post-graphical processors for thermal design applications are increasing. Graphical processors can increase the completeness of thermal models along with the accuracy of the thermal analyses while not greatly increasing the analysis time. FEM solution techniques are applicable to irregular geometries, mixed boundary conditions, nonlinear material behavior, and nonuniform loading conditions.

The FEM is an alternate solution technique to the FDM to solve the same problem. How they divide the geometry into nodes (called discretization) is fundamentally different between the two methods. The FDM uses a lumped node discretization while FEM has nodes at the edges of the geometric lump called an element in FEM terminology. Figure 1 shows the difference between discretization of FEM and FDM. Notice that the FEM has three more nodes than the FDM. The FDM calculates a lumped temperature at the centroid of the lump while the FEM uses interpolating polynomials to describe the variation of temperature within an element. The FEM has a different value at each of the four nodes which can provide temperature gradients over an element.

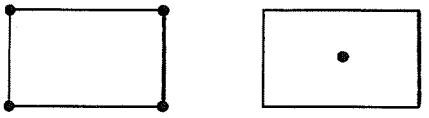

(a) (b)

Figure 1. Two types of discretization. (a) An element used for FEM. (b) A lump used for FDM.

Figure 2 shows the discretization for a rectangular plate with equally spaced nodes and with the same number of nodes for both the FDM and FEM. This discretization causes the FDM lumps at the corners to be 1/4 of the lump size of interior lumps and the edge lumps to be 1/2 of the size of the interior lumps. The FEM has elements of the same size.

Irregular geometries can be represented in FEM. FDM produces an unnatural representation of the irregular geometry and the effective plate boundary becomes jagged as can be seen in Figure 3. Irregular geometry FDM formulations are nontrivial. FEM can handle variable spacing of nodes routinely.

FDM formulation requires an energy balance to be made on each lump, which is relatively straightforward except for irregular geometries. The FEM formulation can be derived by many different techniques. This paper will limit its discussion to the Galerkin weighted residual method.

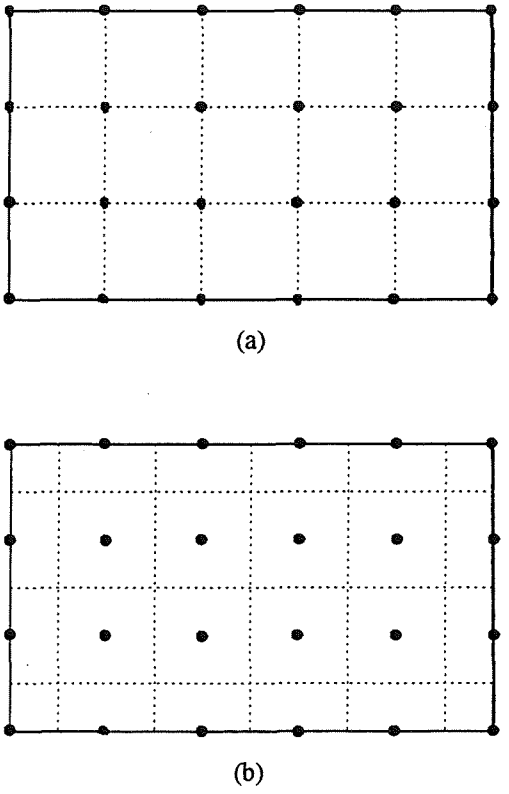

(a)

(b)

Figure 2. Rectangular plate discretized into (a) rectangular elements for FEM use and (b) lumps for FDM use.

Basic Formulations

Number of equations to be simultaneously solved with FEM or FDM can become numerous for large problems. The applicable equations can be programmed into a computer to perform the large number of computations. The accuracy generally improves for both methods as the number of elements (lumps) increases at the cost of increased computational time. The basic theory and approach to the solution of problems for both FEM and FDM is presented for a one-dimensional problem.

FEM Formulation

The governing equation for a transient one-dimensional heat transfer of a fin including conduction, convection, radiation, and internal heat

generation for temperature T, as shown in Figure 4, is given by

$$\frac{d}{dx}\left(kA\frac{dT}{dx}\right) - hP(T - T_a) - \varepsilon\sigma P(T^4 - T_r^4) + Q = \rho c\frac{dT}{dt} \quad (1)$$

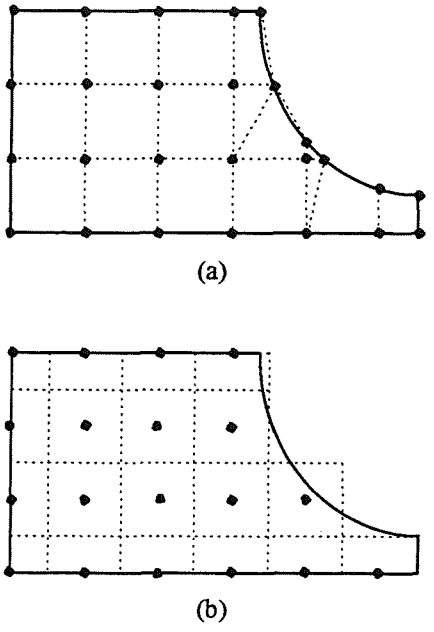

Figure 3. Irregularly shaped plate shown discretized into (a) rectangular, triangular, and quadrilateral elements for FEM use and (b) lumps for FDM use.

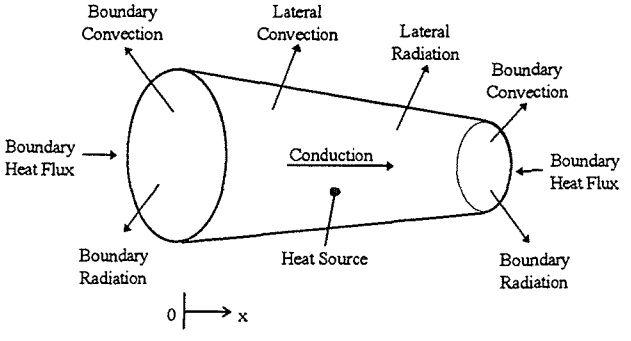

Figure 4. Schematic of one-dimensional heat transfer problem. Note that the boundary heat fluxes may act at a distance (such as the sun).

Except for σ, each of these parameters may be a function of x. In addition, the thermal properties (k, h, ρ, c, and ε) may be temperature dependent. Note that an absolute temperature scale must be used if radiation is present.

One of the most widely used FEM solution techniques is the Galerkin method. The governing equation (Equation 1) is formulated into the FEM with the Galerkin method. The Galerkin approach uses the method of weighted residuals and sets the result equal to zero. The Galerkin method is stated mathematically by

$$\sum_{e=1}^{M}\int_{V^e} W^T R^e dV = 0 \quad (2)$$

where M elements are assumed and the matrix W^T is the transpose of the weighting function matrix. V^e is the volume of the element. The exact solution results when R^e is zero for all points in the domain. For our one-dimensional problem the equation becomes

$$\sum_{e=1}^{M}\int_{L^e} N^T R^e dx = 0 \quad (3)$$

where N^T is the transpose of the shape function matrix which will be described later. L^e is the length of the one-dimensional element. The summation sign will be dropped because we are seeking the finite element characteristics for a typical element. The summation sign is for the assemblage of the complete FEM generation.

The residual term (R^e) from Equation 3 can be replaced by Equation 1 to obtain

$$\int_{L^e} N^T\left[\frac{d}{dx}\left(kA\frac{dT}{dx}\right) - hP(T - T_a) - \varepsilon\sigma P(T^4 - T_r^4) + Q - \rho cA\frac{dT}{dt}\right]dx = 0 \quad (4)$$

Integration of the first term by parts results in

$$N^T kA\frac{dT}{dx}\Big|_{x_i}^{x_j} - \int_{L^e}\frac{dN^T}{dx}kA\frac{dT}{dx}dx - \int_{L^e} N^T hPT dx + \int_{L^e} N^T hPT_a dx - \quad (5)$$

$$\int_{L^e} N^T \varepsilon\sigma P T^4 dx + \int_{L^e} N^T \varepsilon\sigma P T_r^4 dx +$$

$$\int_{L^e} N^T Q dx - \int_{L^e} N^T \rho c A \frac{dT}{dt} dx = 0$$

The first term is related to heat conduction in the x direction by Fourier's law of heat conduction and by inspection of Figure 5. It is only applicable to the elements at each end of the body; all internal contributions cancel each other during the assemblage process. The Fourier's law of heat conduction is written as

$$q_x = -k\frac{dT}{dx} \tag{6}$$

An energy balance at a boundary represented in Figure 5 gives

$$q_x + q_s = q_{cv} + q_r \tag{7}$$

q_s is positive with the heat flux imposed towards the surface. q_s can be from an external heat source such as the sun. $q_s = q_j$ at node j. From Newton's law of cooling

$$q_{cv} = h_j(T - T_{aj}) \tag{8}$$

and from the Stefan-Boltzmann law,

$$q_r = \varepsilon_j \sigma (T^4 - T_{rj}^4) \tag{9}$$

Therefore the first term from Equation 5 at $x = x_j$

$$\begin{aligned} N^T kA\frac{dT}{dx}\Big|_{x=x_j} &= N^T(-q_x A)\Big|_{x=x_j} \\ &= N^T A_j(q_s - q_{cv} - q_r)\Big|_{x=x_j} \\ &= (N^T A_j q_j - N^T A_j h_j T + \\ &\quad N^T A_j h_j T_{aj} - N^T A_j \varepsilon_j \sigma T^4 + \\ &\quad N^T A_j \varepsilon_j \sigma T_{rj}^4)\Big|_{x=x_j} \end{aligned} \tag{10}$$

A similar expression exists at $x = x_i$.

$$\begin{aligned} -N^T kA\frac{dT}{dx}\Big|_{x=x_i} &= (N^T A_i q_i - N^T A_i h_i T + \\ &\quad N^T A_i h_i T_{ai} - N^T A_i \varepsilon_i \sigma T^4 + \\ &\quad N^T A_i \varepsilon_i \sigma T_{ri}^4)\Big|_{x=x_i} \end{aligned} \tag{11}$$

The summation of Equations 10 and 11 can be taken because the minus sign is included for the term on the left of Equation 11.

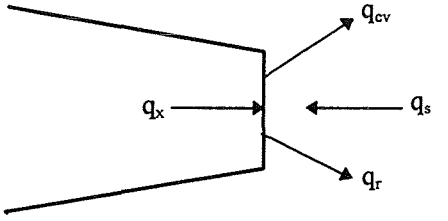

Figure 5. Typical boundary in the one-dimensional heat conduction problem showing the heat fluxes considered in the FEM formulation.

The parameter T is related to the nodal temperatures by

$$T = Na^e \tag{12}$$

T^4 can be written as

$$T^4 = T^3 T = (Na^e)^3 Na^e \tag{13}$$

$\frac{dT}{dt}$ is rewritten as

$$\frac{dT}{dt} = \frac{Na^e}{dt} = N\dot{a}^e \tag{14}$$

Equation 5 element stiffness matrix components and element capacitance term can be represented by the following after substituting Equations 12 - 14.

$$K_x^e = \int_e \frac{dN^T}{dx} kA \frac{dN}{dx} dx \tag{15}$$

$$K_{cv}^e = \int_e N^T hPN dx \tag{16}$$

$$K_r^e = \int_e N^T \varepsilon\sigma P (Na)^3 N dx \tag{17}$$

$$K_{cv_B}^e = N^T h_i A_i N\Big|_{x=x_i} + N^T h_j A_j N\Big|_{x=x_j} \tag{18}$$

$$K_{r_B}^e = N^T A_i \varepsilon_i \sigma (Na)^3 N\Big|_{x=x_i} + N^T A_j \varepsilon_j \sigma (Na)^3 N\Big|_{x=x_j} \tag{19}$$

$$C_{kt}^e = \left[\int_e N^T \rho c A N dx\right]\dot{a} \tag{20}$$

Equation 5 element nodal force vector terms are shown below

$$f_{cv}^e = \int_e N^T h P T_a dx \tag{21}$$

$$f_r^e = \int_e N^T \varepsilon \sigma P T_r^4 dx \tag{22}$$

$$f_Q^e = \int_e N^T Q dx \tag{23}$$

$$f_{cv_B}^e = N^T h_j A_j T_{aj}\Big|_{x=x_j} + N^T h_i A_i T_{ai}\Big|_{x=x_i} \tag{24}$$

$$f_{r_B}^e = N^T A_j \varepsilon_j \sigma T_{rj}^4\Big|_{x=x_j} + N^T A_i \varepsilon_i \sigma T_{ri}^4\Big|_{x=x_i} \tag{25}$$

$$f_{q_B}^e = N^T A_i q_i\Big|_{x=x_i} + N^T A_j q_j\Big|_{x=x_j} \tag{26}$$

The above terms are for a general one-dimensional element. The shape functions (N) must be evaluated to determine the element stiffness matrix, element capacitance term, and element nodal force vector terms.

FEM Shape Functions

A typical one-dimensional element has nodes at i and j at coordinates x_i and x_j, as shown in Figure 6. A polynomial representation of the one-dimensional temperature function can be represented by a unique straight line by

$$T = d_1 + d_2 x \tag{27}$$

where

$$T = T_i @ x = x_i$$
$$T = T_j @ x = x_j$$

T can be substituted to form

$$T_i = d_1 + d_2 x_i$$
$$T_j = d_1 + d_2 x_j \tag{28}$$

Solving for d_1 and d_2 and substituting into polynomial Equation 27 gives

$$T = \frac{x_j - x}{x_j - x_i} T_i + \frac{x - x_i}{x_j - x_i} T_j$$
$$= N_i T_i + N_j T_j \tag{29}$$

or

$$\{T\} = [N]\{a\} \tag{30}$$

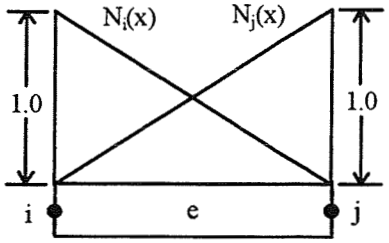

Figure 6. Shape function for two node lineal element.

The shape functions are determined for each element and then assembled with the other elements to form the global stiffness matrix, global capacitance matrix, and the global force vector. Then a system of equations are written in the form

$$C^e \dot{a}^e + K^e a^e = f^e \tag{31}$$

This system of equations are solved for the nodal temperatures, a.

FDM Formulation

The FDM formulation is not as mathematically intensive as the FEM. The terms are relatively easy to derive and apply. The one-dimensional problem above will be continued to formulate the FDM equations.

A typical FDM formulation uses the Crank-Nicholson implicit forward/backward differencing method. The basic equation to be solved is

$$\frac{2CAP_i}{\Delta t}(T_i' - T_i) = \sum_{j=1}^{m} G_{ij}^L T_j - \sum_{j=1}^{m} G_{ij}^L T_i + \sum_{j=1}^{m} G_{ij}^L T_j' - \sum_{j=1}^{m} G_{ij}^L T_i' + \sum_{j=1}^{m} G_{ij}^R T_j^4 - \sum_{j=1}^{m} G_{ij}^R T_i^4 + \sum_{j=1}^{m} G_{ij}^R (T_j')^4 - \sum_{j=1}^{m} G_{ij}^R (T_i')^4 + 2Q_i \tag{32}$$

where capacitance is calculated from

$$CAP_i = \rho cAL \tag{33}$$

conduction can be represented by

$$G_{ij}^{L} = \frac{kA}{L} \tag{34}$$

heat transfer for convection by

$$G_{ij}^{L} = hA \tag{35}$$

radiation heat transfer can be represented by

$$G_{ij}^{R} = \sigma \varepsilon A F_{ij} \tag{36}$$

Q_i is the applied heat load to a node.

Assemblage of these terms into Equation 32 will form a matrix to be solved for the nodal temperatures.

FEM Stiffness Matrix Derivations

The shape function is specific for different types of elements. The FEM formulation identified the element stiffness matrix terms (Equations 15 - 20). The thermophysical properties and geometry will be spatially constant in this paper. However, they can be a function of space, x, which is beyond the scope of this paper.

Each of the element stiffness matrix terms will be evaluated for the one-dimensional problem presented earlier. The element stiffness matrix for conduction needs the derivative of the shape functions. Derivatives of the shape functions are

$$\frac{dN_i}{dx} = \frac{d}{dx}\left(\frac{x_j - x}{x_j - x_i}\right) = -\frac{1}{L}$$
$$\frac{dN_j}{dx} = \frac{d}{dx}\left(\frac{x - x_i}{x_j - x_i}\right) = +\frac{1}{L} \tag{37}$$

Substituting these results into the spatial stiffness matrix (Equation 15)

$$K_x^e = kA\int_{x_i}^{x_j}\begin{bmatrix} -\frac{1}{L} \\ +\frac{1}{L} \end{bmatrix}\begin{bmatrix} -\frac{1}{L} & +\frac{1}{L} \end{bmatrix} dx \tag{38}$$

which results in

$$K_x^e = \frac{kA}{L}\begin{bmatrix} 1 & -1 \\ -1 & 1 \end{bmatrix} \tag{39}$$

where it was assumed k and A are constant.

The convection stiffness matrix term can be written as

$$K_{cv}^e = hP\int_{x_i}^{x_j}\begin{bmatrix} \frac{x_j - x}{L} \\ \frac{x - x_i}{L} \end{bmatrix}\begin{bmatrix} \frac{x_j - x}{L} & \frac{x - x_i}{L} \end{bmatrix} dx \tag{40}$$

The integral is simplified by developing a new shape function defined relative to a coordinate system whose origin is located on the element as shown in Figure 7. This type of system is called a local coordinate system. The shape function for a coordinate system located at node i is obtained by replacing x by $x = x_i + s$. This substitution produces

$$K_{cv}^e = hP\int_0^L \begin{bmatrix} 1 - \frac{s}{L} \\ \frac{s}{L} \end{bmatrix}\begin{bmatrix} 1 - \frac{s}{L} & \frac{s}{L} \end{bmatrix} ds \tag{41}$$

after integration

$$K_{cv}^e = \frac{hPL}{6}\begin{bmatrix} 2 & 1 \\ 1 & 2 \end{bmatrix} \tag{42}$$

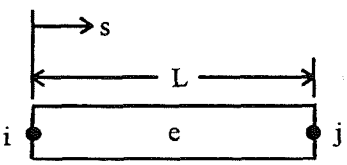

Figure 7. Two-node lineal element showing local coordinate system s.

The radiation term of the stiffness matrix is mathematically convenient to use the serendipity form of the shape function. Shape function in serendipity coordinates is shown in Figure 8 and is given by

$$N_i = \tfrac{1}{2}(1 - r)$$
$$N_j = \tfrac{1}{2}(1 + r) \tag{43}$$

where

$$r = \frac{2(x-\bar{x})}{x_j - x_i} = \frac{x-\bar{x}}{L/2}$$

$$\bar{x} = \frac{x_i + x_j}{2} \tag{44}$$

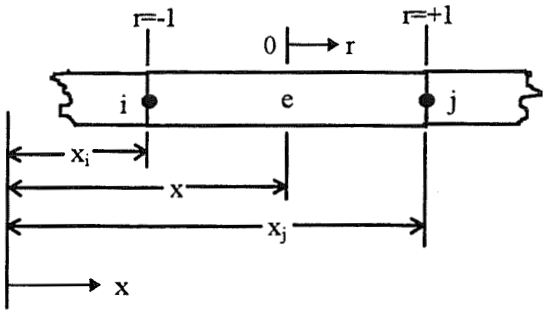

Figure 8. Two-node lineal element showing global coordinate x and serendipity coordinate r.

The radiation matrix term can be written with these serendipity coordinate definition of shape function as

$$K_r^e = \int_{-1}^{+1} N^T \varepsilon\sigma P (Na^e)^3 N \frac{L}{2} dr \tag{45}$$

$$= \int_{-1}^{+1} \frac{\varepsilon\sigma PL}{8} \begin{bmatrix} 1-r \\ 1+r \end{bmatrix} \begin{bmatrix} 1-r & 1+r \end{bmatrix} \left[\tfrac{1}{2}(1-r)T_i + \tfrac{1}{2}(1+r)T_j \right]^3 dr \tag{46}$$

$$= \int_{-1}^{+1} \frac{\varepsilon\sigma PL}{8} \begin{bmatrix} (1-r)^2 & (1-r)(1+r) \\ (1-r)(1+r) & (1+r)^2 \end{bmatrix} \left[\tfrac{1}{2}(1-r)T_i + \tfrac{1}{2}(1+r)T_j \right]^3 dr \tag{47}$$

The above result contains the unknown nodal temperatures (T_i and T_j), which results in a nonlinear equation. This integral can be evaluated with an iterative solution by using the Gauss-Legendre quadrature method.

The convection stiffness matrix term at the boundary must have the shape functions evaluated at x = x_i and x = x_j.

$$\begin{aligned} N_i(x_i) &= 1 \\ N_j(x_i) &= 0 \\ N_i(x_j) &= 0 \\ N_j(x_j) &= 1 \end{aligned} \tag{48}$$

hence

$$K_{cv_B}^e = \begin{bmatrix} 1 \\ 0 \end{bmatrix} h_i A_i \begin{bmatrix} 1 & 0 \end{bmatrix} + \begin{bmatrix} 0 \\ 1 \end{bmatrix} h_j A_j \begin{bmatrix} 0 & 1 \end{bmatrix} \tag{49}$$

$$K_{cv_B}^e = \begin{bmatrix} h_i A_i & 0 \\ 0 & h_j A_j \end{bmatrix} \tag{50}$$

The above equation is for a boundary element with convection present at both ends. Naturally, one of the hA terms will be 0 when no convection is present at an end.

The radiation stiffness matrix term at the boundary is similar to the convection stiffness matrix term at the boundary.

$$K_{r_B}^e = \begin{bmatrix} 1 \\ 0 \end{bmatrix} A_i \varepsilon_i \sigma (T_i)^3 \begin{bmatrix} 1 & 0 \end{bmatrix} + \begin{bmatrix} 0 \\ 1 \end{bmatrix} A_j \varepsilon_j \sigma (T_j)^3 \begin{bmatrix} 0 & 1 \end{bmatrix} \tag{51}$$

$$K_{r_B}^e = \begin{bmatrix} A_i \varepsilon_i \sigma T_i^3 & 0 \\ 0 & A_j \varepsilon_j \sigma T_j^3 \end{bmatrix} \tag{52}$$

Equation 52 is nonlinear and is solved interactively.

Element capacitance term is similar to the convection stiffness matrix term from Equation 41.

$$C_{kt}^e = \rho c A \int_0^L \begin{bmatrix} 1-\frac{s}{L} \\ \frac{s}{L} \end{bmatrix} \begin{bmatrix} 1-\frac{s}{L} & \frac{s}{L} \end{bmatrix} ds \tag{53}$$

$$C_{kt}^e = \frac{\rho c A L}{6} \begin{bmatrix} 2 & 1 \\ 1 & 2 \end{bmatrix} \tag{54}$$

The force vector matrix terms can be derived by the techniques shown for the stiffness matrix terms.

$$f_{cv}^e = hPT_a \int_0^L \begin{bmatrix} 1-\frac{s}{L} \\ \frac{s}{L} \end{bmatrix} ds \tag{55}$$

$$f_{cv}^e = \frac{hPLT_a}{2} \begin{bmatrix} 1 \\ 1 \end{bmatrix} \tag{56}$$

Similarly,

$$f_r^e = \frac{\varepsilon\sigma PLT_r^4}{2}\begin{bmatrix}1\\1\end{bmatrix} \quad (57)$$

$$f_Q^e = \frac{QL}{2}\begin{bmatrix}1\\1\end{bmatrix} \quad (58)$$

The force vector matrix terms at the boundary is

$$f_{cv_B}^e = \begin{bmatrix}1\\0\end{bmatrix}h_i A_i T_{ai} + \begin{bmatrix}0\\1\end{bmatrix}h_j A_j T_{aj} \quad (59)$$

$$f_{cv_B}^e = \begin{bmatrix}h_i A_i T_{ai}\\ h_j A_j T_{aj}\end{bmatrix} \quad (60)$$

Similarly

$$f_{r_B}^e = \begin{bmatrix}A_i\varepsilon_i\sigma T_{ri}^4\\ A_j\varepsilon_j\sigma T_{rj}^4\end{bmatrix} \quad (61)$$

$$f_{q_B}^e = \begin{bmatrix}A_i q_i\\ A_j q_j\end{bmatrix} \quad (62)$$

All these terms are combined in the following equation

$$C^e\dot{a}^e + K^e a^e = f^e \quad (63)$$

where

$$C^e = C_{kt}^e$$

$$K^e = K_x^e + K_{cv}^e + K_r^e + K_{cv_B}^e + K_{r_B}^e \quad (64)$$

$$f^e = f_{cv}^e + f_r^e + f_Q^e + f_{cv_B}^e + f_{r_B}^e + f_{q_B}^e$$

Substituting the terms into equations 63 and 64 leads to

$$\frac{\rho cAL}{6}\begin{bmatrix}2 & 1\\ 1 & 2\end{bmatrix}\begin{Bmatrix}\frac{dT_i}{dt}\\ \frac{dT_j}{dt}\end{Bmatrix} + \begin{bmatrix}\frac{kA}{L}\begin{bmatrix}1 & -1\\ -1 & 1\end{bmatrix} + \frac{hPL}{6}\begin{bmatrix}2 & 1\\ 1 & 2\end{bmatrix}\end{bmatrix}$$

$$+\int_{-1}^{+1}\frac{\varepsilon\sigma PL}{8}\begin{bmatrix}(1-r)^2 & (1-r)(1+r)\\ (1-r)(1+r) & (1+r)^2\end{bmatrix}$$

$$\left[\tfrac{1}{2}(1-r)T_i + \tfrac{1}{2}(1+r)T_j\right]^3 dr +$$

$$\begin{bmatrix}h_i A_i & 0\\ 0 & h_j A_j\end{bmatrix} + \begin{bmatrix}A_i\varepsilon_i\sigma T_i^3 & 0\\ 0 & A_j\varepsilon_j\sigma T_j^3\end{bmatrix}\begin{Bmatrix}T_i\\ T_j\end{Bmatrix} =$$

$$\begin{bmatrix}\frac{hPLT_a}{2}\begin{bmatrix}1\\1\end{bmatrix} + \frac{\varepsilon\sigma PLT_r^4}{2}\begin{bmatrix}1\\1\end{bmatrix} + \frac{QL}{2}\begin{bmatrix}1\\1\end{bmatrix} +\end{bmatrix} \quad (65)$$

$$\begin{bmatrix}h_i A_i T_{ai}\\ h_j A_j T_{aj}\end{bmatrix} + \begin{bmatrix}A_i\varepsilon_i\sigma T_{ri}^4\\ A_j\varepsilon_j\sigma T_{rj}^4\end{bmatrix} + \begin{bmatrix}A_i q_i\\ A_j q_j\end{bmatrix}$$

Example Problem

An example problem is shown solved with the FEM and FDM solution techniques.

FEM Solution

Equation 65 is the governing one-dimensional FEM equation. It assumes constant thermophysical properties. The nonlinear radiation terms causes an iterative solution process. The following iterative solution procedure is adopted.

1. Calculate the non-radiation terms.
2. Assemble the terms to obtain an overall equation.
3. Calculate the radiation term based upon the initial temperatures.
4. Assemble all the terms to obtain the overall equation.
5. Solve the overall equation for the unknown temperatures.
6. Repeat steps 3 through 5 with the radiation terms until the calculated temperature error converges to a specified small number.
7. Repeat steps 3 through 6 for each time step for the desired elapsed time. Use the calculated temperatures from step 6 as the new initial temperatures for step 3.

This procedure is implemented below for a one-dimensional problem with three linear elements as shown in Figure 9. The following thermophysical and geometrical values are given below:

$\rho = 2768$ kg/m^3
c = 921.1 J/kg-K
dt = 0.1 seconds
D = 0.025 m
$A = \pi D^2/4 = 4.909 \times 10^{-4}$ m^2
$L_T = 0.075$ m $\Rightarrow L_e = 0.025$ m
k = 180.7 W/m-K
h = 183 W/m^2-K
$P = \pi D = 0.07854$ m

$\varepsilon = 0.8$
$\sigma = 5.67 \times 10^{-8}$ W/m^2-K^4
$T_a = 300$ K
$T_r = 300$ K
$Q = 50$ W => 2000 W/m
$q = 1400$ W/m^2
$T_1 = 600$ K
$T_{initial} = 450$ K

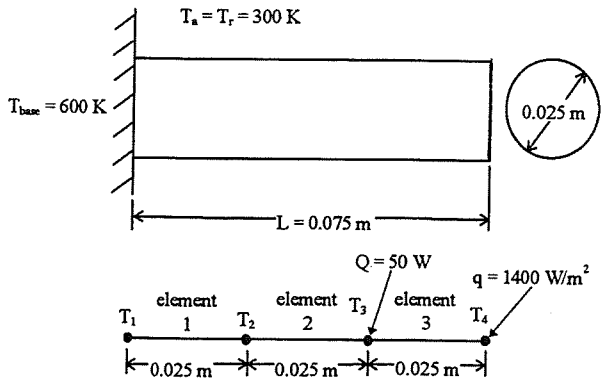

Figure 9. FEM schematic of one-dimensional example problem.

Substitution of these values into Equation 65 for element one produces

$$5.21\begin{bmatrix}2 & 1\\ 1 & 2\end{bmatrix}\begin{Bmatrix}\frac{dT_1}{dt}\\ \frac{dT_2}{dt}\end{Bmatrix}+\begin{bmatrix}3.55\begin{bmatrix}1 & -1\\ -1 & 1\end{bmatrix}+\end{bmatrix}$$
$$0.0599\begin{bmatrix}2 & 1\\ 1 & 2\end{bmatrix}+\begin{bmatrix}0 & 0\\ 0 & 0\end{bmatrix}+\begin{bmatrix}0 & 0\\ 0 & 0\end{bmatrix}+ \qquad (66)$$
$$\begin{bmatrix}0 & 0\\ 0 & 0\end{bmatrix}\begin{Bmatrix}T_1\\ T_2\end{Bmatrix}=\begin{bmatrix}53.9\\ 53.9\end{bmatrix}+\begin{bmatrix}0.361\\ 0.361\end{bmatrix}+$$
$$\begin{bmatrix}0\\ 0\end{bmatrix}+\begin{bmatrix}0\\ 0\end{bmatrix}+\begin{bmatrix}0\\ 0\end{bmatrix}+\begin{bmatrix}0\\ 0\end{bmatrix}$$

Similar equations can be written for elements two and three. A total of 50 W is shown applied to node 3.

$$5.21\begin{bmatrix}2 & 1\\ 1 & 2\end{bmatrix}\begin{Bmatrix}\frac{dT_2}{dt}\\ \frac{dT_3}{dt}\end{Bmatrix}+\begin{bmatrix}3.55\begin{bmatrix}1 & -1\\ -1 & 1\end{bmatrix}+\end{bmatrix}$$
$$0.0599\begin{bmatrix}2 & 1\\ 1 & 2\end{bmatrix}+\begin{bmatrix}0 & 0\\ 0 & 0\end{bmatrix}+\begin{bmatrix}0 & 0\\ 0 & 0\end{bmatrix}+$$
$$\begin{bmatrix}0 & 0\\ 0 & 0\end{bmatrix}\begin{Bmatrix}T_2\\ T_3\end{Bmatrix}=\begin{bmatrix}53.9\\ 53.9\end{bmatrix}+\begin{bmatrix}0.361\\ 0.361\end{bmatrix}+ \qquad (67)$$
$$\begin{bmatrix}0\\ 25.0\end{bmatrix}+\begin{bmatrix}0\\ 0\end{bmatrix}+\begin{bmatrix}0\\ 0\end{bmatrix}+\begin{bmatrix}0\\ 0\end{bmatrix}$$

$$5.21\begin{bmatrix}2 & 1\\ 1 & 2\end{bmatrix}\begin{Bmatrix}\frac{dT_3}{dt}\\ \frac{dT_4}{dt}\end{Bmatrix}+\begin{bmatrix}3.55\begin{bmatrix}1 & -1\\ -1 & 1\end{bmatrix}+\end{bmatrix}$$
$$0.0599\begin{bmatrix}2 & 1\\ 1 & 2\end{bmatrix}+\begin{bmatrix}0 & 0\\ 0 & 0\end{bmatrix}+\begin{bmatrix}0 & 0\\ 0 & 0.0898\end{bmatrix}+ \qquad (68)$$
$$\begin{bmatrix}0 & 0\\ 0 & 0\end{bmatrix}\begin{Bmatrix}T_3\\ T_4\end{Bmatrix}=\begin{bmatrix}53.9\\ 53.9\end{bmatrix}+\begin{bmatrix}0.361\\ 0.361\end{bmatrix}+$$
$$\begin{bmatrix}25.0\\ 0\end{bmatrix}+\begin{bmatrix}0\\ 26.9\end{bmatrix}+\begin{bmatrix}0\\ 0.180\end{bmatrix}+\begin{bmatrix}0\\ 0.687\end{bmatrix}$$

These equations can be rewritten as

$$\begin{bmatrix}10.4 & 5.21\\ 5.21 & 10.4\end{bmatrix}\begin{Bmatrix}\frac{dT_1}{dt}\\ \frac{dT_2}{dt}\end{Bmatrix}+ \qquad (69a)$$
$$\begin{bmatrix}3.67 & -3.49\\ -3.49 & 3.67\end{bmatrix}\begin{Bmatrix}T_1\\ T_2\end{Bmatrix}=\begin{bmatrix}54.3\\ 54.3\end{bmatrix}$$

$$\begin{bmatrix}10.4 & 5.21\\ 5.21 & 10.4\end{bmatrix}\begin{Bmatrix}\frac{dT_2}{dt}\\ \frac{dT_3}{dt}\end{Bmatrix}+ \qquad (69b)$$
$$\begin{bmatrix}3.67 & -3.49\\ -3.49 & 3.67\end{bmatrix}\begin{Bmatrix}T_2\\ T_3\end{Bmatrix}=\begin{bmatrix}54.3\\ 79.3\end{bmatrix}$$

$$\begin{bmatrix}10.4 & 5.21\\ 5.21 & 10.4\end{bmatrix}\begin{Bmatrix}\frac{dT_3}{dt}\\ \frac{dT_4}{dt}\end{Bmatrix}+ \qquad (69c)$$
$$\begin{bmatrix}3.67 & -3.49\\ -3.49 & 3.76\end{bmatrix}\begin{Bmatrix}T_3\\ T_4\end{Bmatrix}=\begin{bmatrix}79.3\\ 82.1\end{bmatrix}$$

The equations for the three elements can be assembled as

$$\begin{bmatrix} 10.4 & 5.21 & 0 & 0 \\ 5.21 & 10.4+10.4 & 5.21 & 0 \\ 0 & 5.21 & 10.4+10.4 & 5.21 \\ 0 & 0 & 5.21 & 10.4 \end{bmatrix} \begin{Bmatrix} \frac{dT_1}{dt} \\ \frac{dT_2}{dt} \\ \frac{dT_3}{dt} \\ \frac{dT_4}{dt} \end{Bmatrix} +$$

$$\begin{bmatrix} 3.67 & -3.49 & 0 & 0 \\ -3.49 & 3.67+3.67 & -3.49 & 0 \\ 0 & -3.49 & 3.67+3.67 & -3.49 \\ 0 & 0 & -3.49 & 3.76 \end{bmatrix} \begin{Bmatrix} T_1 \\ T_2 \\ T_3 \\ T_4 \end{Bmatrix} =$$

$$\begin{bmatrix} 54.3 \\ 54.3+54.3 \\ 79.3+79.3 \\ 82.1 \end{bmatrix} \tag{70}$$

The initial temperatures are used to calculate the radiation terms. The radiation terms are calculated by using the Gaussian quadrature (numerical integration) method. This method evaluates integrals such as

$$I = \int_{-1}^{+1} f(r)dr \tag{71}$$

This integral can be approximated by writing

$$I = \int_{-1}^{+1} f(r)dr = \sum_{i=1}^{n} w_i f(r_i) \tag{72}$$

This integral is evaluated by summing the results at each value of $f(r_i)$ multiplied by the appropriate weighting factor w_i at several sampling points n. Gauss's method chooses the sampling points so that for a given number of points, the best possible accuracy is obtained. Sampling points are located symmetrically with respect to the center of the interval. The number of sampling points can be determined by setting the order of the polynomial equal to 2n - 1. n must be rounded to the next largest integer. Table 1 shows the sampling points and weighting factors for up to three sampling points.

The radiation term is shown below

$$K_r^e = \int_{-1}^{+1} \frac{\varepsilon\sigma PL}{8} \begin{bmatrix} (1-r)^2 & (1-r)(1+r) \\ (1-r)(1+r) & (1+r)^2 \end{bmatrix} \left[\tfrac{1}{2}(1-r)T_i + \tfrac{1}{2}(1+r)T_j\right]^3 dr \tag{73}$$

Table 1. Gaussian Quadrature.

$$I = \int_{-1}^{+1} f(r)dr = \sum_{i=1}^{n} w_i f(r_i)$$

r_i	w_i
n = 1	
0.000000	2.000000
n = 2	
±0.577350	1.000000
n = 3	
0.000000	0.888889
±0.774597	0.555556

This term has a polynomial order of five. Therefore the number of sampling points required for an exact solution is three (5=2n - 1). The first term in the radiation matrix is evaluated with the initial temperatures. The Gaussian quadrature solution process is shown in Table 2.

Table 2. Gaussian Quadrature Solution Process.

i	r_i	w_i	$f(r_i)$	$w_i f(r_i)$
1	-0.774597	0.555556	6.24×10^8	3.47×10^8
2	0.000000	0.888889	1.45×10^8	1.29×10^8
3	0.774597	0.555556	5.17×10^6	2.87×10^6
			$\Sigma =$	4.78×10^8

This process is repeated for the remaining terms in the radiation matrix. The temperatures are also used in the boundary radiation term to produce

$$K_r^e = \frac{\varepsilon\sigma PL}{8} \begin{bmatrix} 4.80 & 1.97 & 0 & 0 \\ 1.97 & 5.62 & 1.22 & 0 \\ 0 & 1.22 & 4.86 & 1.21 \\ 0 & 0 & 1.21 & 2.43 \end{bmatrix} x10^8 \tag{74}$$

$$K_{r_B}^e = \begin{bmatrix} 0.00481 & 0 & 0 & 0 \\ 0 & 0 & 0 & 0 \\ 0 & 0 & 0 & 0 \\ 0 & 0 & 0 & 0.00203 \end{bmatrix} \tag{75}$$

Assemblage of the radiation terms into Equation 70 results in

$$\begin{bmatrix} 10.4 & 5.21 & 0 & 0 \\ 5.21 & 20.9 & 5.21 & 0 \\ 0 & 5.21 & 20.9 & 5.21 \\ 0 & 0 & 5.21 & 10.4 \end{bmatrix} \begin{Bmatrix} \frac{dT_1}{dt} \\ \frac{dT_2}{dt} \\ \frac{dT_3}{dt} \\ \frac{dT_4}{dt} \end{Bmatrix} +$$

$$\begin{bmatrix} 3.67 & -3.49 & 0 & 0 \\ -3.49 & 7.34 & -3.49 & 0 \\ 0 & -3.49 & 7.34 & -3.49 \\ 0 & 0 & -3.49 & 3.76 \end{bmatrix} \begin{Bmatrix} T_1 \\ T_2 \\ T_3 \\ T_4 \end{Bmatrix} = \begin{bmatrix} 54.3 \\ 108.5 \\ 158.5 \\ 82.1 \end{bmatrix} \tag{76}$$

The solution method to the above equation may be accomplished by the two-point recurrence scheme to solve transient thermal analyses of the form

$$C^e \dot{a}^e + K^e a^e = f^e \tag{77}$$

Three different solution methods can be implemented for the solution of Equation 77 by using three different types of finite difference methods on the equation. The three finite difference methods used are the forward, central, and backward difference schemes. The resulting derivations can be summarized into one convenient equation as

$$[C + \theta K dt]a_{t+1} = [C - (1-\theta)Kdt]a_t + [(1-\theta)f_t + \theta f_{t+1}]dt \tag{78}$$

where the parameter θ takes on the values of 0, 1/2, and 1 for the forward, central, and backward difference schemes, respectively. The parameter value θ for FEM can be shown to be either 1/3 or 2/3 based on the Galerkin method. Neither of these values corresponds to any of the results from the finite difference schemes. However, θ = 2/3 is particularly useful because it is more accurate than the backward difference scheme and more stable than the central difference scheme.

The last term in Equation 78 can be simplified to $f_t dt$ with θ = 2/3 since the force vector does not change with time.

Equation 76 can be reformulated into the finite difference scheme for our example as

$$\left[\begin{bmatrix} 10.4 & 5.21 & 0 & 0 \\ 5.21 & 20.9 & 5.21 & 0 \\ 0 & 5.21 & 20.9 & 5.21 \\ 0 & 0 & 5.21 & 10.4 \end{bmatrix} + \frac{2}{3}(0.1) \begin{bmatrix} 3.67 & -3.49 & 0 & 0 \\ -3.49 & 7.34 & -3.49 & 0 \\ 0 & -3.49 & 7.34 & -3.49 \\ 0 & 0 & -3.49 & 3.76 \end{bmatrix} \right] \begin{Bmatrix} T_{1_{t+1}} \\ T_{2_{t+1}} \\ T_{3_{t+1}} \\ T_{4_{t+1}} \end{Bmatrix} =$$

$$\left[\begin{bmatrix} 10.4 & 5.21 & 0 & 0 \\ 5.21 & 20.9 & 5.21 & 0 \\ 0 & 5.21 & 20.9 & 5.21 \\ 0 & 0 & 5.21 & 10.4 \end{bmatrix} - (1-\frac{2}{3})(0.1) \begin{bmatrix} 3.67 & -3.49 & 0 & 0 \\ -3.49 & 7.34 & -3.49 & 0 \\ 0 & -3.49 & 7.34 & -3.49 \\ 0 & 0 & -3.49 & 3.76 \end{bmatrix} \right] \begin{Bmatrix} T_1 \\ T_2 \\ T_3 \\ T_4 \end{Bmatrix} +$$

$$\begin{bmatrix} 54.3 \\ 108.5 \\ 158.5 \\ 82.1 \end{bmatrix} (0.1) \tag{79}$$

which can be rewritten as

$$\begin{bmatrix} 10.7 & 4.98 & 0 & 0 \\ 4.98 & 21.4 & 4.98 & 0 \\ 0 & 4.98 & 21.4 & 4.98 \\ 0 & 0 & 4.98 & 10.7 \end{bmatrix} \begin{Bmatrix} T_{1_{t+1}} \\ T_{2_{t+1}} \\ T_{3_{t+1}} \\ T_{4_{t+1}} \end{Bmatrix} =$$

$$\begin{bmatrix} 10.3 & 5.33 & 0 & 0 \\ 5.33 & 20.6 & 5.33 & 0 \\ 0 & 5.33 & 20.6 & 5.33 \\ 0 & 0 & 5.33 & 10.3 \end{bmatrix} \begin{Bmatrix} T_1 \\ T_2 \\ T_3 \\ T_4 \end{Bmatrix} + \begin{bmatrix} 5.43 \\ 10.9 \\ 15.9 \\ 8.21 \end{bmatrix} \tag{80}$$

Substituting the initial temperatures into the right side of Equation 80 results in

$$\begin{bmatrix} 10.7 & 4.98 & 0 & 0 \\ 4.98 & 21.4 & 4.98 & 0 \\ 0 & 4.98 & 21.4 & 4.98 \\ 0 & 0 & 4.98 & 10.7 \end{bmatrix} \begin{Bmatrix} T_{1_{t+1}} \\ T_{2_{t+1}} \\ T_{3_{t+1}} \\ T_{4_{t+1}} \end{Bmatrix} = \begin{bmatrix} 8589 \\ 14885 \\ 14090 \\ 7044 \end{bmatrix} \tag{81}$$

T_1 is a boundary temperature and does not change with time. Equation 81 becomes

$$\begin{bmatrix} 1 & 0 & 0 & 0 \\ 0 & 21.4 & 4.98 & 0 \\ 0 & 4.98 & 21.4 & 4.98 \\ 0 & 0 & 4.98 & 10.7 \end{bmatrix} \begin{Bmatrix} T_{1_{t+1}} \\ T_{2_{t+1}} \\ T_{3_{t+1}} \\ T_{4_{t+1}} \end{Bmatrix} = \begin{bmatrix} 600 \\ 11896 \\ 14090 \\ 7044 \end{bmatrix} \quad (82)$$

This overall equation can be solved for the temperatures at dt = 0.1 seconds. These temperatures can be used to calculate a new radiation matrix. This process is repeated until the temperature difference during the iterative process is a small number.

The temperatures calculated at dt = 0.1 seconds are then used to calculate the temperatures at dt = 0.2 seconds in the same manner as shown above. The initial temperatures for the radiation terms at dt = 0.2 seconds is given by the resulting temperatures at dt = 0.1 seconds.

The result for this example over time is shown below in Table 3.

Table 3. Example Problem Temperature Solution.

Time, seconds	Temperature, °F		
	T_2	T_3	T_4
0.0	450.0	450.0	450.0
0.1	452.3	449.5	449.9
0.2	454.5	449.0	449.7
0.3	456.6	448.7	449.4
0.4	458.6	448.4	449.2
0.5	460.5	448.2	448.8

The temperatures in Table 3 are physically unreasonable. This initial oscillation is a characteristic of a solution with a consistent capacitance matrix (C^e_{kt}). A lumped capacitance matrix tends to produce smooth initial temperatures.

Consistent Verses Lumped Capacitance Matrix

The consistent capacitance matrix is shown below

$$C^e_{kt} = \frac{\rho cAL}{6}\begin{bmatrix} 2 & 1 \\ 1 & 2 \end{bmatrix} \quad (83)$$

The lumped capacitance matrix is obtained by summing the entries in a given row in the consistent matrix, dividing the result by the total capacitance, and allocating this result to the diagonal entry of the row under consideration. The lumped capacitance matrix is

$$C^e_{kt} = \frac{\rho cAL}{2}\begin{bmatrix} 1 & 0 \\ 0 & 1 \end{bmatrix} \quad (84)$$

The lumped capacitance matrix is similar to the FDM capacitance. The results with a lumped capacitance matrix is shown in Table 4.

Table 4. Example Problem Temperature Solution with a Lumped Capacitance Matrix.

Time, seconds	Temperature, °F		
	T_2	T_3	T_4
0.0	450.0	450.0	450.0
0.1	451.5	450.0	449.7
0.2	452.9	450.0	449.5
0.3	454.3	450.0	449.2
0.4	455.7	450.0	449.0
0.5	457.0	450.1	448.7

This corresponds well with a FDM solution.

FDM Solution

Equation 32 is the governing FDM equation. Equations 33 through 36 are the equations for the terms in Equation 32. The following are the values for Equations 33 through 36.

$$CAP_1 = CAP_4 = \rho cAL_e/2 = 2768*921.1 *(4.909x10^{-4)} *0.025/2 = 15.65$$

$$CAP_2 = CAP_3 = \rho cAL_e = 31.29$$

$$G^L_{12} = G^L_{23} = G^L_{34} = kA/L_e = 180.7 *(4.909x10^{-4})/0.025 = 3.548$$

$$G^L_{1a} = hPL_e/2 = 183*0.07854*0.025/2 = 0.1797$$

$$G^L_{2a} = G^L_{3a} = hPL_e = 183*0.07854*0.025 = 0.3593$$

$$G^L_{4a} = h(A + PL_e/2) = 183*((4.909x10^{-4}) +0.07854*0.025/2) = 0.2695$$

$$G^R_{1r} = \sigma\varepsilon P(L_e/2)F_{ij} = \sigma*0.8*0.07854 *(0.025/2)*1.0 = 0.0007854*\sigma$$

$$G^R_{2r} = G^R_{3r} = \sigma\varepsilon PL_e = \sigma*0.8*0.07854 *0.025*1.0 = 0.001571*\sigma$$

$$G^R_{4r} = \sigma\varepsilon(A + P(L_e/2))F_{ij} = \sigma*0.8 *((4.909x10^{-4}) + 0.07854*(0.025/2)) *1.0 = 0.001178*\sigma$$

$$Q_3 = 50$$

$$Q_4 = 0.6873$$

These values are substituted into Equation 32. This example problem was solved with SINDA/G with Equation 32 solution equation. The results are shown in Table 5.

Table 5. FDM Example Problem Temperature Solution.

Time, seconds	Temperature, °F		
	T_2	T_3	T_4
0.0	450.0	450.0	450.0
0.1	451.5	450.0	449.7
0.2	453.0	450.0	449.5
0.3	454.4	450.0	449.2
0.4	455.8	450.0	449.0
0.5	457.2	450.0	448.7

Summary

The FEM is a powerful tool for thermal analyses. The FEM equations are intensive and expansive. A computer program is recommended to solve the system of equations.

Discretization between the FDM and FEM is different. The FEM can handle irregular geometry better than the FDM. The FDM equations are relatively straight-forward and less complicated.

The FEM formulation for one dimension was derived for conduction, convection, and radiation by the use of the Galerkin weighted residual method. This method can be expanded to two and three dimensions by expansion of the general formulation for one dimension. FDM formulation was also presented.

The FEM shape functions were derived for a linear one-dimensional element. This can be expanded to two- and three-dimensional elements for different polynomial orders. Quadrilateral, triangular, hexagonal, pentagonal, and other shape elements can be derived and applied to FEM.

The FEM formulations and shape functions are used to derive the overall FEM equation. This equation is solved for the nodal temperatures. An example problem demonstrates the solution procedure. FDM was also used for the example problem.

Nonlinear radiation terms lead to an iterative solution process. A computer program to perform the iterative solution and solve the FEM and FDM equations are beneficial.

The solution of the one-dimensional example problem shows the temperature results to be within 1% among the different solution methods. A consistent capacitance matrix tends to cause initial temperature oscillations in the results. A lumped capacitance matrix produces a physically reasonable solution with smooth initial temperature results. Either FEM or FDM can be used to solve thermal analyses.

Figure 10 shows the results of the example problem for FEM with consistent and lumped capacitance matrix and for FDM.

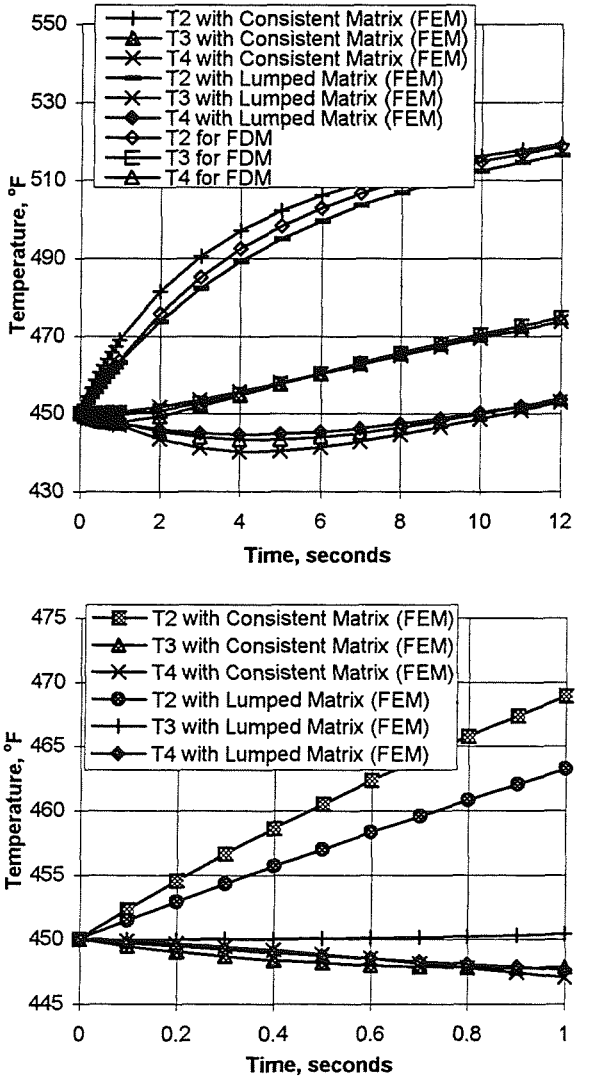

Figure 10. Example Problem Temperature Results.

References

1. F. L. Stasa, *Applied Finite Element Analysis for Engineers*, CBS Publishing, New York, NY, 1985.

2. D. L. Logan, *A First Course in the Finite Element Method*, PWS-KENT Publishing Company, Boston, MA, 1986.
3. S. S. Rao, *The Finite Element Method in Engineering*, Second Edition, Pergamon Press, New York, NY, 1989.
4. K. H. Huebner, E. A. Thornton, and T. G. Byrom, *The Finite Element Method for Engineers*, Third Edition, John Wiley & Sons, New York, NY, 1995.
5. L. J. Segerlind, *Applied Finite Element Analysis*, Second Edition, John Wiley & Sons, New York, NY, 1984.

Appendix

An alternate solution for the terms K_r^e and f_r^e can be obtained and is presented below.

The term $\int_{L^e} N^T \varepsilon\sigma P(T^4 - T_r^4)dx$ from Equation 4 can be rewritten as

$$\int_{L^e} h_r P(T - T_r)N^T dx \tag{85}$$

where

$$h_r = \varepsilon\sigma(T_{avg}^2 + T_r^2)(T_{avg} + T_r) \tag{86}$$

$$T_{avg} = \frac{T_i + T_j}{2} \tag{87}$$

Equation 85 can be solved similarly to K_{cv}^e and f_{cv}^e, resulting in

$$K_r^e = \frac{h_r PL}{6}\begin{bmatrix} 2 & 1 \\ 1 & 2 \end{bmatrix} \tag{88}$$

$$f_r^e = \frac{h_r T_r PL}{2}\begin{bmatrix} 1 \\ 1 \end{bmatrix} \tag{89}$$

Equations 88 and 89 replaces the terms K_r^e and f_r^e in Equation 65. Equation 65 is solved iteratively with these new terms as shown in the example problem.

A NEW TECHNIQUE FOR THERMAL ANALYSIS OF ARTICULATING SPACECRAFT

Kevin Duffy

MAYA Heat Transfer Technologies Limited
Montreal, Canada

Sylvain Rheault

Spar Aerospace Limited
Ste-Anne-de-Bellevue, Canada

ABSTRACT

A new technique has been developed for the numerical simulation of the transient radiative heat exchange induced by the articulation of major spacecraft appendages. The procedure is based on an extension of Oppenheim's method for computation of the environmental heat loads, where the radiative exchange is formulated as a radiosity network and solved using an iterative sparse matrix solver. This approach achieves substantial gains in numerical efficiency by avoiding the repeated reconstruction of the gray body view matrices and by limiting the number of time-varying radiative conductances in the model.

Based on the new scheme, a complete system for modeling articulating structures has been implemented in the I-DEAS TMG thermal analysis software package. The modeling tools include an integrated graphical user interface for characterizing the rotation or translation of subassemblies, and a system for visualizing temperature results on the displaced geometry. The solution algorithm incorporates an intelligent time-marching scheme to minimize the recomputation of view factors during the articulation sequence.

INTRODUCTION

In carrying out a spacecraft thermal analysis, one of the most difficult effects to characterize is the transient radiative heat transfer produced by the motion of slowly articulating appendages or subassemblies. The gradual reconfiguration of the spacecraft external surface geometry in these systems introduces a time dependence in the radiative exchange and reflection patterns, dramatically increasing the complexity of the thermal analysis task.

The most ubiquitous instances of articulated spacecraft structures are solar arrays, which are generally designed to track the sun throughout the orbit. Other familiar examples include tracking antenna systems, reconfigurable sensors, and motorized sunshades. Reconfigurable or articulating vehicles have long been common in manned space missions, particularly those which involve complex docking maneuvers or remote manipulation of large payloads.

Explicit numerical simulation of the transient radiative heat exchange within an articulating system is a formidible proposition. Regardless of whether this is accomplished by traditional view factor methods or direct simulation using Monte Carlo techniques, the computational demands of the procedure are enormously greater than for static surface geometry. Several aspects of the problem contribute to the challenge:

- The motion of the articulated structure must be modeled, propagated, stored, and displayed through its entire sequence. This requires handling and manipulation of a great deal of geometry data.

- The time-varying surface geometry requires that the terms of the radiative exchange matrices be recomputed and stored at many points throughout the articulation sequence. Since calculation of the radiative conductances is often the computational bottleneck for spacecraft thermal analysis, the solution time for this procedure can easily become intolerable.

- To compute environmental heat loads for an articulated structure, the solar and infrared gray body view factor matrices must be reconstructed at every time point with a new set of black body view factors.

- The solution matrix for an articulated structure is highly time-dependent, which greatly increases the requirements for data handling in the solver.

Because of these difficulties, the transient effects of an articulating structure are most often simply neglected in carrying out the vehicle level thermal analysis. Instead, the problem is bounded by performing steady state or transient analysis with the spacecraft geometry fixed in what are anticipated to be the worst case configurations.

Where it does become imperative to model the time-varying radiative exchange, this is often accomplished by hand-crafting a system to compute and manage the transient terms. This typically involves creating a series of snaphots, where the thermal model is configured for a particular point in the orbit and the corresponding radiative conductances and environmental heatloads are computed. The resulting terms are then manually assembled into time varying conductance and heat load tables.

An example of the use of this approach is the thermal analysis of the High Gain Antenna assembly for the EOS-AM1 platform [1]. The HGA assembly, which transmits data to the ground via the TRDSS network, consists of a Casgrain reflector subassembly rigidly attached to a box enclosure which contains the Ku-band transponder.

Since the TDRSS satellites and the EOS spacecraft are orbiting in different flight paths, data transmission is maintained by continuously repositioning the assembly via a dual-axis gimbal mechanism. The orbital geometry and corresponding gimbal rotation angles for the hot case conditions are shown in figures 1 and 2.

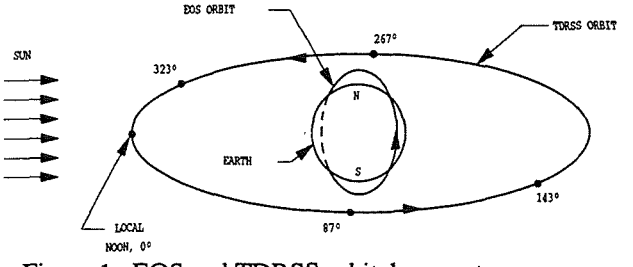

Figure 1: EOS and TDRSS orbital geometry

The I-DEAS TMG software was used to carry out the thermal analysis; the model used for radiator sizing is shown in figure 3. To model the effects of the antenna motion, a methodology was developed which involves constructing and solving discrete thermal models for individual orbital segments, as shown in figure 4. For each segment, the antenna is positioned appropriately

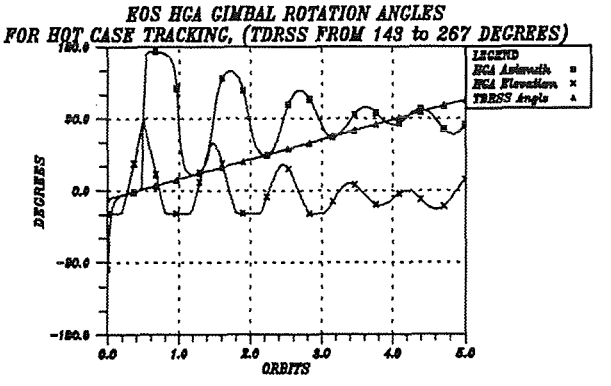

Figure 2: Gimbal rotation angles for the hot case

and the model run to compute radiative conductances and heat loads; the resulting matrix is then identified and stored. To compute orbital temperatures, the individual thermal models are solved sequentially, with the final temperatures from one segment used to initialize the next.

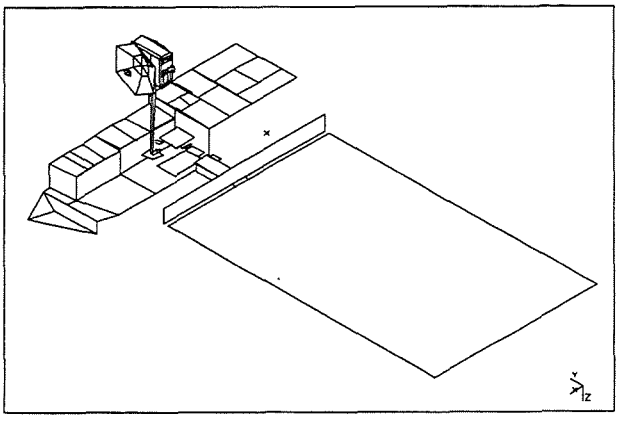

Figure 3: The EOS HGA Thermal Model

It was found that by fully simulating the transient radiative effects of the gimballed reflector, the total radiator surface area could be reduced by 20%, with a corresponding reduction in heater power consumption of approximately 15%.

Although it has been observed in this and other cases that high fidelity simulation of articulating spacecraft systems can be useful in optimizing thermal designs and reducing uncertainties, the practical and technological difficulties in executing such analyses are a significant deterrent. The effort required to implement and validate a computational scheme such as that used for the EOS analysis is substantial, and requires extensive

expertise in the development of numerical simulation software.

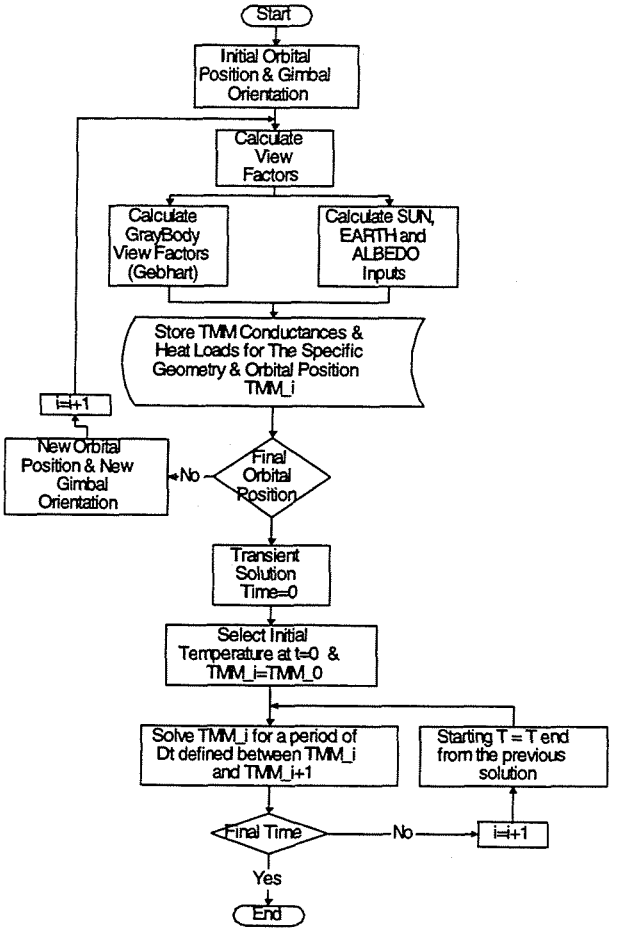

Figure 4: Algorithm for Building and Solving the HGA Thermal Model

As developers of the I-DEAS TMG software system, MAYA Heat Transfer Technologies Limited realized this and set out to develop an efficient and easy-to-use system for simulating the transient thermal behavior of articulating spacecraft.

THE EXTENDED OPPENHEIM'S METHOD

Most spacecraft thermal analysis systems use Gebhardt's Method [2] to compute the distribution of diffusely emitted and reflected radiation between surfaces. This involves using a matrix inversion process to calculate a set of gray body view factors, which represent the fraction of energy arriving at a second surface by all paths including reflections from other surfaces. The radiative heat transfer between two surfaces is then described by the equation

$$Q_{ij} = \sigma A_i \varepsilon_i VFG_{ij} (T_i^4 - T_j^4) \qquad (1)$$

For computation of radiative heating by environmental sources, separate gray body matrices are constructed using the solar and infrared reflective properties of the surfaces, and then solved to determine the distribution of the diffusely reflected component of the incident flux.

One of the main impediments to the efficient implementation of a system for modeling spacecraft articulation is the need to recompute and store the two gray body view factor matrices at many discrete time points. Particularly for large models, the computational and storage requirements of this process become extremely expensive.

To avoid this problem, consideration was directed to the use of Oppenheim's method [3] for spacecraft thermal analysis. It was recognized that this technique has inherent advantages for modeling systems with temperature-dependent surface properties, and it was felt that the method could be adapted to handle time-varying geometry with similar effectiveness.

The Radiosity Formulation

Oppenheim's Method is based on a radiosity formulation of the radiative heat transfer between surfaces. Defining the following terms:

E_b ;
- the blackbody emissive power of a surface = σT^4

G (irradiation) ;
- the total radiative heat flux incident on a surface

J (radiosity) ;
- the total radiative heat flux leaving a surface

The radiosity of a surface is the sum of the emitted and reflected energy:

$$J = \varepsilon E_b + (1-\varepsilon)G$$

The net energy leaving a surface is then

$$q = A(J - G)$$

$$= \frac{\varepsilon A (E_b - J)}{(1 - \varepsilon)}$$

The net energy exchange between two emitting and reflecting surfaces is

$$q_{ij} = A_{ij}F_{ij}(J_i - J_j)$$

Oppenheim's method for formulating the radiative heat transfer equations follows this approach. For every radiating surface, an additional thermal node is created to represent its radiosity potential. This radiosity node is coupled to its parent element with a radiative conductance

$$G = \frac{\sigma A \varepsilon}{1 - \varepsilon} \quad (2)$$

and to all other radiosity nodes with a conductance

$$G_{ij} = \sigma A_i F_{ij} \quad (3)$$

A conductance network of four elements constructed using Oppenheim's method is shown in figure 5.

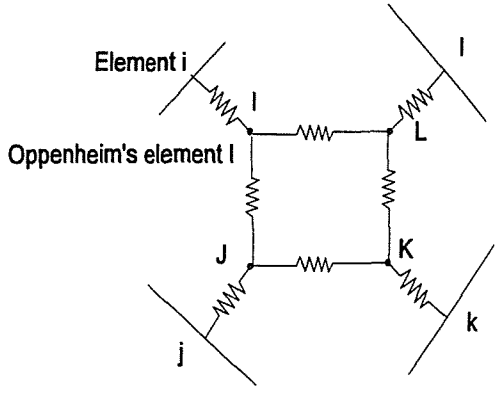

Figure 5: Conductance network using Oppenheim's method

Oppenheim's method offers a number of advantages over Gebhardt's for modeling radiative heat transfer:

- It completely bypasses the step of computing gray body view factors. This substantially reduces solution time and storage requirements.
- Although the resulting conductance matrix is larger, it usually contains significantly fewer terms. Solution speed is thereby enhanced, particularly if sparse matrix solution techniques are adopted. Storage and memory requirements similarly decrease.
- Variable material properties, such as temperature dependent surface emissivity, can be modeled easily and accurately simply by updating the radiosity conductances.
- Surface properties in a model can be changed without recomputing the gray body view factors. This can facilitate design tradeoff studies.

Clearly, the principal advantage of Oppenheim's method for modeling articulated space structures is that it obviates the need to compute gray body view factors at every time point. The time-varying black body view factors can be used directly to update the radiative conductance terms at every time step during the transient solve, much like the approach for modeling temperature-dependent emissivity. This holds out the prospect of much more efficient numerical simulation of radiative heat transfer within articulating systems, both in terms of storage requirements and solution time.

In the past, an important drawback of Oppenheim's method has been that it does not clearly lend itself to the computation of radiative heat fluxes, as Gebhardt's method does. Without a mechanism for using the radiosity approach for the simulation of environmental heating as well as radiative heat transfer, all of its advantages are lost. In order to fully exploit the potential benefits of Oppenheim's method for the analysis of articulating spacecraft, it was therefore necessary to extend the technique to handle radiative heating calculations.

Extension for Radiative Heating

Writing the heat balance equations for the radiosity nodes only, we get for node I:

$$\sum_k G_{I,k}(T_I^4 - T_k^4) = 0 \quad (4)$$

where k is either another radiosity node or the parent surface element of node I. Since each one of them is connected with its parent and other Oppenheim nodes, other surface elements in the rest of the model do not appear in the equation. Using the same procedure for the surface elements yields:

$$Q_i = G_{I,i}(T_I^4 - T_i^4) \quad (5)$$

The value of Q_i represents the net radiative heat load on surface element *i* for a particular set of temperatures.

Now consider a thermal model such as that shown in Figure 5. Assume that the surface elements are illuminated by a radiative source in the thermal infrared spectrum, and that the incident heat flux on each surface is q_{inc}. The flux reflected from each surface is then given by:

$$q_{ref,i} = q_{inc,i}\,(1-\varepsilon_I)$$

A surface in the model which is diffusely reflecting a specified quantity of incident thermal radiation can be alternatively modeled as a fixed temperature source emitting an equivalent amount of heat. Therefore, we can set the temperature of surface element *i* such that

$$\sigma\,\varepsilon_i\,T_i^4 = q_{ref,i}$$

and solve the thermal model (equation 4) to determine the temperatures of the Oppenheim nodes. With these temperatures in hand we can compute the net radiative heat load Q_i for each surface element using equation 5, and then the total radiative heat load for each element using:

$$Q_{abs,i} = Q_i + q_{ref,i}\,A_i + q_{inc,i}\,A_i\,\varepsilon_I \qquad (6)$$

$$= Q_i + q_{inc,i}\,A_i$$

The method is equally applicable for computing the distribution of solar radiative flux within an enclosure.

Solving the Sparse Matrix

The system of equations for the radiosity nodes are linear in T^4, and can be cast in matrix form for solution. Solving this matrix by direct inversion is equivalent to constructing the gray body view factor matrix, which would bring us back to where we started.

A better alternative is to solve the equations with an iterative sparse matrix solver. Modern iterative techniques offer remarkably superior performance versus matrix inversion in terms of both speed and storage requirements.

The I-DEAS TMG package incorporates an advanced iterative solver which is based on conjugate gradient technology. The conjugate gradient method derives its name from the fact that it generates a sequence of conjugate (or orthogonal) vectors, the residuals of the iterates (temperatures, in this case). They are also the gradients of a quadratic functional, the minimization of which is equivalent to solving the temperature equations. If the conductance matrix is **A** and **Q** is the heat flux boundary condition vector, then the system of equations to be solved is

$$\mathbf{A}\cdot\mathbf{T} = \mathbf{Q} \qquad (7)$$

The temperature vector **T(i)** at iteration *i* is updated at each iteration by a multiple $\mathbf{a}_i$ of the search direction vector **dT(i)**:

$$\mathbf{T}^{(i)} = \mathbf{T}^{(i-1)} + \mathbf{a}_i \cdot \mathbf{dT}^{(i)} \qquad (8)$$

The residual vector is defined as

$$\mathbf{r}^{(i)} = \mathbf{Q}^{(i)} - \mathbf{A}\cdot\mathbf{T}^{(i)} \qquad (9)$$

and is computed using

$$\mathbf{r}^{(i)} = \mathbf{r}^{(i-1)} + \mathbf{a}_i \cdot \mathbf{q}^{(i)}$$

where

$$\mathbf{q}^{(i)} = \mathbf{A}\cdot\mathbf{dT}^{(i)}$$

Using the conjugate gradient, the choice of $\mathbf{a}_i$ is

$$\mathbf{a}_i = \frac{\mathbf{r}^{(i)T}\mathbf{r}^{(i)}}{\mathbf{dT}^{(i)T}\cdot\mathbf{A}\cdot\mathbf{dT}^{(i)}} \qquad (10)$$

which minimizes functional of

$$\mathbf{r}^{(i)T}\cdot\mathbf{A}^{-1}\cdot\mathbf{r}^{(i)}$$

over all possible choices of **a**. The search directions are updated using the residuals

$$\mathbf{dT}^{(i)} = \mathbf{r}^{(i)} + \mathbf{b}_{i-1}\mathbf{dT}^{(i-1)} \qquad (11)$$

where

$$\mathbf{b}^{(i)} = \frac{\mathbf{r}^{(i)T}\mathbf{r}^{(i)}}{\mathbf{r}^{(i-1)T}\mathbf{r}^{(i-1)}}$$

The choice of **b(i)** from this equation ensures that **dT(i)** and **r(i-1)** are orthogonal to all previous **A·dT(i)** and **r(i)** respectively. For a symmetric positive definite matrix with s distinct eigenvalues, the method can be proven to converge in less than or equal to s+1 iteration steps.

In I-DEAS TMG, a bi-conjugate gradient variation of the standard method was implemented. The bi-conjugate gradient method generates two sequences of vectors, one based on a system with the original coefficient matrix **A**, and one on $\mathbf{A}^T$. Instead of orthogonalizing each sequence, they are made mutually orthogonal, or "bi-orthogonal". This method uses limited storage and allows the matrix to be non-symmetric.

IMPLEMENTATION OF THE METHOD

Having developed in the Extended Oppenheim's Method a numerical approach which promised to overcome one of the main obstacles to the efficient simulation of articulating spacecraft, it was then undertaken to develop in I-DEAS TMG a complete system for defining, solving, and post-processing articulated spacecraft thermal models.

I-DEAS TMG [4] is a comprehensive software system for numerical simulation of heat transfer and fluid flow. The solution technology is based on a finite volume approach, in which a conservative element-based control volume formulation is used to compute the conductance and capacitance terms for arbitrary element meshes. The system is widely used for spacecraft thermal analysis, and incorporates an extensive set of modeling and solution features, including advanced CAE tools for solid modeling and meshing, and extensive graphical post-processing.

Modeling the Articulation Sequence

The first step was to design a system for defining the motion of articulating spacecraft appendages. The objective was to create a simple and elegant user interface that could accommodate the modeling of complex articulated structures such as remote manipulator systems.

An approach based on the specification of displacement joints was worked out and implemented. In this, the rigid-body motion of a selected set of elements is modeled by characterizing the rotation or translation produced by the driving mechanism or joint. Modeling of compound articulation is enabled by associating outboard joints with a "parent" joint.

The main component of the resulting user interface is the form shown in figure 6, which establishes the procedure for modeling articulation. The user first selects a set of elements which move as a rigid body, then identifies the type of joint which controls the motion. For a Revolute joint, the user selects a point and a vector to specify the rotation axis, then defines the rotation about the joint axis as a constant rate (degrees/second) or as a table of angular displacement versus time. For a Translational Joint, the user selects a vector defining the direction of travel, then specifies the translation along this direction as a constant speed (e.g. m/s) or as a table of linear displacement versus time.

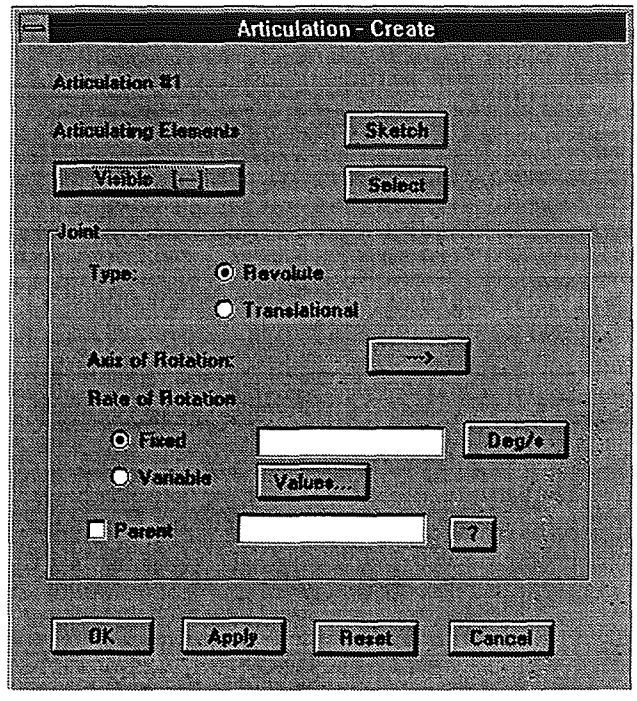

Figure 6: User Interface for Articulation Modeling

For a mechanized assembly containing a series of discrete joints such as the one shown in figure 7, each outboard joint must be associated with a parent. The "child" joint is assumed to be rigidly attached to the parent structure and is translated or rotated accordingly. Several joints can chained together in this fashion to model compound rotations and translations in complex systems.

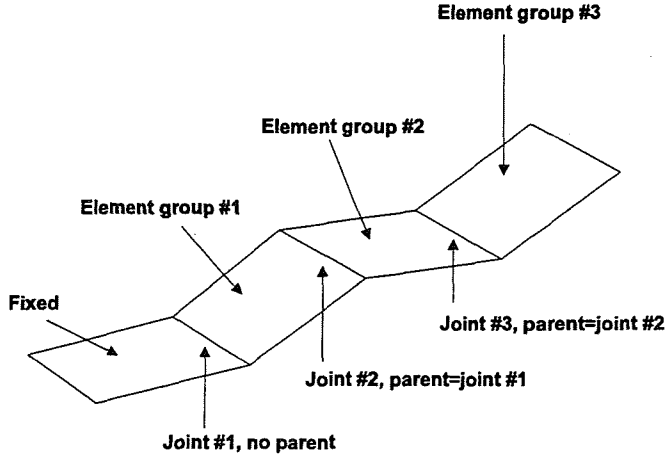

Figure 7: Joint Chaining for Compound Articulation

Constructing and Solving the Thermal Model

The process of building and solving the numerical thermal model is quite complex, and involves several different procedures and algorithms.

Computing Black Body View Factors - One of the largest contributors to overall solution time for spacecraft thermal models is the computation of the black body view factors between radiating surface elements. For an articulated spacecraft, the processing requirements for this task are dramatically increased because of the need to recalculate the view factors at many discrete time points.

Since in most cases the moving surfaces comprise only a small segment of the overall thermal model, it was clear that substantial savings in solution time could be achieved by limiting the recalculation of view factors to only those element pairs affected.

An algorithm was developed to automatically identify and recompute those view factors which can be affected by the motion of the articulating structure at any point in time. It is based on the use of the view factors themselves to identify possible interaction with the articulating segments of the model. Thus the elements whose view factors are to be recomputed at any time step in the articulation sequence are the following:

- All moving elements.
- Any element which has a view factor to a moving element
- Any element which had a view factor to a moving element at the previous time step.

This approach was implemented as a two-step time marching scheme, in which at every time step the software automatically:

1. Recomputes all view factors for every moving surface element;
2. Identifies and recomputes view factors for all elements that have a view factor to a moving element at the current or previous time step.

This scheme requires no user effort or interaction, yet is highly effective in reducing the number of view factors to be computed.

Solar and Earth View Factors - The solar and earth view factors are computed at discrete time points defined by the user. For an articulated spacecraft model, the configuration of the surface geometry is updated at each time point prior to computing these environmental view factors.

The calculation of black body view factors during an articulation sequence is synchronized with the environmental heating calculations, to ensure fully consistent geometry throughout the simulation.

Radiative Heating - Computation of the radiative heat loads is based on the Extended Oppenheim's Method described above. At every time point, the solar and earth view factors are first used to compute incident heat fluxes for all illuminated surfaces. The solution matrix for the enclosure is then assembled from equation 4 using the corresponding black body view factors, and solved using the conjugate gradient method.

Assembly of the Solution Matrix - Via equations 2 and 3, the black body view factors are used to assemble a matrix of time-varying radiative conductances. A multi-point table is set up for each non-constant term in the radiative conductance matrix; the solver interpolates values from these tables at every time point during the transient solution.

The environmental heat loads computed for the spacecraft are constructed in a similar fashion as time-varying boundary conditions on the model.

Data Handling Scheme - In order to efficiently handle the very large quantities of data required to model articulating spacecraft, a direct access binary model file was implemented for the code. This provides much more compact storage of the data, substantially reduces data retrieval time, and improves precision.

Solving the Model - Thermal models of articulated spacecraft can be fairly difficult to solve because the solution matrix can change so dramatically over time. It has been found that the most effective solution strategy is to use an implicit technique in combination with the conjugate gradient solver. A Newton-Raphson iteration scheme was introduced and found to be very effective in reducing solve time for complex articulated models.

Results Postprocessing

As part of the capability for simulating articulating structures, a post-processing feature was developed to provide visualization and animation of the articulation sequence.

During model solution, the motion of the articulated structure is propagated according to the joint definitions. At every time point in the articulation

sequence, all nodal coordinates are captured as time-tagged deformation results. Using the post-processing capabilities of the I-DEAS software, these nodal deformation datasets can be applied to the thermal model to display the actual displaced geometry or to animate the induced motion. Thermal model results can also be post-processed on the deformed geometry.

CONCLUSIONS

The new software system for the simulation of articulated structures provides an effective means to address one of the most challenging spacecraft thermal analysis problems. The modeling tools are designed to minimize the effort required to characterize the motion of subassemblies and appendages, and provide effective graphical visualization of the resultant displacements. The innovative solution approach enables the simulation to be carried out in a single pass, and minimizes both solution time and data storage requirements

It is antipated that, in the near future, the simulation tools will be extended to provide modeling of the heat transfer across sliding contact surfaces, enabling more precise modeling of joints and mechanisms. In the longer term, the new solution technology holds out the prospect for real-time thermal simulation of complex orbital operations, such as the manipulation of large payloads by man-controlled or intelligent robotic systems.

REFERENCES

1. Bonsang, F., Fang, Z., St-Pierre, D., Theophanous, P., "EOS-AM Spacecraft High Gain Antenna Thermal Design and Analysis", SAE 951750, 25th International Conference on Environmental Systems, San Diego, California, July 1995.

2. Gebhardt, B., "Unified Treatment for Thermal Radiation Heat Transfer Processes - Gray, Diffuse Radiators and Absorbers", paper no. 57-A-34, ASME, 1957.

3. Oppenheim, A,K., "Radiation Analysis by the Network Method", Trans. ASME, vol. 78, pp. 725-735, 1956.

4. Structural Dynamics Research Corporation, "I-DEAS TMG Technical Summary", Structural Dynamics Research Corporation, 2000 Eastman Drive, Cincinnati, Ohio 45150-2789, February 1991.

MODELING OF WATER INJECTION INTO A VACUUM

John W. Alred
Hernandez Engineering, Inc., Houston, TX

L. Nicole Smith and K. C. Wang
Lockheed Martin, Houston, TX

Forrest E. Lumpkin and Steven M. Fitzgerald
NASA/JSC, Houston, TX

Abstract

A loosely coupled two-phase vacuum water plume model has been developed. This model consists of a source flow model to describe the expansion of water vapor, and the Lagrangian equations of motion for particle trajectories. Gas/Particle interaction is modeled through the drag force induced by the relative velocities. Particles are assumed traveling along streamlines. The equations of motion are integrated to obtain particle velocity along the streamline. This model has been used to predict the mass flux in a 5 meter radius hemispherical domain resulting from the burst of a water jet of 1.5 mm in diameter, mass flow rate of 24.2 g/s, and stagnation pressure of 21.0 psia, which is the nominal Orbiter water dump condition. The result is compared with an empirical water plume model, deduced from a video image of the STS-29 water dump. To further improve the model, work has begun to numerically simulate the bubble formation and bursting present in a liquid stream injected into a vacuum. The technique of smoothed particle hydrodynamics was used to formulate this simulation. A status and results of the on-going effort are presented and compared to results from the literature.

Introduction

The Orbiter dumps a combination of waste and condensate water from a port-side, heated, knife-edge nozzle, approximately every 3 days. The narrow jet of water injected into vacuum quickly bursts into a disperse plume of vapor, water droplets, and ice particles. The expanding plume may make contact with surfaces, and therefore stick and leave solid contents as permanent deposits. The optical properties of the impacted surfaces may be affected to a degree that inhibits their proper function. Phenomena that occur when a liquid stream is injected into a vacuum environment have been studied by Fuchs and Legge[1] and by Muntz and Dixon[2]. In general, as a liquid stream is discharged into a vacuum, due to the sudden drop of pressure, the stream becomes superheated and vapor bubbles may form inside the stream. As the bubble continues to grow, it eventually reaches a critical size which causes the jet to burst into water droplets and ice fragments. The fragments form a conically shaped plume. The burst distance and the characteristic cone angle are affected by the initial stream velocity, temperature and diameter. The effect of these parameters on the burst distance and the characteristic cone angle were studied. The results of these parametric studies are presented in the following section. For the purpose of predicting the extent of contamination due to the Orbiter water dump, an engineering model has been developed to model the fast expanding gas vapor and the conical cloud of ice fragments. This model consists of a source flow model to describe the vapor phase of the plume, and the Lagrangian equations of motion for particle trajectories. The interaction between the particle and gas is modeled through only the drag induced by the relative velocities[3]. Particle number density along the plume centerline was deduced from a vacuum venting test conducted at Arnold Engineering Development Center (AEDC)[4,5]. A normal distribution function is used to describe the particle number density in the polar direction. The variance of this distribution may vary and two values of distribution variance based on the plume cone half angle have been examined. Given a location with respect to the nozzle exit, this model can predict mass flux at the specified location due to the dump. This paper will provide a detailed description of the model and the numerical procedure used. This model has been used to generate the mass flux in a 5 meter radius hemispherical domain resulting from the burst of a water jet of 1.5 mm in diameter, mass flow rate of 24.2 g/s and stagnation pressure of the jet is equal to 21.0 psia, corresponding to the nominal Orbiter water dump condition. The result is compared with the result obtained from a purely empirical model, deduced from a video image of the STS-29 water dump[6]. Model improvements via a new numerical simulation will then be discussed.

Cavitation of Liquid Streams in a Vacuum

The equation of motion for the radius R_b of a bubble in a viscous liquid as a function of time is

$$R_b\ddot{R}_b + \frac{3}{2}\dot{R}_b^2 = \frac{\Delta P}{\rho_l} - \frac{2\sigma}{\rho_l R_b} - \frac{4\mu\dot{R}_b}{\rho_l R_b} \qquad (1)$$

where σ is the surface tension, ρ_l is the density of the liquid stream, and μ is the viscosity[7]. ΔP is the pressure difference driving the bubble expansion and can be expressed as

$$\Delta P = p_{vb} - \frac{\sigma}{R_0} - \frac{p_v}{2} \tag{2}$$

where p_{vb} is the vapor pressure of the liquid at the bubble wall temperature. The vapor pressure is given by the Clausius-Clapeyron equation

$$p_v = p_R \exp\left(-\frac{m_l l_v}{kT_s}\right) \tag{3}$$

where p_R is a constant obtained empirically, m_l is the mass of a liquid molecule, l_v is the heat of vaporization, k is the Boltzmann constant, and T_s is the surface temperature. The reduction of the surface temperature with time of a water stream due to evaporation as given in Fuchs and Legge[1] is

$$T_0 - T_s(t) = \frac{1}{\sqrt{\pi \rho c_p \alpha}} \int_0^t \frac{\dot{q}(\tau)}{\sqrt{t-\tau}} d\tau \tag{4}$$

where α is the thermal conductivity, T_0 is the initial stream temperature, and $T_s(t)$ is the stream surface temperature at time t.. The time-dependent surface heat transfer for vaporization is

$$\dot{q}(t) = \frac{m_l n_{vs}}{4} \bullet \sqrt{\frac{8kT_s}{\pi m_l l_v}} \tag{5}$$

where n_{vS} is the vapor number density at temperature T_S. The definite integral of equation (4) has the interesting property that it is dominated by the value of integrand near $t = \tau$.. A useful approximation, as given in Muntz and Dixon[2], which permits a simple explicit expression to be derived, is to assume that $\dot{q}$ is constant at its value at the end of the time interval. It follows that the surface temperature can then be obtained by solving the following non-linear equation

$$T_0 - T_s(t) = \frac{\sqrt{4\alpha t/\pi \rho c_p}}{\alpha} \dot{q}(t) \tag{6}$$

where c_p is the specific heat at a constant pressure.

Equation (1) is solved by using a third order Runge-Kutta integrator[8]. At each time step, equation (6) is solved to obtain stream temperature. From Muntz and Dixon[2], in order for a vapor bubble to exist or grow, its internal pressure must be at least

$$p_b = p_s + \sigma/R_0 + 2\sigma/R_b \tag{7}$$

where p_s is surface pressure of the jet stream, R_0 is the radius of the stream, and R_b is the radius of the bubble. If we assume there are no temperature gradients in the stream, the internal bubble pressure must be the vapor pressure and $p_s = p_v/2$, or $p_s = 0$ for a very cold surface. The bubble must have at least a radius of R_b as solved for in equation (7), if the bubble is to begin growing. The equilibrium bubble radius, or minimum radius that will permit growth is

$$R_{be} = \frac{2\sigma}{(p_v/2 - \sigma/R_0)} \tag{8}$$

or, for a cold stream surface,

$$R_{be} = \frac{2\sigma}{(p_v - \sigma/R_0)} \tag{9}$$

It is assumed that bursting takes place when a bubble grows to be the size of the stream, and that the perpendicular particle velocity is equal to the growth rate of the bubble, $\dot{R}_b$. Therefore, the cone half angle of the region containing majority of ice fragments is given by

$$\theta = \arctan(\dot{R}_b / V_0) \tag{10}$$

where V_0 is the initial stream velocity. Equation (1) has been solved for a 1.5 mm stream at various temperatures and velocities. Figure 1 shows the effect of stream temperature to the bubble growth rate. The result is plotted as R_b/R_0 versus a non-dimensional time (tV_0/R_0). Note that the stream is assumed to have burst at $R_b/R_0 = 1$. From Figure 1, we can see that the burst distance decreases with increasing stream temperature. Figure 2 shows the effect of stream velocity on the burst distance. Again, the result is plotted as R_b/R_0 versus the non-dimensional time. From this figure, we can see that the burst distance increases with increasing stream velocity. Figure 3 is a composite plot of burst distance versus stream temperature at various stream velocities. Again, the decrease of burst distance with increasing temperature is clearly shown. Figure 4 is a composite plot of burst distance versus stream velocity at various stream temperatures. Figure 5 is a composite plot of burst angle versus temperature at two different velocities. From this figure we can see that the burst cone angle increases with increasing temperature, and also the cone angle decreases with increasing velocity.

Plume Flow

After bursting, the liquid stream becomes a cloud of gas, liquid droplets and ice fragments. In this work to date, we assume all liquid droplets are solidified. Therefore, only the gas phase and ice particles are being considered in this paper. However, with the SPH technique and the SPHINX model, our ultimate goal is the modeling of gas, liquid drops, and solid particles.

Gas Phase

The fast expansion of the gas phase is characterized by high Mach numbers and velocity; and, therefore, almost straight streamlines, which seem to originate at the burst point. This type of flow can be describe by a source flow model[9]. In such a flow the density at a distance r from the burst point is given by

$$\frac{\rho}{\rho_0} = \frac{A_p}{r^2}\left(\cos\frac{\pi}{2}\frac{\theta}{\theta_{lim}}\right)^{2/(\gamma-1)} \tag{11}$$

where ρ is the stagnation density, θ is the polar angle, θ_{lim} is the limiting angle of the expanding gas, and γ is the ratio of specific heats. A_p is a constant which is calculated by mass flow considerations

$$A_p = \frac{u^*/(2u_{lim})}{\int_0^{\theta_{lim}} \left(\cos\frac{\pi}{2}\frac{\theta}{\theta_{lim}}\right)^{2/(\gamma-1)} \sin\theta d\theta} \tag{12}$$

where u^* is the velocity at sonic condition. u_{lim} is the limiting velocity and is given by

$$u_{lim} = \sqrt{\frac{2\gamma}{\gamma-1}RT_0} \tag{13}$$

where R is the specific gas constant and T_0 is the stagnation temperature. The velocity at a distance r from the burst point is computed from the isentropic expansion relation

$$u^2\left[\frac{1}{M^2(\gamma-1)} + \frac{1}{2}\right] = \frac{a_0^2}{\gamma-1} \tag{14}$$

where a_0 is the stagnation speed of sound. The Mach number M is computed from the area Mach number relation

$$\left(\frac{A}{A^*}\right)^2 = \frac{1}{M^2}\left[\frac{2}{\gamma+1}\left(1+\frac{\gamma-1}{2}M^2\right)\right]^{(\gamma+1)/(\gamma-1)} \tag{15}$$

The area Mach number relation is solved by using the Newton's method.

Particle Phase

The particulate model is taken from Holcomb[3], which implements a Lagrangian treatment for the particles. The particles are assumed to be solid (no mass transfer or size change) and dilute (negligible volume in comparison to the gas), but the gas/particle system is assumed to be in non-equilibrium, in that there are relative velocities between ice particles and the expanding gas. The Lagrangian treatment of the particles, also referred to as the particle trajectory model, utilizes the natural equations of motion of the individual particles.

Particle/gas momentum interaction term accounts for the acceleration which the gaseous phase imparts on the solid particles. The Lagrangian equations of motion for the particles are

$$\frac{dR_p}{dt} = u_p \tag{16}$$

$$\frac{du_p}{dt} = \frac{D}{m}(u_g - u_p) \tag{17}$$

where R_p and u_p are position and velocity of particle along a streamline. u_g is the velocity of the gas at the streamline location and D is a drag related term and is given by

$$D = \frac{\pi}{2}r_p^2\rho_g C_d|u_g - u_p| \tag{18}$$

$$C_d = \frac{24}{Re_p}\left[1+\frac{1}{6}Re_p^{\frac{2}{3}}\right] \quad for\ Re_p < 1000 \tag{19}$$

$$C_d = 0.424 \quad for\ Re_p > 1000 \tag{20}$$

where Re_p is the Reynolds number based on the particle diameter. Equations (16) and (17) are integrated using a third-order variable step Runge-Kutta integrator. At each time step, u_g is computed from equations (14) and (15).

Initial Results and Discussion

The model described above has been coded and used to predict the mass flux in a 5 meter radius hemispherical domain, resulting from the burst of a water jet from a nominal Orbiter water dump. The diameter of the jet is 1.5 mm, the stagnation pressure is 21.0 psia and the mass flow rate equals to 24.2 g/s. A vacuum water venting experiment was conducted at the AEDC 4- by 10-ft Research Vacuum Chamber (RVC) during 1983. Average particle sizes, particle number

densities and mass fraction were either measured or deduced from test data[4,5]. It was found that particle number density varies as $1/r^2$ down the centerline of the plume. The number density in the polar direction has a bell shaped distribution from the centerline of the plume. These observations have been incorporated into the model. Two particle sizes were chosen, large particle with mean diameter of 1.0 mm and small particle with mean diameter of 0.15 μm. The mass fraction of the large particle is 0.78; the mass fraction of the small particle is 0.02; and the mass fraction of the gas is 0.20. Number density distribution of particles varies as $1/r^2$ down the plume centerline; and a normal distribution function was used to describe number density distribution in the polar direction. The value of the number density at a reference point was scaled down from the AEDC test, such that the mass flow rate is equal to 24.2 g/s. The reference point is at 1.0 cm down stream of the nozzle exit or the burst point. Standard deviation of the normal distribution function was set equal to either the bursting half angle or half of the bursting half angle. The former is designated as the 1σ case and the latter as the 2σ case. The results are then compared with the result obtained form an empirical model deduced form a video image of the STS-29 water dump[6]. Figure 6 shows the mass flux contours obtained from the empirical model. Figure 7 shows the mass flux contours obtained from the 1σ case. Figure 8 shows the comparison of mass flux at r = 5.0 m. This figure is plotted as mass flux versus polar angle, with 0 degree at the centerline of the plume. Figure 9 is an expanded view between 0 and 20 degrees of Figure 8. Figure 10 shows the mass flux contours plot of the 2σ case. Figure 11 shows the comparison of mass flux at r = 5.0 m between the 2σ case and the empirical model. Again, the figure is plotted as mass flux versus polar angle. Figure 12 is an expanded view between 0 and 20 degrees of figure 11. From these plots, we can see that fairly good comparison between the engineering model described in this document and the empirical model was obtained. The result from the empirical model falls somewhere in between the 1σ and the 2σ cases.

Model Improvements

The current model for the Orbiter water dump is based on the semi-empirical results from the literature[2,4,5]. However, a mathematical model of the liquid flow into the vapor/ice cloud is desired. In general, as a liquid stream is discharged into a vacuum, due to the sudden drop of pressure, the stream becomes superheated and vapor bubbles may form inside the stream. As a bubble continues to grow, it eventually reaches a critical size which causes the jet to burst into water droplets and ice fragments. The fragments form a conically shaped plume. The burst distance and the characteristic cone angle are affected by the initial stream velocity, temperature and diameter. The technique of Smooth Particle Hydrodynamics (SPH) was chosen to build this model. The intent of the model improvement using SPH is to model the bubble formation and bursting

Smoothed Particle Hydrodynamics

SPH is a relatively new technique for hydrodynamic calculations. It is a gridless Lagrangian method using a pseudo-particle interpolation method to compute smooth hydrodynamic variables, thus solving the Lagrangian equations of hydrodynamics. Each pseudo-particle has a mass, Lagrangian position and velocity, and internal energy, whereas other quantities are derived by interpolation or from constitutive relations. The major advantages of SPH are its relative ease of coding and its ability to handle irregular geometries and boundary conditions. A major disadvantage to SPH is it seldom "crashes" if something unphysical is done. Hence, one must continually ascertain that physical properties are conserved or realistic. Excellent reviews of the SPH method are given in Monaghan[10,11] and Benz[12].

A copy of an SPH code named SPHINX was obtained from the Los Alamos National Laboratory (LANL). This particular code had been tested and verified on a number of projectile impacts (see Figures 13-16) and astrophysical problems[13,14]. However, the physical properties of radiative cooling, evaporative cooling, and surface tension were lacking in SPHINX. Work has been begun at JSC to implement these effects into an SPH formulation and add these models to SPHINX. Work has also been initiated at LANL to update SPHINX to make it more responsive to the Orbiter water dump problem. Unfortunately, the results of these efforts were not ready at the time of pre-conference publication. It is hoped that these results will be presented at the conference.

Conclusions

From the previous section, one can see that the result obtained from the engineering model described in this document agrees well with the empirical model deduced form the video image. The main uncertainties of the engineering model are particle sizes, and number density distribution. To improve the model, further analysis of the available test data to derive correlation between particle sizes, number density, and distribution variance, versus initial stream condition will be conducted. Theoretical modeling of the bursting phenomenon will be accomplished to further improve the model. This update will focus on the use of the SPHINX code.

Acknowledgements

The authors wish to acknowledge the support of Jeff Arend, Tom Farrell , Ron Mikatarian, and Carlos Soares of the International Space Station Office on this project. Also, the authors express their utmost appreciation for the support and efforts of the staff of the X-Division at the Los Alamos National Laboratory (LANL). In particular, a hearty thank you is extended to Dr. Charles Wingate at LANL for his extraordinary help and comments.

References

1. Fuchs, H. and Legge H., ``Flow of a Water Jet into Vacuum,'' Acta Astronautica, Vol. 6, 1979, pp. 1213-1226.

2. Muntz, E. P. and Dixon, M., ``Characteristics, Control, and Uses of Liquid Streams in Space,'' AIAA-85-0305, Jan. 1985.

3. Holcomb, J. E., ``Generalized Implicit Flow Solver (GIFTS) Code,'' 19th JANNAF Exhaust Plume Technology Subcommittee Meeting, CPIA Pub. 586, pp. 241-252, May 1991.

4. Curry, B. P., Bryson, R. J., Seiber, B. L., and Jones, J. H., ``Selected Results from an Experiment Venting an H_2O Jet into a High Vacuum,'' AEDC-TR-84-28.

5. Curry, B. P., Bryson, R. J., Seiber, B. L., and Jones, J. H., ``Additional Results from an Experiment Venting an H_2O Jet into a High Vacuum,'' AEDC-TR-85-3.

6. Hakes, C. L., Rios, E. R., Warrington, D. J., Soares, C. E., and Stafford, D., "International Space Station External Contamination Assessment," JSC-27364, March 1996.

7. Van Stralen, S. and Cole, R., ``Boiling Phenomena,'' Edited by S. Van Stralen and R. Cole, McGraw-Hill, New York, 1979, Vol. 1, Chap. 7, p. 197.

8. Panton, R. L., ``Incompressible Flow,'' John Wiley & Sons, 1984.

9. Dettleff, G., ``Plume Flow and Plume Impingement in Space Technology,'' Prog. Aerospace Sci. Vol. 28, pp. 1-77, 1991.

10. Monaghan, J. J., "An Introduction to SPH," Comput. Phys. Comm., Vol. 48, pp. 89-96, 1988.

11. Monaghan, J. J., "Smoothed Particle Hydrodynamics," Annu. Rev. Astron. Astrophys., Vol. 30, pp. 543-574, 1992.

12. Benz, W., "Smooth Particle Hydrodynamics: A Review"; "The Numerical Modeling of Nonlinear Stellar Pulsations," J. R. Buchler (ed.), pp. 269-288, 1992.

13. Wingate, C., R. Stellingwerf, R. Davidson, and M. Burkett, "Models of High Velocity Impact Phenomena," Int. J. Impact Engng., Vol. 14, 819-830, 1992.

14. Mandell, D.,C. Wingate, and L. Schwalbe, "Simulation of a Ceramic Impact Experiment Using the SPHINX Smooth Particle Hydrodynamics Code," 16th International Symposium on Ballistics, San Francisco, CA, Sept. 23-28, 1996.

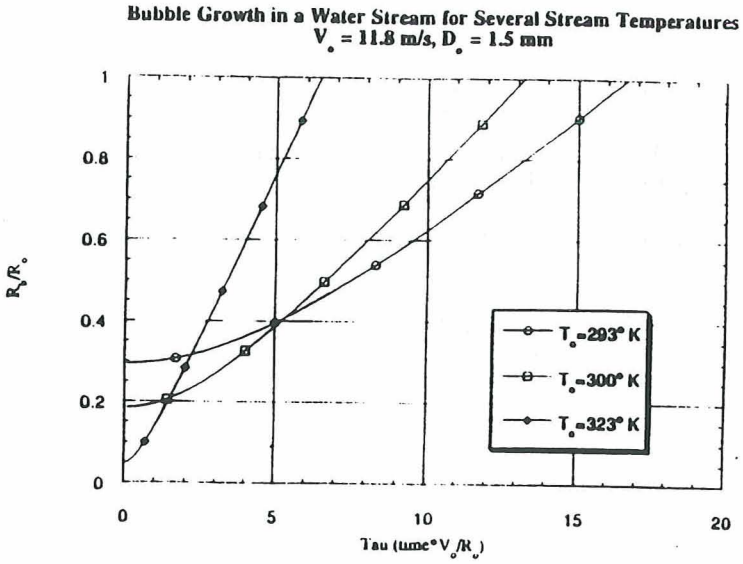

Figure 1 : Effect of Temperature on Bubble Growth

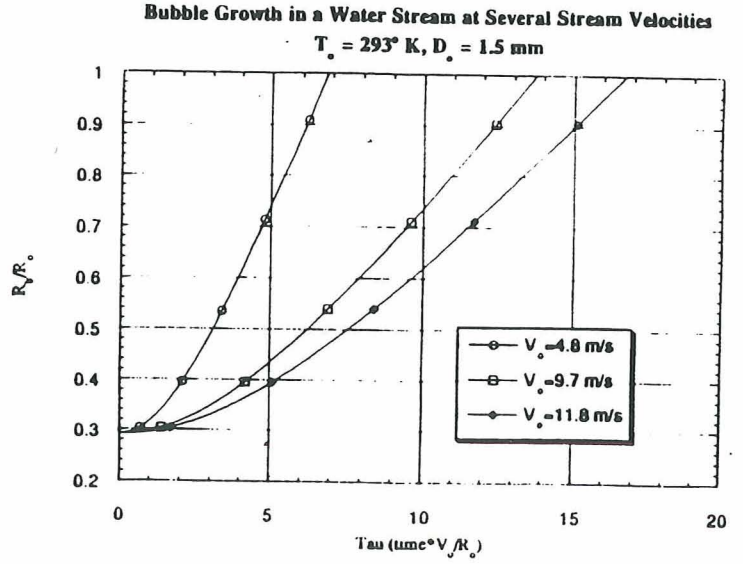

Figure 2 : Effect of Stream Velocity on Bubble Growth

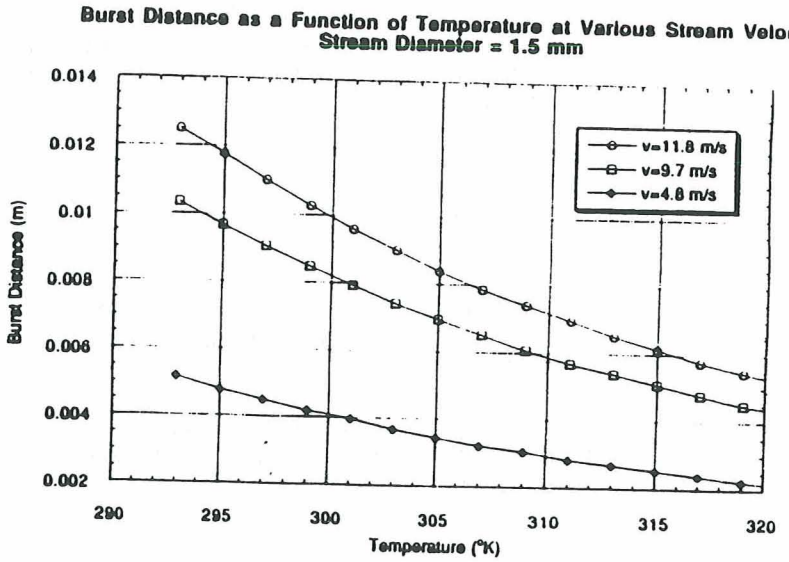

Figure 3 : Composite Plot of Burst Distance versus Stream Temperature

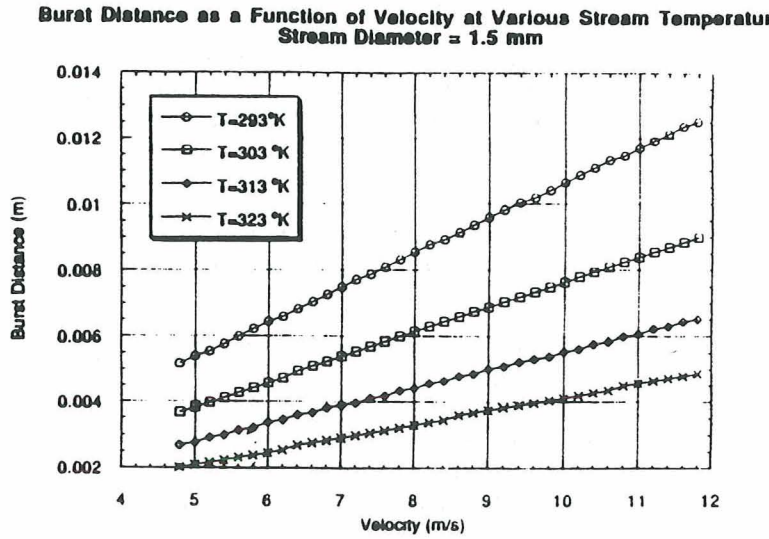

Figure 4 : Burst Distance versus Stream Velocity

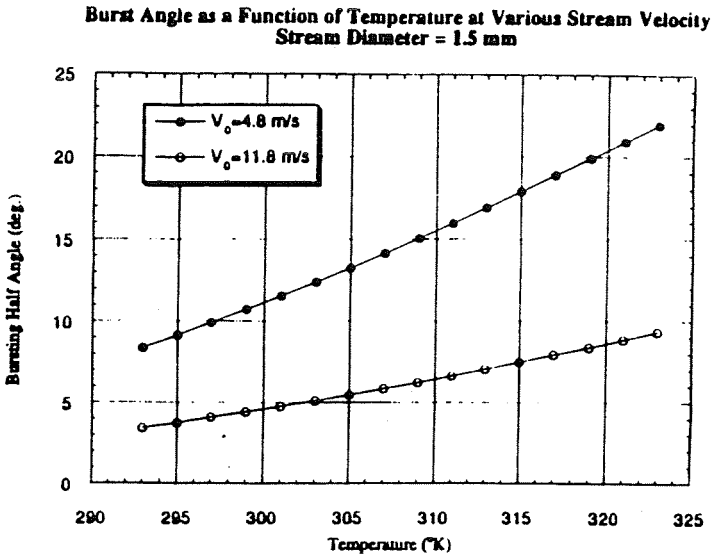

Figure 5 : Composite Plot of Plume Cone Half Angle versus Stream Temperature

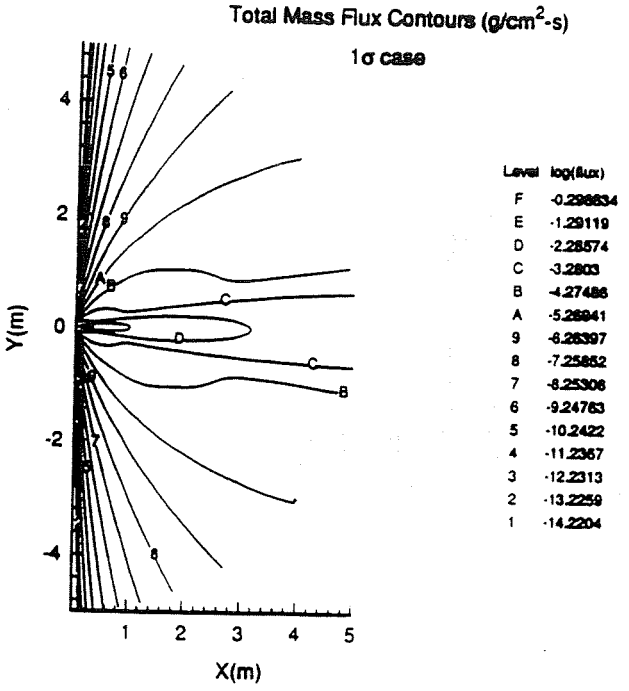

Figure 7 : Mass Flux Contours for the 1σ case

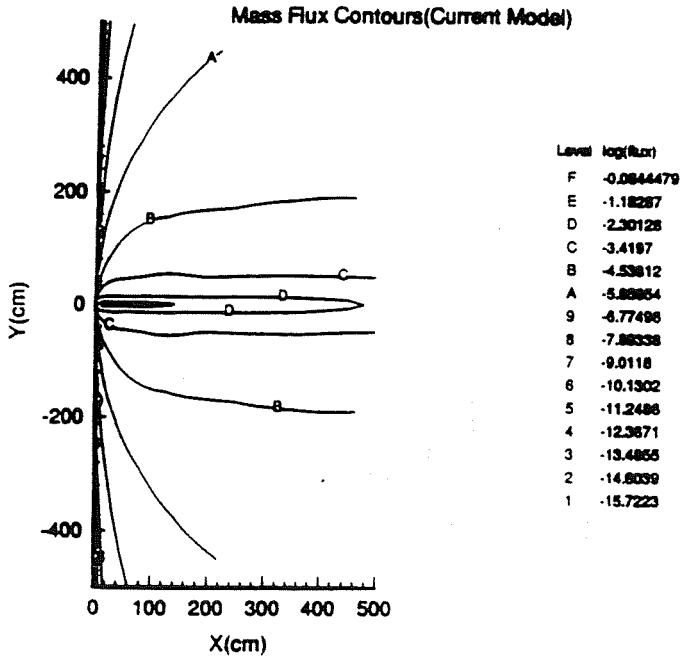

Figure 6 : Mass Flux Contours of Empirical Model

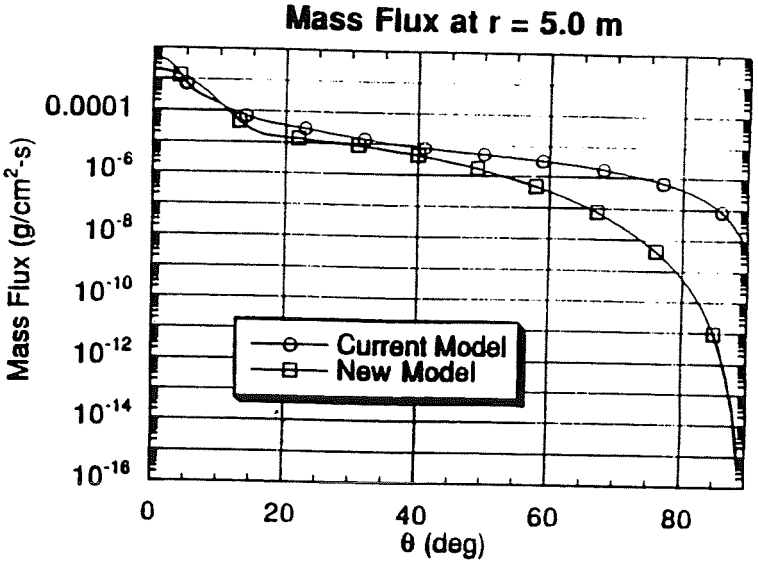

Figure 8 : Comparison of Mass Flux at r=5m for the 1σ case and the Empirical Model

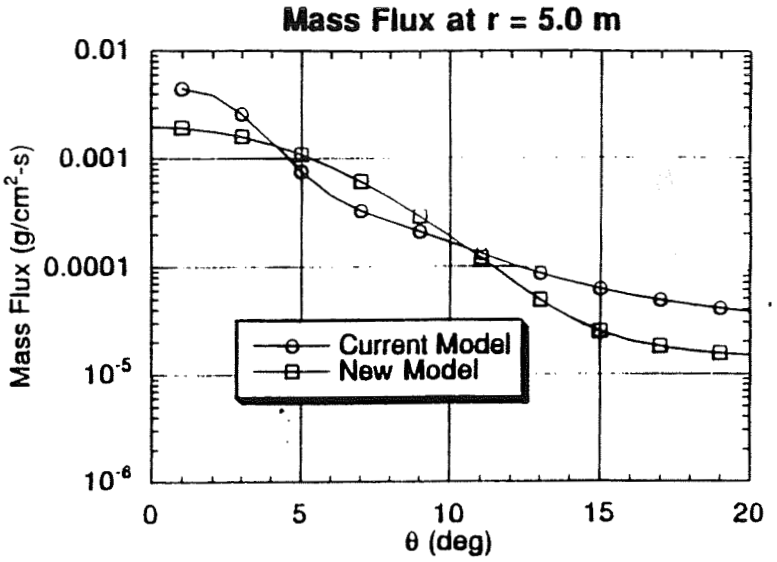

Figure 9 : Expanded View (0-20 degrees) of Figure 8

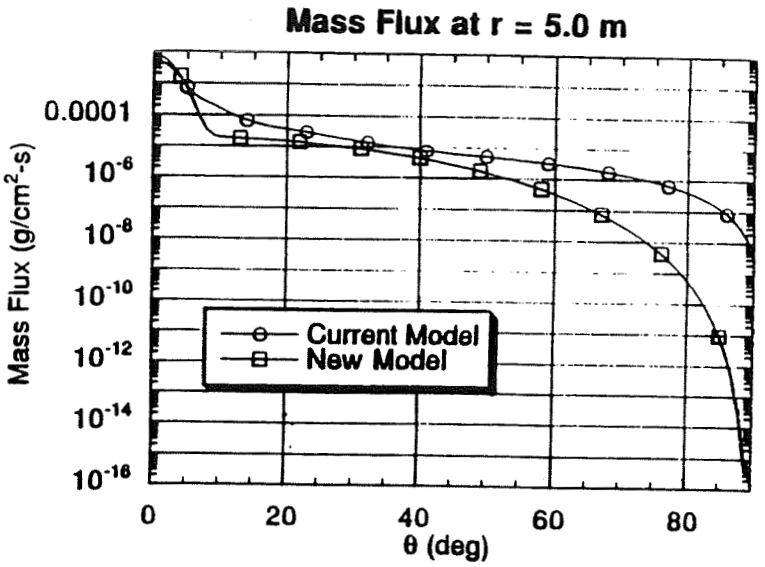

Figure 11 : Comparison of Mass Flux at r=5m for the 2σ case and the Empirical Model

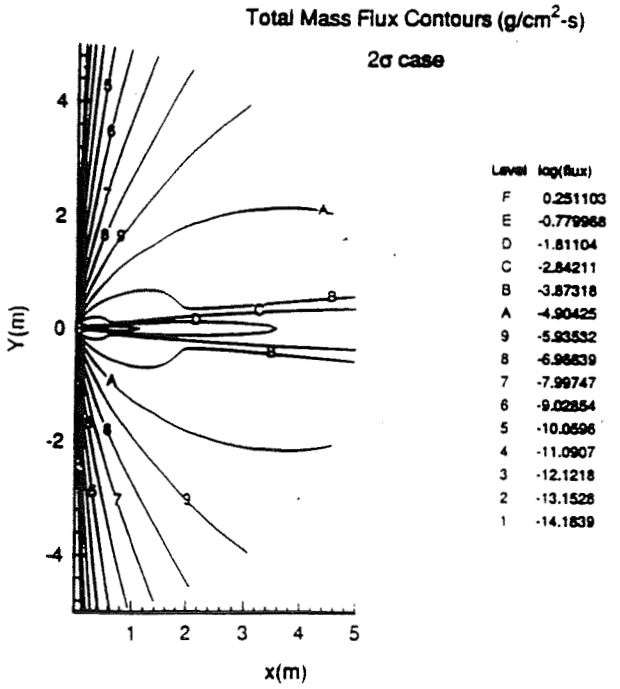

Figure 10 : Mass Flux Contours of the 2σ Case

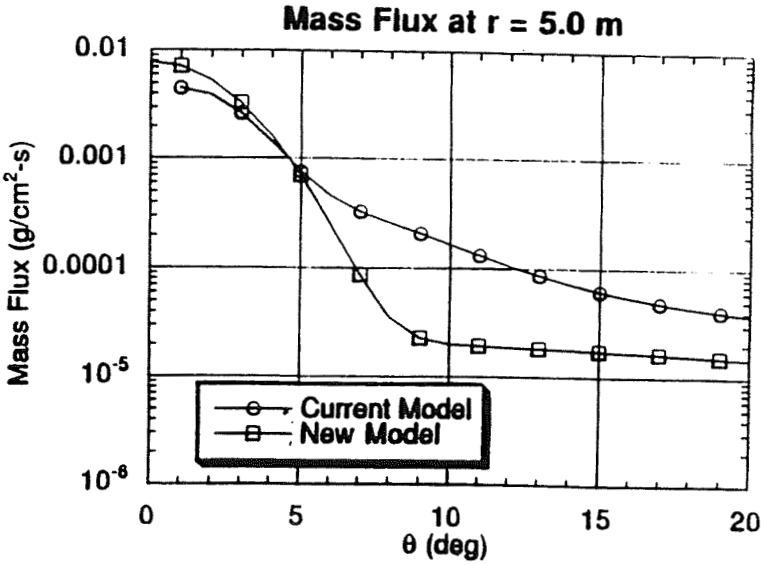

Figure 12 : Expanded View (0-20 degrees) of Figure 11

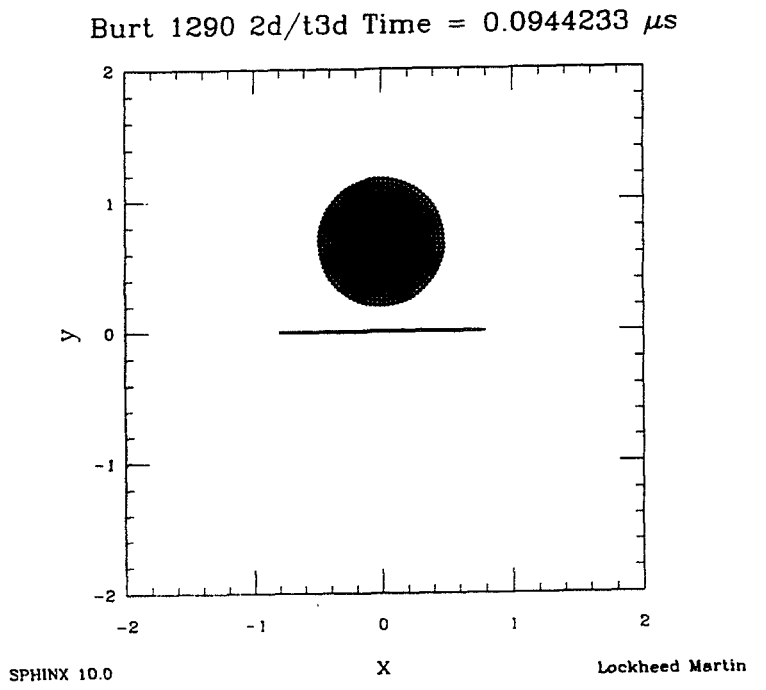

Figure 13 : SPHINX Simulation of the Impact of Aluminum Sphere on an Aluminum Plate t = 0.0944233 μs

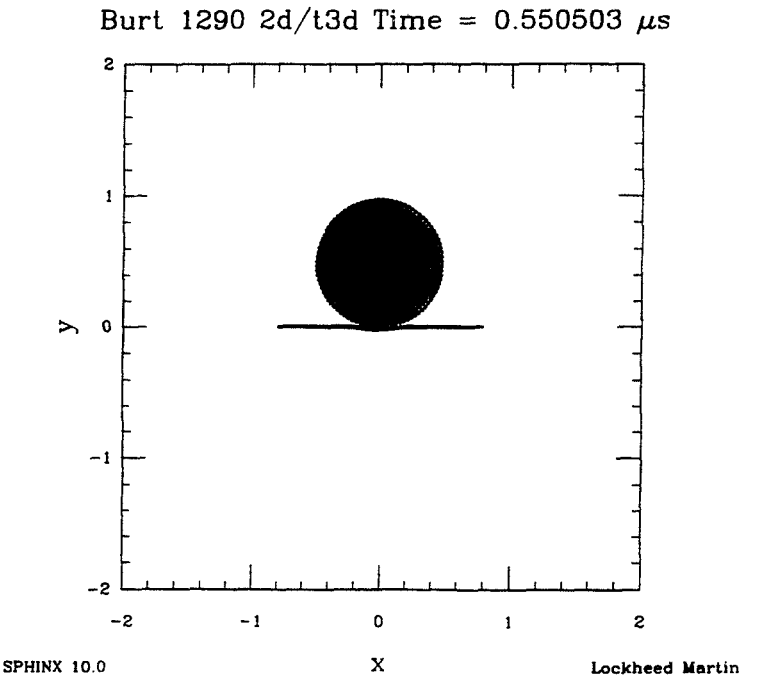

Figure 14 : SPHINX Simulation of the Impact of Aluminum Sphere on an Aluminum Plate t = 0.550503 μs

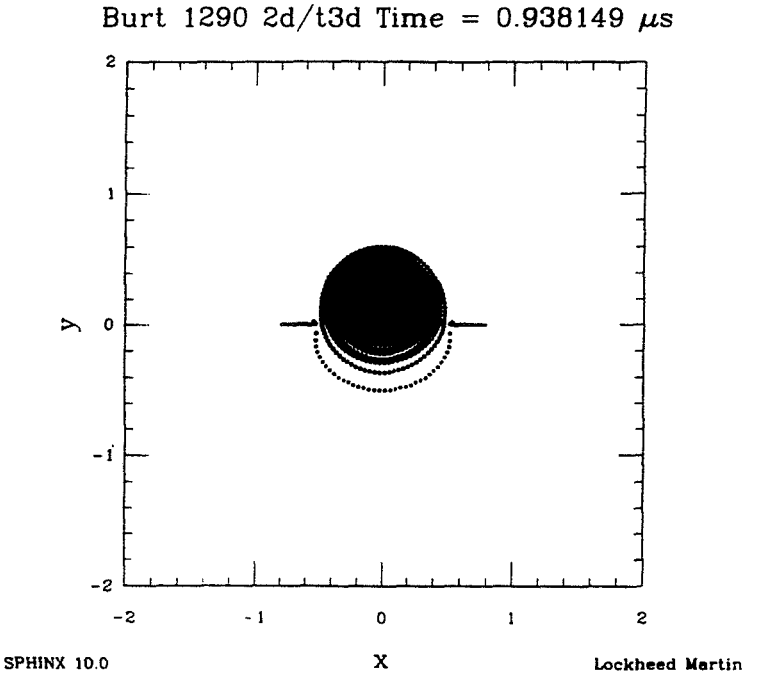

Figure 15 : SPHINX Simulation of the Impact of Aluminum Sphere on an Aluminum Plate t = 0.938149 μs

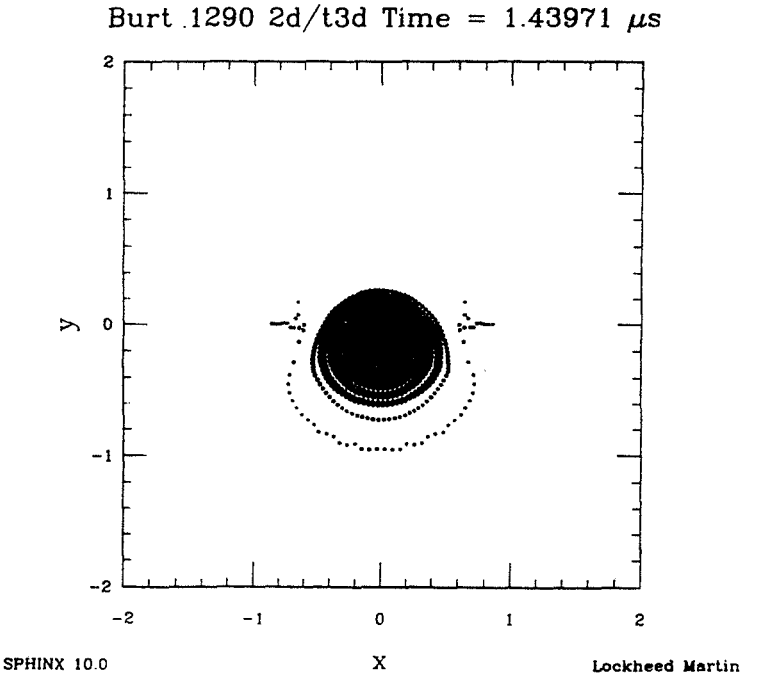

Figure 16 : SPHINX Simulation of the Impact of Aluminum Sphere on an Aluminum Plate t = 1.43971 μs

The Personal Computer Thermal Analysis Program

by
Brian Dunaway and Richard Westberry
Boeing North American
Houston, TX

Abstract

The *Personal Computer* (PC) *Thermal Analysis Program* (*PCTAP*) is a user-friendly C++ object-oriented Windows-language transport phenomena analysis program designed to replace various UNIX and VAX-based software, such as the Thermal Radiation Analyzer System (TRASYS) and the Systems Improved Numerical Differencing Analyzer (SINDA). *PCTAP*, which is run on a single PC, eliminates the dependency upon highly utilized mainframe systems and cumbersome mainframe-oriented software. It also accomplishes the same solutions with far greater flexibility and accessibility, employing interfaces in a more user-controlled Windows environment. The *PCTAP* is currently employed by Boeing North American (BNA) to predict mission performance of the Orbiter Environmental Control and Life Support System (ECLSS).

Introduction

The BNA ECLSS/Payload compatibility analysis group is required to analyze the Orbiter ECLSS for each mission according to requirements associated with the Orbiter, customer payloads (located in the payload bay (PLB) or middeck), and docked assemblies such as the Space Station *Mir* and the International Space Station (ISS).

Analysis of the Orbiter ECLSS, which includes the Atmospheric Revitalization Subsystem (ARS), Atmospheric Revitalization Pressure Control Subsystem (ARPCS), and Active Thermal Control Subsystem (ATCS), involves energy (heat and electricity) and mass (O_2, N_2, H_2O, CO_2, Freon, and waste products) transfer among the Orbiter systems, crew, payloads, docked assemblies, and extravehicular environment. Typical mission parameters that affect the Orbiter ECLSS include launch date and time, Orbiter flight attitudes, Orbiter and paylaod electrical/heat loads, and Orbiter configuration. Special mission-specific vehicle and payload requirements may include water transfers to *Mir* or ISS, control of heat and gaseous O_2, N_2, H_2O, and CO_2 among the Orbiter and *Mir* or ISS cabin air environments, pressure and concentration control associated with Extravehicular Activities (EVAs), supply and waste water dump inhibits, and Flash Evaporator Subsystem (FES) inhibits.

The most typical parameters that are examined in order to determine compatibility among the various vehicle and payload systems include supply water use, cabin air temperature (through all phases of flight), and cooling fluid temperature provided to PLB payloads.

Several tools are employed to perform the entire compatibility analysis, but the primary dependence must be upon software that incorporates all aspects of the ECLSS, and can be easily adapted to the changing conditions through the duration of a full mission.

The finite-difference SINDA model of the Orbiter ECLSS provides an environment in which it is very cumbersome to make configuration changes. Also, because SINDA is on a shared platform, it is subject to delays due to increased user CPU requirements and system crashes.

Especially with the advent of new requirements that often necessitate last-minute re-analysis, it is crucial that flexible and comprehensive transport phenomena analysis software exists that will quickly ensure all vehicle and payload requirements are satisfied.

Approach

It was determined that user-friendly, PC-based software would provide the best solution for analyzing the integrated Orbiter, payload, and docked vehicle systems.

Running software on a single PC would eliminate the dependency upon highly utilized mainframe systems and cumbersome mainframe-oriented software. It would also accomplish the same solutions with far greater flexibility and accessibility, employing user-friendly interfaces in a more user-controlled Windows environment.

The software would have the flexibility to employ models that could be developed and modified as vehicle systems change. By use of event files which contain simple, intuitive commands, the characteristics of individual missions could be built as inputs to the model; for example, the opening of the PLB doors, or the definition of payload electrical and heat loads, would be represented in these event files.

By moving the ECLSS model to the PC environment, each analyst would have execution, storage, and processing management control. This new control would give the analyst the ability to work on larger and more complex analyses.

Development

The *PCTAP* was adapted from the SINDA thermal math model of the Orbiter ECLSS system. However, *PCTAP* can be employed to analyze thermal *and* mass transport.

It was decided that the most effective way to achieve a user-friendly interface was to develop a C++ object-oriented Windows language program. (The code was developed using the Borland C++ version 4.0 software.) *PCTAP* was created in this environment as a generic thermal analyzer that would provide a platform for ECLSS analysis. This form of programming allows the programmer to develop small models of different thermal heat transfer devices, such as heat exchangers and tubes, and then link and modify these models to form the overall *PCTAP*. By having small user-definable models, users can easily build models of any system, then import these into the *PCTAP*. It also allows parameters to be redefined anywhere in the mission flow through event files that the user can customize for each mission. In addition, the overall program can be modified by developing new module programs and linking them to existing *PCTAP* modules.

The process typically employed to model heat transfer phenomena involves finite difference methods. However, the difficulty in using a finite difference scheme lies in the process of breaking the physical system into a set of differential equations. The nodalization process for defining complex elements (heat exchangers, flash evaporators, radiators, etc.) can yield very large and complex sets of differential equations. Thus, the alternative that is often preferred, as with the ECLSS SINDA model, is to approximate the behavior of complex elements with correlated equations. In fact, in the ECLSS SINDA model, only tubes and cold plates were modeled using the finite difference method. Since there is not a significant amount of heat transfer associated with the tubes, it was decided to abandon the finite difference method for the PC domain. In *PCTAP*, the ECLSS system was broken into its constituent elements (tubes, coldplates, heat exchangers, etc.), and then a solution process was defined that transfers fluid from one element to another.

The creation of *PCTAP* was made substantially easier by utilizing object-oriented programming methods, which allow programmers to group both data and code into an object. For example, a tube may be defined as an object which would include a character string name, floating point values for length and diameter, and a function called Calculate_Outlet that calculates an outlet temperature based on a provided inlet temperature and a tube bulk temperature. After *PCTAP* was created, generalized models were written for each of the Orbiter ECLSS systems in several flight configurations for use by *PCTAP*.

Elimination of TRASYS Analysis

In order to establish complete independence from the mainframes, it was proposed that an alternative method for determining Orbiter radiator fluxes be created that would replace submitting TRASYS runs for every mission attitude. Therefore, a TRASYS database was generated containing all the fluxes employed by *PCTAP* for every combination of Orbiter, Earth, and Sun positions throughout the range of seasons, altitudes, and inclinations. The basis for this database is that every orbital position and attitude (independent of altitude) can be defined, with the Orbiter as the reference, as a solar clock and cone angle and Earth clock and cone angle. The total electromagnetic flux that meets each Orbiter node surface can be characterized as having three constituents: solar radiation, Earth albedo radiation, and Earth infrared radiation. Software was written to extract the solar, albedo, and infrared fluxes for each of the nodes required (18 for the stowed case, 22 for the deployed case). The generation of this database was accomplished on a Cray.

The software *flxout* was written in order to: (1) employ Mission Operations Directorate (MOD)-provided attitude timeline files to determine the correct solar and Earth clock and cone angles; (2) extract the appropriate solar, albedo, and infrared fluxes from the TRASYS database; (3) modify the fluxes based

upon altitude, orbital position, inclination, and time of year; and (4) store the fluxes in a [.rf] event file, which is compatible with *PCTAP*.

Operation

In addition to the [.rf] file, other file modules are used for *PCTAP* input to reflect mission-specific events and characteristics. All *PCTAP* input files are written in easy-to-use syntax. The [.ev] file reflects mission event timelines that include FES operation, water dumps, radiator configuration, Flow Proportioning Module configuration, Freon Coolant Loop flow rates, etc. The [.pay] file reflects the mission-specific heat loads for the middeck, PLB, avionics bay, etc. The Orbiter-related mission-specific heat loads are contained in the [.hl] file, and can be created using the generic MOD-provided electronic TRAM files.

A mission-specific [.run] file implements the use of all of these input files, employing the appropriate models, and executes the *PCTAP*. A recent improvement to *PCTAP* is the ability to have real-time on-screen plotting capability. When the run is completed, an output file is generated from which data manipulation can be performed, including a very user-friendly *PCPLOT* program that generates plots for any *PCTAP*-generated parameter.

Expanding Analysis

Development continues on *PCTAP* and system-specific models in order to make ECLSS analysis more seamless, flexible, and powerful; such as, inclusion of ARS interfaces with *Mir* and ISS, and implementation of software that determines the solar flux that passes through the Orbiter windows through all mission phases.

CRYOGENIC TANK ANALYSIS PROGRAM

Scott Willen, Gregory J. Hanna, Kevin R. Anderson
Technology Applications, Inc.
Boulder, CO 80303

Abstract

The Cryogenic Tank Analysis Program (CTAP) is a software package that provides rapid, accurate modeling and analysis of complex cryogenic storage and supply systems. CTAP predicts the thermodynamic state of a tank fluid based on quasi steady-state solutions of the first law of thermodynamics for a closed, isothermal system. It includes all of the common cryogens and uses equations of state developed at the National Institute of Standards and Technology (NIST). The system model consists of a pressure vessel, insulation, tank supports, fill, vent, and outflow lines. It has provisions for liquid and gas flow into or out of the tank, pressurization via heaters or helium pressurant, liquid or vapor expulsion, and a thermodynamic vent system option. The user can select from twelve different operating scenarios and has available a wide variety of options for tank size, geometry, materials of construction, pressure-vessel supports, and insulation models. Built-in databases provide structural and thermal material properties. It incorporates a graphical user interface (GUI) for ease of modeling cryogenic systems. Its graphical and tabular output formats enable the user to readily conduct parametric analyses and easily visualize, interpret, and present the results.

Nomenclature

A = area
C_P = specific heat
E = Young's modulus
F = radiation form factor
G = conductance
h = enthalpy
k = thermal conductivity
L = cylindrical length
$\dot{m}$ = mass flow rate
N = numbers of layers MLI
P = pressure
Q = heat leak
R = tank radius
T = temperature
t_w = tank wall thickness
V = tank volume
v = specific volume
α = tank stretch parameter
ε = emissivity
ν = Poisson's ratio
ρ = density of tank fluid (liquid + vapor)
σ = Stefan-Boltzmann constant
θ = specific heat input
ϕ = energy derivative

Subscripts
i = in
l = liquid
o = out
v = vapor

Introduction

The thermodynamic state of the cryogenic fluid in a storage and supply system cannot readily be determined using closed-form solutions or simple iterative techniques. Detailed knowledge of the heat energy into and out of the system, fluid inflow and outflow, thermal capacity and elasticity of the storage vessel, and the thermodynamic properties of cryogenic fluids at each instant of time are necessary. To adequately define the time varying cryogenic fluid state requires a complex computer code that simultaneously calculates these variables and iterates quasi-steady-state solutions at each instant of time.

The Cryogenic Tank Analysis Program was developed for NASA/JSC as a subroutine for their EASY-5X system modeling program. CTAP calculates the thermodynamic state of a cryogenic fluid in a tank or dewar based upon a quasi steady-state solution of the first law of thermodynamics for a closed, isothermal system. It incorporates insulation system heat leak, tank fluid pressurization, liquid or vapor expulsion, and fluid property subroutines based upon NIST developed equations of state.

Model description

The basic tank system, shown in Figure 1, consists of a pressure vessel containing the cryogen, insulation, tank supports, fill, vent, and outflow lines. The thermodynamic system is bounded by the outside surface of the pressure vessel with provisions for both liquid and gas flow into and out of the tank. The system volume is variable to account for

pressure vessel thermal contraction and expansion under pressure.

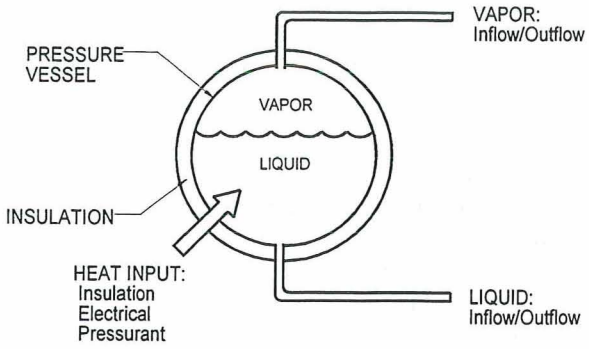

Figure 1 Cryogenic tank thermal analysis model

The user has a variety of options for tank size, shape, materials of construction, pressure-vessel supports, insulation, and fluid operating scenario. These input options are user specified, and all thermodynamic values describing system performance are returned for plotting, control, or inputs into other analyses.

Fundamental equations for time dependent fluid behavior in a cryogenic tank were developed through application of the first law of thermodynamics and expressed as a time derivative of pressure (dP/dt). In its complete form, the dP/dt equation is quite lengthy and includes provisions for the thermal capacitance of the tank wall as well as tank stretching under pressure. For two-phase single-component cryogenic systems, the dP/dt equation can be simplified (ignoring tank stretch and wall capacitance) to:

$$dP/dt = \{Q + \dot{m}_o[h_l-(v_l/(v_v-v_l))h_{lv} - h_o] - \dot{m}_i[h_l - (v_l/(v_v-v_l))h_{lv} - h_i]\}/\rho V(\partial u/\partial P) \quad (1)$$

Equation (1) can be further simplified using the specific heat input (θ) and energy derivative (ϕ):

$$\theta = v(\partial h/\partial v)_v = -\rho(\partial h/\partial \rho)_\rho \quad (2)$$

$$\phi = = v(\partial P/\partial u)_v \quad (3)$$

For two-phase systems, specific heat input θ can be written for liquid or vapor expulsion as:

$$\theta_l = h_{lv}(v_l/(v_v-v_l))$$

$$\theta_v = h_{lv}\ (v_v/(v_v-v_l))$$

By evaluating these thermodynamic functions and selecting the appropriate simplified form of the dP/dt equation, most cases can be solved as simple algebraic equations. The different forms of the dP/dt equation used in CTAP are:

No mass flow (tank lock-up), $dP/dt = \phi Q/V$ (4)

Liquid expulsion (const. P), $Q = \dot{m}_o\theta_L$ (5)

Vapor expulsion (const. P), $Q = \dot{m}_o\theta_V$ (6)

Variable press. expulsion, $dP/dt = (\phi/V)[Q-\dot{m}_o\theta]$ (7)

Including tank stretch in equation 7 yields,

$$dP/dt = [\phi(Q-\dot{m}_o\theta)]/[V(1+\alpha)] \quad (8)$$

The term α in equation (8) is the tank stretch parameter, the change in volume per unit volume of the tank due to internal pressure. For high-pressure systems (e.g. supercritical storage), tank stretch can have a significant impact on the accuracy of the model. For spherical and cylindrical tanks, the tank stretch parameter is given by:

$$\alpha = [\rho\theta\phi(2\pi(1-\nu)R^4)]/[Et_wV] \text{ (spherical)} \quad (9)$$

$$\alpha = \rho\theta\phi\pi(2.5-\nu)R^4L)]/[Et_wV] \text{ (cylindrical)} \quad (10)$$

Cylindrical tanks with hemispherical heads use a combination of Equations (9) and (10) to calculate tank stretch; this approach is also used for cylindrical tanks with 2:1 elliptical heads. An elliptical head will stretch less than a hemispherical head of the same pressure capability; however, the difference is slight, and using the hemispherical head stretch relationship does not introduce a significant error.

Detailed heat-transfer models for evacuated and foam insulations are included in CTAP as user-selected options. A schematic representation of the evacuated insulation system model is shown in Figure 2. This option includes multilayer insulation, vapor-cooled shields (VCS), instrumentation and heater wires, plumbing penetrations, and tank supports. The user specifies the number of layers of multi-layer insulation (MLI), vapor cooled shields (if any), and the area-to-length ratio (A/L) and material of each conductive element. The temperature dependent thermal conductivities for the conductive elements are included in CTAP's property database.

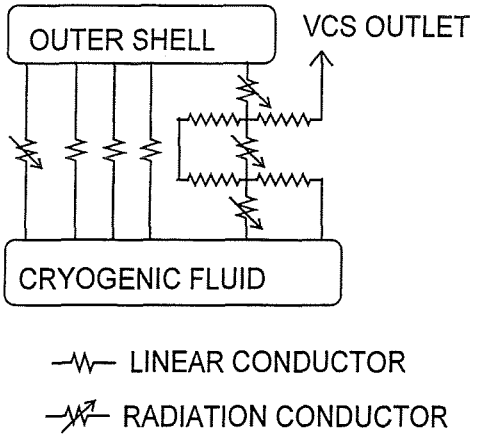

Figure 2 Heat transfer model schematic, evacuated insulation

The thermal analysis subroutine is based on Fourier's law of conduction heat transfer and includes radiation heat transfer. Both classical radiation theory and empirical correlations, incorporating interstitial conduction and compaction effects for MLI performance, are included in CTAP. The steady-state energy balance at a node (including a VCS vent gas mass flow contribution) is written as

$$\Sigma G(T_i - T_x) + \dot{m}C_p(T_i - T_{i-1}) = 0 \qquad (11)$$

where G = kA/L, T_x is the temperature of all nodes attached to node (i), T_{i-1} is the vent gas upstream node temperature, and $\dot{m}C_p$ is the mass flow rate times the specific heat of the vented gas. Equation (11) is rearranged for calculating the temperature at various nodes as:

$$T(i) = [\Sigma GT_x + \dot{m}C_pT_{(i-1)}]/[\Sigma G + \dot{m}C_p] \qquad (12)$$

ΣGT_x is the sum over all paths connected to node (i) and ΣG is the sum of the kA/L values for all paths connected to node (i). The equation for classical radiation heat transfer, with N>>1is:

$$Q_{rad} = [FA\sigma\varepsilon/2(N+1)][T_i^4 - T_x^4] \qquad (13)$$

Within CTAP, equation (13) is incorporated into the thermal model by calculating $G = (Q_{rad}/\Delta T)$.

Model operation

CTAP requires a series of input variables and returns values for table and plot routine entries. The input variables define the operating scenario, fluid, initial fluid state, the tank and its associated descriptive parameters, and the external thermal environment. These input variables are entered through a graphical user interface (GUI) with pull-down menus for all user inputs. Each menu heading is connected to multiple sub-menus that guide the user through the input data required to build a model system. Figure 3 shows the basic CTAP user screen with the helium pressurization option sub-menu. Many variables are provided as defaults or suggested values to simplify data entry. Once all data are entered, the user clicks the "Run CTAP" button and execution begins.

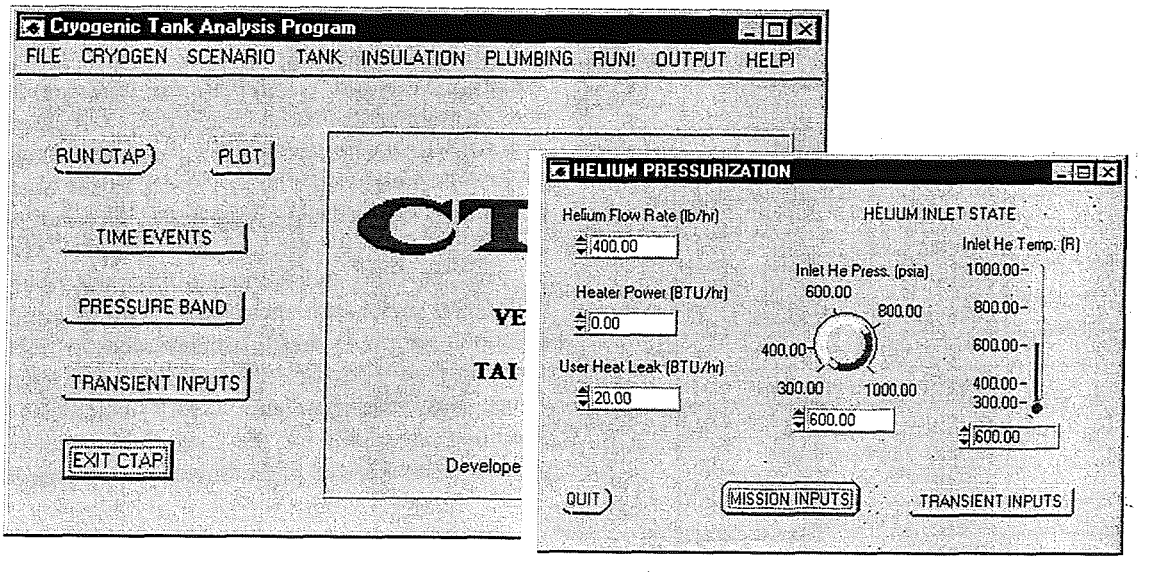

Figure 3 Basic CTAP user screen

CTAP provides the user with twelve different fluid operating scenario options:

Case 1: Constant pressure boiloff or expulsion for supercritical fluid
Case 2: Constant pressure expulsion for liquid
Case 3: Constant pressure expulsion for vapor
Case 4: Tank lockup pressure rise rate (dP/dt)
Case 5: Constant pressure heat input requirements for a given mass flow, supercritical fluid
Case 6: Constant pressure heat input requirements for a given mass flow of liquid
Case 7: Constant pressure heat input requirements for a given mass flow of vapor
Case 8: Supercritical tank blowdown
Case 9: Variable pressure liquid expulsion (user provides Q heater and mass flow)
Case 10: Variable pressure vapor expulsion (user provides Q heater and mass flow)
Case 11: Thermodynamic vent system
Case 12: Helium pressurization

Note that in Cases 1-3, the user may determine expulsion rates with no heater (Q heater = 0), or the user may add a heater power to the background heat leak. Cases 8-10 offer the user the most flexibility, since heater power and mass flow can be cycled off and on, and the tank pressure profile can be generated as a function of time.

Available output data are summarized in Table I. CTAP includes plotting capabilities that allow the user to plot and print a variety of output data as a function of time. These output data can also be saved for later use or for comparison with other runs. In addition to the CTAP plotting package, the output file can be read into a spreadsheet program such as Microsoft Excel™.

Table I CTAP Output Parameters

Variable	Description
Tfout	Cryogen temperature
Qleak	Heat leak
Qheat	Heater power
xmrate	Mass flow rate out of tank
DPDt	Pressure-time derivative
DDDt	Density-time derivative
TS1	Shield 1 temperature
TS2	Shield 2 temperature
TS3	Shield 3 temperature
QS1	Shield 1 heat load
QS2	Shield 2 heat load
QS3	Shield 3 heat load

A driver program reads the user input and evaluates fluid cases, mission events such as outflow, and pressure control requirements. After assigning the appropriate values to all of CTAP's internal variables, the driver program "calls" the core CTAP routines to obtain updated values of all system parameters. These updated values are then used in the next iteration, and the process continues until a "time end" or other stop condition is encountered. During each iteration, the driver program also writes output to the screen and to a file.

All transient solutions require selection of a properly sized time step. If the time step is too small, model execution time becomes excessively long. If the time step is too large, the accuracy of the solution suffers. In balancing these factors, CTAP suggests a time step to the user such that approximately 1000 time steps are taken during model execution. CTAP also reduces the user time step by a factor of ten any time conditions change too rapidly. While this approach provides rapid, accurate solutions for most applications, the user is free to specify a time step other than the CTAP recommended value.

For steady-state solutions, CTAP returns single values that describe the state of the cryogenic system (temperatures, heat flows, and/or mass flows). For transient solutions, CTAP returns a time history of the tank including pressure, temperature, density, and other parameters of interest.

When CTAP is run, it initializes the fluid conditions and determines the fluid properties. Temperatures and mass flow rate through the vapor-cooled shield (if one is present) are then passed to the thermal subroutines that calculate heat leak. If steady-state boiloff is desired, the solution routine iterates between the fluid and thermal subroutines until the boiloff rate matches the heat leak. In all other cases, execution returns to the fluid subroutines to find the remaining thermodynamic parameters. The returned values are then set and CTAP completes its execution, returning for the next time step. This process is summarized in the flowchart in Figure 4.

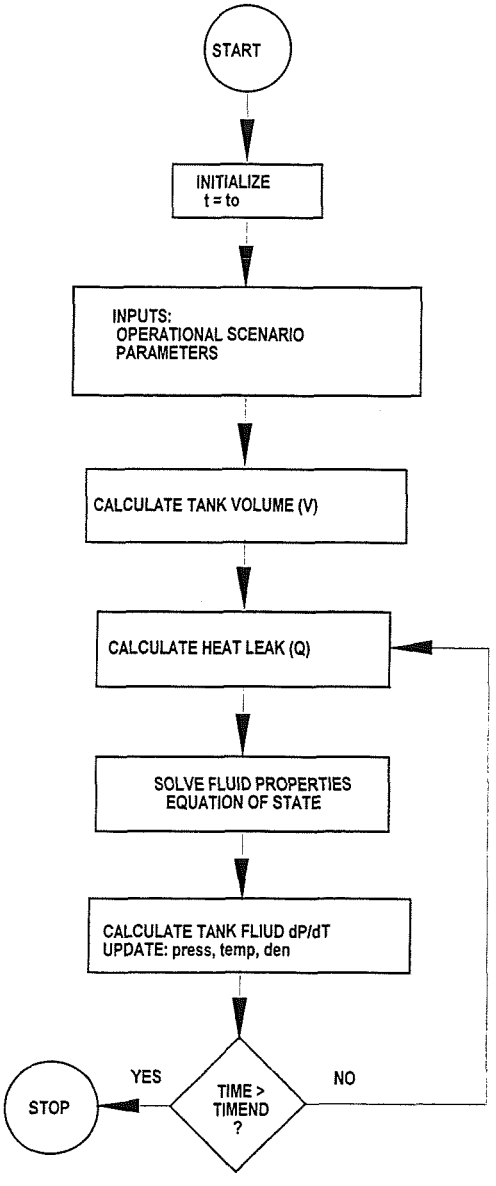

Figure 4 CTAP Program Flow Chart

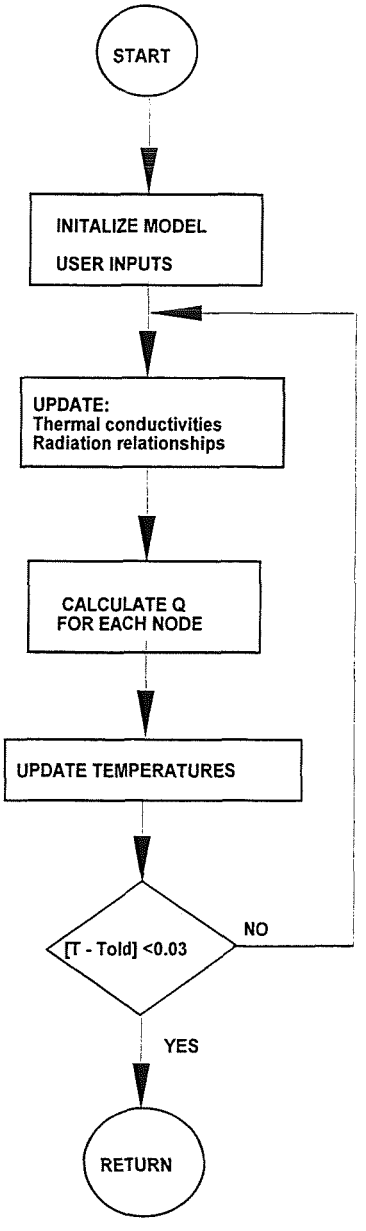

Figure 5 CTAP Thermal Analysis Flowchart

CTAP can be broadly divided into a fluid model and a thermal model. Each model contains multiple subroutines for the required calculations. Flowcharts for CTAP thermal and fluid models are given in Figures 5 and 6, respectively. The thermal model iterates to find a solution until the "old" value of temperature is within 0.03°R of the "new" value, then returns to the main program. Once the value of the tank heat leak (and in some cases mass flow rate) have been determined from the thermal model, the fluid model completes its execution without iteration.

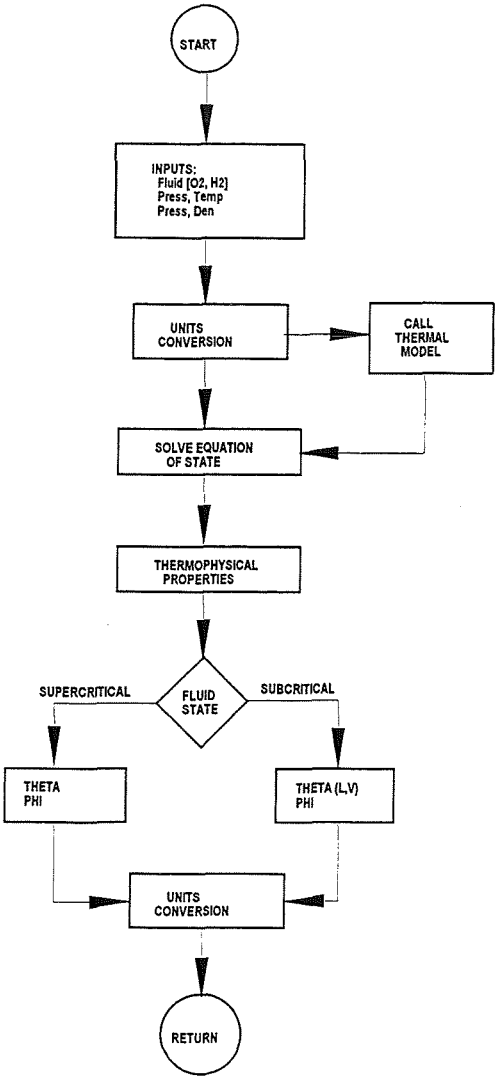

Figure 6 CTAP Fluid Analysis Flowchart

Case 11 allows the user to control cryogenic tank pressure using a thermodynamic vent system. The heat leak through the TVS is computed according to the following expression:

$$Q_{TVS} = \eta \dot{m}_{TVS} (h_{CRYO} - h_{VENT}) \qquad (16)$$

where η is the efficiency of the TVS, $\dot{m}_{TVS}$ the mass flow rate of cryogen through the TVS, h_{CRYO} is the enthalpy of the cryogen at tank pressure and density and h_{VENT} is the enthalpy of the cryogen vapor at the vent pressure and tank temperature. The algorithm for solving the above equation is shown by the flow chart in Figure 7.

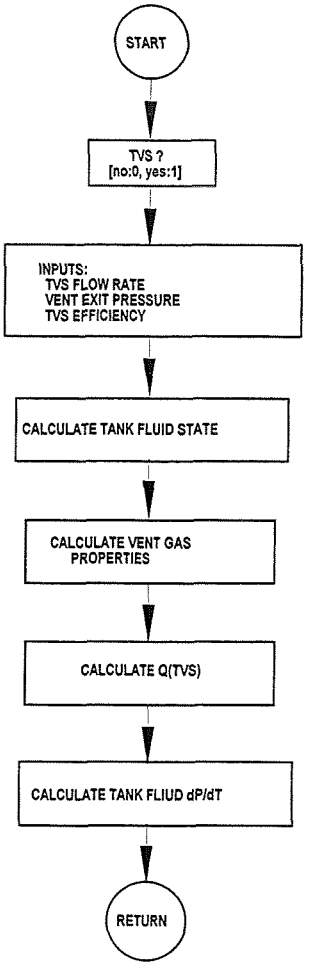

Figure 7 Theromdynamic vent system flow chart

The helium (He) pressurization system option (Case 12) allows for tank pressurization using an external helium source. Both the sensible heats from the helium pressurant and the ullage volume displacement are used in the solution routine, as shown by the flow chart in Figure 8. The iterative technique used to determine when the He and cryogen reach equilibrium in the tank is summarized below:

1) Compute the masses of cryogen and He based on initial values.
2) Compute heat input into the system, ($Q_{tot} = Q_{parasitic} + Q_{He} + Q_{user}$).
3) Determine state point of cryogen (density and enthalpy). The enthalpy of the fluid is computed according to:

$$h_{CRYO} = h_0 + \Delta t(Q_{TOT} + \dot{m}_L(h_0 - h_L) + \eta \dot{m}_{TVS}(h_0 - h_{TVS}))/\dot{m}_0 \qquad (17)$$

where h_0 is the initial enthalpy of the cryogen, Δt is the dwell time of the He pulse, $\dot{m}_L$ the mass flow rate of cryogen out of the tank, h_L the liquid enthalpy of the cryogen in the tank, $\dot{m}_{TVS}$ mass flow rate of cryogen through the TVS (if prescribed), h_{TVS} the enthalpy of the cryogen at the vent pressure of the TVS and temperature of the tank and m_0 is the initial mass of the cryogen in the tank.

4) Using the pressure and temperature of the state point found in step 3, compute He density.
5) Monitor hardfill conditions.
6) Check if the density of He is within a set tolerance of its initial value. If so the solution returns the current state of the system including needed derivatives, if not iteration is carried out until convergence is met.

A two-fluid model is used to account for the ullage volume that is displaced by the helium pressurant. This effect is comparable to reducing the overall volume of the tank by the helium volume as computed at equilibrium conditions in step 4 above.

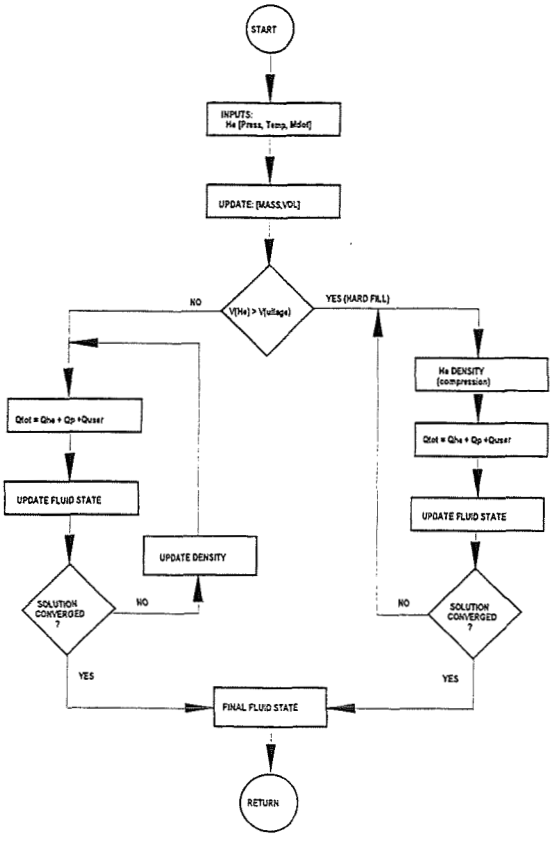

Figure 8 Helium pressurization system

Example problems

To illustrate the features and capabilities of CTAP, three example problems were run:

Tank lock-up: A ten cubic-foot liquid hydrogen dewar has a heat leak of 6 watts and is filled to the 95% level (5% ullage). After stabilizing at 15 psia, the vent line is closed and the hydroden self-pressurizes. The pressure rise rate (dP/dt) is shown in Figure 9. The shallow portion of the curve (low dP/dt) corresponds to the liquid hydrogen absorbing the heat leak, condensing the ullage gas, and expanding to fill the ullage space. After the liquid fills the entire tank volume, any further expansion compresses the liquid. As liquid is nearly incompressible, the pressure rise rate increases dramatically, shown by the steep dP/dt portion of the curve.

Constant pressure outflow, supercritical oxygen: A five-pound per hour flow rate of oxygen is required to operate a fuel cell. The oxygen is stored in a one-cu-ft dewar at an initial storage pressure and density of 950 psia and 50 lb/ft^3 respectively. A 200-watt heater is used to maintain the oxygen pressure between 800 and 900 psia during outflow. Figure 10a shows the tank pressure and heater power over an eight-hour expulsion; Figure 10b shows the oxygen mass and its temperature during the twelve-hour outflow period.

Zero-g storage and supply: A 10 cu-ft liquid oxygen (LOX) tank stores 500 pounds of saturated oxygen at 350 psia. It is equipped with a liquid acquisition device, TVS, and helium pressurization system. The total system heat leak is 16 BTU/hr. Every 24 hours, 60 pounds of liquid oxygen is withdrawn from the tank at a rate of 60 lb/hr. A TVS is used to maintain tank pressure between 340 and 360 psia; its vent rate is fixed at 2.5 lb/hr, its inlet pressure is the tank pressure, and its outlet pressure is 5 psia. The helium pressurant is stored at 4500 psia and 600°R and its flow rate is 0.15 lb/hr. This system is illustrated by Figure 11; its performance is shown in Figure 12. The left ordinate is the mass flow rates of the oxygen, TVS, and helium pressurant. The right ordinate is the tank pressure. This example uses case 12, which incorporates the case 9 and 11 TVS and variable pressure liquid outflow codes.

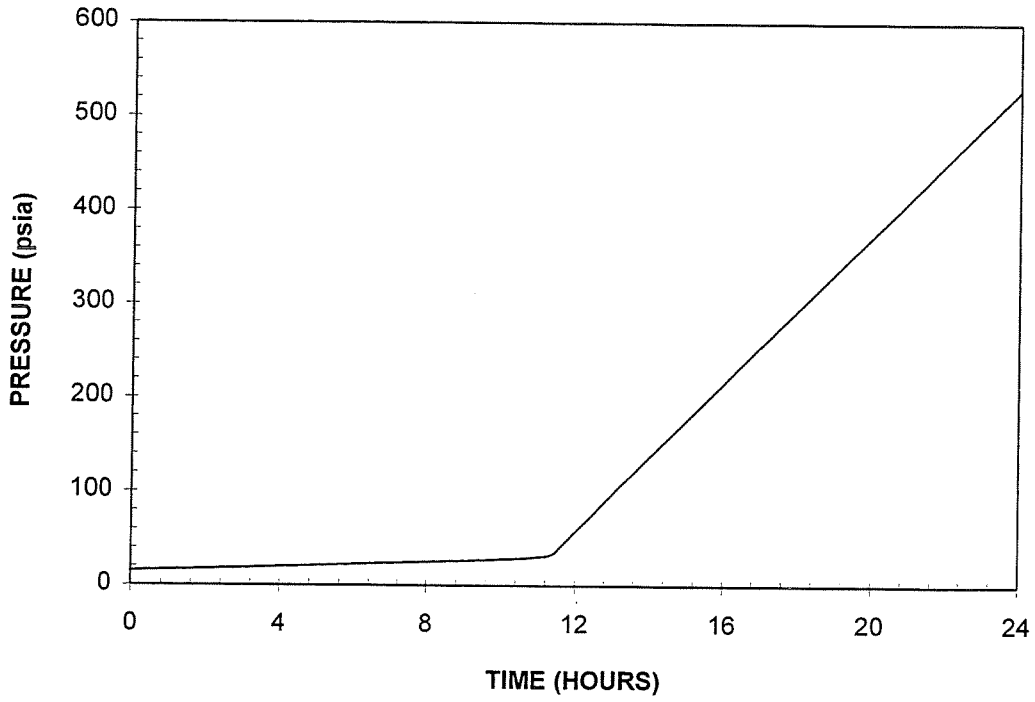

Figure 9 Hydrogen tank lock-up, pressure-time profile

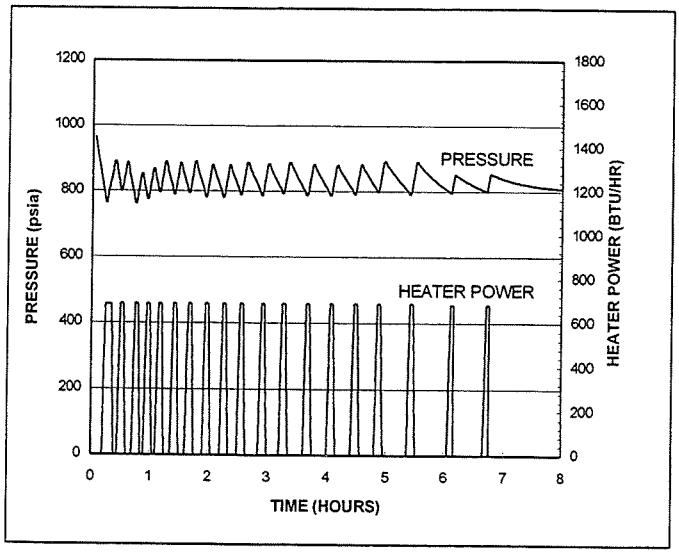

Figure 10a Supercritical oxygen expulsion, pressure and heater power profiles

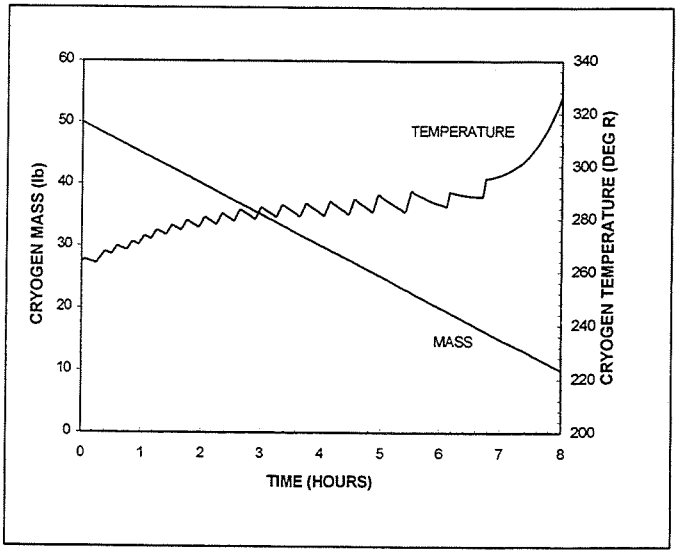

Figure 10b Supercritical oxygen expulsion, oxygen mass and temperature profiles

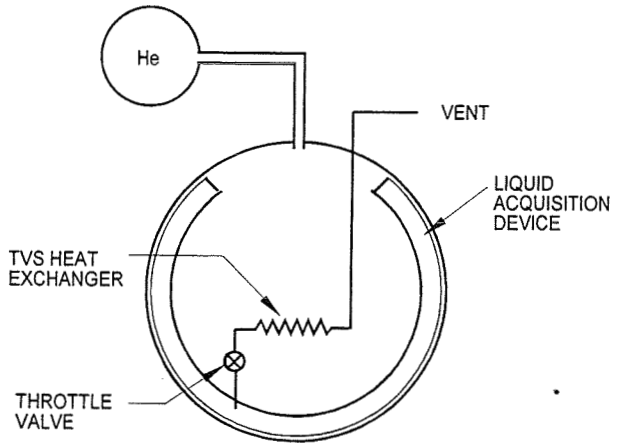

Figure 11 Oxygen tank configuration for 0-g operation

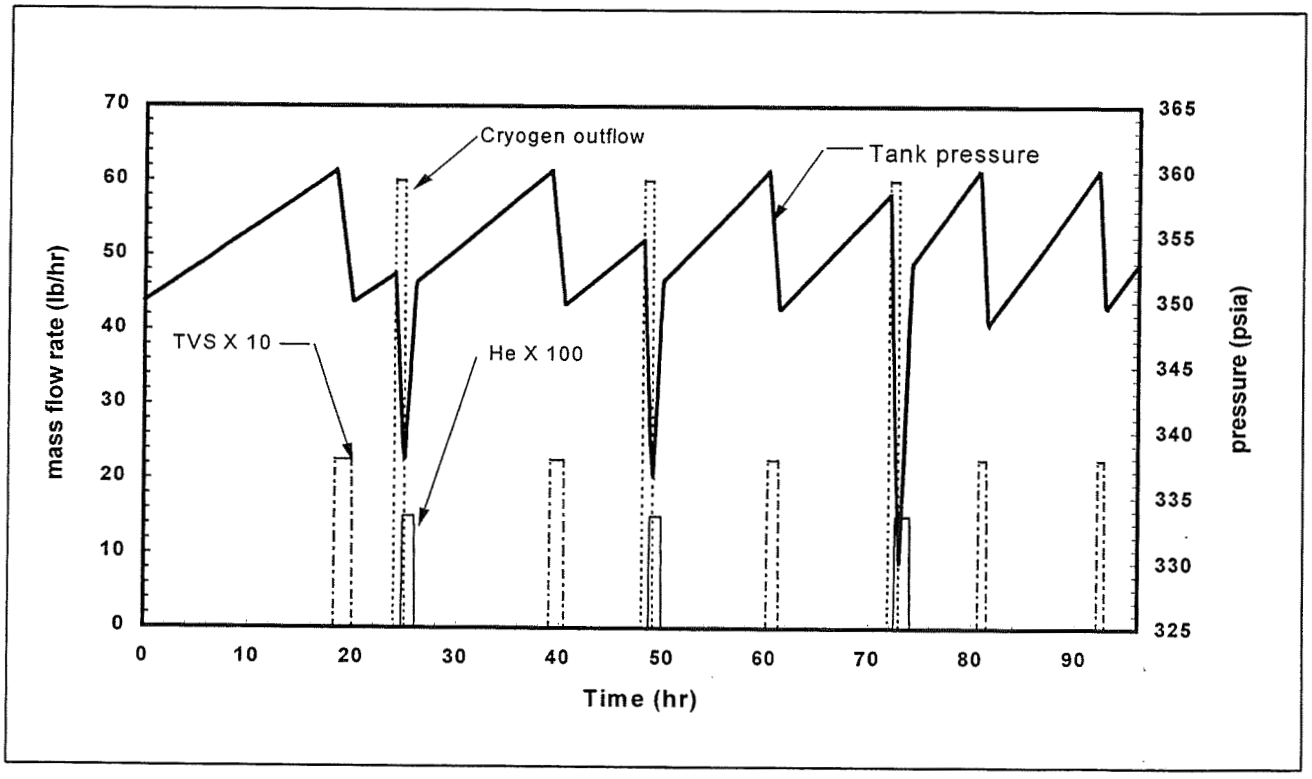

Figure 12 Mass flow rates and pressure profiles for 0-g LOX expulsion

X-38 CABIN CONDENSATION STUDY

Bradley D. Eckhardt
Lockheed Martin Engineering & Science Services
Houston, TX

Abstract

The International Space Station's (ISS) X-38 Crew Return Vehicle is being developed to provide emergency crew escape capabilities for the ISS. The X-38, a lifting-body vehicle, will be attached to the ISS while in orbit with a Soyuz-style docking ring allowing air exchange between the X-38 cabin and the ISS. During certain ISS orbital positions, adiabatic external surface temperatures on the X-38 can reach as low as -129 (C). Although the X-38 is constructed with a Thermal Protection System (TPS) which includes insulation in the vehicle structure, an analysis of various proposed Environmental Control and Life Support System (ECLSS) designs is required to determine if condensation can occur in the cabin during these "cold case" conditions. An analysis was performed using PHOENICS, a finite-volume code [1] to model fluid flow and heat transfer characteristics within the cabin using a simplified model of the cabin geometry. Boundary conditions at the cabin wall were provided as heat fluxes by a NASA/JSC aeroshell heat leak study of the X-38 TPS using Thermal Synthesizer System (TSS). Development of the TSS and PHOENICS X-38 models continues, however preliminary results indicates local inside cabin wall temperatures can fall below cabin dew points, thereby providing conditions conducive to condensation.

Nomenclature

Velocity	(m/s)
Temperature	(C)
Volumetric Flow Rate	(m^3/s)
Heat Flux	(W/m^2)

Introduction

The purpose of this study is to determine if condensation can occur in the X-38 cabin during "cold case" conditions while attached to the ISS in orbit. Because of the complex nature of the fluid flow and heat transfer phenomena which occur within the cabin, Computational Fluid Dynamic (CFD) methods were used to model these phenomena. Two issues were of major concern in developing a CFD model of the X-38 cabin: the implementation of boundary conditions and the complexity of the cabin geometry. Although the focus of the study is on conditions in the cabin, boundary conditions between the cabin and the X-38 external structure need to be integrated into the cabin model since conditions outside the cabin provide the heat sink. Therefore, an effort was made to integrate boundary conditions between the PHOENICS X-38 cabin model and an existing TSS model of the X-38 external structure. Since heat fluxes through the TSS model are in turn dependent on boundary conditions at the cabin wall interface, wall temperatures were provided by The PHOENICS cabin model as boundary conditions to the TSS model. Several iterations of exchanging boundary conditions between the cabin and TPS models are needed to converge on a solution until wall temperatures and fluxes do not change significantly with new iterations. Secondly, the cabin geometry includes a proposed ECLSS system which includes a ventilation duct designed to distribute air over the inside cabin walls. This type of air distribution is designed to maintain surface temperatures above cabin dew points along the inside cabin walls, where condensation is most likely to occur. Separate PHOENICS models of the cabin and the ventilation duct were developed in order to simplify the cabin model and to allow for a more detailed and accurate model of the flow distribution in the ventilation duct to be developed. Boundary conditions pertaining to air flow from the ventilation system are interchanged between the two models. The cabin model will be the focus of this paper .

Model Development

A model of the cabin geometry was developed assuming a plane of symmetry located along the centerline traveling from the fore to aft and nadir to zenith directions (see Figure 1). The cabin model geometry includes the cabin pressure vessel, a simplified geometry of the hatch interface with the ISS, and the outer surfaces and the outlet ports of a proposed ventilation duct design. The grid was generated using a body-fitted coordinate system. The grid for the non-rectangular cabin geometry was developed in coordination

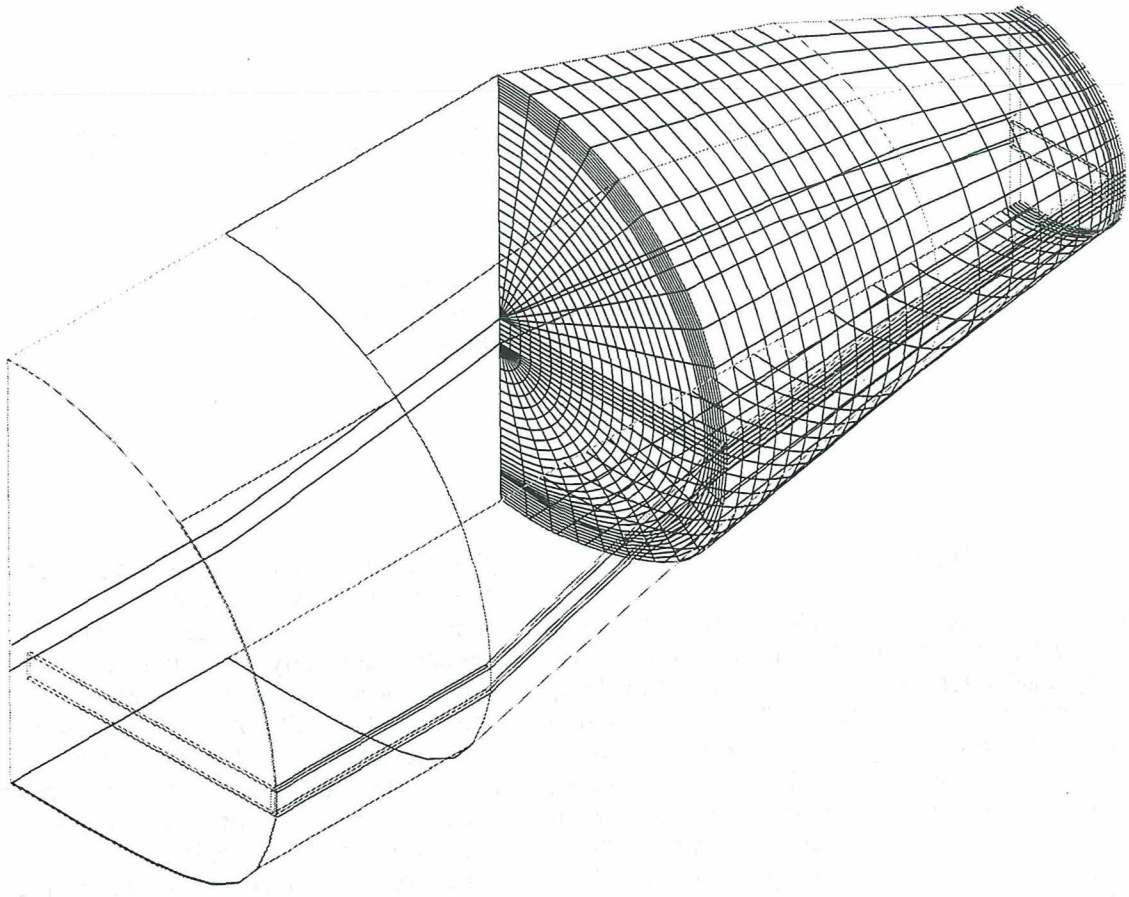

Figure 1. PHOENICS X-38 Cabin Model Geometry and Grid.

with PHOENICS North America Inc.. Two major criteria were considered when developing the grid. First, the grid must include the geometry of the proposed ventilation duct which includes the outer surface areas of the duct as well as the outlet ports of the duct. where supply air flows into the cabin. As stated above, air flow through the ventilation duct is modeled in a separate PHOENICS model. The ventilation duct geometry is included in the cabin model in order to account for effects on air flow in the cabin the ventilation duct may cause. However, the duct geometry is modeled as a solid aluminum blockage and heat transfer between the duct and the cabin is based on conduction through the aluminum. In addition, the grid must be able to accommodate various aperture configurations since these configurations may need to be modified after the grid is completed in order to achieve the optimum air distribution needed to maintain wall temperatures above cabin dew points. These aperture configurations can include small openings and therefore the grid must be adequately refined in this region of the cabin. The second criteria requires that the grid is adequately refined to be able to predict heat and mass transfer sufficiently, especially near the cabin wall where accurate prediction of local surface temperatures is necessary for this application.

PHOENICS uses a structured grid in which the number of cells on opposite sides of a four sided frame must be equal. For this application, certain points of singularity of selected frames within the domain are overlapped, creating a "rotational" grid occupying the regions in the domain defined by a geometry with curved surfaces. The "rotational" grid conforms well to the curved geometry of the cabin and was developed because problems with non-orthogonal cells arose when a "rectangular" grid was used in these regions. A "rectangular" grid was developed for the region occupied by the ventilation duct which has a rectangular geometry with dimensions .101 by .038 (m). In the cabin geometry, the ventilation duct is located along the widest section of the cabin pressure vessel and runs the entire length of the cabin and across the fore and aft bulkheads (see Figure 1) . Both rectangular and rotational type grids were incorporated into the domain using a technique recommended by PHOENICS Inc.. Using this method, the refinement of the grid in the region of the ventilation duct also provides for a more refined grid in the region close to the cabin walls which is beneficial if heat and mass transfer close to the cabin walls is to be modeled accurately. A cross-section of the grid is depicted at approximately half the distance along the Z axis in Figure 1 along with a projection of the grid onto a section of the pressure vessel wall. The cabin pressure vessel is aluminum and has dimensions of .05, .006, and .002 (m) for the thickness of the fore and aft bulkheads and

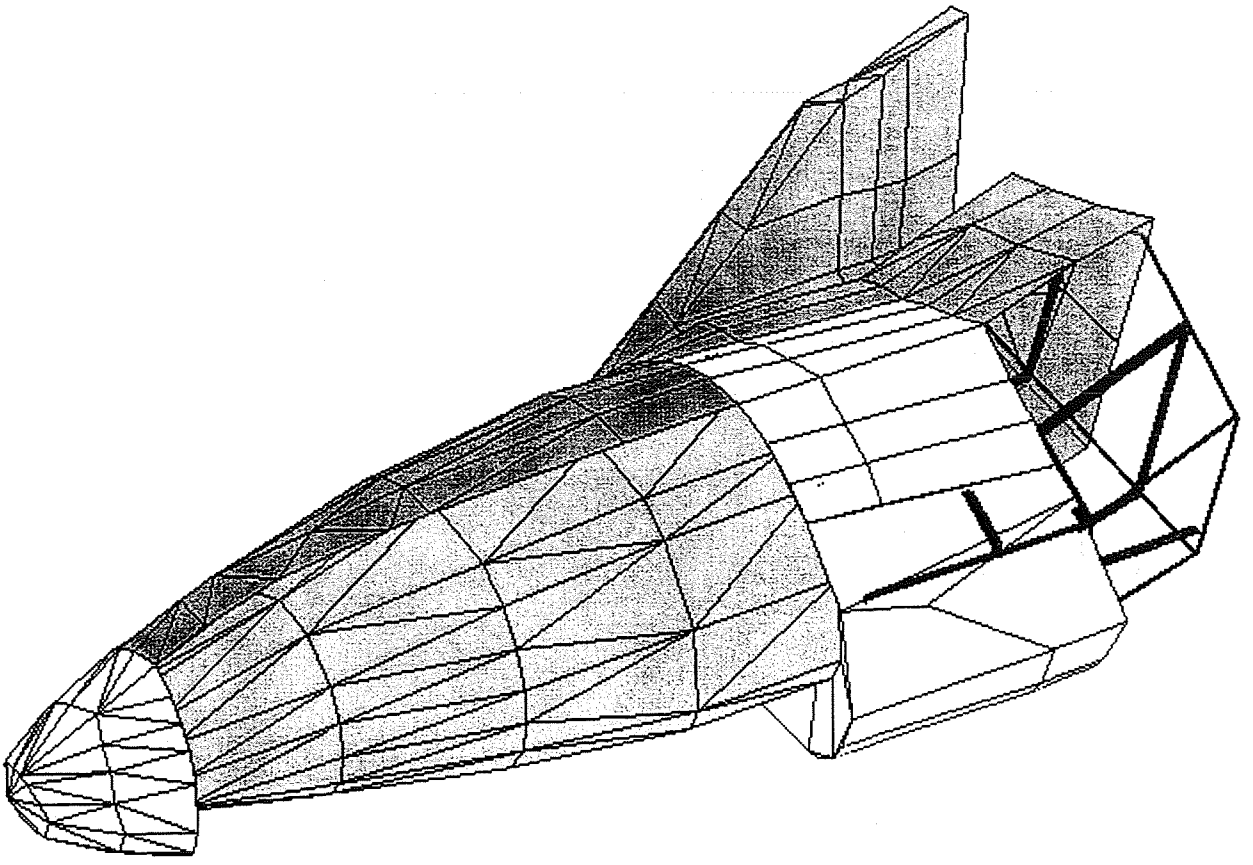

Figure 2. Thermal Synthesizer System X-38 Thermal Protection System Geometry.

the side walls respectively. Conductive resistance in the normal direction to the pressure vessel surface is assumed negligible for all surfaces except the fore bulkhead due to the thin dimensions of the pressure vessel.

Implementation of boundary conditions in the model includes two main areas of concern: inlet flow rates from the ventilation duct and heat transfer through the cabin walls. The development of a grid to permit the implementation of inlet flow rates from the ventilation duct is discussed above. Supply air volumetric flow rates of 2.33 (m^3/s) at 21.1 (C) are the current design requirements for this model. The current aperture configuration in the ventilation duct is designed to distribute the air flow based on the amount of surface area of the cabin walls. As the surface area decreases in the aft to fore direction, air flow rates from the ventilation duct decrease. Boundary conditions are imposed at selected cells along the ventilation duct grid by specifying the velocity of the fluid across the cell face.

Modeling heat transfer through the cabin pressure vessel required an effort to integrate boundary conditions between the PHOENICS X-38 cabin model and a TSS model of the X-38 Thermal Protection System. Because heat transfer rates vary over the surface of the pressure vessel, local heat fluxes were used in both the cabin and the TPS model. Local heat fluxes were calculated for each pressure vessel node in the TSS model. The nodes in the TSS model are comprised of triangular surfaces (see Figure 2). These local heat fluxes are then applied as boundary conditions in the PHOENICS model at their counterpart nodes. These "boundary condition" nodes in the PHOENICS cabin model were developed using the corresponding spatial coordinates of the pressure vessel nodes in the TSS model (see Figure 1). Since heat fluxes through the TSS model are in turn dependent on boundary conditions at the cabin wall interface, wall temperatures were provided by The PHOENICS cabin model as boundary conditions to the TSS model. Mean local wall temperatures for the corresponding nodes between the two models are calculated from the PHOENICS X-38 cabin model results and input into the TSS model. Several iterations of exchanging boundary conditions between the cabin and TPS models are needed to converge on a solution until wall temperatures and fluxes do not change significantly with new iterations.

Results

The X-38 cabin and TPS models are currently still under development. Efforts in this phase of the project are focused on iterating boundary conditions (local mean heat fluxes and cabin wall temperatures) between the two models. The sim-

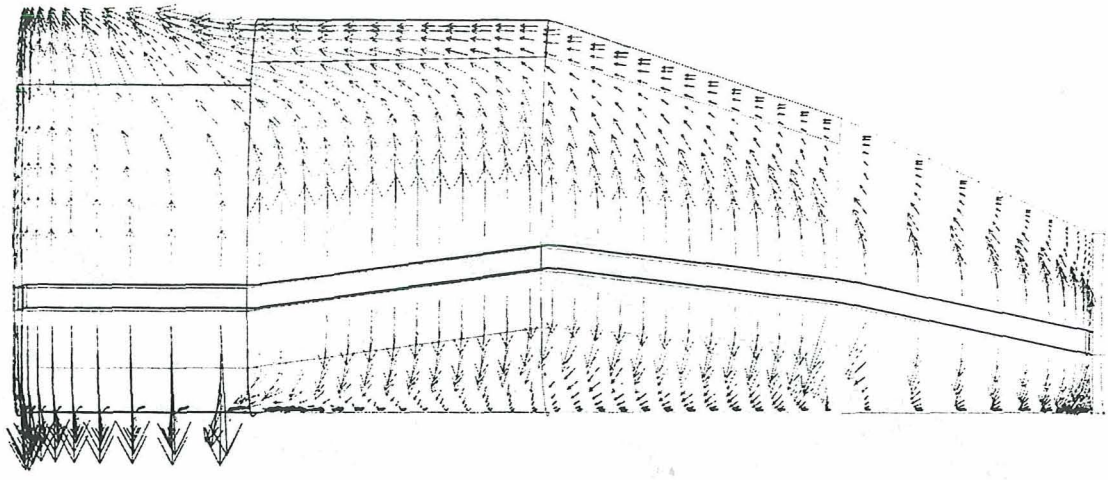

→ 1.28E-01 Min: 5.72E-05 Max: 2.59E-01

Figure 3. PHOENICS X-38 Cabin Model Flow Field (Ycell=2).

ulation was conducted for steady state conditions. Initial examination of the simulation results indicates the flow field predicted by PHOENICS follows expected streamlines. Figure 3 shows velocity vectors (m/s) in the grid plane which includes the cells in the ventilation duct where the supply air enters the cabin (i.e. Ycell=2). The velocity vectors, which vary in magnitude and direction, demonstrate that the type of ventilation duct air distribution required is essentially achieved and that the air flows towards the outlet hatch. Further examination of the numerical simulation results verifies that the mass flow rates balance between the inlet and outlet openings. At the current iteration between the cabin and TPS X-38 models, TSS calculated local heat fluxes through the cabin pressure vessel total 185 (W/m^2). Local mean cabin pressure vessel wall temperatures range between 9.66 and 15.99 (C). A cabin dew point of 12.7 (C) is used as the current design requirement for the study. Further iterations are needed to achieve an energy balance between the cabin and TPS models. Provided an energy balance can be achieved, the ventilation duct air distribution may need to be modified as well in order to increase local temperatures above cabin dew points if possible. Future work may involve modifications to the cabin geometry to include internal obstructions such as electronics equipment, which can effect flow fields and heat transfer within the cabin.

REFERENCES

1. Patankar, V. S., Numerical Heat Transfer and Fluid Flow, Hemisphere, NY, 1980.

Orbital Thermal Environment Measurements and Comparisons to Analysis

Joseph M. Lepore

John V. Iovine
EVA Systems Analysis Group
Lockheed Martin
Houston, TX

ABSTRACT

Thermal environment data collected during Space Shuttle missions is compared to predicted results using two analysis methods. A Thermal Cube Assembly (TCA) was flown aboard three Space Shuttle missions to determine incident heat fluxes at a particular attitude, vehicle orientation, and TCA location. This information was used to support on-orbit verification of Extra-Vehicular Activity (EVA) space suit modifications. The flight data are also being used to obtain on-orbit transients to verify thermal environment model predictions for future missions. Radiometers were used to measure the environment sink temperature in six directions. The TCA contains twelve radiometers, six of which measure total incident radiation and six to measure radiation in the infra-red (IR) wavelengths only. Each face of the TCA contains one total and one IR radiometer. Each radiometer was calibrated using a thermal vacuum chamber and an environmental simulator. Flight data were converted to environment sink temperatures using calibration equations. Analysis predictions were made using both the Thermal Synthesizer System (TSS) and the Thermal Radiation Analyzer System (TRASYS) for environmental calculations and the Systems Improved Numerical Differencing Analyzer (SINDA) for temperature calculations. In general, TSS sink temperature predictions showed better agreement with flight data than TRASYS. In several instances, both analysis methods had significant discrepancies when compared to flight data. Sources of error for analysis results using both calculation methods are discussed.

NOMENCLATURE

IR - Infra-Red

EMU - Extra-vehicular Mobility Unit

EVA - Extra-Vehicular Activity

SINDA - Systems Improved Numerical Differencing Analyzer

TCA - Thermal Cube Assembly

TMM - Thermal Math Model

TRASYS - Thermal Radiation Analyzer System

TSS - Thermal Synthesizer System

-YLV - orbiter wing to Earth

+ZLV - orbiter bottom to Earth

-ZSI - orbiter bay to Sun

+ZSI - orbiter bottom to Sun

INTRODUCTION

In order to provide on-orbit verification of EVA suit modifications, it was necessary to obtain flight environment data during several Space Shuttle missions. Acquisition of such data served to both verify that the exposed environment met the requirements needed to assess suit modifications and obtain on-orbit transients to verify model predictions for future missions. Due to rapid changes in the environment during day to night cycle transitions, it was determined that using radiometers to measure incident heat flux would provide the best results. Radiometers were found to react faster than thermocouples during these transitional periods. The radiometers were housed in the TCA and positioned near EVA activities in the Space Shuttle payload bay during STS-63, STS-69, and STS-72. The most comprehensive set of flight data was obtained during STS-72, and this will be the focus of subsequent discussions. Calibration of the radiometers was performed during thermal vacuum testing using a blackbody enclosure to simulate environments ranging from -130 to 150 °C. A unique calibration equation was then derived from test data for each radiometer to determine an environmental sink temperature for a given millivolt (mV) signal and radiometer temperature. Comparisons between flight data and both TRASYS and TSS analytical predictions were made.

DISCUSSION

BACKGROUND - The TCA was utilized during two EVA's on STS-72. During each EVA, a TCA was located at a different location along the port side of the Space Shuttle payload bay. Each face of the six-sided TCA is approximately 0.23 meters square. Both radiometer temperature and mV data were retrieved from each TCA. Radiometer calibration equations were used to process the TCA flight data for comparison with Thermal Math Model (TMM) post flight predictions.

The radiometers chosen for use in the TCA were manufactured by Concept Engineering. Each cylindrical radiometer is 3.2 cm in diameter and 3.8 cm long. The total weight of each radiometer is approximately 100 grams. On each face of the TCA were one Infra-Red (IR) radiometer to measure only radiation in the IR band and one total radiometer to measure both solar and IR radiation. IR radiometers were selected because a calibrated solar source was unavailable for testing. The IR radiometers are similar to the total radiometers except they are fitted with a Germanium window to block solar radiation. Calibration of the radiometers was performed in two steps. First, a coarse calibration was used to obtain data for a wide range of environment temperatures. The radiometers were exposed at 55 °C intervals to temperatures ranging from -130 to 150 °C. Radiometer temperature and mV signals were recorded for use in deriving calibration equations for each unit. Following the STS-72 mission, a second calibration was performed, concentrating on the coldest environments experienced during the second EVA of that mission (-46 to -129 °C) [1]. Sample post flight calibration curves are presented in figure 1. Radiometer temperature and mV signal for each environmental sink temperature tested are shown. The six total and six IR radiometers used during EVA #2 were tested. All of the total radiometers produced consistent mV readings that were subsequently used to re-calculate the cold STS-72 EVA #2 environments using flight data. For all but one of the total radiometers, test data confirmed the previous calibration. Several inconsistencies in mV readings were observed for the IR radiometers during post flight testing. For sink temperatures below -87 °C, four of the six IR radiometers produced questionable readings. The remaining two IR radiometers had inconsistencies in the -46 to -73 °C sink temperature range.

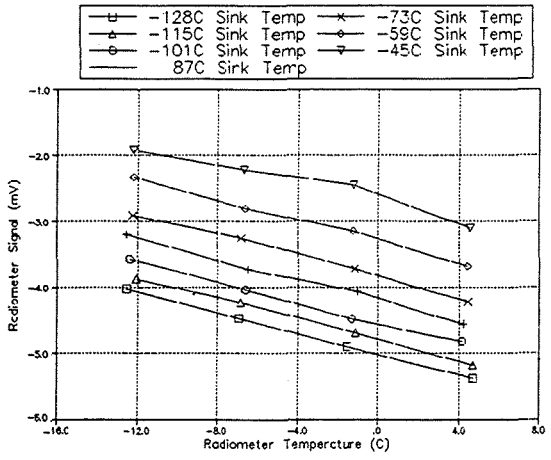

Figure 1. Sample calibration curves from post flight testing

An integrated STS-72 TMM, including a fully correlated model of the TCA, was used to predict on-orbit temperatures and incident heat fluxes for both total and IR radiometers. The TMM was originally constructed using TRASYS, and later converted to TSS for additional analysis. Analysis was originally performed for two configurations using TRASYS. Due to discrepancies between flight data and predicted TRASYS results during the second EVA, additional analysis was performed using TSS. The second EVA was analyzed with and without an Extra-vehicular Mobility Unit (EMU) present during the orbiter bottom to Earth (+ZLV) night pass of EVA #2. The EMU is the suit an astronaut wears during EVA. Since the astronaut did not remain stationary during the EVA, an approximate positioning was used. An EMU was included in the analysis for this portion of EVA #2 since it was determined that a significant amount of shading was present. The TMM was run using as-flown attitudes, including thermal conditioning prior to the TCA leaving the airlock. The location of the EMU relative to the TCA is depicted in Figure 2.

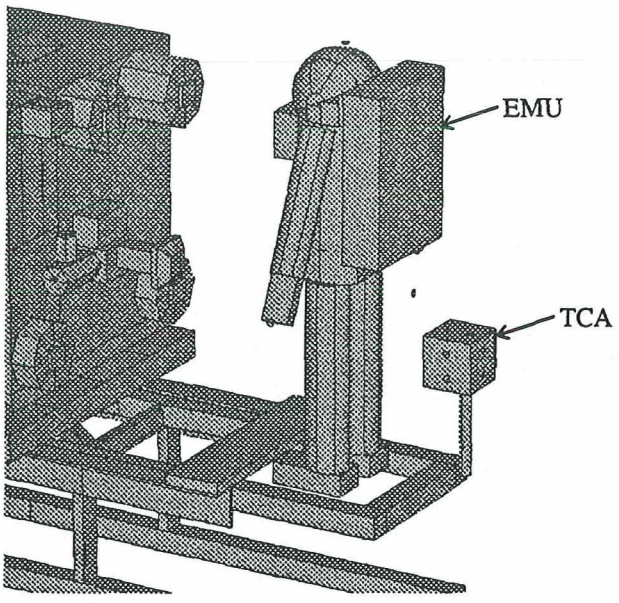

Figure 2. EMU and TCA relative locations during STS-72 EVA #2.

The TCA provided flight temperature and mV data for total and IR radiometers on each side of the TCA. Original calibration results were calculated using calibration equations to convert flight data into incident heat flux values, which were then used to calculate black body sink temperatures using the following equation:

$$T = (Q/\sigma)^{1/4}$$

where Q is the total incident flux, and σ is the Stefan-Boltzmann constant. New calibration results were calculated using post flight calibration test data to determine sink temperatures for a given radiometer temperature and mV reading. The post flight calibration test data was only used when radiometer and environment sink temperatures were within the range of tested values. When flight data was out of range, the original calibration equations were used.

TRASYS employs a double summation method for form factor calculations. The form factors are then converted to radiation conductors using the Gebhart calculation method. The grey body information is also used to calculate heating rates for each surface. TSS uses Monte Carlo ray tracing to calculate radiation conductors and heating rates. For the STS-72 TCA geometric model, TSS was used to selectively shoot rays until each value had a weighted error of 10 percent or less. Additional rays were then shot for all TCA surfaces to further reduce the percent error of the radiation conductors and heating rates that most affect the TCA radiometers.

RESULTS - Flight radiometer temperature and mV data from each TCA during STS-72 EVA #1 were converted to heat flux values by using the original radiometer calibration equations. Heat flux values were then converted to blackbody sink temperatures for each of the total radiometers. A six-direction average sink temperature comparison for EVA #1 showed close agreement between flight data and TRASYS model predictions during the night cycles of the orbiter wing to Earth (-YLV) orbit (Figure 3). Average sink temperatures ranged from -51 to -62 °C during these periods. Flight data comparisons to TRASYS model predictions for STS-69 using the same total radiometers [2] during night cycles had also shown close agreement. Flight data from the day cycles indicate that direct and reflected solar radiation from the Earth for a TCA located near the orbiter sill longeron can vary significantly depending on the precise orientation of the orbiter during a wing to Earth attitude. Model refinements would be required to accurately simulate this configuration. Analysis of EVA #1 using TSS was not performed.

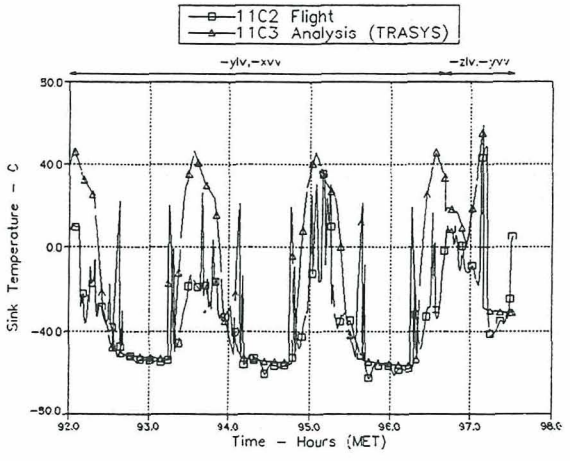

Figure 3. 6-side average sink temperature (STS-72 TCA, EVA #1)

Of the 12 IR radiometers used during both EVA's, negative heat flux values were calculated for 4 of them, indicating a discrepancy between the calibration equations and the flight data. During EVA #1, the six-direction average flight IR heat flux is approximately 63 W/m^2 less than predicted. In comparing IR heat flux data on each side of the TCA, it was found that the flight IR heat flux data are consistently less than the predicted values. Flight IR heat flux data are approximately 63 to 126 W/m^2 less than predicted on

each side of the TCA. Although it appears that the transient trends of the flight heat flux data during EVA #1 correspond quite well to model predictions, a shift in the flight heat flux profiles would be required to achieve correspondence with model predictions. Flight data comparisons to TRASYS model predictions for STS-69 using the same radiometers [2] confirm these IR heat flux differences.

During the second EVA, flight radiometer temperature and mV data were converted to heat flux values by using both the original and post flight radiometer calibration data. Again, heat flux values were converted to blackbody sink temperatures for each of the total radiometers. IR radiometers were not used in comparisons to model results due to the inconsistencies in the IR calibration test data. The sink temperatures were used for comparison with predicted values from the original TRASYS analysis [3]. Night cycle sink temperature predictions using TRASYS were found to be 17 to 33 °C colder than flight data. The average EMU environment sink temperature during a 32-minute orbiter bottom to Earth (+ZLV) night pass of EVA #2 was -54 °C from flight data as compared to -88 °C from the original TRASYS analysis. TRASYS analysis with EMU shading effects near the TCA resulted in a -83 °C average temperature during the same 32-minute period, a 5 °C improvement. The same analysis was also performed using models converted from TRASYS to TSS. The 32-minute average sink temperature using TSS environment data was -82 °C without the EMU, and -79 °C when the EMU was included. Data obtained from the post flight calibration testing was used to re-calculate sink temperatures from the flight data. The 32-minute average flight sink temperature using new calibration data was -62 °C. Comparison of flight sink temperatures using the new calibration data and the TSS analytical results (with EMU effects) reveals a 17 °C temperature difference. A summary of 32-minute average sink temperatures is presented in Table 1.

Calculation Method	Sink Temp.
flight data, original calibration	-54 °C
flight data, new calibration	-62
TSS, with EMU effect	-79
TSS	-82
TRASYS, with EMU effect	-83
TRASYS	-88

Table 1. 32-minute 6-direction average sink temperatures (+ZLV attitude) for STS-72 EVA #2

Figure 4 compares 6-direction average sink temperatures using TRASYS, TSS, and flight data. Flight data curves using calibration equations and post flight calibration test data are very similar except in the coldest portions of the timeline. Close agreement between all analytical methods and flight data is exhibited during most of the day cycles, with the exception of the orbiter bay to Sun (-ZSI) portion of EVA #2. During this period, TRASYS predictions were approximately 17 °C warmer than flight data. TSS analysis results showed close agreement with flight data during this period. TSS also produced slightly better agreement with flight data during night cycles, with the most significant occurring during the 32-minute +ZLV night pass of EVA #2. TRASYS and TSS with EMU shading effects as compared to flight data using post flight calibration data are summarized in Table 2.

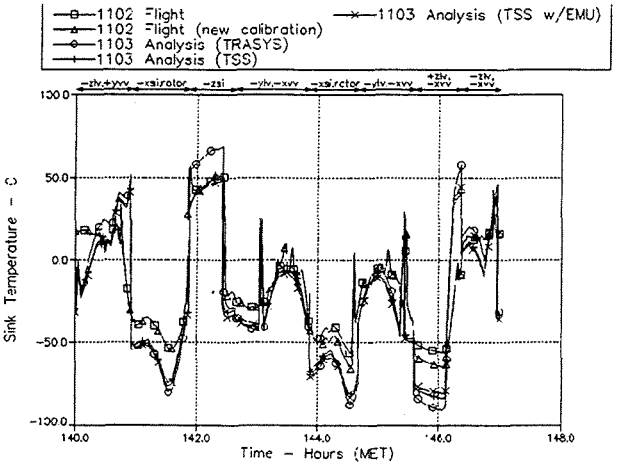

Figure 4. 6-side average sink temperature (STS-72 TCA, EVA #2).

face	flight	TRASYS	Δ	TSS	Δ
+ X	-69 °C	-93 °C	24 °C	-91 °C	22 °C
+ Y	-54	-75	21	-70	16
+ Z	-30	-52	22	-43	13
- X	-76	-94	18	-93	17
- Y	-90	-94	4	-96	6
- Z	-98	-127	28	-124	26

Table 2. Minimum Sink Temperatures (+ZLV attitude) for EVA #2, including EMU

Agreement with flight data improved in 5 of the 6 directions using the TSS calculation method. These improvements ranged from 1 to 9 °C.

Figures 5-10 compare sink temperatures for the various calculation methods on each side of the TCA. Referring to figure 5, sink temperatures for the radiometer in the +X direction decreased approximately 38 °C when post flight calibration test data was used during two of the night cycles. The use of the post flight calibration test data instead of the original calibration equations had minimal effect on the other 5 total radiometers. The -Z direction, most affected by EMU shading, had the largest sink temperature difference between flight and model predictions (Figure 8). Sink temperatures in the -Z direction were approximately 75 °C warmer in the TSS analysis with the EMU near the TCA. Although further investigation into the amount of EMU shading on this side of the TCA may account for the sink temperature differences, it should be noted that a change in sink temperature from -98 to -127 °C in the -Z direction (Table 2) would affect the 6-direction average by less than 3 °C. Directional results using TRASYS with the EMU shading effects are not included. Significant differences in predicted night cycle sink temperatures, without EMU effects, are demonstrated in the +Z and +Y directions (figures 6 and 9). TSS predicted values are approximately 8 °C warmer than TRASYS values during the night cycles in these directions.

STS-72 EVA #2 flight data from an IR radiometer on the Earth facing side of the TCA during periods of orbiter wing to Earth (-YLV) exposure ranged from 94 to 189 W/m^2. The predicted flux value for this radiometer was approximately 236 W/m^2, which compares favorably to a typical planetary flux. Both flight data and analysis of a total radiometer on the Sun facing side of the TCA during EVA #2 were within 40 W/m^2 of a typical solar constant of 1351 W/m^2. Total radiometers provided further agreement with planetary and albedo fluxes during both STS-69 and STS-72. In the -Z direction during STS-69 day cycles of an orbiter bottom to Sun (+ZSI) orbit, total radiometer flight data and model predictions were both approximately 565 W/m^2 [2]. STS-72 flight and model predictions in the -Y direction during wing to Earth (-YLV) day cycles were 550 W/m^2 [3].

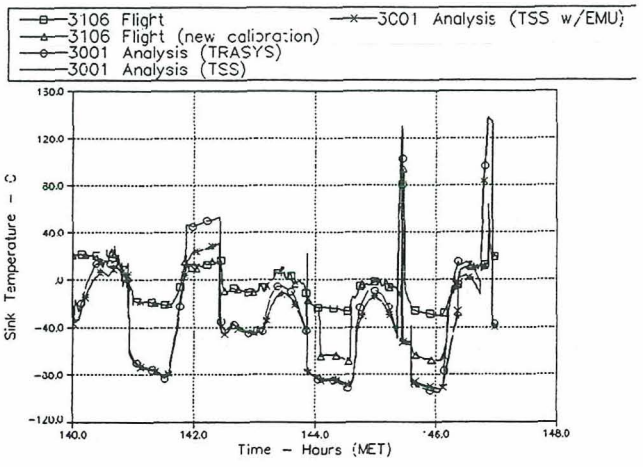

Figure 5. +X sink temperature (STS-72 TCA, EVA #2).

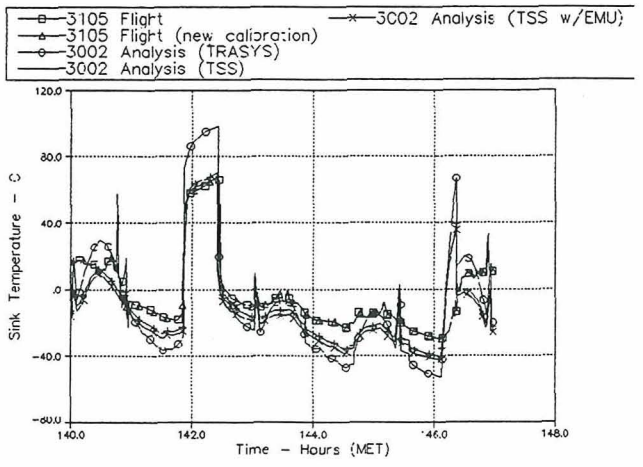

Figure 6. +Z sink temperature (STS-72 TCA, EVA #2).

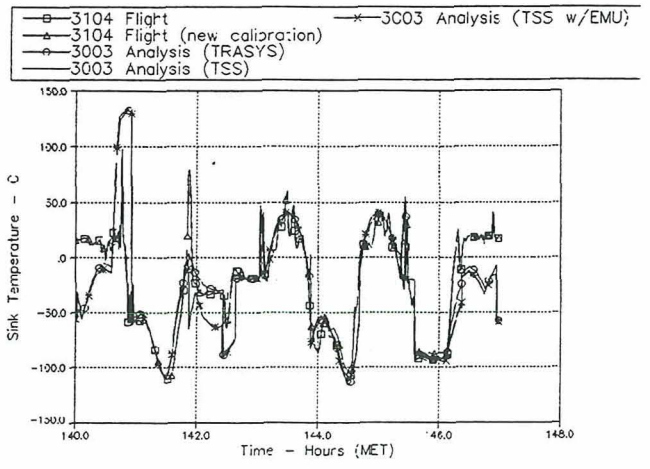

Figure 7. -Y sink temperature (STS-72 TCA, EVA #2).

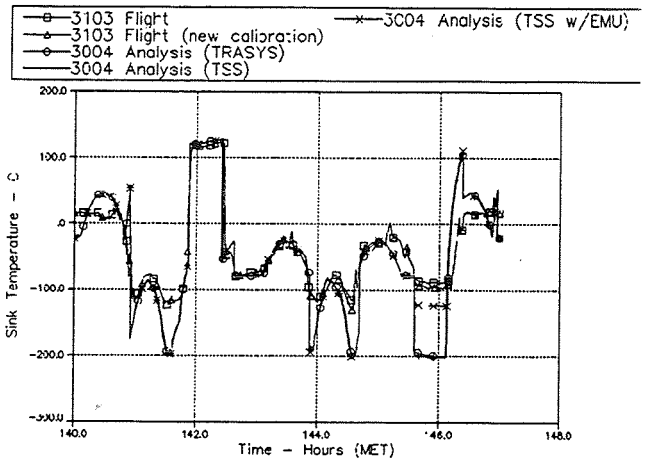

Figure 8. -Z sink temperature (STS-72 TCA, EVA #2).

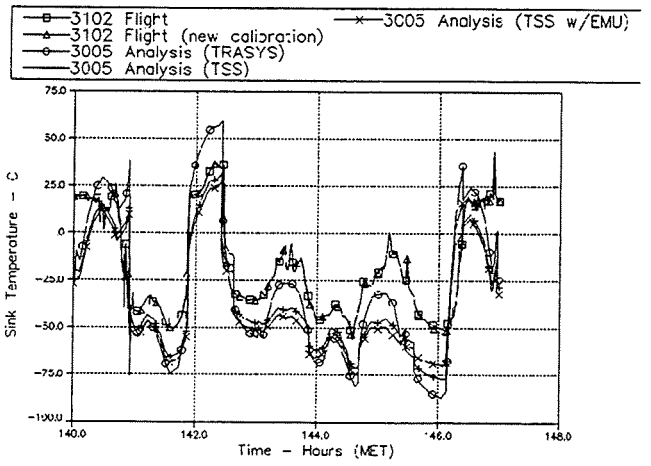

Figure 9. +Y sink temperature (STS-72 TCA, EVA #2).

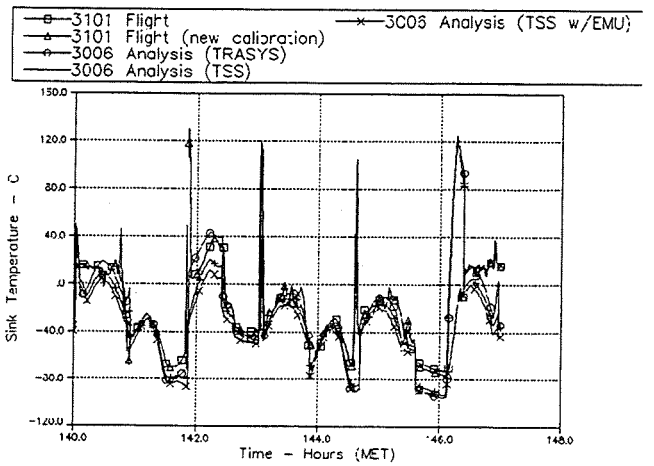

Figure 10. -X sink temperature (STS-72 TCA, EVA #2).

SOURCES OF ERROR - TRASYS accuracy is a function of the aspect ratio of each surface, proper nodal divisions, and minimizing surfaces that overlap in the same plane. No error calculations are made by TRASYS.

Since TSS utilizes Monte Carlo ray tracing to calculate radiation conductors and heating rates, accuracy improves as the number of rays increases. Construction of the geometric model is less likely to induce error in TSS. As with TRASYS, TSS will lose accuracy for surfaces that overlap in the same plane. Radiation conductor error is a function of the number of rays, the interchange factor, and the confidence interval. For results presented in this paper, a confidence interval of 90 percent was used for all calculations. The number of rays were selectively chosen depending on the interchange factor. Direct incident heating rate error in TSS is a function of how much the cosine of the angle to the source changes. The direct incident error is usually lower than the reflected component. Reflected heating rates are governed by the same statistics as radiation conductors.

When comparing TSS and TRASYS results, and calculation error, it is important to note the differences in the calculation methods. TRASYS will calculate the same value every time, without any assessment of accuracy. TSS is a statistical process that will calculate a different value every time it is run (assuming the analysis begins with a different random number seed). That is why TSS also calculates a percent error. For each calculated TSS value, there is a 90 percent chance that it is within the percent error. As the number of rays increase, the TSS model will converge on the correct answer for a given geometry without overlapping surfaces in the same plane.

CONCLUSIONS

Analysis predictions for extreme cold attitudes were conservative using both calculation methods when compared to total radiometer flight data. Although the amount of hot attitude flight data was limited, TSS predictions showed significant improvement over TRASYS. The transient response of the radiometers had excellent correlation to both calculation methods. Analysis of total radiometer flight data as compared to preflight and post flight calibrations showed repeatability. Analysis of IR radiometer flight data was less encouraging, possibly due to poor Germanium window performance. Incorporating a calibrated solar source into further calibration testing may provide additional insight.

ACKNOWLEDGMENTS

Chi-Min Chang NASA/JSC TCA subsystem lead, Michael K. Ewert NASA/JSC Technical Monitor, and Bruce C. Conger Lockheed Martin Project Manager.

REFERENCES

1. Lepore, J.M.; "STS-72 TCA Data Comparisons Using TSS, TRASYS and Post Flight Calibration Test Results", LMES, HDID-E40D-444, July 23, 1996.

2. Lepore, J.M.; "STS-69 Post Flight Analysis - Thermal Cube Assembly", LMES, HDID-E-251, December 18, 1995.

3. Lepore, J.M.; "STS-72 TCA Post Flight Analysis Final Report", LMES, HDID-E40D-353, April 5, 1996.

AEROTHERMAL PERFORMANCE CONSTRAINTS FOR SMALL RADIUS LEADING EDGES OPERATING AT HYPERVELOCITY

Paul Kolodziej, Jeffrey D. Bull, and Frank S. Milos
Thermal Protection Materials and Systems Branch
NASA Ames Research Center
Moffet Field, CA

Thomas H. Squire
ELORET/Thermosciences Institute
NASA Ames Research Center
Moffet Field, CA

Abstract

Small radius leading edges and nosetips were used to minimize wave drag in early hypervelocity vehicle concepts until further analysis demonstrated that extreme aerothermodynamic heating blunted the available thermal protection system materials. Recent studies indicate that ultra-high temperature composite (UHTC) materials are shape stable at temperatures approaching 3033 K and will be available for use as sharp leading edge components in the near future. Steady-state aerothermal performance constraints for UHTC components are presented in this paper to identify their non-ablating operational capability at altitudes from sea level to 90 km. An integrated design tool was developed to estimate these constraints. The tool couples aerothermodynamic heating with material response using commercial finite element analysis software and is capable of both steady-state and transient analysis. Performance during entry is analyzed by transient thermal analysis along the trajectory. The thermal load condition from the transient thermal analysis is used to estimate thermal stress. Applying the tool to UHTC materials shows that steady-state, non-ablating operation of a HfB_2/SiC (A-7) component is possible at velocities approaching Earth's circular orbital velocity of 7.9 km/s at altitudes approaching 70 km.

Nomenclature

C_T	heat transfer coefficient	(W/cm^2-K)
h	enthalpy	(J/kg)
h_D	dissociation enthalpy	(J/kg)
Le	Lewis number = 1.4	
p	pressure	(Pa)
Pr	Prandtl number = 0.71	
q_{cond}	solid heat conduction	(W/cm^2)
q_{FI}	aerothermodynamic heating	(W/cm^2)
R_N	radius of wing or nosetip	(m)
$\bar{r}$	normal distance from axis of symmetry to body surface	(m)
T	temperature	(K)
T_r	recovery temperature for heat transfer	(K)
T_{max}	maximum TPS temperature	(K)
U	velocity	(m/s)
x	coordinate in local streamwise direction	(m)
ε_{TH}	total hemispherical emittance	
μ	dynamic viscosity	(kg/m-s)
ρ	density	(kg/m^3)
σ	Stefan Boltzman constant	(W/m^2-K^4)

Subscripts

e	boundary layer edge
$t2$	total conditions, behind shock
w	wall
0	stagnation point
∞	freestream
2	behind shock

Superscripts

n	= 0 for nosetip
	= 1 for wing leading edge

Introduction

Because of the aerodynamic advantages, it is important to examine the feasibility of hypervelocity vehicles with sharp leading edges for operation as commercial reusable launch vehicles (RLV's). An important technology for implementing sharp body RLV concepts are shape stable (e.g. non-ablating) sharp leading edge components. Much of the research on these components has focused on developing actively-cooled technologies. Life-cycle costs of actively-cooled leading edges are likely to be of the same order of magnitude as other actively-cooled structures, such as rocket nozzles. Passive, non-ablating, sharp leading edge components with a less complex re-flight certification will inherently have lower life-cycle costs. From this perspective, an

enabling technology for sharp body RLV concepts is the ultra-high temperature ceramic (UHTC) material, such as the zirconium and hafnium diboride composites currently under development by the Thermal Protection Materials and Systems Branch at NASA Ames.[1] UHTCs have a unique combination of mechanical, thermal, and chemical properties that enable the fabrication of very small radius, sharp leading edges, for operation at hypervelocity. To efficiently implement passive, non-ablating, sharp UHTC leading edge components for these new RLV concepts it is necessary to understand: a) their non-ablating operational envelope, and b) their structural thermal behavior. This paper describes an integrated design tool named PERFORM/COSMOS that was developed to provide this capability.

Aerothermal Performance Constraints

Of the many different design approaches that have been used over the past 40 years one of the most useful for quickly assessing the feasibility of a vehicle design with regard to thermal protection system (TPS) capability is the aerothermal performance constraint. This approach uses the properties of the TPS material and the geometry of the leading edge to define a steady-state "non-ablating performance" constraint on the flight envelope. By definition, the surface temperature ($T_{w,0}$) at the stagnation point is constant on this constraint and can be assigned to the maximum non-ablating use temperature of the TPS material ($T_{max,0}$). A surface energy balance at the stagnation point of the leading edge determines the relationship between temperature ($T_{w,0}$), aerothermodynamic heating from the boundary layer fluid ($q_{Fl,0}$), and thermal conduction ($q_{cond,0}$) into the TPS material

$$q_{Fl,0} - q_{cond,0} = \sigma \varepsilon_{TH} T_{w,0}^{\ 4}$$
$$\text{or} \qquad (1)$$
$$T_{w,0} = \left(\left(q_{Fl,0} - q_{cond,0} \right) / \sigma \varepsilon_{TH} \right)^{1/4}$$

For TPS materials with low thermal conductivities $q_{cond,0} << q_{Fl,0}$, and Eq. (1) is simplified to a form commonly known as the equilibrium re-radiated wall temperature boundary condition

$$T_{w,0} = \left(q_{Fl,0} / \sigma \varepsilon_{TH} \right)^{1/4} \qquad (2)$$

For laminar stagnation point heating rates on a hemispherical nose or unswept wing leading edge, the aerothermodynamic heating rate can be determined from an engineering correlation such as the Fay and Riddell expression

$$q_{Fl} = \frac{0.67}{\mathrm{Pr}} \left(\rho_w \mu_w \right)^{0.1} \left(\rho_{t2} \mu_{t2} \right)^{0.4} \times \left\{ 1 + \left(Le^{0.52} - 1 \right) \left(h_D / h_{t2} \right) \right\} \times \left\{ h_{t2} - h_w \right\} \left(\frac{\beta}{2^n} \right)^{1/2} \qquad (3)$$
$$\beta = \left(2 \left(p_{t2} - p_\infty \right) / \rho_{t2} \right)^{1/2} / R_N$$

At low velocities $q_{Fl,0}$ is small and $T_{w,0} < T_{max}$, while at high velocities $q_{Fl,0}$ is large and $T_{w,0} > T_{max}$ causing ablation. An algorithm (PERFORM) was developed to iterate on velocity in this manner until $T_{w,0} = T_{max}$ for altitudes from 0 to 90 km. Rarefied flow effects in the fluid and surface catalycity of the material become important at high altitude and must be accounted for in the analysis. Reference 2 discusses how these effects can be handled.[2]

Two examples of steady-state, non-ablating aerothermal performance constraints are shown in Fig. 1 for a sharp 2D leading edge, or wing component. The constraint neglecting conduction will be discussed first. This component is made from ZrB2/SiC (A-10) with a radius of 0.254 cm and a semi-vertex angle of 5 degrees. Temperature dependent material properties for ZrB2/SiC (A-10) are available in the TPS*X* database.[3] Aerothermal performance constraints for this component are determined using a single-use temperature of 2861 K. For reference, the trajectory (144141) used to design the Shuttle TPS in the 1970s is also shown in Fig. 1.

As altitude increases the aerothermal performance constraint shifts to higher velocities because of decreasing freestream density. It is useful to examine the component performance at constant altitude. When operated on the left-side of the constraint at lower velocities, the component can be continuously operated without ablation. On the right-side of the constraint at higher velocities, operation is possible but ablation begins to blunt the leading edge. It is important to recognize that transient operation on the right-side of the constraint is possible for short duration. Aerothermal performance constraints neglecting conduction have been used in earlier studies of sharp leading edges for hypersonic vehicles.[4]

Because UHTC materials are good thermal conductors at high including the effect of thermal conduction significantly alters the aerothermal performance constraint. The base of the component where it attaches to the airframe is modeled as an adiabatic boundary condition to simulate a worst case

scenario. As expected, solid conduction cools the stagnation point and the aerothermal performance constraint shifts to higher velocities as shown in Fig. 1. This ZrB2/SiC (A-10) component is capable of steady-state operation without ablation at velocities approaching Earth's circular orbital velocity of 7.9 km/s at altitudes approaching 77 km.

The wing of the Space Shuttle Orbiter was designed with a radius of approximately 30 cm for non-ablating operation along the 144141 trajectory. Between 77 and 65 km the 144141 trajectory and the aerothermal performance constraint with conduction practically coincide, indicating this UHTC component is capable of non-ablating operation during a nominal Shuttle entry. Since drag is proportional to area, reducing the leading edge radius from 30 to 0.245 cm reduces the leading edge area by a factor of 122 for identical wing spans. Minimizing this area significantly reduces the pressure drag associated with the leading edge. Although estimating the total drag on wing components is more complicated, this comparison indicates the potential for minimizing pressure drag by utilizing sharp leading edges.

Thermal Conduction

Including thermal conduction adds an order of magnitude in complexity to the analysis because of the interaction between the leading edge geometry and the external flow. To maintain simplicity and a focus on the UHTC material, an engineering correlation was used to determine the aerothermodynamic heating downstream of the stagnation point. For simple geometries such as axisymmetric cones and wedges at zero angle of attack, the downstream pressure distribution (controlling the aerothermodynamic heating) can be determined from curve fits of existing data.[5,6] The heating distribution around the leading edge is calculated from a correlation developed for these types of pressure gradients.[7]

$$\frac{q_{FI}}{q_{FI,0}} = \frac{\bar{r}^n \left[\frac{\rho_e \mu_e}{(\rho_e \mu_e)_0}\right] (u_e/u_\infty)}{\left\{2^{n+1}\left(\frac{du_e/u_\infty}{dx}\right)_0 f(x)\right\}^{1/2}} \frac{(h_{t2}-h_w)}{(h_{t2}-h_w)_0} \qquad (4)$$

$$f(x) = \int_0^x \left[\frac{\rho_e \mu_e}{(\rho_e \mu_e)_0}\right] \frac{u_e}{u_\infty} \bar{r}^{2n} dx$$

The pressure distribution is used to construct a table of boundary layer edge properties by an isentropic expansion from the stagnation point conditions. It is important to account for the effects of dissociating, equilibrium air on these properties by using a suitable thermodynamic algorithm such as ACE.[8]

Commercial finite element analysis software, such as COSMOS, usually provide several methods for specifying the thermal boundary condition at the surface.[9] The T-type convective condition:

$$q_{FI} = C_T(T_r - T_w) \qquad (5)$$

is used to couple the fluid heat transfer from PERFORM to the material response in COSMOS.[10] Several iterations between PERFORM and COSMOS are required to converge on T_w.

Steady-State Thermal Analysis Benchmark

Comparing engineering correlations to higher fidelity numerical techniques reduces uncertainty and builds confidence. For this reason, the sharp leading edge component described above is identical to one used in previous work examining techniques to couple a hypersonic flow field solver with a multidimensional thermal response model (BLIMPK/COSMOS).[11] To minimize the number of elements an axisymmetric, half-plane geometry is used to represent the component. For comparison, a steady-state thermal analysis was performed with and neglecting conduction at a velocity equivalent to Mach 15 at an altitude of 30.48 km. At these conditions the component operates on the right-side of the aerothermal performance constraints shown in Fig. 1 and should exceed the maximum use temperature of 2861 K.

Figure 2 compares the surface temperature profiles from PERFORM/COSMOS and BLIMPK/COSMOS neglecting conduction. Although good agreement occurs near the stagnation point, the temperature of the wedge aft-body is about 130 K lower. Similar results are shown in Fig. 3 for surface temperature profiles with conduction. Again, there is good agreement near the stagnation point while the temperature of the wedge aft-body is lower. The discrepancy between the two methods may be due to differences in the downstream pressure profiles.

Good agreement near the stagnation point indicates that the aerothermal performance constraints shown in Fig. 1 accurately represent the non-ablating, steady-state operational limits of the component. The lower downstream temperature profile from PERFORM/COSMOS has a negligible effect on the stagnation point, but may become important when

designing an attachment between the component and the airframe.

Transient Thermal Analysis Benchmark

In the design of reusable, sharp UHTC leading edge components for hypervelocity flight there are two thermal modes of failure to be addressed. The first is failure by ablation, or melting of the surface, which in severe cases causes a shape change that may gradually affect the aerodynamics. The second is failure by thermal stress fracture, which may abruptly affect the aerodynamics and perturbs the vehicle motion. Because of the high cost of repairing or replacing these components, reusable designs must be capable of nominal performance without failure over a 50 mission life-cycle under normal operations.

Initial ablation occurs when the stagnation point of the leading edge exceeds the single-use temperature of the UHTC material. With a few modifications, the PERFORM/COSMOS integrated design tool can also be used to perform a transient thermal analysis along the trajectory to estimate when this occurs. To build confidence, a comparison was performed between PERFORM/COSMOS and one of the established analysis tools for nosetip thermal response named ASC.[12]

The component used in this comparison is made from a HfB_2/SiC (A-7) nosetip with a radius of 0.358 cm and a semi-vertex angle of 5.25 degrees. From arcjet tests, the maximum single-use temperature of HfB_2/SiC (A-7) has been estimated to be approximately 3033 K. A conical frustum made from ZrB_2/SiC (A-10) interfaces the nosetip to the support structure as shown in Fig. 4. The back wall is adiabatic and the temperature dependent material properties are from the TPS*X* database. In previous work (see Ref. 1), this component was fabricated and successfully tested in an arcjet at a stagnation point temperature of 3033 K. Because of this successful experience it was used as a preliminary design in the development of a nosetip for the SHARP-B01 flight demonstration. SHARP-B01 is the first hypervelocity flight demonstration of a UHTC leading edge component.[13]

In a transient thermal analysis both initial conditions and time dependent boundary conditions must be specified. For typical entry trajectories, the component is cold soaked during exo-atmospheric flight to a uniform initial temperature, and the transient boundary conditions correspond to the time, altitude, and velocity of the trajectory. In this case, the initial temperature is 233.3 K and the boundary conditions correspond to a nominal trajectory for a ballistic reentry vehicle (RV). Although rarefied flow phenomena and surface catalycity effects on aerothermodynamic heating of sharp leading edges at high altitude are important, this comparison was done using only continuum, fully catalytic heating for simplicity.

Stagnation point temperatures from PERFORM/COSMOS and ASC are shown in Fig. 5 as a function of altitude. At temperatures greater than 3033 K ablation occurs and the analysis terminates. The size of the discrete time step in the transient boundary condition causes a small overshoot above 3033 K. Temperatures from PERFORM/COSMOS are greater than ASC for the entire altitude range. Because of the higher aerothermodynamic heating, PERFORM/COSMOS terminates at 55.8 km, while ASC terminates at 50.7 km. The discrepancy between these results should be addressed by performing a comparison to a high fidelity benchmark consisting of a direct simulation Monte Carlo (DSMC) method coupled to a material thermal response model such as COSMOS. Estimates of q_{FI} from DSMC methods are useful for comparison to estimates of q_{FI} from engineering correlations at high altitude, where rarefied flow effects are important.

Surface temperature profiles from both solvers are shown in Fig. 6 at their respective termination altitudes. As expected, the surface temperature profile from PERFORM/COSMOS is greater than ASC because it terminated with a higher stagnation point temperature. Downstream of the stagnation point both temperature profiles decrease in a similar manner. The maximum discrepancy occurs at the tangent point between the hemispherical nose and the conical frustum where the temperature from PERFORM/COSMOS is approximately 230 K greater than ASC.

Figure 7 compares the transient thermal analysis of this component with the corresponding non-ablating, steady-state aerothermal performance constraint for 3033 K. This HfB_2/SiC (A-7) component is capable of steady-state operation without ablation at velocities approaching Earth's circular orbital velocity of 7.9 km/s at altitudes approaching 70 km. This is approximately 7 km lower in altitude than the constraint for the ZrB_2/SiC (A-10) component discussed earlier. At 64.5 km the transient analysis crosses the constraint with a stagnation point temperature of 2225 K. The temperature continues to increase during descent until ablation occurs at 55.8 km, approximately 8.7 km after crossing the constraint. This analysis demonstrates the capability for short time operation without ablation on the right-side of the constraint.

Transient Thermal Stress Analysis

Although operating along the aerothermal performance constraint eliminates failure by ablation it is important to recognize that failure by thermal stress fracture may still occur. Rapid, transient heating causes large temperature gradients along the longitudinal axis of the sharp UHTC leading edge component as shown in Fig. 6. As the temperature increases during entry the UHTC material undergoes a multi-dimensional thermal expansion creating internal stress. The resultant stress levels cause failure when the appropriate failure criteria is exceeded. It is important to recognize that the abrupt, step increase in heating experienced by components tested in arcjet facilities is a worst case scenario. For this reason, arcjet facilities are effective in discerning failure by thermal stress fracture. However analyzing this behavior is difficult because of the large uncertainty in the flow environment of arcjet facilities. With a few modifications, the PERFORM/COSMOS integrated design tool can also be used to perform a transient thermal stress analysis of a component operating along a trajectory.

The first step in performing a transient, thermal stress analysis is to determine the thermal load condition resulting from the transient heating along a trajectory. In PERFORM/COSMOS, the thermal load condition is stored by the final step in the transient thermal analysis. By simply terminating the transient thermal analysis at the appropriate time, a thermal load condition can be stored from any point along a trajectory. The thermal load condition that corresponds to the temperature profile shown in Fig. 6 is used here for consistency.

The second step specifies the boundary conditions that are assigned to constrain the displacement caused by thermal expansion and attachment. For this axisymmetric, half-plane geometry the nodes along the longitudinal axis are constrained to displacement along this axis. As a simple attachment, a single node on the longitudinal axis at the back wall is constrained to zero displacement in all directions. In the final step, COSMOS is configured in the normal manner for a static and linear stress analysis with a thermal load condition.

Figure 8 shows the Von Mises element stresses in the sharp UHTC leading edge component caused by thermal expansion. A maximum stress of 126.2 MPa occurs at the surface of the HfB_2/SiC (A-7) slightly behind the tangent point of the cone and hemisphere. Centered on the axis at approximately the same longitudinal distance is another region of high stress with a maximum of approximately 110.3 MPa. Directly behind this region is an example of the stress caused at an interface between two materials with different thermal expansion coefficients. As expected, stress decreases with increasing distance from the stagnation point where temperature and its gradient are lower. Stress in the cooler ZrB_2/SiC (A-10) is less than 0.8 MPa.

In the simplest evaluation, failure by thermal stress fracture may occur where the stress exceeds the failure criteria. For UHTC components, it is important to recognize that there is a large uncertainty in using this simple evaluation because it is difficult to accurately measure the physical properties of high temperature materials. Historically, this uncertainty has been managed by designers of thermal protection systems through an iterative process involving the fabrication and testing of components to failure. Eventually the material property measurements, analysis capability, and component testing converge to provide a consistent methodology for cost-effective implementation. From this perspective, these stress levels currently serve as useful guidelines in the design of UHTC components.

Conclusions

By analysis of ground facility measurements and flight demonstrations of sharp UHTC leading edge components it will eventually be possible to accurately identify the appropriate non-ablating aerothermal performance constraints for RLV operations. An integrated design tool named PERFORM/COSMOS was developed to provide preliminary estimates of these constraints to designers of hypervelocity vehicles. In addition, this tool is capable of transient thermal analysis along entry trajectories. The thermal load condition from this transient analysis may be used to estimate stress levels in UHTC components. This tool was used in analyzing a preliminary design of the UHTC nosetip for the SHARP-B01 flight demonstration.

Acknowledgment

This work benefited from the expertise Tom Kowalski of Fusion Design has demonstrated with the COSMOS software and his ability to transfer this knowledge to others. Joan S. Salute of NASA Ames Research Center provided an enabling organizational structure during the SHARP-B01 preliminary design phase which assisted in focusing the work described in this paper. This work was partially supported by NASA Contract NAS2-14031 to ELORET.

References

[1] Bull, J. D., Rasky, D. J., Tran, H. K., and Balter-Peterson, A., "Material Response of Diboride Matrix Composites to Low Pressure Simulated Hypersonic Flows," NASA CP-3235 Part 2, May 1994, pp 653-673.

[2] Kolodziej, P., "Aerothermal Performance Constraints for Hypervelocity Small Radius Unswept Leading Edges and Nosetips," NASA TM 112204, July 1997.

[3] Squire, T. H., Milos, F. S., Hartlieb, G. C., and Rasky, D. J., "TPSX: Thermal Protection Systems Expert and Material Property Database," Proceedings of the Fourth International Conference on Composites Engineering, Ed. David Hui, July 1997, pp 937-938.

[4] Hill, M. L., "Materials for Small Radius Leading Edges for Hypersonic Vehicles," J. of Spacecraft and Rockets, Vol. 5, No. 1, Jan. 1968, pp. 55-61.

[5] Cleary, J. W., "Theoretical Aerodynamic Characteristics of Sharp and Circularly Blunt-Wedge Airfoils, " NASA TR R-202, July 1964.

[6] Cleary, J. W., "An Experimental and Theoretical Investigation of the Pressure Distribution and Flow Fields of Blunted Cones at Hypersonic Mach Numbers," NASA TN D-2969, Aug. 1965.

[7] Marvin, J. G. and Sinclair, A. R., "Convective Heating in Regions of Large Favorable Pressure Gradient," AIAA Journal, Vol. 5, No. 11, Nov. 1967, p.1940-1948.

[8] Acurex Corp., "User's Manual Aerotherm Chemical Equilibrium Computer Program (ACE 81)," Acurex Report UM-81-11/ATD, August 1981.

[9] Lashkari, M., "COSMOS/M User Guide, Volume 1," Structural Research and Analysis Corp., Santa Monica, CA, April 1992.

[10] Chen, Y. K., and Milos, F. S., "Solution Strategy for Thermal Response of Nonablating Thermal Protection Systems at Hypersonic Speeds, " AIAA Paper 96-0615, Jan. 1996.

[11] Molvik, G. A., Milos, F. S., Chen, Y.-K., and Squire, T. H., "Computation of High-speed Flow Fields with Multidimensional Solid Heat Conduction," AIAA Paper 95-2116, June 1995.

[12] Rafinejad, D.,Dahm, T. J., Brink, D. F., Abbett, M. J., and Wolf, C. J., "Passive Nosetip Technology (PANT II) Program, Volume 2. Computer User's Manual: ABRES Shape Change Code (ASCC)," Acurex Corp., Rept. SAMSO-TR-77-11, Mountain View, CA, Oct. 1976

[13] http://kauai.arc.nasa.gov/projects/sharp/sharp.html

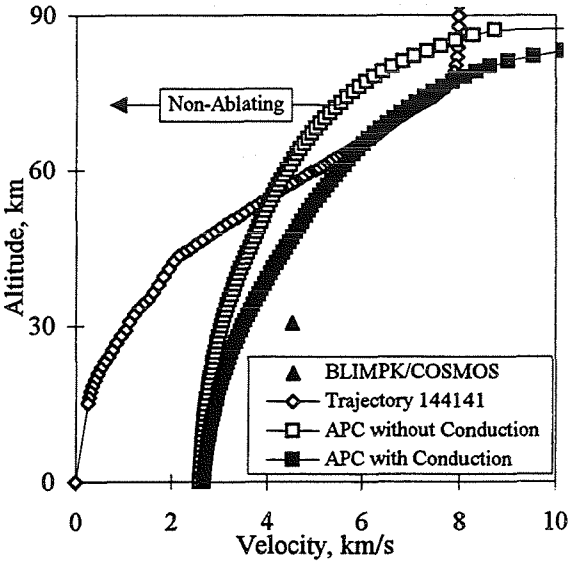

Figure 1, Steady-state aerothermal performance constraint (APC), with conduction and without conduction for 2D leading edge.

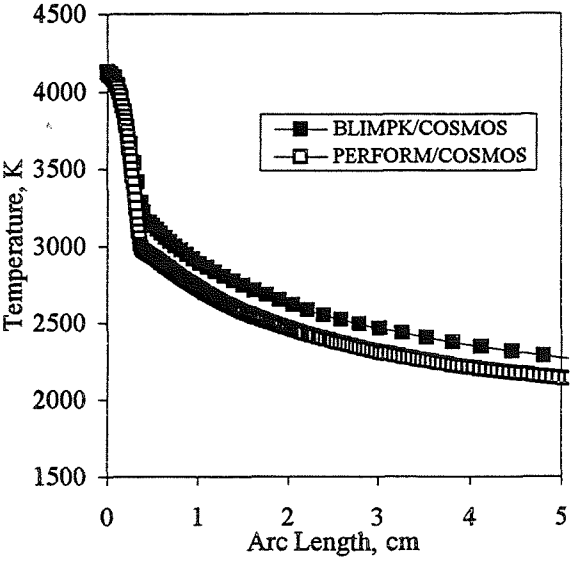

Figure 2, Steady-state surface temperature profiles without conduction.

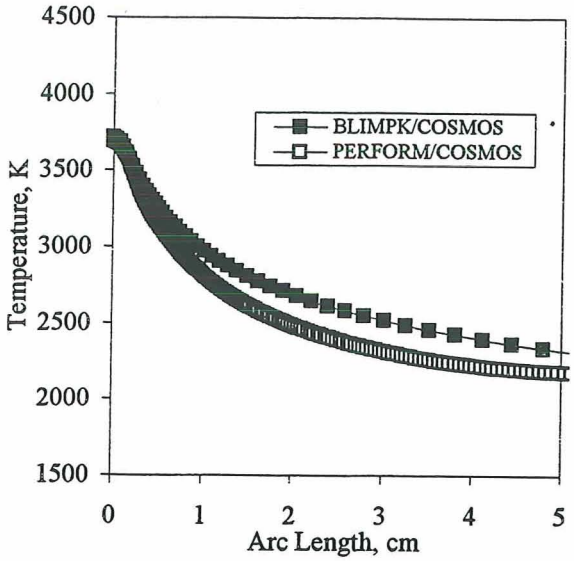

Figure 3, Steady-state surface temperature profiles with conduction.

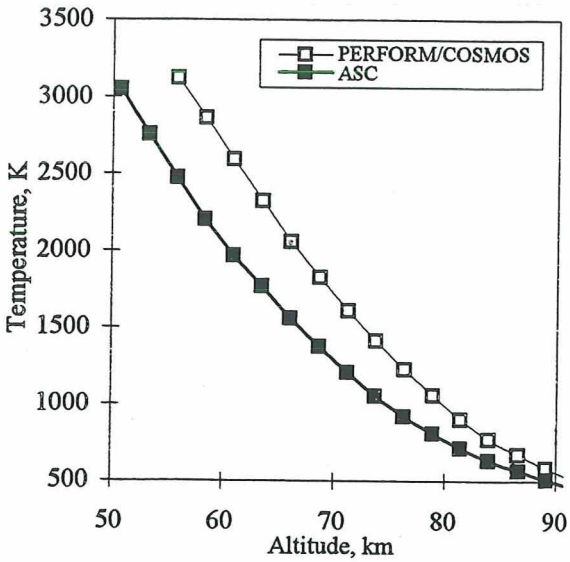

Figure 5, Transient stagnation point temperatures.

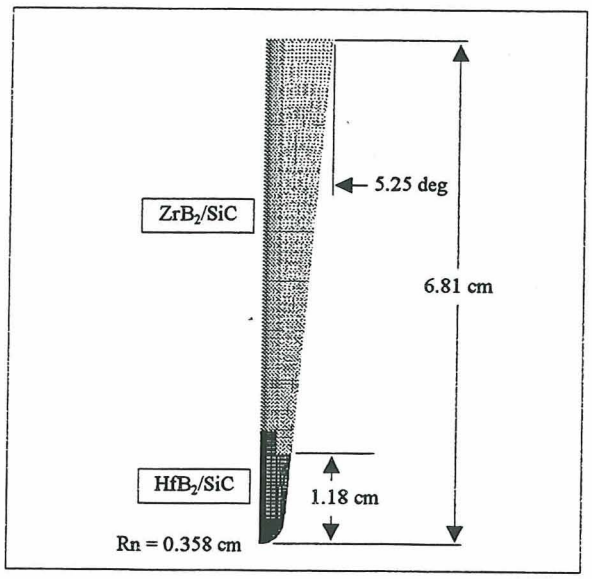

Figure 4, Geometry of UHTC leading edge component.

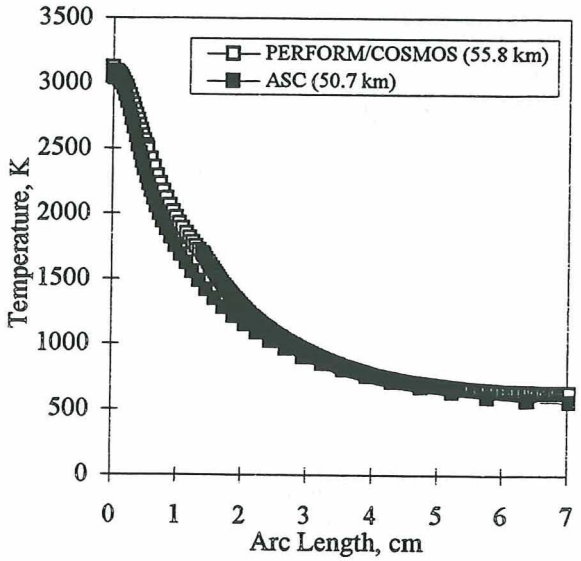

Figure 6, Transient surface temperature profiles with conduction.

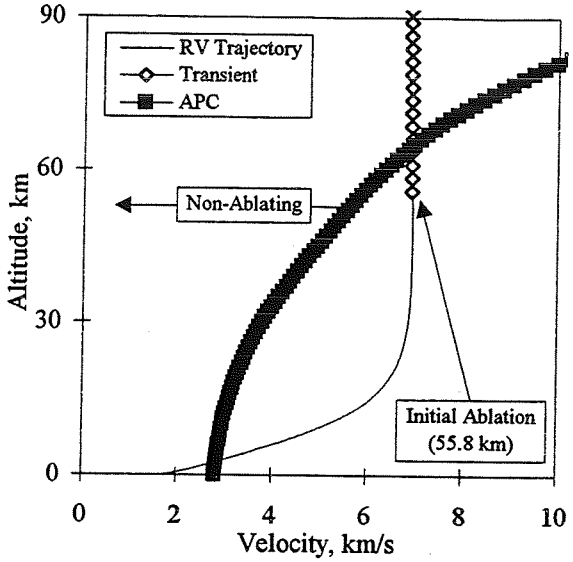

Figure 7, Comparison between transient response and steady-state aerothermal performance constraint (APC).

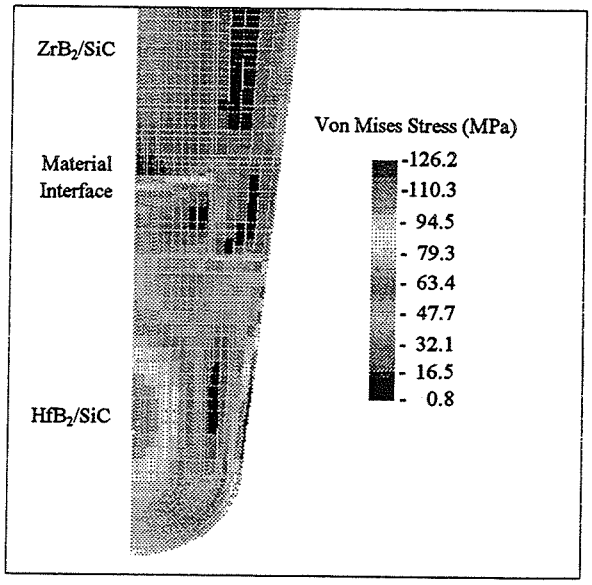

Figure 8, Thermal stress near the stagnation point of the UHTC leading edge component.

SPACECRAFT ORBITAL DEBRIS REENTRY AEROTHERMAL ANALYSIS

Wm. C. Rochelle,* Robin E. Kinsey,** Ethan A. Reid,** and Robt. C. Reynolds+
Lockheed Martin, Houston, TX

Nicholas L. Johnson++
NASA/JSC, Houston, TX

Abstract

In the past 40 years, thousands of objects have been placed in Earth orbit and are being tracked. Space hardware reentry survivability must be evaluated to assess risks to human life and property on the ground. The objective of this paper is to present results of a study to determine altitude of demise (burn-up) or survivability of reentering objects. Two NASA/JSC computer codes - Object Reentry Survival Analysis Tool (ORSAT) and Miniature ORSAT (MORSAT) were used to determine trajectories, aerodynamics, aerothermal environment, and thermal response of selected spacecraft components. The methodology of the two codes is presented, along with results of a parametric study of reentering objects modeled as spheres and cylinders. Parameters varied included mass, diameter, wall thickness, ballistic coefficient, length, type of material, and mode of tumbling/spinning. Two fragments of a spent Delta second stage undergoing orbital decay - stainless steel cylindrical propellant tank and titanium pressurization sphere - were evaluated with ORSAT and found to survive entry, as did the actual objects. Also, orbital decay reentry predictions of the Japanese Advanced Earth Observing Satellite (ADEOS) aluminum and nickel box-type components and the Russian COSMOS 954 satellite beryllium cylinders were made with MORSAT. These objects were also shown to survive reentry.

Introduction

Since the launch of Sputnik I, thousands of man-made objects are in orbit around Earth, and at least 9000 larger objects are being tracked by the U. S. Space Command Space Surveillance Network. These objects include active payloads as well as orbital debris - inactive payloads, spent upper stages, operational debris, and fragmentation debris from more than 140 on-orbit explosions. The orbital debris environment is increasing with time and represents an increasing risk to future space programs. Government organizations have been investigating responses to this growing problem.[1]

Two of the measures which have been implemented into NASA safety guidelines[2] are the removal of on-board stored energy at the end of mission life to prevent future accidental explosions and the limitation of the lifetime of debris objects in low Earth orbit to 25 years to prevent future growth of the orbital debris environment by on-orbit collisions. The guideline to restrict the lifetime of orbital debris applies in particular to payloads and upper stages after completion of their mission. The most feasible alternative for programs to adopt in order to implement this guideline is to use atmospheric drag and reentry heating to remove these objects from orbit. Because atmospheric reentry has been adopted as a method to respond to this guideline, it is essential that NASA be able to evaluate and limit the risk associated with these reentry events. Thus, NASA has also adopted a safety guideline for reentry risk.

To predict this risk in a form suitable for consideration during program development, NASA has sponsored a study at NASA/JSC to develop and implement tools to work this problem from early in program development, when design concepts are developed and material usage is being planned, through critical design review, when the evaluation can be made with less uncertainty. The tools described in this paper were developed during this project and are part of an international effort to better understand the problem of reentry survivability.

The objective of this paper is to present an evaluation of orbital debris reentry to determine the point of demise (burn-up) or survivability of the object. Two NASA/JSC computer codes - Object Reentry Survival Analysis Tool (ORSAT)[3] and Miniature ORSAT (MORSAT)[4] - were used to determine the trajectories, aerodynamics, aerothermal environment, and thermal response of selected spacecraft components. These codes have been validated[5,6] by providing good comparison of predicted demise altitude with the flight-measured value of a Sandia fuel rod undergoing orbital decay. With these codes, the trajectory of a parent body is assumed to decay down to an altitude where this body breaks into smaller fragments. These fragments then

*Group Lead, Advanced Systems Group
**Cooperative Engineering Student, Adv. Sys. Grp.
+Project Manager, Orbital Debris Projects
++Senior Scientist for Orbital Debris, Space Science Br.

follow a trajectory down to where they either demise or impact the ground.

The remainder of this paper will summarize the methodology in both the MORSAT and ORSAT codes. The assumptions in the various parametric and spacecraft reentry analyses investigated will then be described. The principal results of the 6-month investigation will be presented, including a parametric study of spheres and cylinders of variable materials undergoing orbital decay. Variables for the spheres include mass, diameter, wall thickness, and ballistic coefficient. For the cylinders, four modes of tumbling and/or spinning were also considered.

In addition, the results of an orbital decay of the Delta rocket second-stage fragments including a stainless steel propellant tank and a titanium helium-pressurization sphere are presented. The results of orbital decay of aluminum and nickel alloy components of the Japanese NASDA Advanced Earth Observing Satellite (ADEOS)[7] are described. Finally, the orbital decay results of the Russian COSMOS 954 satellite[8,9] beryllium cylinders will be discussed.

Methodology

The details of the method of analysis in the MORSAT and ORSAT programs have been presented previously.[5,6] The specific input/output features of MORSAT are contained in the MORSAT 1.5 User's Manual.[4] Similarly, the detailed operational features of ORSAT are presented in the ORSAT 4.0 User's Manual.[3] A short summary of five general areas (models) of the code are presented below and are categorized as: trajectory/atmosphere model, aerodynamics model, aerothermodynamics model, thermal analysis and demise model, and reentry risk analysis model.

Trajectory/Atmospheric Model

Two options or initial conditions exist in the codes for trajectory analysis - targeted entry and entry from decaying orbit. The targeted entry permits the prediction of hardware impact locations on the Earth without assessing the reentry survivability (i.e., predicting the heating loads on the object). The most common mode of entry is orbital decay in which the heating loads and demise altitude may be computed, but not the actual impact points.

For either entry option, a 3-degree-of-freedom trajectory is computed using four equations derived in an Earth-fixed reference frame. These equations, which are derived assuming a spherical, rotating Earth, include the time-rate of change of altitude, longitude, relative velocity, and flight path angle. The components of the Earth's angular velocity expressed in the wind-axis system are contained in the equations. A fourth-order Runge-Kutta numerical integration scheme is used to solve the equations to obtain the object's altitude, relative velocity, flight path angle, and longitude at each time step.

The atmospheric model in the two codes is the 1976 Standard Atmosphere Model. Interpolation in this model produces the atmospheric density, pressure, temperature, speed of sound, and mean free path at each time step.

Aerodynamics Model

In the trajectory equation for relative velocity, there is a term which includes the drag force (with the drag coefficient, C_D). The drag coefficients in the codes are computed by various means, depending on the shape of the body (i.e., sphere, cylinder, flat plate, or box) and on the flow regime (continuum, transition, or free molecule) of the body at the particular time point. The details of all these drag coefficients have been discussed previously.[5]

For a sphere, the continuum drag coefficient is a constant at 0.92 for values of the Knudsen No., Kn (defined as mean free path divided by diameter), of less than 0.01. For spheres in the free molecular regime, where Kn >1.0, the drag coefficient is a constant value of 2.0. In the continuum regime, the value of C_D for spinning cylinders entering broadside is 1.22, and in free molecular flow, it is 2.0. For spinning cylinders entering end-on, tumbling end-over-end, or with random tumbling, the continuum and free molecular values of C_D are a function of the cylinder diameter divided by its length. The drag coefficient for a tumbling flat plate is 0.707 for continuum flow and 1.273 for free molecule flow. For tumbling boxes, these respective values are 1.42 and 2.55 (approximately twice those for a tumbling flat plate).

In the transition regime where $0.01 < Kn < 1.0$, a bridging function of C_D vs. Kn is used for spheres and broadside spinning cylinders. For tumbling cylinders, C_D is scaled to the variation for a sphere. For end-on cylinders, C_D varies linearly with Kn from the

continuum to free molecular regimes. Integral methods are used with a bridging function for tumbling flat plates and boxes.

Aerothermodynamics Model

The net heating rate to an object is equal to the hot wall heat rate (which is a function of the cold wall heat rate) plus the oxidation heat rate minus the reradiation heat rate. The cold wall convective stagnation point heating rate for spheres is based on the Detra, Kemp, and Riddell equation for continuum flow.[10] The free molecular heat rate is equal to one half the density times velocity cubed times an accommodation coefficient of 0.9. For Kn > 10, the free molecule value is used for the cold wall stagnation heat rate. For Kn < 0.001, the continuum value is used. For 0.01 < Kn < 10, the Stanton No. interpolated from empirical data is used. Finally, for 0.001 < Kn < 0.01, a power relation is used to determine the Stanton No.

The average cold wall heating rate is computed as the stagnation point heat rate for a sphere multiplied by a factor which accounts for the type of body (sphere, cylinder, flat plate, or box). The cylinder factors are a function of the diameter divided by the length of the cylinder for free molecular and continuum flow. In the transition regime, a variation of Stanton No. vs. Kn is used. For flat plates in free molecular flow, the Stanton No. is computed as a function of the speed ratio. For flat plates in continuum flow, a function of stagnation point heating to a sphere is used based on the length/width ratio of the plate. In the transition flow regime, an exponential bridging function is used for the flat plate. For boxes, the average cold wall heating rates use integral, empirical, and exponential bridging functions for free molecule, continuum, and transition flow, respectively.

The hot wall heat rate is equal to the cold wall value multiplied by the wall enthalpy ratio. The oxidation heat rate is based on an empirical constant times the cold wall heat rate times the oxide heat of formation as used in ORSAT. This term is currently not in the MORSAT code (to provide for a conservative situation or survivability of the object). Finally, the reradiation heat rate is a function of wall temperature to the 4th power times the material surface emittance. The higher the emittance, the lower the net heat rate, and better chance of object survival.

Thermal Analysis and Demise Model

Two methods are used to obtain the surface temperature and point of demise of the object. The first is the lumped mass model and is used with MORSAT because it is the quickest method to use. The net heat rate is integrated over time to obtain the heat load. The heat load is reduced by 60% for a sphere and by 33% for a cylinder to account for the progressively smaller size of the object, with a linear decrease in mass with time. The heat load is multiplied by the object surface area to obtain the total absorbed heat. The surface temperature at any time is computed as the initial temperature plus the total absorbed heat divided by the object mass times its specific heat. After the melting temperature is reached, the surface temperature is held constant until the absorbed heat reaches the material heat of ablation. This heat of ablation is defined as the sum of the mass times the heat of fusion of the material plus the melt - initial temperature difference times the mass times specific heat. At this point, the object is considered to burn up or demise. However, if the absorbed heat never reaches the heat of ablation, the object will not burn up even though it has exceeded its melting temperature.

The second method of predicting surface temperature or point of demise is the nodal thermal math model which is used only with ORSAT. The 1-D heat conduction equation is solved by using a forward-time-central-space finite difference solution in spherical or cylindrical coordinates for up to 20 nodes in the model. Multiple types of material may be incorporated in the model with thermal conductivity input as a function of temperature. After the absorbed heat reaches the heat of ablation of the outer layer, the layer is removed by an assumed shear force, and the net heat rate is applied to the next layer. The mass and diameter change after each layer removal. The process continues until all layers reach their respective heat of ablation based on the decreased mass after each layer is removed. Unlike MORSAT, the surface temperature may drop after the melting temperature is removed if the net heat rate to the surface is decreasing.

Reentry Risk Analysis Model

In MORSAT, for objects that survive reentry, the debris area is computed by using the maximum cross sectional area of the object and adding a 0.3 m border around the object. The total debris area equals the sum of the individual fragment areas that have broken off the original parent body. The expected number of casualties (i.e., risk) equals the probability of impact on land mass

times the population of the land area in the latitude band times the debris area divided by the land area.

Assumptions in Analyses

Parametric Study

The MORSAT code was used to predict entry heating rates and loads, absorbed heats, temperatures, demise altitude, and/or survivability of metallic spheres and cylinders. Five materials were considered in this analysis: aluminum, copper, stainless steel, titanium, and beryllium. Three object variables were considered: thickness (0 - 100 mm), diameter (0.05 - 1.0 m), mass (0.1 - 30 kg), ballistic coefficient (10 - 1000 kg/m^2), and surface emittance of 1.0 and 0.3. Both solid and hollow spinning spheres were evaluated. Hollow cylinders of 3.0 m length with a 0.5 m diameter were considered with four modes of entry. These included end-on spinning (no tumbling), random tumbling and spinning, broadside spinning (no tumbling), and end-over-end tumbling and spinning.

A parent object for all fragments consisting of a sphere of diameter of 1.852 m with a mass of 1300 kg was used based on an example (SPARTAN spacecraft) in the user's manuals.[3,4] A breakup altitude of 78 km was assumed for all objects. In some cases, results from ORSAT were used to compare with those of MORSAT.

Delta 2nd Stage

The Delta II rocket was launched on April 24, 1996 to deliver a Ballistic Missile Defense Organization (BMDO) Midcourse Space Experiment (MSX) payload to orbit. On January 22, 1997, the 2nd stage of the Delta rocket reentered the atmosphere. Two fragments survived entry: a stainless steel cylindrical propellant tank which landed near Georgetown, Texas and a titanium helium-pressurization sphere which landed near Seguin, Texas. Post-flight photographs of these cylindrical and spherical fragments are shown in Figs. 1 and 2, respectively. The cylinder showed evidence of surface melting; however, the sphere did not, with only some slight discoloring.

The MORSAT and ORSAT codes were run to determine the entry conditions and survivability of the two fragments. The parent body was assumed to be the Delta 2nd stage empty cylindrical tank with a length of 5.97 m, diameter of 2.44 m, and mass of 919 kg as seen in Fig. 3a. Figure 3b presents a pre-flight photo of this stage showing the pressurized spheres and the engine on the left of the photo. Initial dimensions of the stainless steel cylinder which survived were obtained at the NASA/JSC shipping and receiving area and were later adjusted with better measurements obtained from McDonnell Douglas as shown in Fig. 4. Originally, the initial breakup altitude was assumed to be 78 km. However, a later reconstructed best-estimate trajectory was furnished by Aerospace Corp., and was used to establish initial conditions at breakup. From this trajectory, the breakup altitude was determined to be 80.58 km, with a relative velocity of 7668 m/sec, an inclination angle of 96.6°, and a relative flight path angle of -0.545°.

From Fig. 4, the diameter of the stainless steel cylinder was determined to be 1.742 m. An average thickness was determined to be 1.49 mm, resulting in an inner radius of 0.8696 m and outer radius of 0.8711 m. An effective length was determined to be 1.853 m assuming an effective length of the hemispherical end caps was one half the radii. This is because the codes only model flat-faced cylinders and not cylinders with hemispherical end caps. A mass of 267 kg as obtained from McDonnell Douglas was used for the cylinder. The titanium sphere was weighed at JSC to be 30.6 kg, with a sphere diameter of 0.60 m. Using the density of titanium as 4437 kg/m^3, an average thickness of 6.3 mm was obtained. Surface emittances of 1.0 and 0.3 were considered for both fragment materials. Three nodes were used in the ORSAT thermal analysis.

ADEOS

The National Space Development Agency (NASDA) of Japan launched the ADEOS satellite (seen in the sketch of Fig. 5) aboard a Japanese H2 rocket on Aug. 17, 1996. In a document[7] NASDA described an analysis of survivability of various ADEOS fragments after the breakup of the parent body satellite as it undergoes a hypothetical orbital decay reentry.

This NASDA ADEOS analysis was evaluated, and an independent, similar reentry survivability study was performed using MORSAT for two ADEOS fragments: the Advanced Visible and Near Infrared Radiometer (AVNIR) unit and the EPS unit battery. Most of the assumptions used by MORSAT described below were contained in the NASDA document.[7] The parent body before breakup was assumed to be a spinning cylinder entering broadside with a diameter of 4.5 m, a length of 5.0 m, and a mass of 3000 kg. The altitude at breakup of the parent body was assumed to be 80 km.

The two fragments (AVNIR and EPS battery) were considered to be random tumbling rectangular parallelepipeds (boxes). The AVNIR had dimensions of 1.0 m x 1.0 m x 0.4 m with a mass of 250 kg. The EPS battery had dimensions of 0.22 m x 0.26 m x 0.29 m with a mass of 46.7 kg. Two values of wall emittance of the AVNIR were considered: 0.2 and 0.9, while that of the EPS battery was assumed to be 0.85. The AVNIR material was an aluminum alloy, and the EPS battery material was a nickel alloy. The initial wall temperature of the AVNIR was 773 K and that of the EPS battery was 273 K.

COSMOS 954

The Russian COSMOS 954 satellite was launched on Sept. 18, 1977 and crashed in the Northwest Territories of Canada on Jan. 24, 1978.[8] A total of 49 pieces of beryllium fragments from this satellite were found on the ground. Included in this debris were 33 beryllium rods about 2 cm in diameter and 10 cm long, weighing about 50 - 60 g each and six larger solid beryllium cylinders about 10 cm in diameter and 40 cm long, weighing about 3600 g each. These larger cylinders were investigated with the MORSAT code using the random tumbling and spinning option.

The parent body was considered to be a cylinder of 1.3 m dia., 5.8 m length, and 1250 kg mass.[9] This cylinder was assumed to be a spinning body entering broadside with breakup occurring at 78 km. The initial wall temperature was taken as 300 K, and a wall emittance for beryllium was assumed to be 0.3.

Results

Parametric Analysis

Figure 6 presents a plot of the demise altitude from MORSAT as a function of the mass of solid spheres. Five materials were considered in the study: copper, aluminum, stainless steel, titanium, and beryllium. However, beryllium survived for all values of mass and is not shown on the plot. The survivability points on this figure are the points slightly beyond the highest mass for each material (i.e., if the aluminum sphere mass is greater than 16 kg, it will survive). It is seen that copper has the highest mass at the survival point, followed by aluminum, stainless steel, and titanium.

In Fig. 7 the demise altitude is plotted as a function of the diameter of solid spheres using MORSAT. The same five materials were considered as for Fig. 6. However, beryllium spheres survived even at the smallest diameters. It is seen that for the same diameter, aluminum spheres burn up at higher altitudes, followed by copper, stainless steel, and titanium spheres.

Figure 8 presents the demise altitude as a function of sphere thickness for a 0.05 m dia. hollow sphere of various materials using MORSAT. The demise altitude appears to flatten out as the thickness reaches the value for a solid sphere (25 mm). It is seen that for aluminum, copper, and stainless steel spheres, as the thickness decreases, a higher demise altitude is reached. However, for titanium, the hollow sphere reaches a peak demise altitude around 5 mm thickness, but at lower thickness, this altitude decreases until for values less than 0.3 mm, it survives. Also, for beryllium hollow spheres, the object survives for all values of thickness.

In Fig. 9 the results of Fig. 8 are shown as a function of ballistic coefficient, W/C_DA, where W is the weight (mass) of the hollow sphere and A is the cross-section area of the 0.05 m diameter sphere. Since the flow regime is near continuum ($Kn < 0.01$), the drag coefficient is around 0.92. The cross section area is a constant, so the primary variable in ballistic coefficient is the mass, which is computed as the product of material density times volume of the sphere (based on the thickness). The trends of this plot for a 0.05 m diameter sphere are similar to those of Fig. 8, with the titanium sphere beginning to survive at the low thicknesses. The value on the right of each curve represents the maximum thickness (or solid sphere).

Figure 10 presents a similar plot to Fig. 9 with the demise altitude plotted as a function of ballistic coefficient, but for a diameter of 0.20 m. In this figure only three curves are shown, as the titanium sphere survives for all values of ballistic coefficient. Also, it is seen that the stainless steel begins to survive at low values of ballistic coefficient (similar to the titanium sphere in Fig. 9). The values on the right of the copper and stainless steel curve also show the beginning of survivability. For a larger diameter of 0.3 m (not shown), the stainless steel sphere survived at all values of ballistic coefficient, and only the aluminum and copper spheres burned up.

In Figs. 9 and 10, the demise altitude drops as the ballistic coefficient increases. This is in contrast to the plot shown in Refs. 5 and 6 for demise altitude increasing with ballistic coefficient. However, in these references, this plot was for a fixed thermal mass with the thickness maintained constant at 3 mm with ballast

added to the sphere to increase the aerodynamic mass and the ballistic coefficient. In Figs. 9 and 10, the thermal mass is the same as the aerodynamic mass with ballistic coefficient varying with the wall thickness.

In Fig. 11, the demise altitude is shown as a function of sphere thickness for an aluminum sphere of various diameters. The 0.1 m dia. sphere (like the 0.05 m dia. sphere in Fig. 8) burns up at all thicknesses. Each larger sphere survives at decreasing thicknesses. The 1.0 m dia. aluminum sphere survives at thicknesses greater than only 3 mm.

Figures 12 and 13 present the demise altitude as a function of cylinder thickness for 0.5 m diameter, 3.0 m long aluminum and copper cylinders, respectively. It is seen that the end-on spinning case has the highest altitude of demise because the heating is applied only on the front face and not distributed over the body like the other modes. Using the other three modes of entry, the cylinders survive around the same altitude (35 - 42 km). For the same thickness, the aluminum cylinders burn up at a higher altitude than the copper cylinders. Stainless steel and titanium cylinders survive (not shown in this plots), even at the lowest thickness, except for the end-on mode where they burn up around 75 km and higher.

In Fig. 14 the heat of ablation and absorbed heat to a 0.10 m dia. aluminum sphere is plotted as a function of altitude for 5 thicknesses from 2.5 mm to 50 mm. When the absorbed heat reaches the heat of ablation, this altitude is the demise altitude. The change in slope occurs when the surface temperature reaches the melting temperature and the reradiation heat rate is a constant. These temperatures are shown in Fig. 15 for the same size sphere and thicknesses.

Delta 2nd Stage

Figure 16 shows the ORSAT-predicted heating rate components (cold wall, hot wall, net, oxidation, and reradiation) to the Delta 2nd stage titanium sphere. An oxidation heating factor of 1.0 (maximum value) was used in this analysis. The peak cold wall heat rate is about 35 W/cm^2 and drops significantly after about 100 sec. After the net heat rate reaches zero, the reradiation heat rate drops. The stainless steel cylinder heat rate components are shown in Fig. 17. An oxidation heating factor of only 0.4 could be used before the cylinder survived. The reradiation heat rate stays at a constant value from 50 to 150 sec because this is at the melt temperature of stainless steel.

Figures 18 and 19 show the surface temperatures on the Delta sphere and cylinder as a function of time. Both of these cases used a surface emittance of 0.3. If a value of 1.0 had been used, the temperature and reradiation heat rate would have been lower. The titanium sphere was within 100 K of its melt temperature of 1943 K; however, the stainless steel cylinder reached its melt temperature of 1728 K and stayed there for about 100 sec. From visible observation of the cylinder, it was evident that the cylinder surface had melted on one end (yet it survived).

In Figs. 20, 21, and 22, the altitude, relative velocity, and flight path angle are plotted as a function of downrange from the breakup point. It is seen that the sphere landed about 170 km further than the cylinder. The relative distance between Georgetown and Seguin, Texas is about 135 km; hence, the difference in predicted downrange is somewhat close to the actual value. The sphere is traveling at a faster velocity, higher altitude, and less negative flight path angle. Thus, the sphere would be expected to land at a farther location than the cylinder.

ADEOS

Figures 23 and 24 show the heating rate components to the aluminum AVNIR and EPS battery, respectively, vs. time. The net heat rate is higher with emittance of 0.2 than 0.9, with the reradiation heat rate higher at 0.9. The heating rates to the EPS battery are more than twice as high for the AVNIR because of the smaller dimensions of the AVNIR. Since MORSAT was used, no oxidation heating was considered.

In Figs. 25 and 26 the absorbed heat and heat of ablation for the aluminum AVNIR and nickel EPS battery are shown, respectively. Since the heat of ablation is not reached in either case, the objects survived (same as the NASDA analysis). The melt temperatures of each material are reached in the MORSAT analysis; however, these temperatures were not reached in the NASDA analysis.

The debris casualty area computed by MORSAT was 2.56 and 0.77 m^2 for the AVNIR and EPS battery, respectively. This is comparable to the values reported in the NASDA analysis.

COSMOS 954

Figure 27 presents the heating components vs. time for the beryllium cylinder for the COSMOS 954 entry.

Because of the small size of this cylinder, the heating rates were very high - 96 W/cm^2 for the cold wall value and 90 W/cm^2 for the net value. As with the ADEOS cases, no oxidation heating was used with MORSAT. Although the time of impact to the ground was 510 sec, the plot was stopped at 300 sec for clarity.

In Figure 28 the absorbed heat and heat of ablation to the beryllium cylinder are presented. It is seen that the absorbed heat never reaches the heat of ablation of beryllium even though the heating rates are so high. This is because of the extremely high heat of fusion of beryllium (nearly three times higher than that of titanium). The peak surface temperature was 1446 K (not shown), which was 111 K lower than the beryllium melting temperature of 1557 K.

Conclusions

This six-month study sponsored by NASA/JSC has investigated reentry heating, demise altitude, and/or survivability of spacecraft objects undergoing orbital decay. The study used the JSC MORSAT and ORSAT codes for the reentry analysis. The parametric analysis for spheres and cylinders assessed effects of variable thickness, diameter, ballistic coefficient, and material, plus effects of spinning and tumbling for cylinders. In general, aluminum and copper objects tend to burn up in the atmosphere, whereas beryllium, stainless steel, titanium, and nickel objects tend to survive. Two fragments of the Delta 2nd stage rocket were investigated and were predicted to survive and land within 35 km of the actual difference in location between impact points (Georgetown and Seguin, Texas). Predictions for the two NASDA ADEOS fragments showed the objects survived entry, as did the analysis for the COSMOS 954 beryllium cylinders which landed in Canada. The methods used in this study may be applied to almost all existing or future satellites to establish their survivability during entry and risk to human life and property on the ground.

Acknowledgments

The authors wish to acknowledge the help of Chris Madden (NASA/JSC), Stan Bouslog (Rohr, Inc.), Brian Ross (NASA/Goddard), and K. C. Wang (Lockheed Martin - Skunk Works) who were the original developers of the MORSAT and ORSAT orbital debris reentry codes. Thanks are also extended to Bill Ailor (Aerospace Corp.) who provided the COSMOS 954 data and other information, and to Benjamin Mains (Aerospace Corp.) who supplied the Delta 2nd stage reconstructed best-estimate trajectory for the cylindrical and spherical tanks.

References

1. "Interagency Report on Orbital Debris," Executive Office of the President of the United States, The National Science and Technology Council Committee on Transportation Research and Development, 1995.

2. "NASA Safety Standard Guidelines and Assessment Procedures for Limiting Orbital Debris," NSS 1740.14, August 1995.

3. Ross, B. P., Madden, C. B., and Bouslog, S. A., "A User's Guide for the Object Re-entry Survival Analysis Tool (ORSAT) Version 4.0," JSC-26311, August 1993.

4. Bouslog, S. A., Ross, B. P., and Madden, C. B., "User's Guide for Miniature - ORSAT (Object Reentry Survival Analysis Tool): MORSAT - Version 1.5," JSC-26869, Rev. A, September 1995.

5. Bouslog, S. A., Wang, K.-C., Ross, B. P., and Madden, C. B., "Reentry Survivability and Risk Analysis," JSC-27232, September 1995.

6. Bouslog, S. A., Ross, B. P., and Madden, C. B., "Space Debris Reentry Risk Analysis," Paper 94-0591 presented at 32nd Aerospace Sciences Meeting, Reno, NV, Jan. 10-13, 1994.

7. Harashima, O., "Actions Items of NASA/NASDA 5th W. G. Meeting on M. S. A., including attachment, 'The Study of the Casualty Area Due to the Debris Surviving,'" Letter to Wayne R. Frazier, NASA/HQ, Code QS, N97-411-1, April 11, 1997.

8. Hanafee, J. E., "Analysis of Beryllium Parts for COSMOS 954," Lawrence Livermore Laboratory UCRL-52597, Oct. 25, 1978.

9. "Use of Nuclear Power Sources in Outer Space," Report A/AC.105/C.1/WG.5/L.24/ADD.2, Committee on the Peaceful Uses of Outer Space, General Assembly United Nations, Feb. 26, 1990.

10. Detra, R. W., Kemp, N. H., and Riddell, F. R., "Addendum to 'Heat Transfer to Satellite Vehicles Re-entering the Atmosphere,'" *Jet Propulsion*, Vol. 27, No. 12, Dec. 1957.

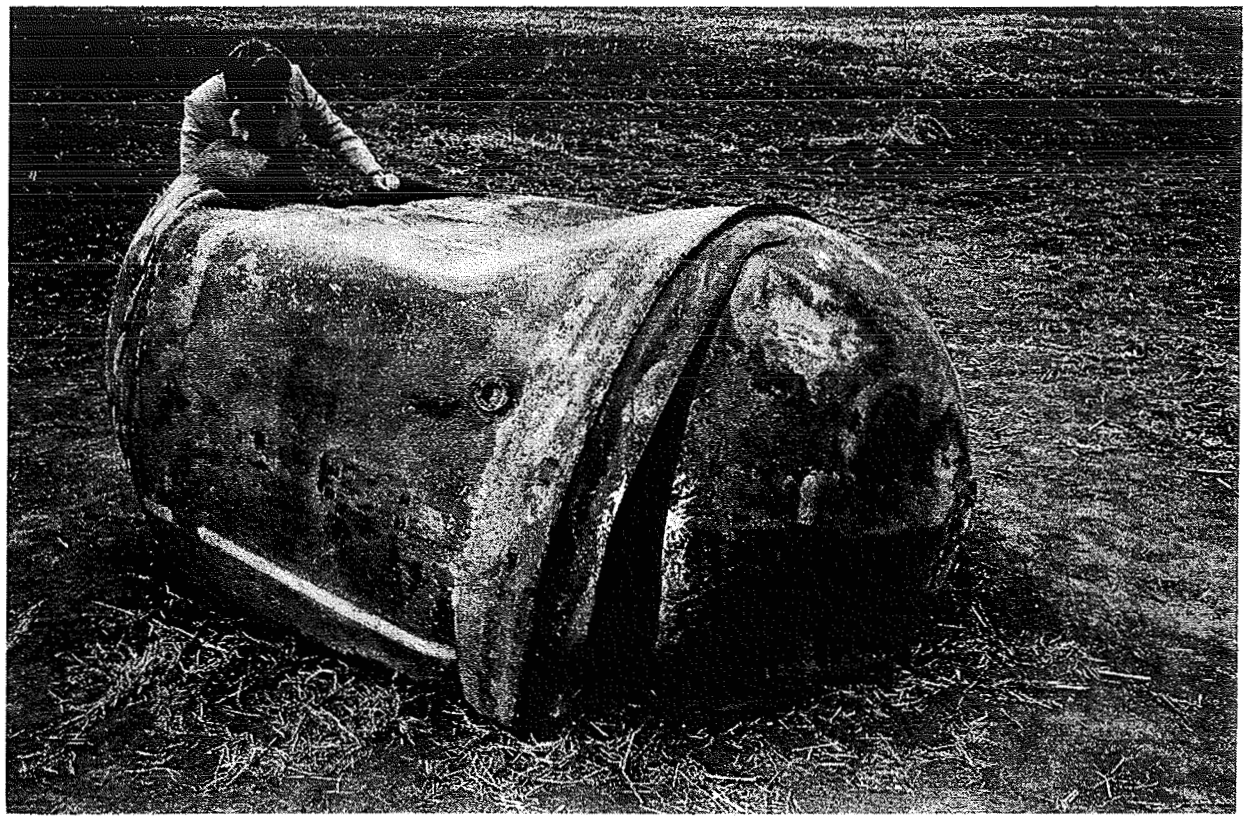

Fig. 1 Delta 2nd Stage Stainless Steel Cylinder Propellant Tank at Impact Point near Georgetown, TX

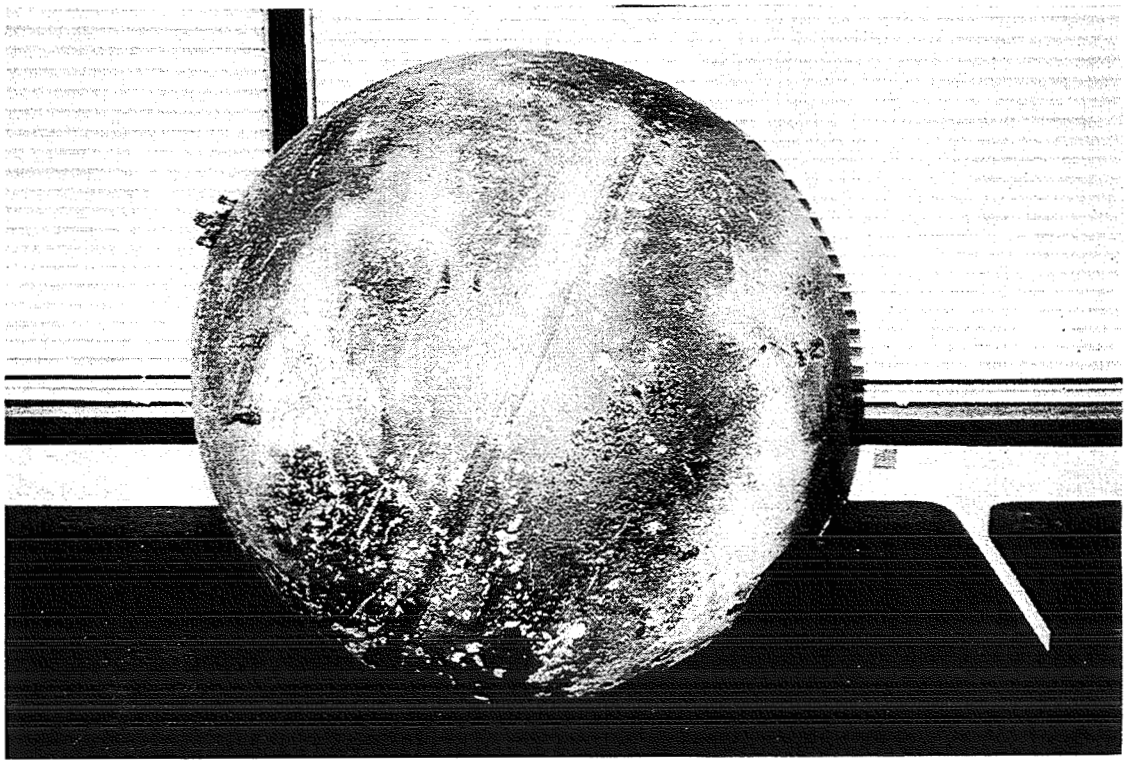

Fig. 2 Delta 2nd Stage Titanium Helium-Pressurization Sphere which Landed near Seguin, TX

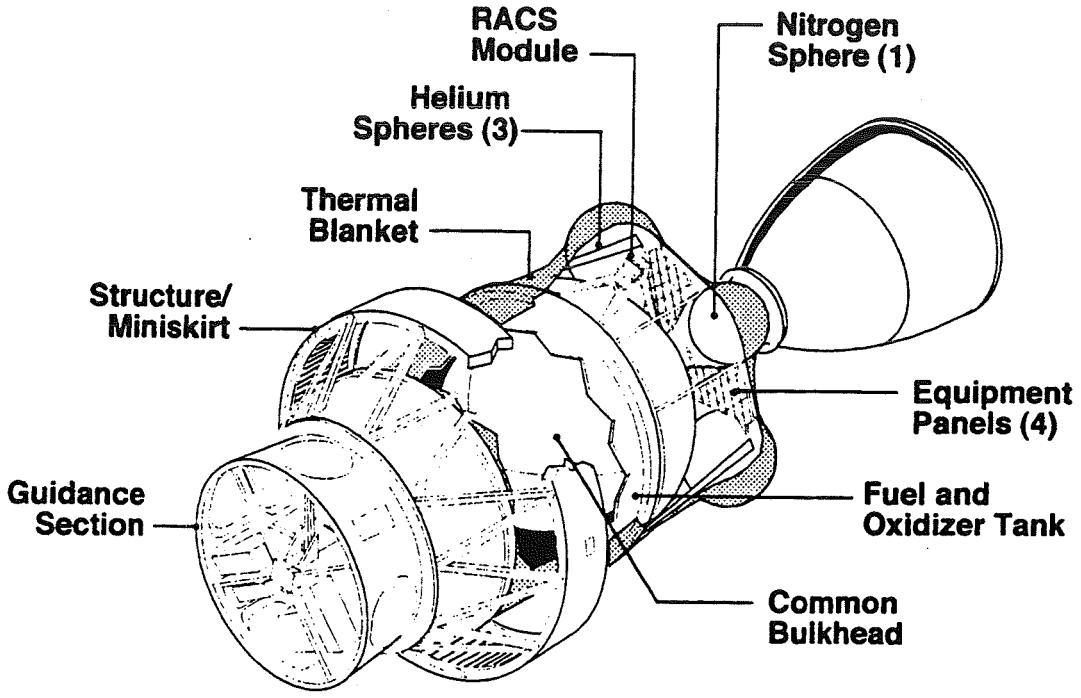

Fig. 3a Sketch of Delta 2nd Stage Assembly

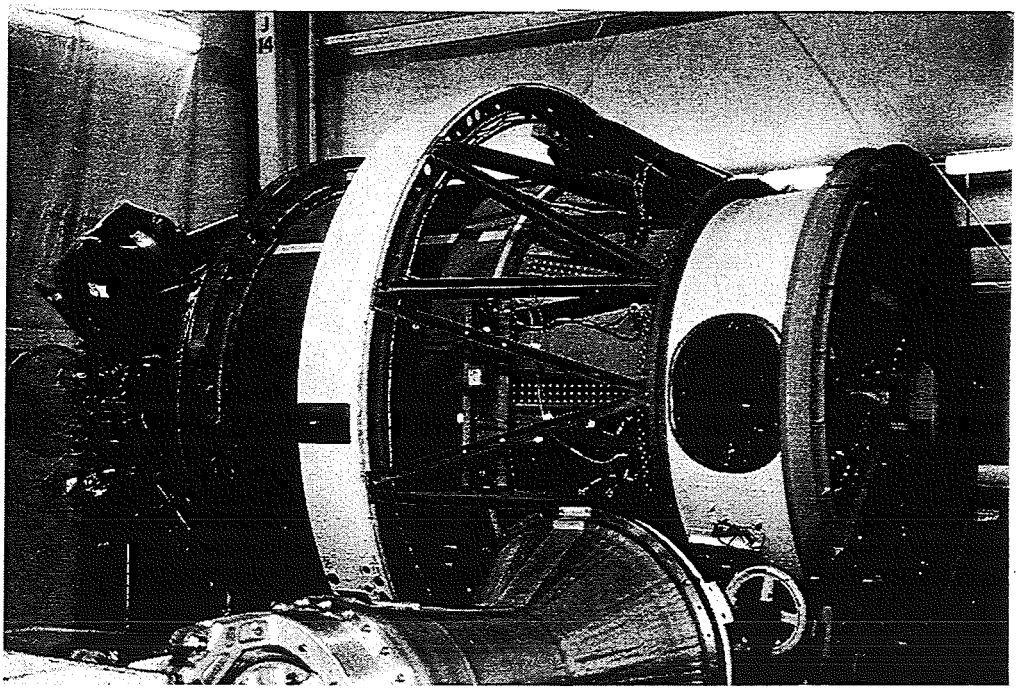

Fig. 3b Pre-Flight Photograph of Delta 2nd Stage Assembly

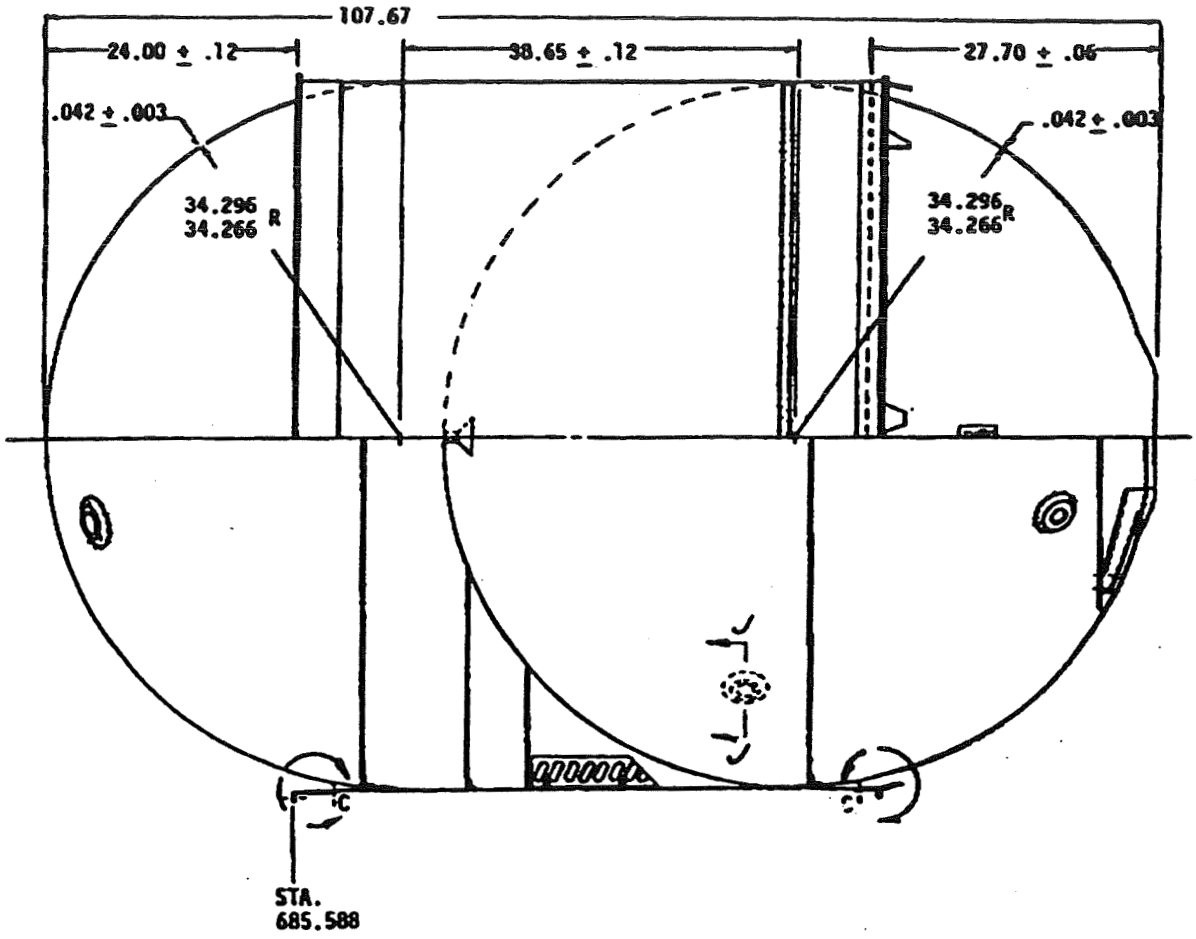

Fig. 4 Dimensions of Delta 2nd Stage Stainless Steel Cylindrical Propellant Tank

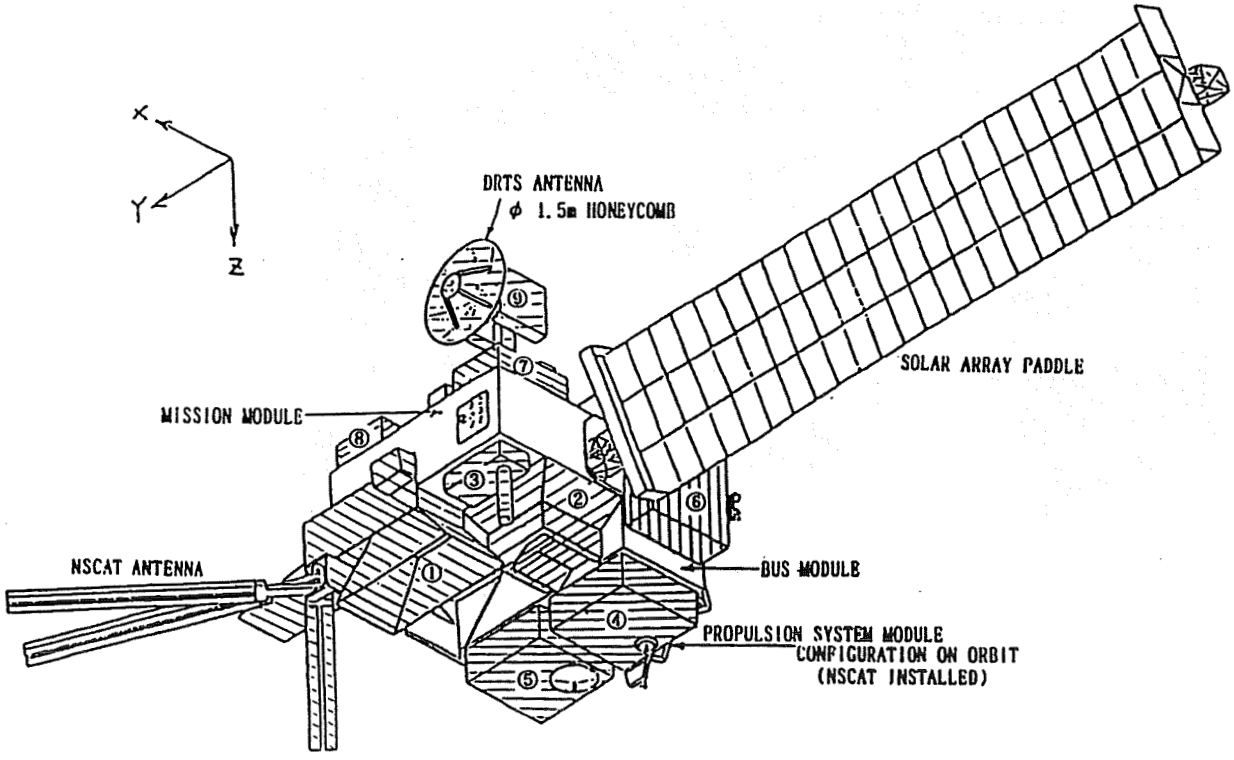

Fig. 5 Japanese Advanced Earth Observing Satellite (ADEOS) Configuration

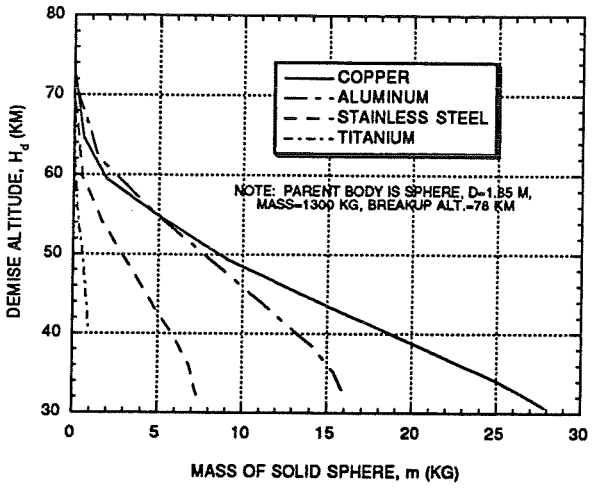

Fig. 6 Demise Altitude vs. Mass for Solid Sphere of Various Materials

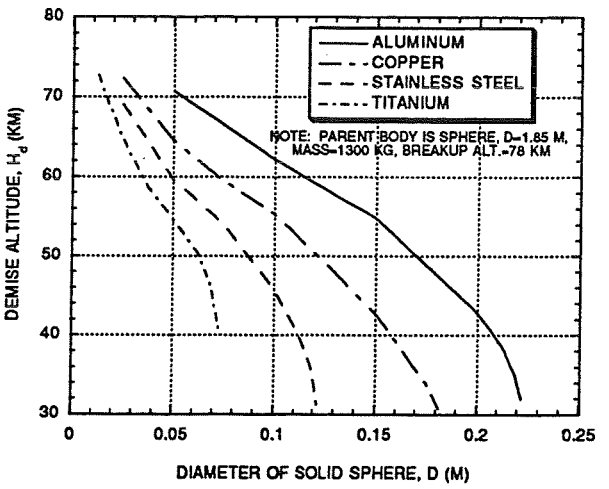

Fig. 7 Demise Altitude vs. Diameter for Solid Spheres of Various Materials

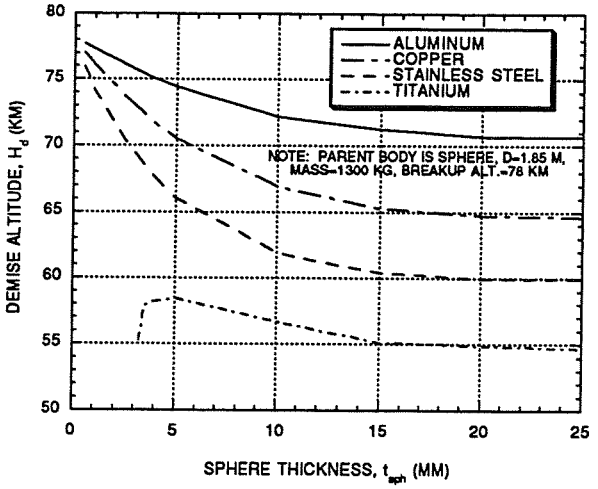

Fig. 8 Demise Altitude vs. Sphere Thickness for 0.05 m Dia. Sphere of Various Materials

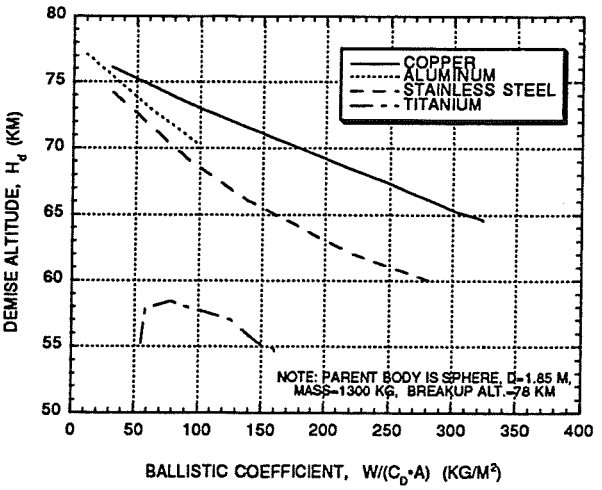

Fig. 9 Demise Altitude vs. Ballistic Coefficient for 0.05 m Dia. Sphere of Various Materials

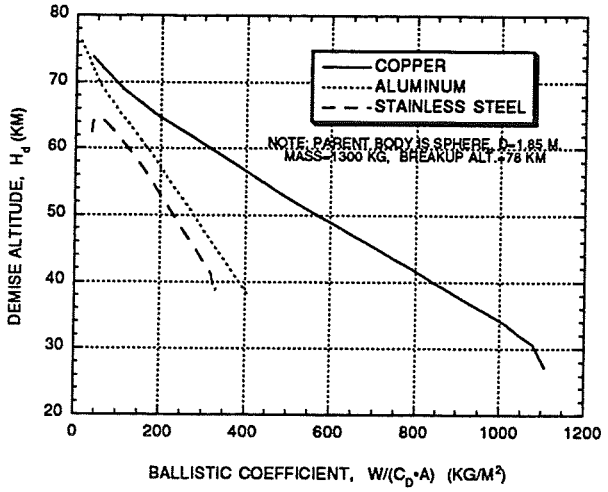

Fig. 10 Demise Altitude vs. Ballistic Coefficient for 0.20 m Dia. Sphere of Various Materials

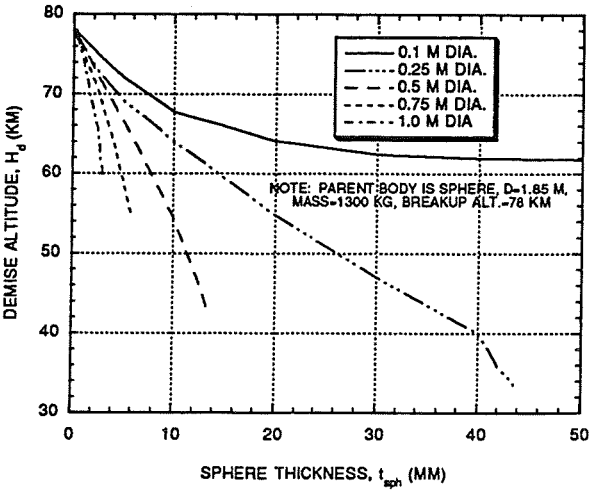

Fig. 11 Demise Altitude vs. Sphere Thickness for Aluminum Sphere of Various Diameters

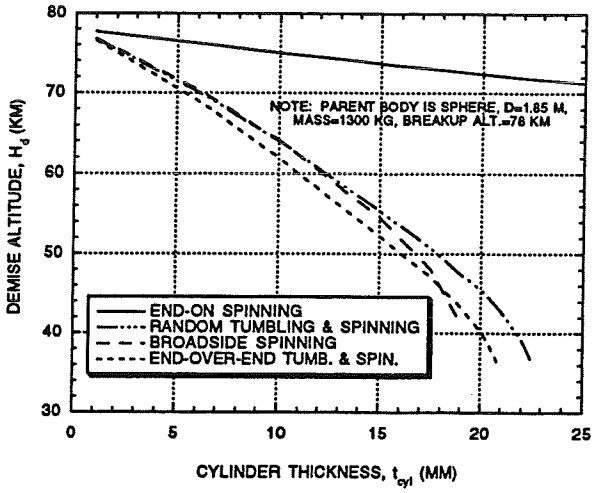

Fig. 12 Demise Altitude vs. Cylinder Thickness for 0.5 m Dia., 3.0 m Long Aluminum Cyl.

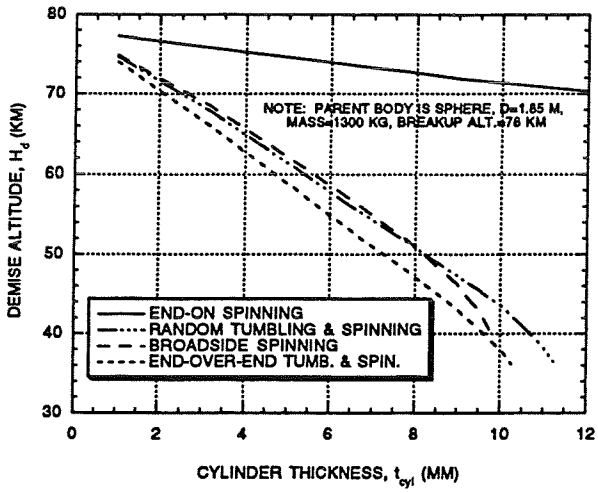

Fig. 13 Demise Altitude vs. Cylinder Thickness for 0.5 m Dia, 3.0 m Long Copper Cylinder

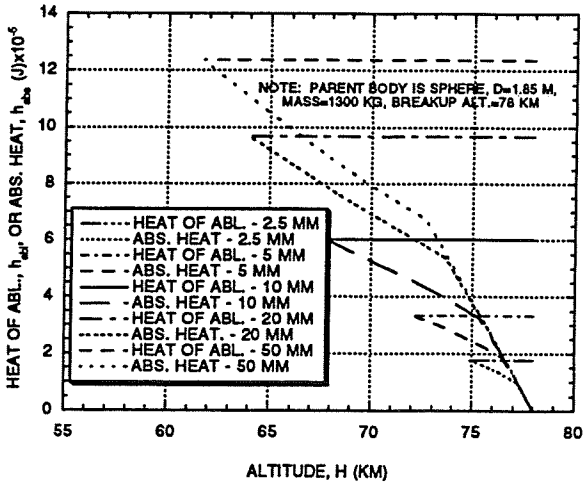

Fig. 14 Heat of Ablation & Absorbed Heat to 0.10 m Dia. Al Sphere for Various Thick. vs. Alt.

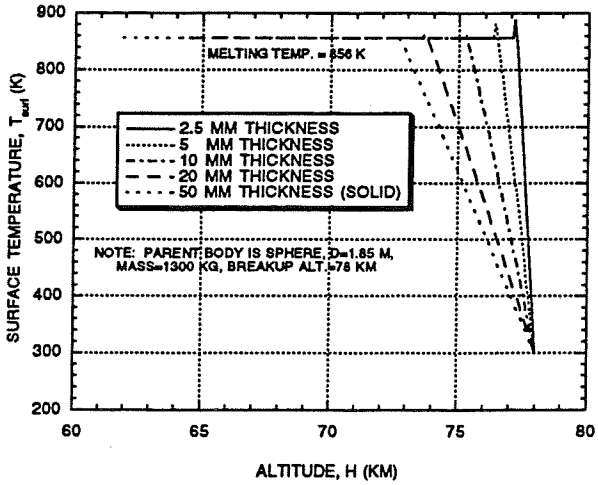

Fig. 15 Surface Temperature on 0.10 m Dia. Al Sphere for Various Thicknesses vs. Altitude

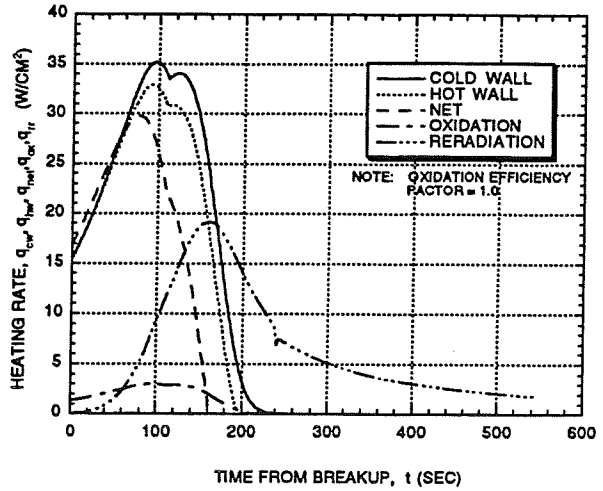

Fig. 16 Heating Rate Components to Delta 2nd Stage Titanium Sphere vs. Time from Breakup

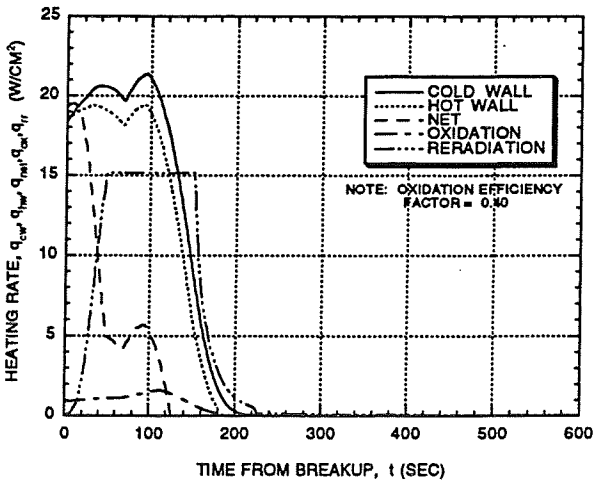

Fig. 17 Heating Rate Components to Delta 2nd Stage Stainless Steel Cyl. vs. Time from Breakup

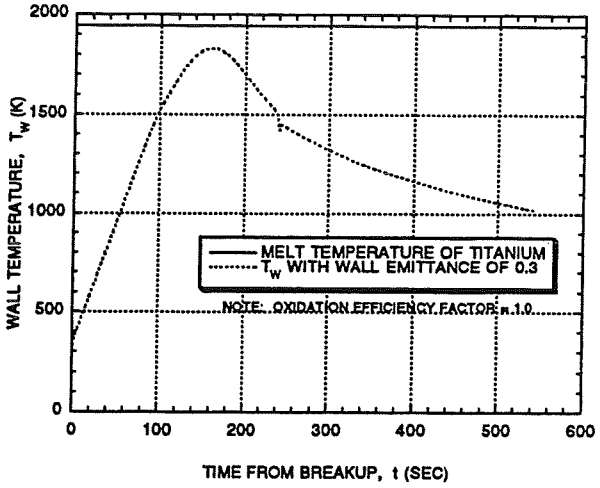

Fig. 18 Wall Temperature for Delta 2nd Stage Titanium Sphere vs. Time from Breakup

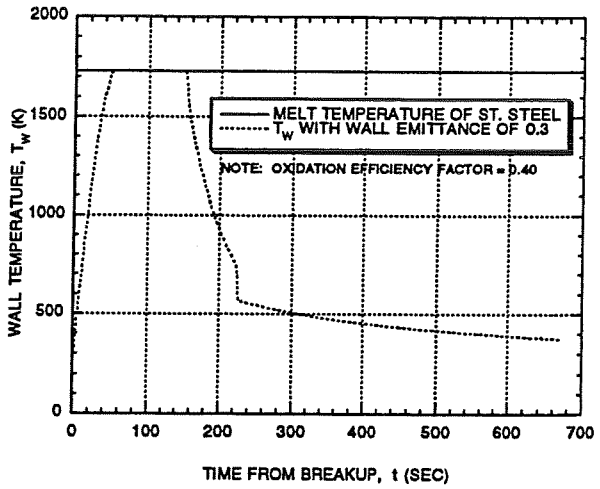

Fig. 19 Wall Temperature for Delta 2nd Stage Stainless Steel Cyl. vs. Time from Breakup

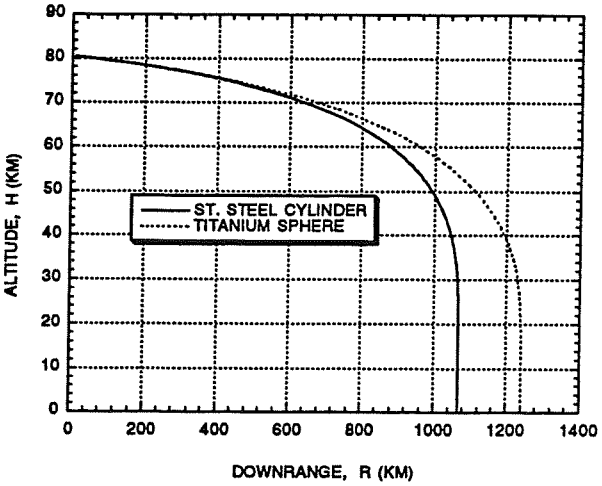

Fig. 20 Altitude for Delta 2nd Stage Fragments vs. Downrange

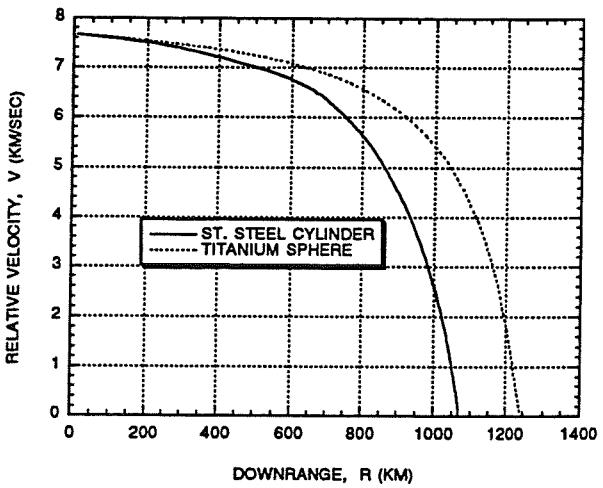

Fig. 21 Relative Velocity for Delta 2nd Stage Fragments vs. Downrange

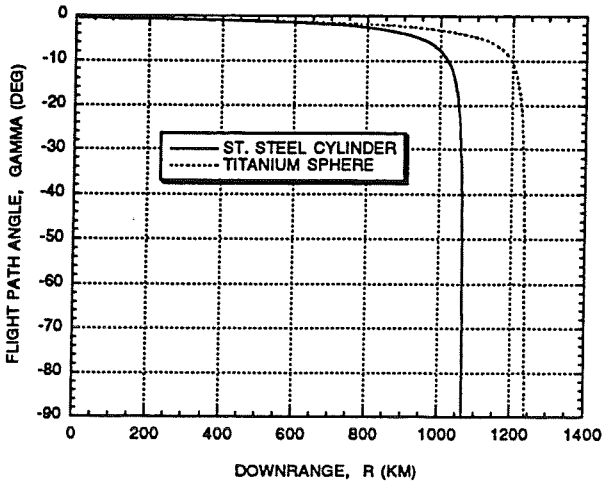

Fig. 22 Flight Path Angle for Delta 2nd Stage Fragments vs. Downrange

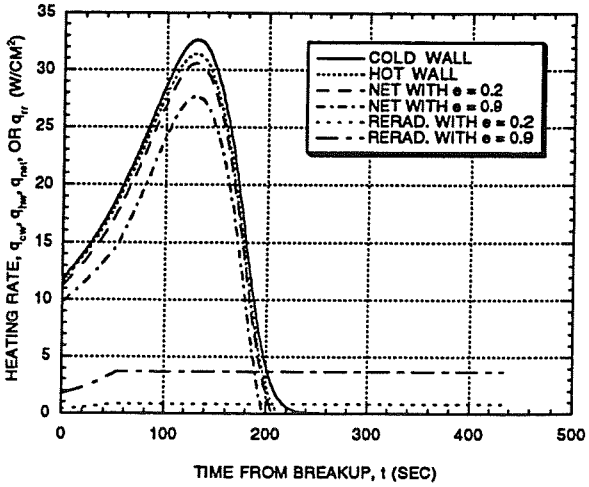

Fig. 23 Heating Rate Components to ADEOS Al AVNIR Box vs. Time from Breakup

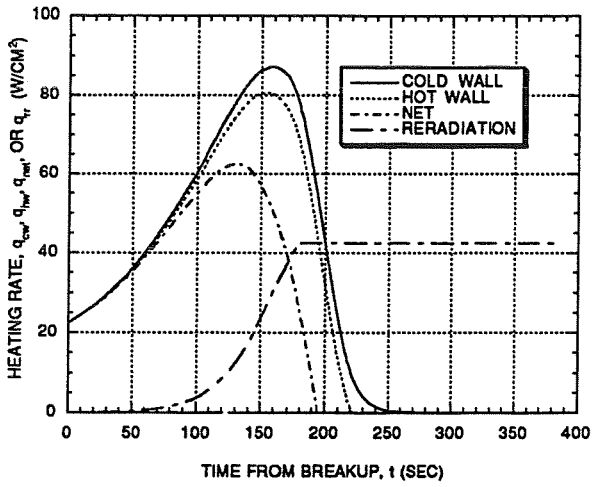

Fig. 24 Heating Rate Components to ADEOS Nickel EPS Battery Box vs. Time from Breakup

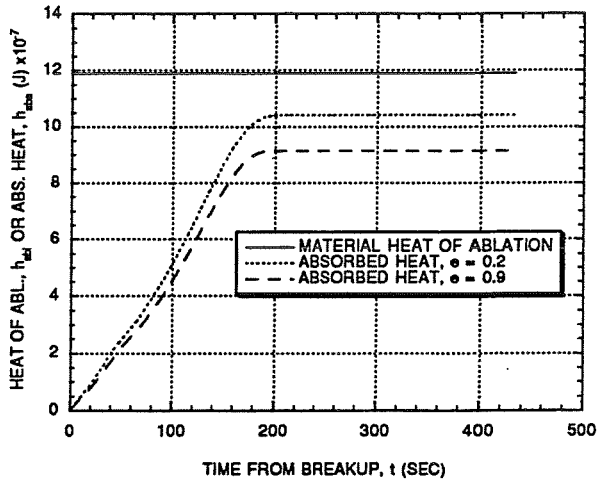

Fig. 25 Heat of Ablation & Absorbed Heat to ADEOS Al AVNIR Box vs. Time from Breakup

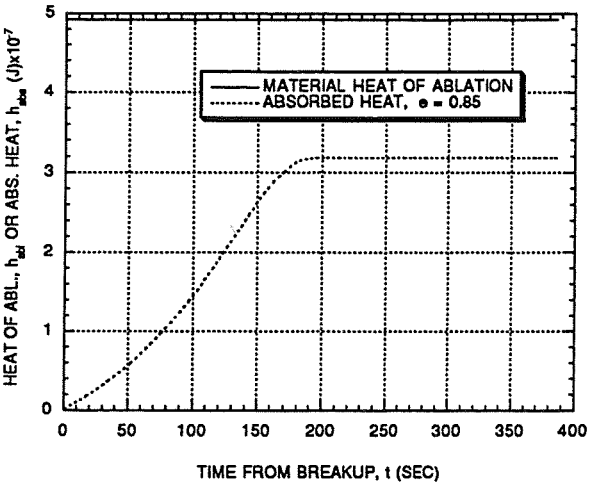

Fig. 26 Heat of Ablation & Absorbed Heat to ADEOS EPS Battery Box vs. Time from Breakup

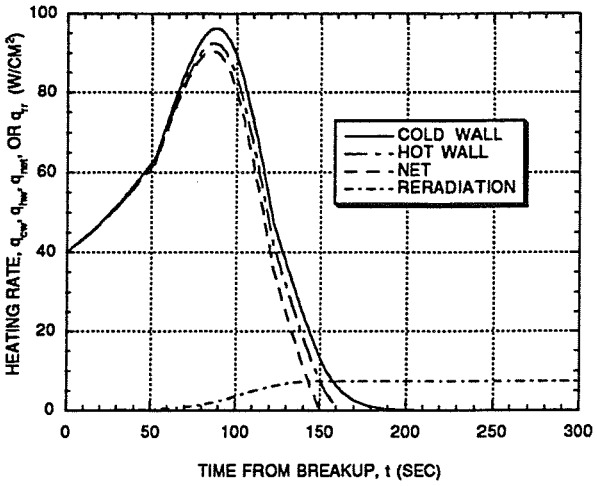

Fig. 27 Heating Rate Components to COSMOS 954 Beryllium Cylinder vs. Time from Breakup

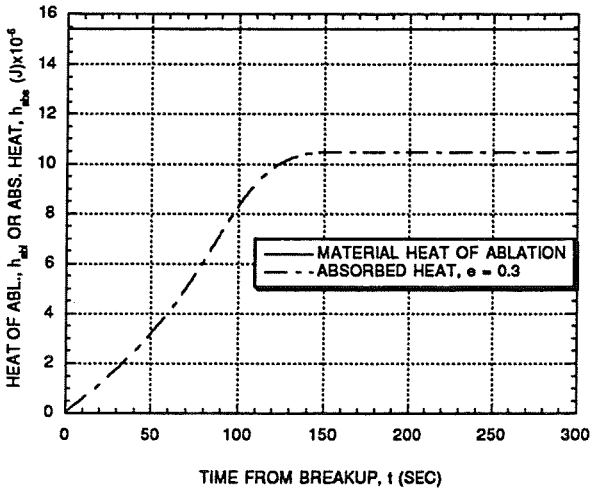

Fig. 28 Heat of Ablation & Absorbed Heat for COSMOS 954 Be Cyl. vs. Time from Breakup

COMPARISON OF ORBITER PRCS PLUME FLOW FIELDS USING CFD AND MODIFIED SOURCE FLOW CODES

Wm. C. Rochelle,* Robin E. Kinsey,** and Ethan A. Reid**
Lockheed Martin, Houston, TX

Phillip C. Stuart+ and Forrest E. Lumpkin+
NASA/JSC, Houston, TX

Abstract

The Space Shuttle Orbiter will use Reaction Control System (RCS) jets for docking with the planned International Space Station (ISS). During approach and backout maneuvers, plumes from these jets could cause high pressure, heating, and thermal loads on ISS components. The object of this paper is to present comparisons of RCS plume flow fields used to calculate these ISS environments. Because of the complexities of 3-D plumes with variable scarf-angle and multi-jet combinations, NASA/JSC developed a plume flow-field methodology for all of these Orbiter jets. The RCS Plume Model (RPM), which includes effects of scarfed nozzles and dual jets, was developed as a modified source-flow engineering tool to rapidly generate plume properties and impingement environments on ISS components. This paper presents flow-field properties from four PRCS jets: F3U low scarf-angle single jet, F3F high scarf-angle single jet, DTU zero scarf-angle dual jet, and F1F/F2F high scarf-angle dual jet. The RPM results compared well with plume flow fields using four CFD programs: General Aerodynamic Simulation Program (GASP), Cartesian (CART), Unified Solution Algorithm (USA), and Reacting and Multi-phase Program (RAMP). Good comparisons of predicted pressures are shown with STS-64 Shuttle Plume Impingement Flight Experiment (SPIFEX) data.

Introduction

In May 1998 the first segment of the International Space Station (ISS), the Russian Functionalni Gruznoi Blok (FGB), is scheduled to be launched. About 5 years later, the entire 110 m x 75 m x 40 m ISS will be completely assembled. During build-up of this space station, Orbiter Primary and Vernier Reaction Control System (PRCS and VRCS, respectively) jet plumes will impinge upon ISS components while the Orbiter is docking, possibly causing high pressure and heating environments on critical components. One such build-up configuration is seen in Fig. 1 which shows the Orbiter docking at Pressurized Mating Adapter (PMA)-2 during ISS Flight 6A. High impingement environments could arise with the F1F/F2F plume impinging on the bottom of the P6 +x radiator or the F3U plume impinging on the P6 solar array and the Space Station Remote Manipulator System (SSRMS).

The methodology for evaluating Orbiter plumes and impingement effects on both Mir Space Station and ISS components has been underway at NASA/JSC for the past three years. This includes plume flow-field characteristic tests in the JSC Chamber A vacuum chamber[1,2] and development of the RCS Plume Model (RPM)[3-5] and the higher-fidelity CFD/DSMC model.[6] For validation of the analytical models, plume impingement pressure, force, and heat flux data was obtained from Orbiter RCS jet firings from Shuttle Plume Impingement Flight Experiment (SPIFEX).[7-9]

Plume impingement heating environments to specific ISS components have been presented recently.[10,11] An updated plume heating model for the continuum regime was presented a few months ago[12] using the plumes discussed in the present paper. These heating environments were shown to vary as a function of distance between ISS docking ports, location in Orbiter approach cone, location along component, radius of component, and for solar arrays, the array feather angle.

The present paper focuses on the plume flow-field properties used to obtain the heating environments. These plumes were generated by both the engineering model (RPM) as well as by more exact CFD solutions. The remainder of the paper will include a description of the Orbiter jet locations and the PRCS jet coordinate system. A discussion of the SPIFEX configuration on which plume flow field and heating models were validated is also described. The flow-field methodology of the five types of plume programs considered will be briefly summarized, and results, including flow-field property contours and comparisons of properties between the methods, will be presented. In addition, comparisons of impingement pressure with SPIFEX data at the location of specific test points will be given.

*Group Lead, Advanced Systems Group
**Cooperative Engineering Student, Adv. Sys. Grp.
+Aerospace Engineer, Aeroscience Branch

Orbiter Jet Locations and PRCS Coordinate System

A sketch of the Orbiter RCS jet locations and plume centerline firing directions is presented in Fig. 2. There are 38 870-lb thrust PRCS jets and six 24-lb thrust VRCS jets on the Orbiter (all using N_2O_4/monomethyl hydrazine as the propellant), as seen in this figure. Several of the PRCS jets on the forward module have a large scarf angle to conform to the contour of the Orbiter. These include the forward-firing jets (F1F, F2F, and F3F) with a nominal scarf angle of 65° and the downward-firing jets (F1D-F4D) with a nominal scarf angle of 59°. The upward-firing PRCS jets in the forward module (F1U, F2U, and F3U), together with two of the side-firing jets in this module (F1L and F2R) have a nominal scarf angle of 23°. The other two side-firing PRCS jets on the forward module (F3L and F4R) and the left and right-firing jets on either side of the tail (L1L-L4L and R1R-R4R) have a nominal scarf angle of 16°. The up-firing, down-firing, and aft-firing PRCS jets in the aft module all have a zero scarf angle.

The principal PRCS jet used for docking maneuvers is the F3U single jet. Whenever the forward-firing jets are used, they always fire together, producing the F1F/F2F dual-jet plume. Also, the up-firing, down-firing, or aft-firing jets on either side of the vertical tail fire together (e.g., R1U/L1U), producing a dual-jet plume. When the up-firing jets fire, this is referred to as the Dual-Tail-Up (DTU) jet. In addition, if the F3U jet fires while the DTU jet is firing, the jets fire in the "norm-z" mode with three intersecting plumes.

In Fig. 3, the Orbiter PRCS coordinate systems are shown for: (a) the single-jet, unscarfed nozzle; (b) the dual-jet, unscarfed nozzle; (c) the single-jet scarfed nozzle; and (d) a schematic of the Orbiter forward module showing the multiple-jet scarfed nozzles. From these figures, the scarf angle, ξ; distance, r, from nozzle exit to an object in the plume; azimuth angle, θ, from the centerline; clock angle, ϕ, around the nozzle; and thrust vector angle, ψ, may be seen.

SPIFEX Configuration

Figure 4 presents a sketch of the equipment used for the SPIFEX operation. The experiment arm was mounted at the end of a 10-m long boom which was attached to the end of the Shuttle Remote Manipulator System (RMS). This figure shows the general position of the arm above the F3U jet plume. Two plates were on the experiment arm containing instrumentation - Load Measuring System (LMS) plate and Plume Impingement Characterization System (PICS) plate. Four heat flux sensors were on the LMS plate and three on the PICS plate. The PICS plate contained four pressure sensors (absolute and differential capacitance manometers and Sentran and Kistler gages). Pressure measurements could also be deduced by dividing the force measurement by the plate area. This SPIFEX data will be compared with impingement pressures obtained from plume flow fields discussed below.

Plume Flow-Field Methodology

This section discusses the plume flow-field methodology for the RPM code[3,4] and the CFD programs: General Aerodynamic Simulation Program (GASP),[13] Cartesian (CART) code, Unified Solution Algorithm (USA)[14] program, and the Reacting and Multi-phase Program (RAMP).[15] Plume runs were made with the RPM, GASP, CART, and RAMP codes, while the results of the USA code were furnished by Rockwell.[14] The F3U plume was generated by the RPM, GASP, and RAMP codes, the F3F plume was run for the RPM and GASP codes, the DTU plume was predicted by RPM and GASP, and the F1F/F2F plume was generated by RPM, CART and USA.

RPM

The RPM code uses modified source flow relations to predict plume dynamic pressure for a nozzle for a given value of ξ as a function of r, θ, ϕ, chamber pressure, ratio of specific heats, combustion efficiency, and limiting streamline angle. The relation between distances and angles is seen in Fig. 3. In RPM, the plume velocity is constant with azimuth angle in the inviscid core until the limiting streamline is reached, which divides the inviscid core and viscous boundary layer. The velocity decreases across the boundary layer to account for energy losses. Inside the shock interaction region of dual-jet plumes, RPM dynamic pressures are amplified by factors obtained from fits of CFD and DSMC solutions for the DTU plume. For the F1F/F2F plume, RPM dual-jet amplification factors were further adjusted based on SPIFEX data. The RPM model uses velocity and static pressure curve fits in the shock interaction region to envelope the region predicted by the CFD solutions (described below).

GASP and CART

The GASP code was used for the nozzles and plumes of the F3U zero scarf-angle (axisymmetric) jet, the F3U 22.7° scarf-angle jet, the F3F 65.0° scarf-angle jet, the

zero scarf-angle DTU jets, and the nozzle of the 64.8° scarf-angle F1F/F2F dual jet. Because of the extreme scarf angle coupled with the proximity of the nozzles to the Orbiter centerline, problems occurred in producing a grid of adequate quality using GASP for the F1F/F2F plume. Thus, the JSC CART code, a purely Cartesian flow solver that automatically clusters grid points to gradients in the flow field, was used for this plume.

The thin-layer Navier-Stokes equations were solved with the Baldwin-Lomax[16] turbulence model using a 500 K constant wall temperature. A finite-rate chemistry model with eleven species (CO, H_2, N_2, NO, O_2, OH, CO_2, H_2O, H, N, and O) was used with 86 reactions and vibrational equilibrium. By the time the flow had reached the nozzle exit, it was chemically frozen; hence, in the plume, the chemical reactions were disabled, and the flow was frozen along streamlines.

The initial conditions in the combustion chamber using GASP were based on results of the NASA/Lewis Chemical Equilibrium Composition (CEC) code[17] with a 2-temperature range curve-fit inside the nozzle and a single harmonic oscillator model in the plume for the thermodynamic properties. The flow solver used a Roe-averaging 3rd-order Monotone Upstream-centered Scheme for Conservation Laws (MUSCL) technique.[18] The models used with the CART plume solution were similar to those used with GASP in the plume, except that the Van Leer[19] flux calculation was used.

USA

With the USA code, the Navier-Stokes equations were solved with a finite volume scheme (same as with GASP). These equations result in five independent variables for 3-D calculations and four variables for axisymmetric/2-D calculations. The same 11 species and 86 reactions as used by GASP were used with the USA code with finite-rate chemistry in the nozzle and frozen flow in the plume. A modified Baldwin-Lomax turbulence model was used for the flow inside the axisymmetric and scarfed nozzles. For plume calculations with single and dual scarfed nozzles, the USA code used second-order accuracy (while the GASP code used third-order accuracy). The USA code used a 1-temperature curve-fit for thermodynamic properties for both the nozzle and plume. For the scarfed nozzle, the USA code had a 65° inclined plate blending into the Orbiter contour and turning 90° downward at the nose. This was in contrast to the 65° continuous flat plate for the CART and GASP solutions which did not follow the contour of the Orbiter near the nose. The flow-field output of the USA code was in Plot3d[20] format. However, to be compatible with the CART solutions, the Plot3d format was changed to Tecplot[21] format.

RAMP

The RAMP nozzle and plume code has the capability to run a reacting, 2-phase (gas-particle) solution using a shock-capturing finite-difference numerical operator with a variable oxidizer to fuel (O/F) distribution. For the axisymmetric PRCS solution for the F3U jet, an equilibrium/frozen single-phase (gas only) solution was used with the flow chemically frozen along streamlines downstream of the throat (similar to the GASP and USA solutions). A transonic solution with the wall geometry input both upstream and downstream of the throat, including throat radius of curvature, was used. A variable O/F ratio distribution was assumed in the nozzle and plume with an 11-point variation from O/F = 2.2 along the nozzle centerline to O/F = 0.8 at the wall where the MMH fuel is dumped.

The NASA/Lewis CEC code[17] was run initially to obtain thermochemical properties for the RAMP nozzle solution. Then RAMP was run for inviscid flow inside the nozzle. The Boundary Layer Integral Matrix Procedure - Version J (BLIMPJ) code[22] was then run inside the nozzle to obtain the viscous boundary layer flow including displacement thickness along the wall. An assumed wall temperature distribution varying from 1303 K at the throat to 1234 K at the exit plane (0.236 m from the throat) was used. The RAMP code was then run for a modified nozzle wall with the BLIMPJ displacement thickness subtracted off the wall. The BLIMPJ code was run a second time to further adjust the wall boundary layer, and a combined inviscid/boundary layer start line at the exit plane was used for input to the RAMP plume run. This axisymmetric plume was thus used for the F3U plume comparison with RPM and GASP solutions.

Results

Plume Flow-field Contours

Figure 5 presents RPM-predicted dynamic pressure contours for the F3U single-jet plume with a 22.7° scarf angle as a function of distance along the Z-axis. In Fig. 5 (a) the contours are shown for the X-Z plane, and in Fig. 5 (b), they are shown for the Y-Z plane. It is seen that the X-Z plane contours are symmetric with respect to the X = 0 axis, while in Fig. 5 (b), the Y-Z contours are shifted slightly downward. Because of the closeness

of the flow-field properties in the two planes, properties from this RPM plume were compared with those of axisymmetric GASP and RAMP plumes. In Fig. 5 (b) several of the SPIFEX test points are shown, at which measured impingement pressures were used to compare with predicted values (discussed later).

In Fig. 6 the dynamic pressure contours are presented for the DTU dual-jet plume as computed by the RPM code. The X-Z view of Fig. 6 (a) shows the shock-interaction region in between these jets, the axes of which are separated by a distance of 6.8 m. The Y-Z view of Fig. 6 (b) shows a stagnation region, but not a shock interaction region. No significant SPIFEX data was taken for this plume.

Figure 7 presents the RPM contours of dynamic pressure for the F1F/F2F dual-jet plume. In Fig. 7 (a) the X-Z view shows the shock interaction region between these jets, the axes of which are separated by a distance of only 0.74 m. The effect of the high scarf angle may be seen in Fig. 7 (b) showing the thrust vector sloping downward to the right. In this plot, the actual Y-axis is the negative value of that shown in Figs. 3 (c) and 3 (d) such that the thrust vector is sloping upward, away from the Orbiter body. Several SPIFEX test points are also shown in this figure.

In Figs. 8 and 9 the RAMP and GASP F3U axisymmetric PRCS plume dynamic pressure contours are shown, respectively. A continuum flow line limits the GASP solution to about Z = 18 m on the axis. It is seen that the contour values are fairly close between the GASP and RAMP values, especially along the axis and compare well with the RPM contours in Fig. 5 (as discussed later). The presence of a reflected shock may be seen in both the RAMP and GASP plots.

Figure 10 presents the DTU plume contours of dynamic pressure in the Y-Z plane as computed by the GASP code. This plot represents a cut across the plume in the Z-direction at 12 m. The shock contour is shown in this figure, with a minimum value at Y = 0, increasing in the X-direction for higher values of Y. This dual-jet plume has two unscarfed nozzles; hence, the flow variables for Y < 0 are the same as those for Y > 0. The center of a single jet may be seen at X = 3.4 m. The shock location compares favorably with that of the RPM DTU plot of Fig. 6 at the same location.

In Figs. 11, 12, and 13, F3F single-jet and F1F/F2F dual-jet plume contours are shown of density, velocity, and molecular weight, respectively, at Z = 2.0 m as a function of Y and X. The contours were computed by GASP for the F3F jet and by CART for the F1F/F2F jet. Both jets have the same high scarf angle (65°), and the F3F jet axis has been shifted over to X = 0.37 m to put it at the same location as the axis of one of the F1F/F2F jets. Figure 11 shows the shock location of the F1F/F2F dual jet which has a similar pattern to that of the DTU dual jet shown in Fig. 10. However, the F1F/F2F contours are not symmetric with respect to the Y = 0 axis like those of the DTU contours because of the high scarf angle of the F1F/F2F jet. The contours in Figs. 12 and 13 show the maximum values of velocity and molecular weight occurring at the axis (X = 0.37 m). In all three figures, the contours of the F3F and F1F/F2F plume (outside the shock) are comparable, in spite of the difference in the two codes.

Distribution of Flow Properties

In Fig. 14 the distribution of the F3U dynamic pressures along the plume axis is shown with a comparison of the RPM, RAMP, and GASP results interpolated from Figs. 5, 8, and 9, respectively. For values of Z > 1 m, the RPM dynamic pressures are slightly lower than the GASP values, which are slightly lower than the RAMP values. The RAMP and GASP curves show a shock structure for Z < 0.5 m (also seen in Figs. 8 and 9, respectively). This shock structure cannot be obtained from the RPM code since it is a modified source-flow code, and its solution actually starts at Z = 1 m.

The distribution of dynamic pressures across the F3U plume computed from GASP, RAMP, and RPM solutions is shown in Fig. 15 at Z = 10 m from the exit plane. All three predictions are close at low values of Y, with a deviation occurring at larger values of Y where the plume is more rarefied.

Figure 16 presents the GASP and RPM distribution of density across the F3F plume in the X-direction at Z = 12.5 m and Y = 1.0 m. The GASP and RPM values are very close for Z < 2 m, with GASP values above those of RPM from 2 to 9 m. The trend reverses itself at larger values of X. In Figs. 17 and 18, the GASP and RPM dynamic pressure and velocity distribution around the F3F plume is shown as a function of clock angle, ϕ, at Z = 12.5 m and θ = 36°. It is seen that the dynamic pressures are fairly close between the two methods, and the velocities are very close.

Figure 19 presents a comparison of density from the DTU plume as a function of X at Z = 18 m from the exit. It is seen that the RPM-predicted location of the

dual-jet shock at X = 1.7 to 2.2 m is very close to the prediction from GASP. The GASP values of density are slightly higher than those of RPM inside the shock and are slightly lower than those of RPM outside the shock (for X > 2.2 m).

In Fig. 20 the dynamic pressures from the CART, USA, and RPM codes are plotted for the F1F/F2F dual-jet plume as a function of Z along the X-Z plane of symmetry. All three of the curves are fairly close for Z > 2 m, with RPM generally the highest. There is a large difference between RPM and both CART and USA for Z < 2 m; however, no component of the ISS would be within 3 - 4 m of the exit of this plume because of the high heating rates at this distance.[11] In the range of Z from 9 - 15 m, all three methods show very good correlation with SPIFEX data (described below).

Figure 21 shows a distribution of dynamic pressure across the F1F/F2F plume at Z = 2 m vs. X using CART, USA, and RPM. The CART and USA values are close inside the shock (X < 0.5 m), while the RPM predictions are generally in between the USA and GASP values for X > 1.5 m. In Fig. 22 a comparison of CART and RPM dynamic pressure for the F1F/F2F plume at Z = 5.0 m is shown as a function of Y along the plane of symmetry. The CART values are slightly higher than those of RPM except for Y < -4 m where the two methods are very close. The CART flow field was terminated for values of Y > 2.3 m.

SPIFEX Data Comparisons

Figure 23 presents a bar chart showing the comparison of impingement pressures measured by SPIFEX for the F3U jet with RPM, RAMP, and GASP predictions. In this and the next two figures, the SPIFEX pressures are the measured loads divided by the area of the LMS plate. Distances from the nozzle exit plane to the sensor, r, of 12.2 to 23.2 m are included in Fig. 23 at nominal azimuth angles, θ of 2° and 15°. The RPM values show excellent agreement with data. The RAMP and GASP values are slightly higher than the data. These impingement pressures are computed by adding the static pressure to the product of pressure coefficient times dynamic pressure. For GASP and RAMP, the pressure coefficient was taken to be 2.0; for RPM it is calculated and is always somewhat less than 2.0. No values for GASP are shown for r = 18.3 and 23.2 m since this is outside the computational domain.

In Fig. 24 a bar chart is presented showing the comparison of RPM and GASP predictions of impingement pressure with SPIFEX data for the F1F plume (same as F3F plume) as a function of clock angle, ϕ, around the nozzle. For most cases the RPM and GASP values are in good agreement with the data. Test points 56 and 126 show the SPIFEX data higher than either RPM or GASP predictions.

Figure 25 presents the RPM, CART, and USA predicted impingement pressures with SPIFEX measured pressure data for the F1F/F2F dual jet as a function of θ for $\phi = 180°$. Three values of r are shown from 9.15 to 15.2 m. In most all cases, there is very good agreement between data and prediction by RPM and the two CFD codes.

Conclusions

This paper has presented sample plume flow fields from Orbiter PRCS jets. Examples were shown of plumes from low scarf-angle single jets, high scarf-angle single jets, zero scarf-angle dual jets, and high scarf-angle single jets. It was seen that results from the JSC RPM engineering model compare well with the flow fields generated from the higher-fidelity GASP, CART, USA, and RAMP CFD codes. The RPM predictions of impingement pressure were shown to compare very well with measured SPIFEX impingement pressures for the low scarf-angle F3U jets and reasonably well with the high scarf-angle F1F and F1F/F2F SPIFEX data. In summary, the plume flow fields from the RPM code appear to be validated satisfactorily to use in prediction of pressure and heating environments to space station components.

Acknowledgments

The authors wish to acknowledge the support of Jeff Arend of the JSC Space Station Office on this project. Thanks are also extended to Jay LeBeau and Steve Fitzgerald of NASA/JSC for plume solutions and comments and to Ruston Hughes and Stan Bouslog (formerly with Lockheed Martin) who helped develop the RPM code.

References

1. Fitzgerald, S. M., Rocha, A. R., Bouslog, S. A., Hughes, J. R., and Leahy, K. S., "Far-Field Plume Characterization Testing in Support of Space Station Plume Impingement Methodology Validation," Paper 94-2636 presented at 18th AIAA Aerospace Ground Testing Conference, Colorado Springs, CO, June 20-23, 1994.

2. Stueber, M. J., "Plume Characterization Test Report for the NASA/JSC Chamber A Vacuum Facility: Vol. I," JSC-32321, Oct. 1994.

3. Fitzgerald, S. M., Bouslog, S. A., and Hughes, J. R., "Model for Predicting Orbiter PRCS Impingement Loads and Heating," JSC-26507, Rev. A, June 1995.

4. Fitzgerald, S. M. and Bouslog, S. A., "Orbiter PRCS Plume Impingement Toolkit: RPM Version 3.0.1," JSC-26583, Rev. A, Sept. 1996.

5. Rochelle, W. C., Hughes, J. R., and Leahy, K. S., "Model for Predicting Orbiter PRCS Plume Heating to International Space Station Alpha (ISSA)," Lockheed AS-107-94, Aug. 25, 1994.

6. Lumpkin, F. E., Stuart, P. C., and LeBeau, G. J., "Enhanced Analyses of Plume Impingement During a Combined CFD and DSMC Methodology," Paper 96-1877 presented at 31st AIAA Thermophysics Conference, New Orleans, LA, June 17-20, 1996.

7. Machin, R. A., Stueber, M. J., Rocha, A. R., Leahy, K. S., Hughes, J. R., White, M. K., Rochelle, W. C., and Fitzgerald, S. M., "Shuttle Plume Impingement Flight Experiment (SPIFEX) Data Reduction, Vol. I - Test Description and Results," JSC 27030, June 1995.

8. Rochelle, W. C., Hughes, J. R., Leahy, K. S., and Fitzgerald, S. M., "Shuttle Plume Impingement Flight Experiment (SPIFEX) - Heat Flux Measurement and Predictions," Paper 96-0349 presented at AIAA 34th Aerospace Sciences Meeting, Reno, NV, Jan. 15-18, 1996.

9. Fitzgerald, S. M., Hughes, J. R, and Leahy, K. S., "Shuttle Plume Impingement Flight Experiment (SPIFEX) - Pressure and Load Plate Measurements," Paper 96-0611 presented at AIAA 34th Aerospace Sciences Meeting, Reno, NV, Jan. 15-18, 1996.

10. Rochelle, W. C., Hughes, J. R., DeVenezia, J., Bouslog, S. A., Leahy, K. S., and Fitzgerald, S. M., "Plume Impingement Heating to International Space Station (ISS)," Paper 95-2132 presented at 30th AIAA Thermophysics Conference, San Diego, CA, June 19-22, 1995.

11. Rochelle, W. C., Hughes, J. R., Kinsey, R. E., and Caram, J. M., "Heat Transfer from Space Shuttle PRCS Plumes to Components of International Space Station," Paper 96-3965 presented at 1996 AIChE/ASME/ANS/AIAA National Heat Transfer Conference, Houston, TX, Aug. 3-6, 1996.

12. Rochelle, W. C., Kinsey, R. E., Ruby, D. G., Stuart, P. C., and Lumpkin, F. E., "Orbiter Exhaust Plume Impingement Effects on International Space Station," Paper presented at 23rd JANNAF Exhaust Plume Technology Meeting, Sunnyvale, CA, April 8-11, 1997.

13. McGrory, W. D., Stack, D. C., Applebaum, M. P., and Walthers, R. W., "GASP Version 2.2 - The General Aerodynamic Simulation Program," AeroSoft, Inc., 1993.

14. Dominik, D., Fu, T., et. al., "Space Shuttle RCS Plume Flow Field," Rockwell International Report SSD95D0163, April 1995.

15. Smith, S. D., "Update to the RAMP2 Computer Program," SECA-FR-93-19, December 1993.

16. Baldwin, B. S. and Lomax, H., "Thin Layer Approximation and Algebraic Model for Separated Turbulent Flows," Paper 78-257 presented at 16th AIAA Aerospace Sciences Meeting, Reno, NV, Jan. 16-18, 1978.

17. Gordon, S. and McBride, B. J., "Computer Program for Calculation of Complex Chemical Equilibrium Compositions, Rocket Performance, Incident and Reflected Shocks, and Chapman-Jouguet Detonations," NASA SP-273, March 1976.

18. Roe, P. L., "Approximate Riemann Solver, Parameter Vectors, and Difference Schemes," *Journal of Computational Physics*, Vol. 43, pp. 357-372.

19. Van Leer, B., "Towards the Ultimate Conservative Difference Scheme V. A Second Order Sequel to Godunov's Method," *Journal of Computational Physics*, Vol. 32, 1979, pp. 101-136.

20. Walatka, P. P. and Buning, P. G., "PLOT3D User's Manual," NASA TM 101067, March 1989.

21. "Tecplot User's Manual - Version 7," Amtec Engineering, Inc., Aug. 1996.

22. Evans, R. M. and Morse, H. L., "Boundary Layer Integral Matrix Procedure BLIMP-J User's Manual," Aerotherm UM-75-64, July 1975.

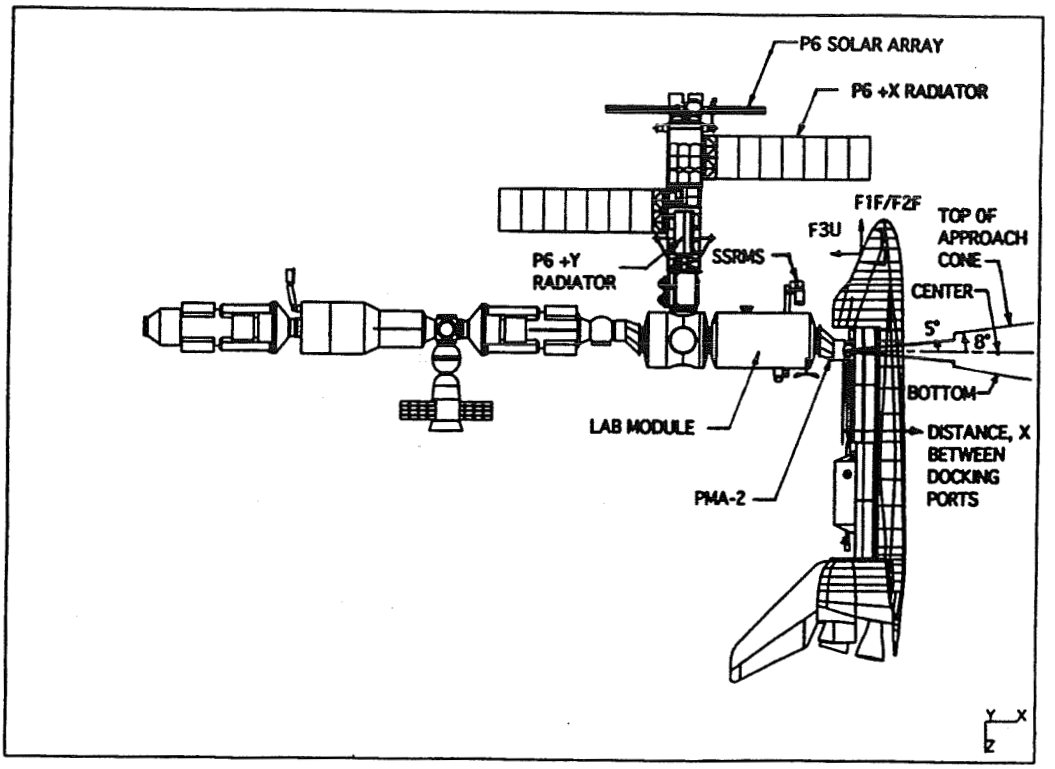

Fig. 1 X-Z Plane View of International Space Station for Flight 6A

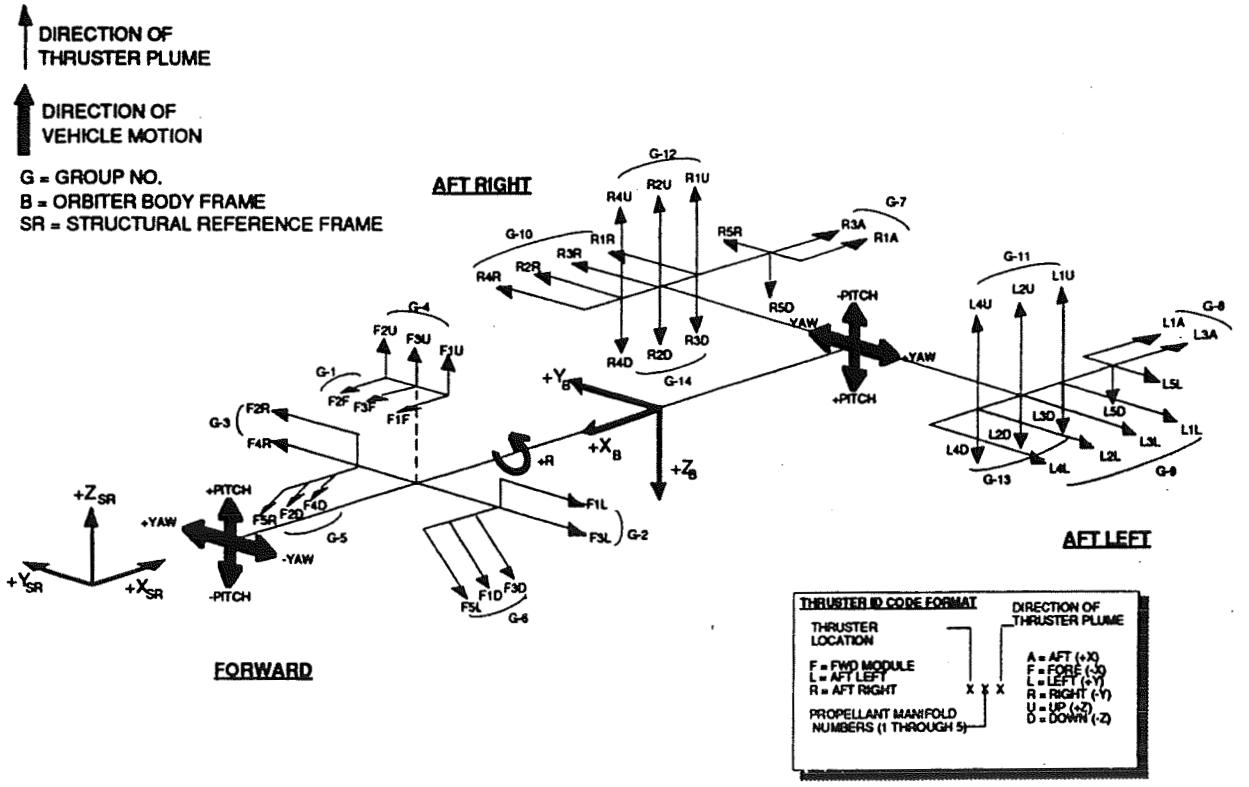

Fig. 2 Orbiter RCS Jet Locations and Plume Directions

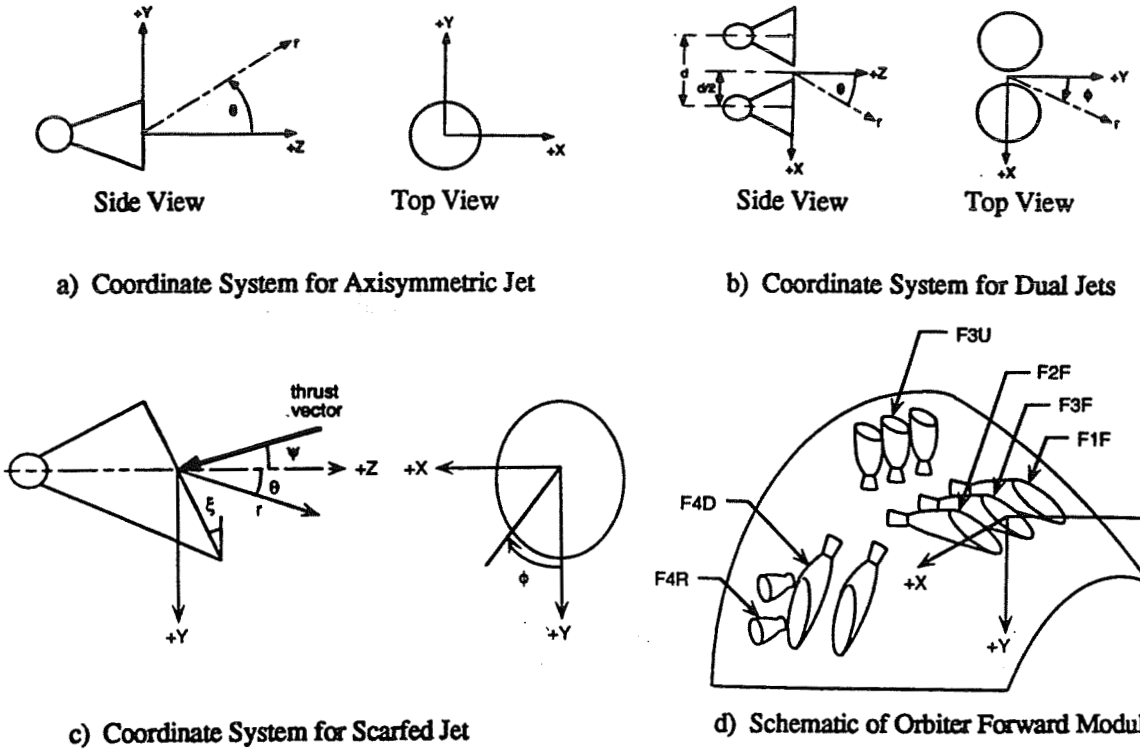

Fig. 3 Orbiter PRCS Jet Coordinate System

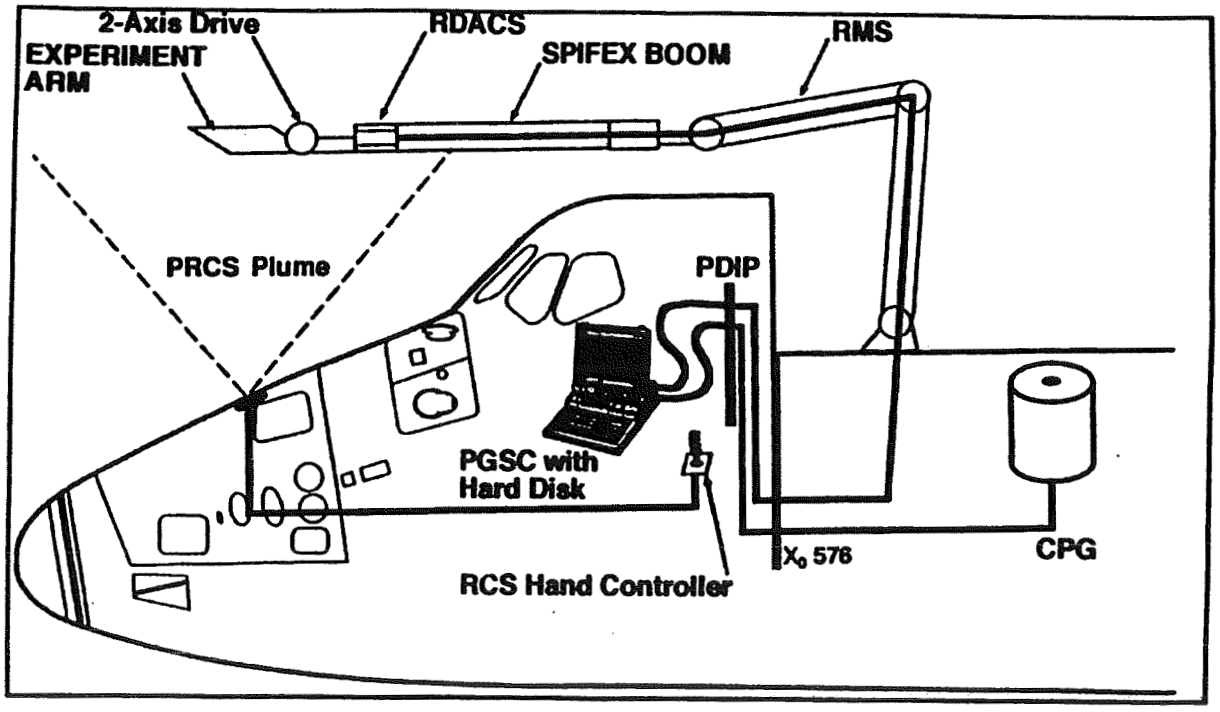

Fig. 4 Overview of Equipment Used for SPIFEX Operations

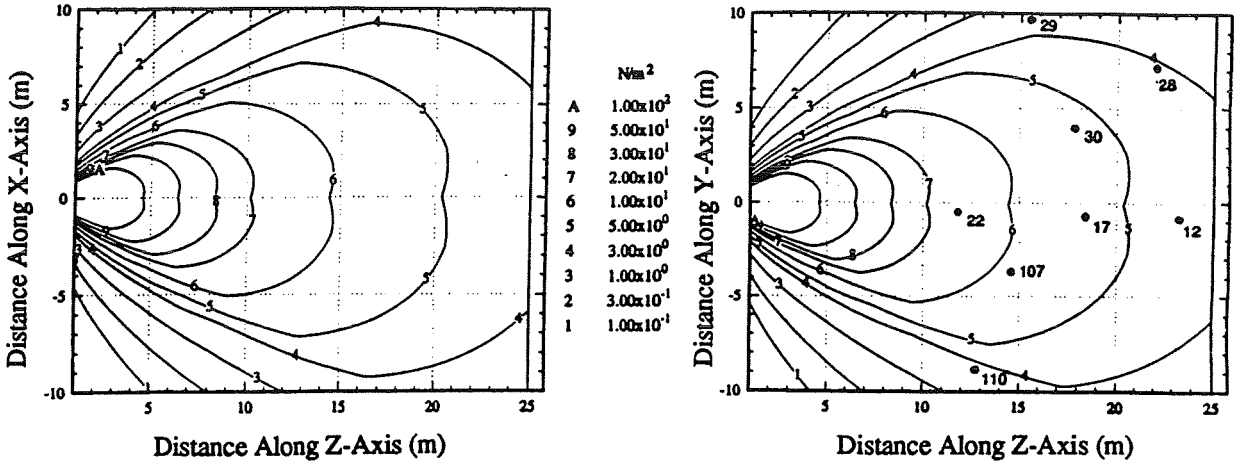

a) X-Z Plane b) Y-Z Plane

Fig. 5 RPM Dynamic Pressure Contours for F3U Single-Jet Plume

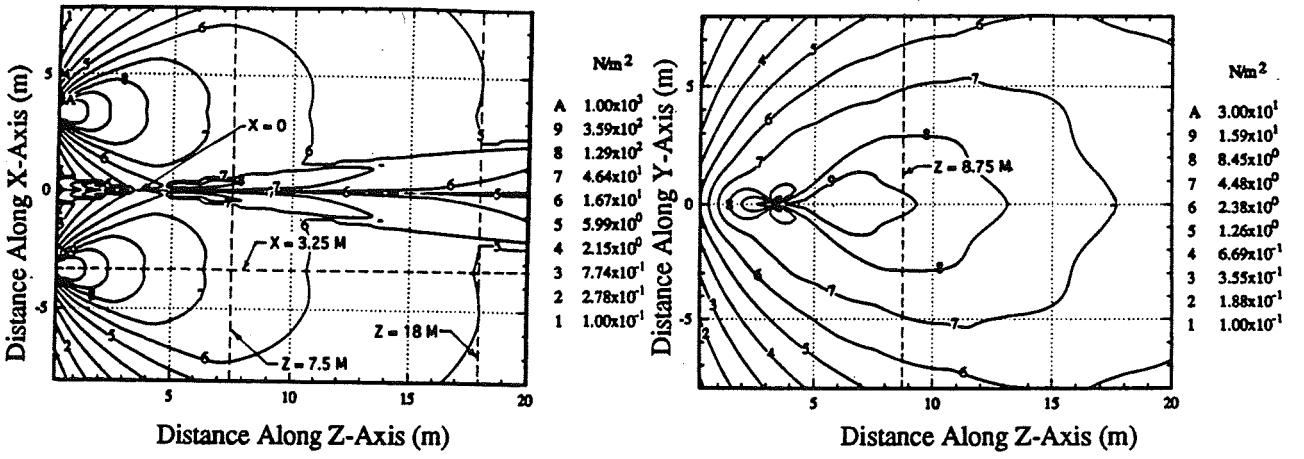

a) X-Z Plane b) Y-Z Plane

Fig. 6 RPM Dynamic Pressure Contours for DTU Dual-Jet Plume

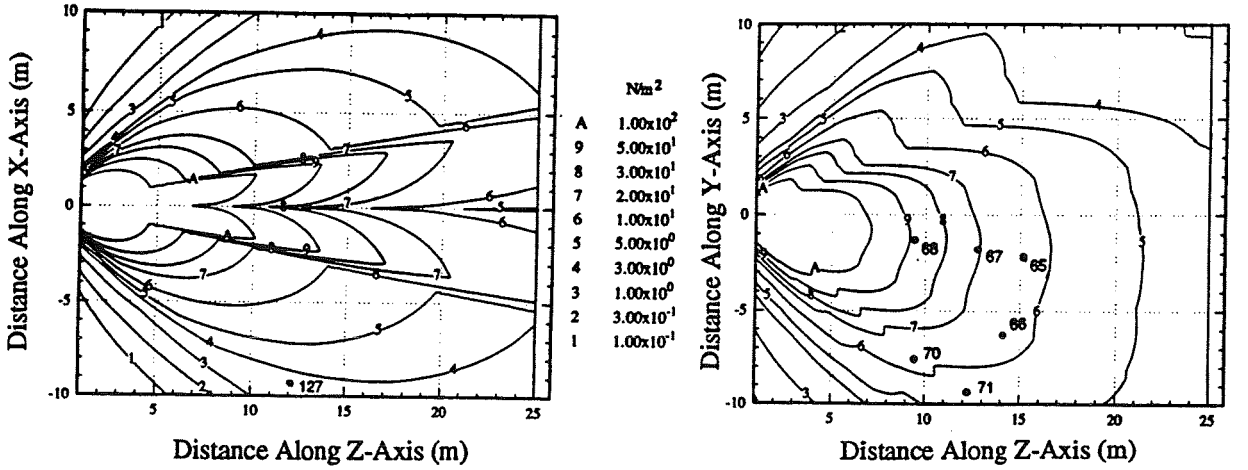

a) X-Z Plane b) Y-Z Plane

Fig. 7 RPM Dynamic Pressure Contours for F1F/F2F Dual-Jet Plume

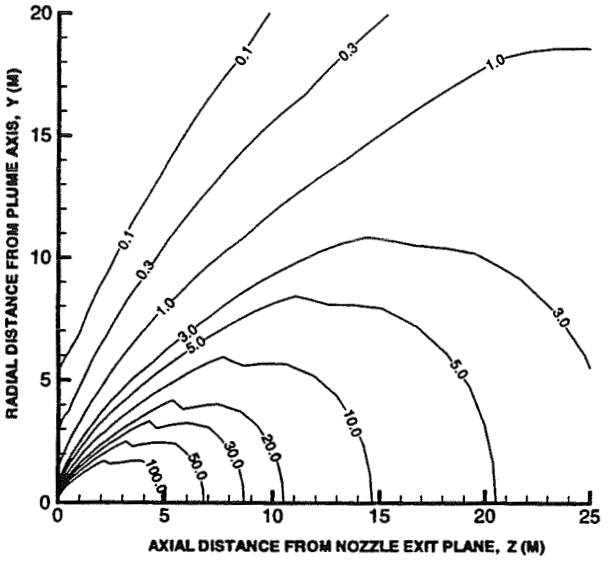

Fig. 8 RAMP Dynamic Pressure Contours (N/m^2) for F3U Axisymmetric Plume in Y-Z Plane

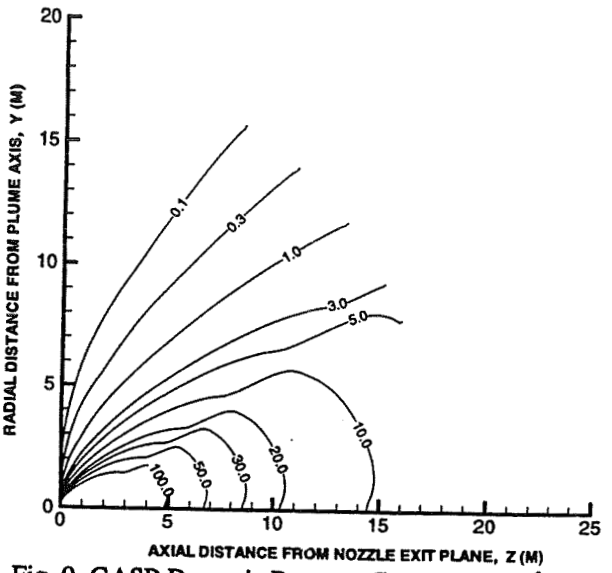

Fig. 9 GASP Dynamic Pressure Contours (N/m^2) for F3U Axisymmetric Plume in Y-Z Plane

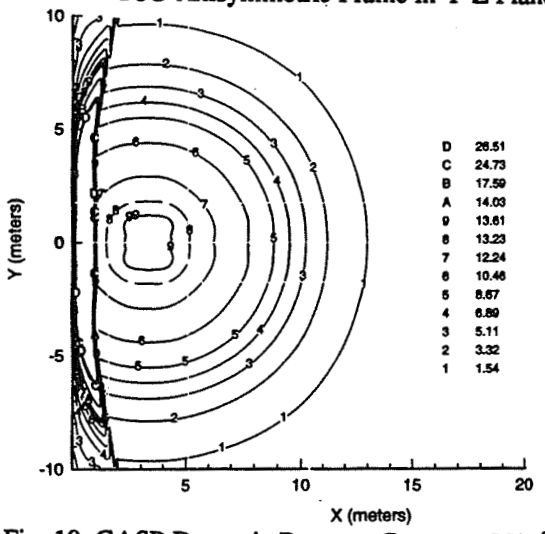

Fig. 10 GASP Dynamic Pressure Contours (N/m^2) for DTU Dual-Jet Plume in Y-X Plane (Z=12 m)

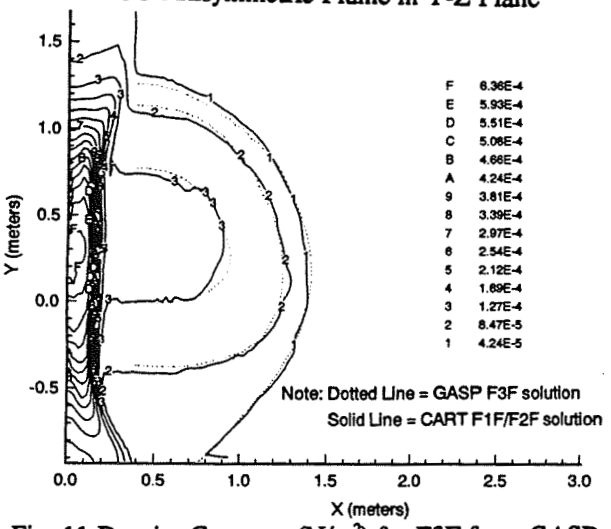

Fig. 11 Density Contours (N/m^2) for F3F from GASP and for F1F/F2F from CART (Z=12.0 m)

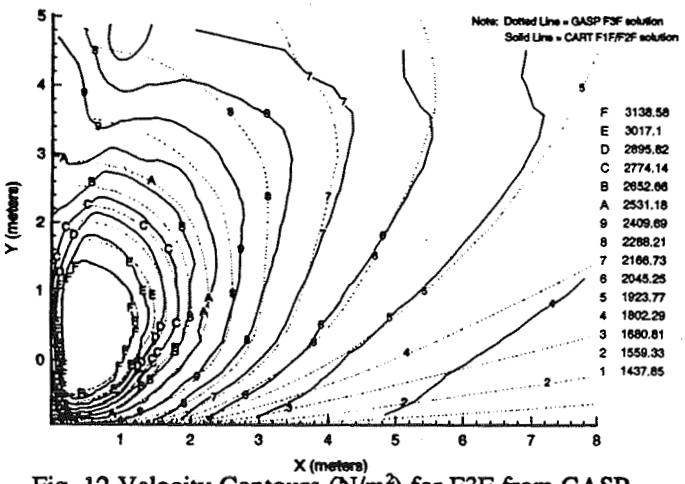

Fig. 12 Velocity Contours (N/m^2) for F3F from GASP and for F1F/F2F from CART (Z=12.0 m)

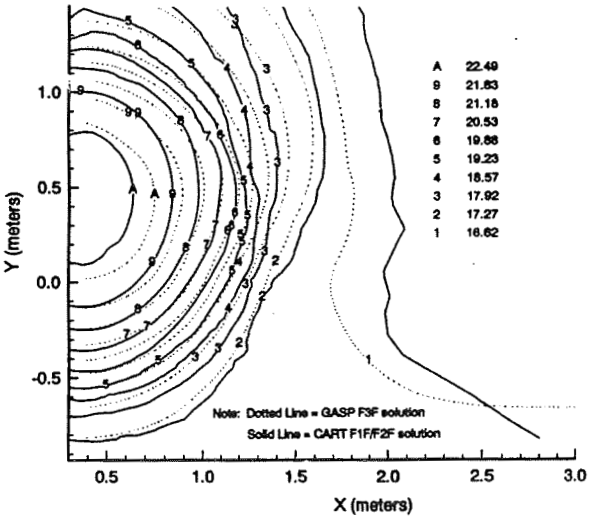

Fig. 13 Molec. Wt. Contours for F3F from GASP and for F1F/F2F from CART (Z=12.0 m)

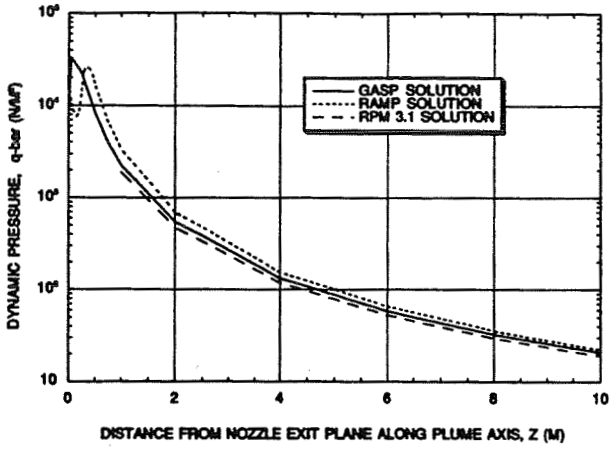

Fig. 14 GASP, RAMP, and RPM F3U Plume Dynamic Pressure vs Z Along Plume Axis

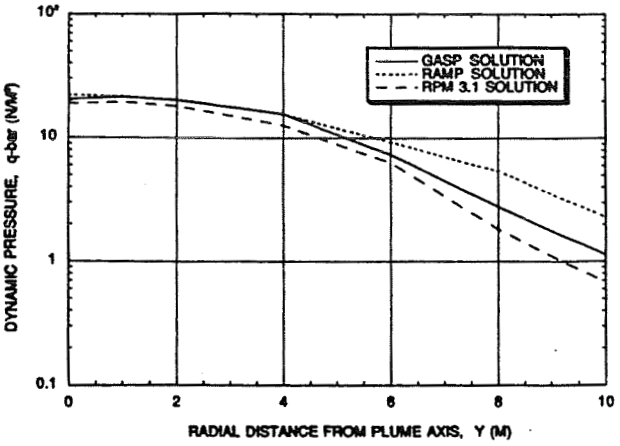

Fig. 15 GASP, RAMP, and RPM F3U Plume Dynamic Pressure vs Y for Z=10 m

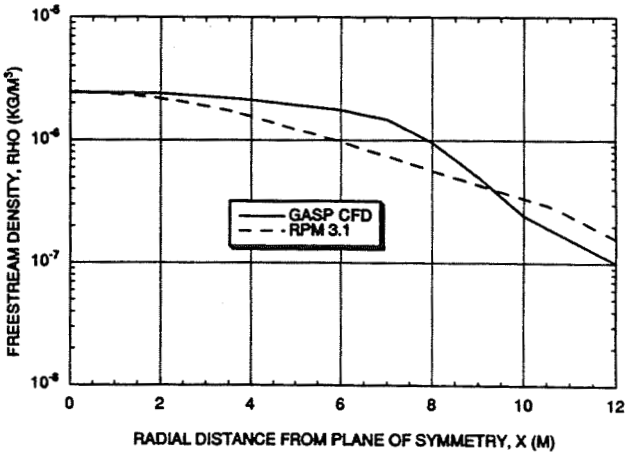

Fig. 16 GASP and RPM F3F Plume Density vs X for Z = 12.5 m and Y=1.0 m

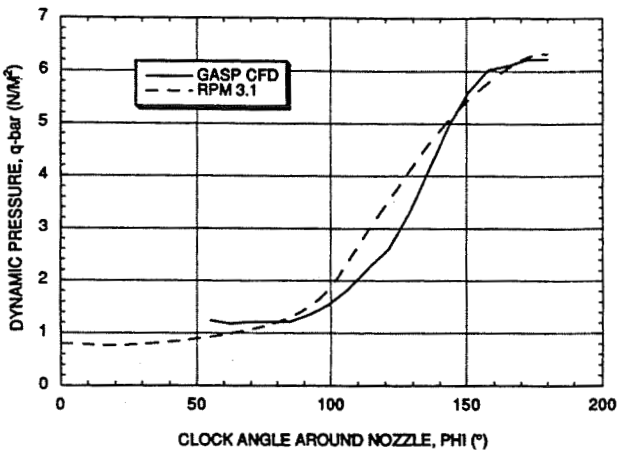

Fig. 17 GASP and RPM F3F Plume Dynamic Pressure vs ϕ at Z=12.5 m and θ=36°

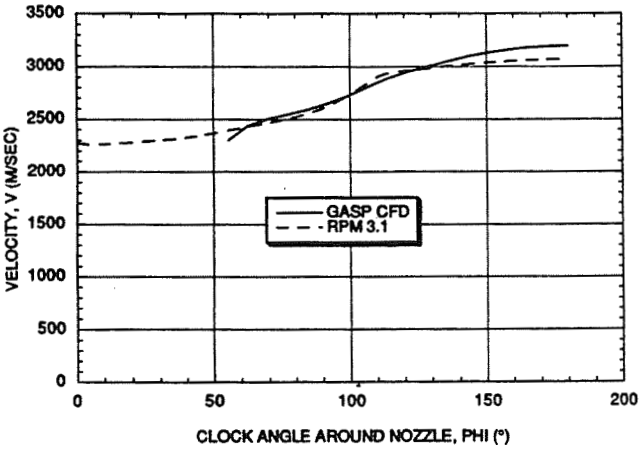

Fig. 18 GASP and RPM F3F Plume Velocity vs ϕ at Z=12.5 m and θ=36°

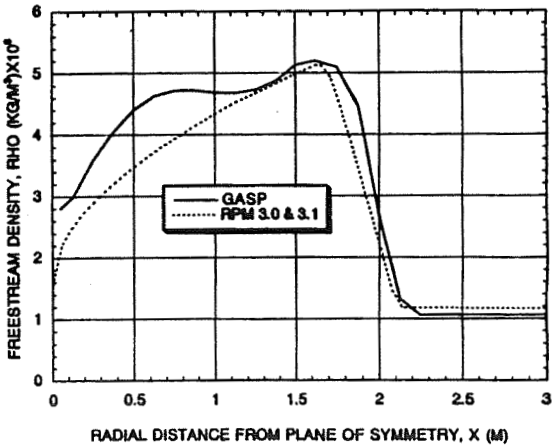

Fig. 19 GASP and RPM DTU Plume Density vs X at Z=18 m

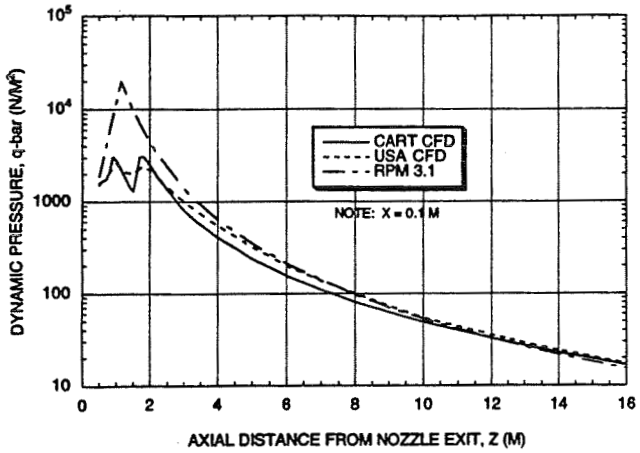

Fig. 20 CART, USA, and RPM F1F/F2F Plume Dynamic Pressure vs Z Along Plume Axis

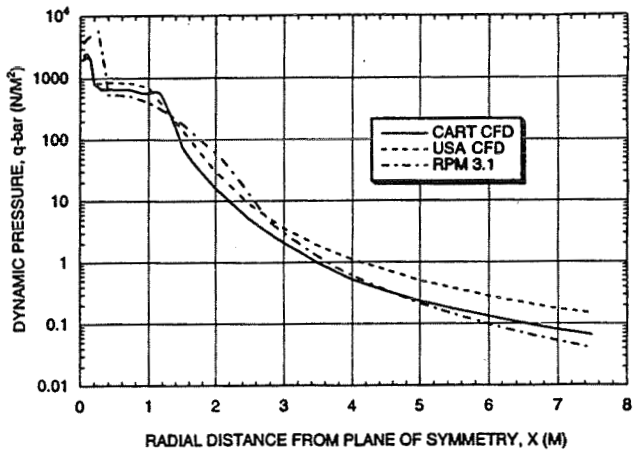

Fig. 21 CART, USA, and RPM F1F/F2F Plume Dynamic Pressure vs X at Z = 2.0 m

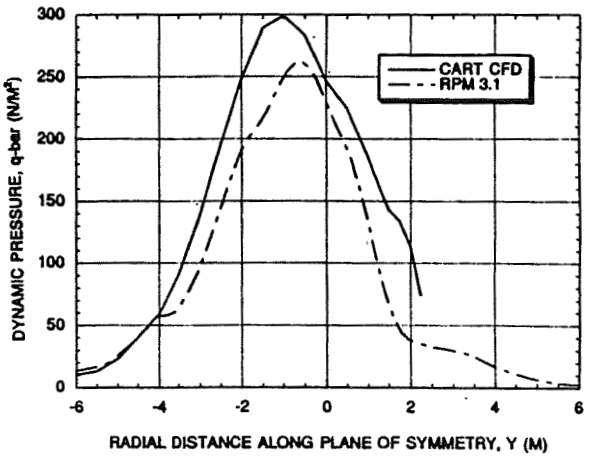

Fig. 22 CART and RPM F1F/F2F Plume Dynamic Pressure vs Y at Z = 5.0 m

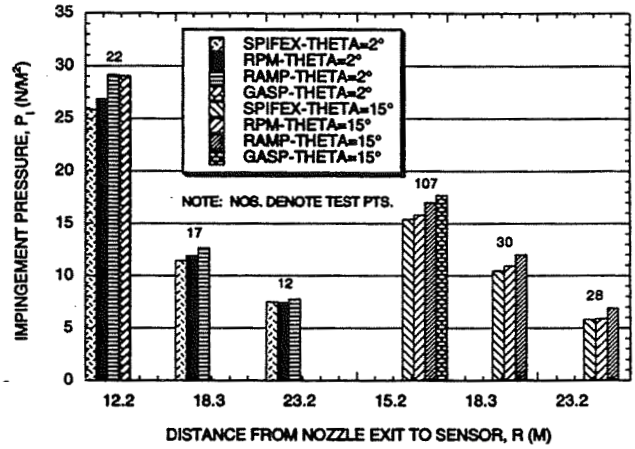

Fig. 23 SPIFEX, RPM, RAMP, and GASP F3U Impingement Pressure vs r for θ = 2° and 15°

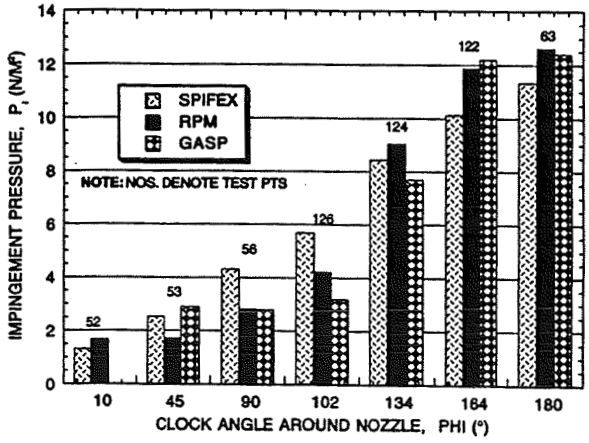

Fig. 24 SPIFEX, RPM, and GASP F1F Impingement Pressure vs ϕ for r=15 m, θ = 36°

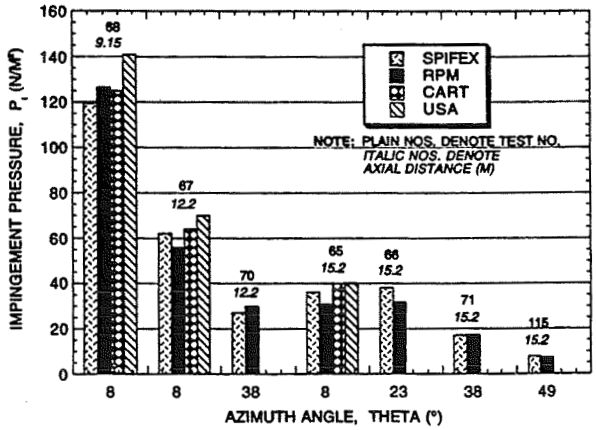

Fig. 25 SPIFEX, RPM, CART, and USA F1F/F2F Plume Impingement Pressure vs θ for r=9.2, 12.2, and 15.2 m

X-34 High Pressure Nitrogen Reaction Control System Design and Analysis

Brian A. Winters, P.E.*
Orbital Sciences Corporation
Dulles, Virginia

Trey Walters, P.E.†
Applied Flow Technology
Woodland Park, Colorado

Abstract

The X-34 program is developing a reusable launch vehicle that will be capable of reaching Mach 8 and 250,000 feet. The X-34 vehicle will carry a 5,000 psia cold gas nitrogen reaction control system that will be used for augmentation of vehicle control at high altitudes and velocities. The nitrogen is regulated to 1,100 psia and directed to 10 thrusters oriented to provide control capability about all three axes. Orbital Sciences Corporation of Dulles, Virginia has the responsibility for design and performance verification of the system as prime contractor for the X-34 program. *Applied Flow Technology's Arrow* compressible network analysis software was evaluated, selected, and purchased for analyzing the reaction control system performance. The software package uses a graphical interface for network model development and includes unique features such as sonic flow calculations with real gas properties that were crucial for performing X-34 system verification. The results of the analysis confirmed the system is properly configured to meet mission objectives. These results will be verified through component and subsystem level testing of the reaction control system.

Introduction

The X-34 program is a joint industry/government project to design, develop, test, and operate a small, fully-reusable vehicle that demonstrates technologies and operating concepts applicable to future Reusable Launch Vehicle (RLV) systems. The X-34 is an air-launched, fully-reusable, liquid-fueled system that draws heavily on hardware and procedures developed for other demonstrated launch systems including space shuttle, DC-X/XA, Pegasus, and Taurus.

RLV technologies embedded in the vehicle include an all-composite primary airframe structure, composite fuel tank, an advanced leading edge thermal protection system (TPS), and autonomous flight control with safe abort capabilities. The X-34 vehicle is carried uprange by Orbital's L-1011 carrier aircraft, can perform missions that reach to Mach 8 and 250,000 feet, land horizontally on a conventional runway, and can quickly be prepared for subsequent flights using aircraft-style turnaround operations. A high operational rate of up to 25 flights per year, with rapid integration and low operating cost per flight is achieved through a simple, maintainable design.

Orbital Sciences Corporation (Orbital) is the prime contractor responsible for the design, development, fabrication, integration, and flight testing of the X-34 test bed demonstration vehicle. This baseline flight test program (BFTP) includes two flights to verify the integration with the carrier aircraft, performance of the vehicle, operation of ground support equipment, and ground crew operations. The vehicle will not reach maximum altitude or velocity performance capability during this phase of the program. The option flight test program (OFTP) will gradually expand these limits on the vehicle until the target design parameters are reached. In addition to expanding the performance envelope of the vehicle, the OFTP will demonstrate the RLV operability of the X-34 through 25 flights in one year and completion of two flights within a 24 hour period. A crucial part of this performance expansion is the ability to maintain control of the vehicle in the near-vacuum of the extreme flight envelope.

Prior to the first flight of X-34, the vehicle and all its subsystems will be rigorously tested to ensure the designs are capable of withstanding the expected flight environments. Tests reaching the component level will verify static/dynamic structural margins, functional performance, electrical/avionic system compatibility, maintainability, and safety. Subsystems will be integrated together for a variety of ground-based testing including vibration, propulsion static fire and cold flow, and captive carry integration.

---

* Senior Mechanical Engineer
† President

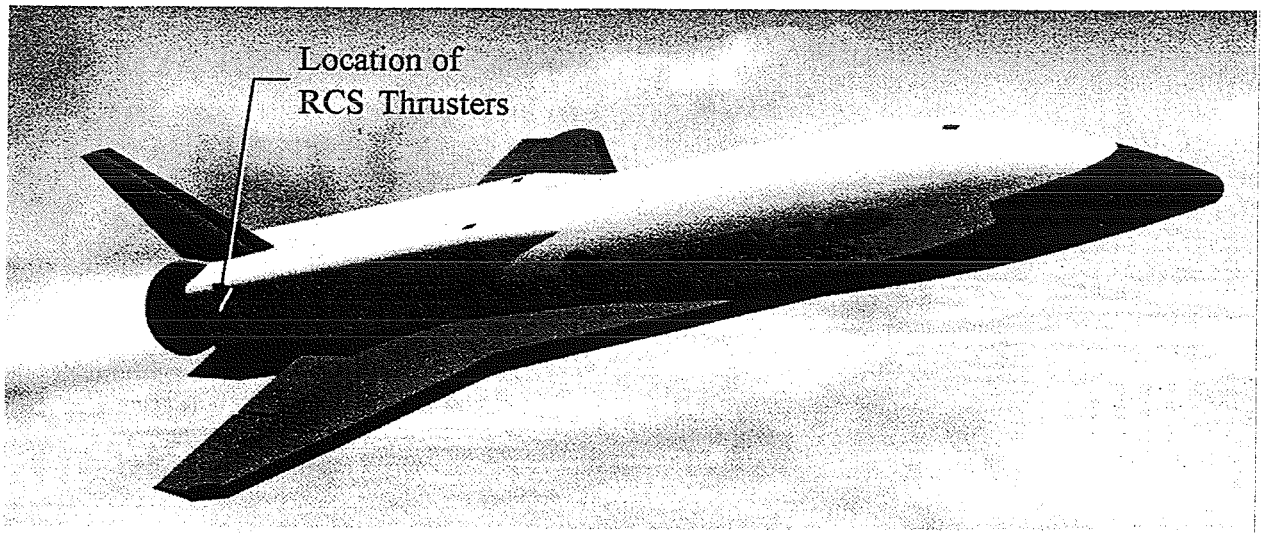

Figure 1 - X-34 Vehicle In Flight

First flight of the vehicle is planned for the fourth quarter of 1998. The X-34 vehicle, shown above in Figure 1, is approximately 58 feet long with a wing span of nearly 28 feet.

Propulsion System Requirements

Propulsion system functions required to support the X-34 program objectives include:

- generating thrust to meet mission velocity and altitude targets,
- controlling vehicle direction/orientation when control surfaces are incapable of providing sufficient response,
- dumping excess propellants to reduce vehicle weight and safe the systems in nominal and abort flights, and
- protecting ground and flight crews through redundancy and operational safeguards.

The X-34 propulsion system is separated into two major subsystems to meet these complex requirements: the main propulsion system (MPS) and reaction control system (RCS).

Main Propulsion System

The purpose of the X-34 MPS is to generate the thrust necessary for the X-34 vehicle to meet mission trajectory requirements. The X-34 MPS features conventional rocket technology, off-the-shelf components, and a low-cost reusable engine based on NASA-MSFC Fastrac technology to provide Mach 8 performance with low development, maintenance, and operations cost. All of the basic propulsion subsystems are simple in design, construction, and require minimal maintenance to meet operability requirements. The propellants used, kerosene (RP-1) as fuel and liquid oxygen (LO2) as oxidizer, are non-toxic to avoid specialized handling procedures. Subsystems are segregated to avoid complexity, maximize safety, and avoid potential interferences. Other published papers discuss the design and development of the MPS in more detail. [1]

Reaction Control System

The RCS is used to provide vehicle directional control during periods of flight during which control surface effectiveness is insufficient to meet commanded maneuvers or respond to atmospheric disturbances. This reduced effectiveness is caused by lower atmospheric density at the high X-34 flight altitudes and "shadowing" of the vehicle vertical tail by the fuselage at high angles of attack during reentry. The RCS installations provide directional control through torque generated by thrusters, fired alone or in various combinations, whose lines of force do not pass through the vehicle center of gravity (CG).

RCS Installation/Design Description

The X-34 mission requirements (operability and maintainability) and available vehicle resources (mass, power, and volume) required a RCS that was simple in design. Details on the system architecture will be

described at a high level in this paper; other papers are available that discuss this subject in more depth.[1]

The X-34 RCS is a cold gas propulsion system that uses nitrogen stored at high pressure (5,000 psia). These systems are not the most efficient in delivering impulse to perform maneuvers. However, they use available ("off-the-shelf") hardware, are easy to maintain, and perform reliably. These aspects, as well as meeting mission performance requirements, best supported the X-34 program objectives leading to the selection of the cold gas nitrogen system.

The RCS is activated prior to release of the X-34 from the L-1011 carrier aircraft. The system performs a variety of self-checks to verify component health and system integrity. The system is placed in a standby mode while the vehicle is released from the L-1011 and propelled, by the MPS, to the required shutdown altitude and velocity. The X-34 continues to climb in the ever-thinning atmosphere until it peaks at maximum altitude. Once the atmospheric density is lower than a pre-determined threshold level, the vehicle controls switch the RCS to an active mode. The RCS thrusters are then used to orient the vehicle until aerodynamic surface effectiveness on the vehicle returns to desirable levels. Once the thrusters are no longer needed, the RCS is transitioned to a purge mode. In this mode, opposing thrusters are opened to reduce system pressure without generating a resulting torque on the vehicle. This process allows for the safe approach by the ground crew once the vehicle has landed and come to rest. The thrusters are closed and the system is placed in a shutdown mode once the remaining propellant has been removed from the system.

A simplified schematic of the system is shown in Figure 2. The layout of the system follows the classic arrangement for a cold gas propulsion system. The major components of the system shown include the propellant (high pressure, gaseous nitrogen), pressure regulator, control valves, and thruster nozzles. The isolation valve is used to retain the propellant in the tanks prior to the standby mode. This valve is opened to allow the propellant to flow to the rest of the system.

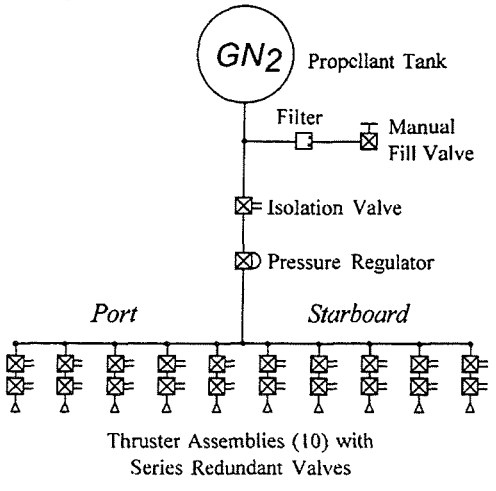

Figure 2 - Simplified RCS Schematic

The primary RCS design challenge was the packaging of the components in the vehicle. Space was severly limited and occupied primarily by the MPS installation. The thrusters are mounted as separate assemblies, one on the port side and one on the starboard side, on the vehicle side panels. This integral assembly allows the panels and thrusters to be removed in one operation to permit access to internal vehicle components quickly and easily. The RCS thruster panel assembly can also be tested as a separate dedicated unit as required.

A drawing of this installation concept is shown in Figure 3. This isometric view shows both RCS panels in the installed configuration without vehicle structure or TPS included. Nitrogen propellant arrives at the panels through tubing from the propellant tanks located in the front of the vehicle.

RCS Analysis

An analysis is required to verify the RCS will deliver the expected force from each thruster during operation. The vehicle control system will be programmed to expect constant thrust from the RCS, within some tolerance. Variations in thrust can be accommodated but must be know a priori. Since there is no combustion involved, the analysis can be performed as the study of a compressible flow network. A variety of aspects makes this analytical effort particularly challenging.

Analytical Challenges

Four aspects of this study make this analysis unique; compressible flow with multiple choked orifices, real gas effects, heat transfer, and multiple firing combinations. Undoubtedly, the flow will choke at the throats of the nozzles with the high system pressure directed to the low (near-vacuum) environment. Assumptions of ideal gas will no longer hold true at the high system pressures (up to 5,000 psia) and low temperatures (below 0°F). Rapid changes in pressure through the regulator and long runs of tubing allow significant heat transfer which also must be

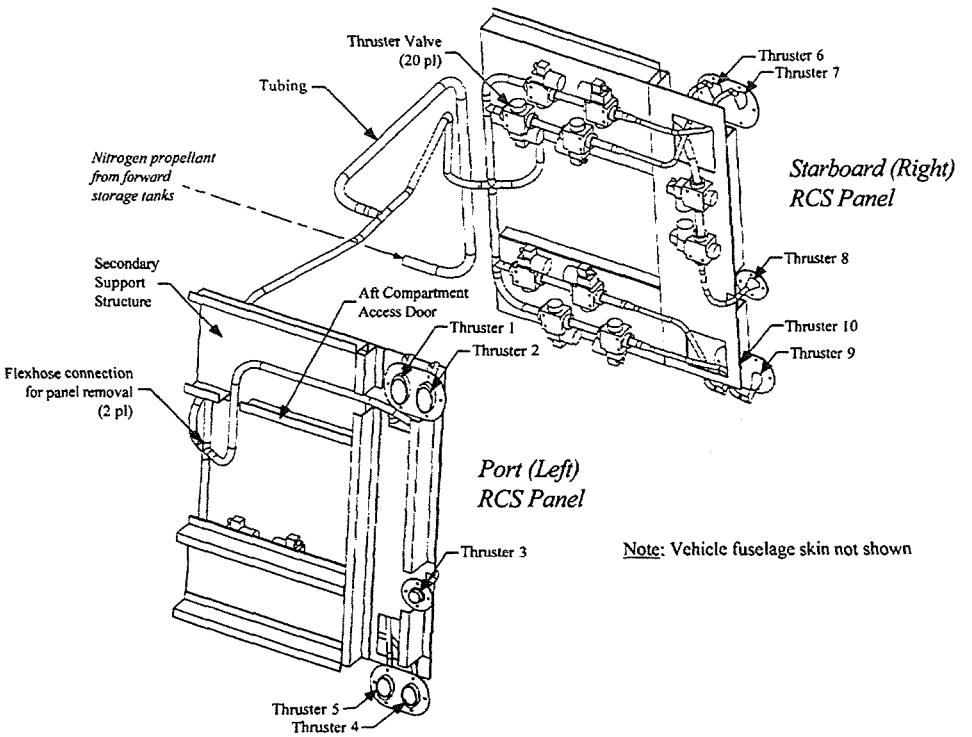

Figure 3 - Aft RCS Installation

considered. Finally, the installation of ten thrusters can also be fired in many different combinations, complicating the configurations of networks that must be analyzed. Each of these aspects will be discussed in detail.

Compressible Flow

The flow of gases in piping systems involves complexities not shared by flowing liquids. The changing density along a constant diameter pipe results in a changing velocity because of mass balance requirements. Further, the density is directly coupled to the gas temperature through an equation of state. The gas temperature thus changes along the pipe, even for a perfectly insulated pipe.

Another distinct phenomenon in compressible flow is that of sonic velocity. The sonic velocity is the maximum macroscopic "communication time" between gas molecules. The gas velocity cannot exceed the sonic velocity, thus flow discontinuities (i.e., shock waves) can occur in the piping system when pressure and/or flow requirements cannot be supplied at subsonic velocities. This results in "sonic" choking, which means alterations in boundary conditions downstream of a shock wave cannot change the flow rate in the pipe. The X-34 nitrogen RCS will experience such conditions, and a proper analyses must take into consideration these issues.

Heat Transfer

The thermal environment of a gas piping system is of importance because the gas temperature is linked to density and pressure by an equation of state. In addition, when gas delivery temperatures are important, as they are at the X-34 RCS thrusters, the thermal environment must be properly modeled or inaccurate thruster predictions will be obtained. To provide the needed accuracy, a complete energy balance must be performed for each pipe computing section, as well as all diverging or converging branch sections.

Real Gas Properties

The most basic relationship between gas pressure, density and temperature is through the ideal gas equation. A number of analytical simplifications result when a gas can be considered ideal. Further, the gas enthalpy is an important parameter, and the relationship of enthalpy to temperature can take on several forms. Again, the most basic is that the enthalpy change is directly proportional to temperature change (the proportionality constant being the specific heat at constant pressure). When combined with the ideal gas assumption, this is sometimes referred to as a perfect

gas. In reality, the enthalpy is dependent on both temperature and pressure.

The X-34 nitrogen propellant will be stored at pressures up to 5,000 psia. The ideal gas model breaks down at such high pressure conditions. For example, at 70° F, nitrogen departs from the ideal gas law by 16%. In addition, with pressure dropping from 5,000 psi to vacuum conditions through the thrusters, the perfect gas law for enthalpy also does not apply. A real gas model must be used for the nitrogen to properly predict the fluid dynamics and thermodynamics of the X-34 RCS system.

Thruster Firing Combinations

The ten thrusters installed in the vehicle could conceivably be fired in 100 (10^2) different combinations. Obviously, some of these combinations do not make sense from the standpoint of orienting the vehicle. Firing opposing yaw thrusters is effective in reducing propellant load. It does not, however, provide a net torque on the vehicle and is not an effective means to control the vehicle. Each of the 100 firing combinations was examined to identify the primary thrusting modes. These modes are the combination of thrusters that are fired to achieve a specified response from the vehicle. These responses include pure roll, pitch, and yaw maneuvers. The specific cases chosen for study will be described shortly.

Equation Derivation

The first three unique aspects of this analysis are handled by representing them through governing physical mathematical expressions. Unknowns in these expressions are solved for the various firing combinations (the last unique aspect) through different computational techniques. First, the governing equations will be derived.

Compressible Flow

There are five governing equations that apply to a gas flowing in a constant area pipe:

Mass:

$$\frac{d\rho}{\rho}+\frac{dV}{V}=0 \tag{1}$$

Momentum:

$$dP+\frac{1}{2}\rho V^2\frac{f}{D}dx+\rho V dV=0 \tag{2}$$

Energy:

$$\dot{m}\,d\left(h+\frac{1}{2}V^2\right)=q \tag{3}$$

Equation of State:

$$P=Z\rho RT \tag{4}$$

and Mach Number:

$$M=\frac{V}{\sqrt{\gamma ZRT}} \tag{5}$$

Among the five equations there are five unknowns: P, T, ρ, V, and M. Other parameters such as Z, $\dot{m}$, f, Z, h and γ are functions of the five unknowns. The heat rate, q, is a boundary condition supplied from other calculations.

Basing the equations on a constant area pipe helps to simplify the equations. However, area changes are possible from pipe to pipe, and also at branching sections. It is therefore helpful to work with stagnation conditions, which combine the thermodynamic and fluid dynamic effects into single entities.

Perhaps the best starting point for discussing stagnation properties is enthalpy. If the energy state changes due to elevation changes are small (as they usually are for gas systems), a statement of the First Law of thermodynamics is

$$h_1+\frac{V_1^2}{2}+\frac{q}{\dot{m}}=h_2+\frac{V_2^2}{2}$$

The stagnation enthalpy is thus defined as,

$$h_o=h+\frac{V^2}{2}$$

It can then be said that in the absence of heat transfer (i.e., $q = 0$), the stagnation enthalpy in a pipe is constant.

Following from this definition is that of the classic definition of stagnation temperature,

$$T_o = T\left(1+\frac{\gamma-1}{2}M^2\right)$$

which can be shown to be valid for real gases as well. Definitions of stagnation pressure and density follow similarly.

By combining these definitions with the governing equations (Eqns. 1-5), the following equation can be obtained:

$$\frac{dP_o}{P_o} = -\frac{\gamma M^2}{2}\left(\frac{fdx}{D}+\frac{dT_o}{T_o}+\frac{dZ}{Z}+\frac{d\gamma}{\gamma}\right) \quad (6)$$

which, after integration, becomes

$$P_{o,2} = P_{o,1}\exp\left[-\frac{\gamma\overline{M}^2}{2}\left(\frac{f}{D}(x_2-x_1)+\ln\frac{T_{o,2}}{T_{o,1}}+\ln\frac{Z_2}{Z_1}+\ln\frac{\gamma_2}{\gamma_1}\right)\right] \quad (7)$$

where the bar over the parameters represents the average over the computing section. This method takes a fixed length step x_2 - x_1, and marches down each pipe. The nature of the change in stagnation temperature is related to heat transfer, to be discussed in the next section.

Another form of the preceding equation (Eqn. 6) is as follows,

$$\frac{dM^2}{M^2} = F_{To}\frac{dT_o}{T_o}+F_f\frac{fdx}{D}+F_{To}\frac{dZ}{Z}+F_{To}\frac{d\gamma}{\gamma} \quad (8)$$

where

$$F_{To} = \frac{\left(1+\gamma M^2\right)\left(1+\frac{\gamma-1}{2}M^2\right)}{1-M^2}$$

$$F_f = \frac{\gamma M^2\left(1+\frac{\gamma-1}{2}M^2\right)}{1-M^2}$$

Integrating the Eqn. 8 yields

$$x_2 = x_1 + \frac{\ln\frac{M_2^2}{M_1^2} - \overline{F}_{To}\ln\frac{T_{o,2}}{T_{o,1}} - \overline{F}_{To}\ln\frac{Z_2}{Z_1} - \overline{F}_{To}\ln\frac{\gamma_2}{\gamma_1}}{\overline{F}_f\frac{f}{D}} \quad (9)$$

In this method the length step is variable, depending on the velocity.

When a branching section is encountered, the mass and energy must balance. The following equations must therefore be satisfied at all branching sections:

Balance Mass at Branches

$$\sum_{j=1}^{n}\dot{m}_{ij} = 0 \quad (10)$$

Balance Energy at Branches

$$\sum_{j=1}^{n}\dot{m}_{ij}\left(h_{ij}+\frac{1}{2}V_{ij}^2\right) = 0 \quad (11)$$

Heat Transfer

The stagnation enthalpy changes because of heat transfer. However, convective heat transfer is dependent on the gas stagnation *temperature*, not enthalpy. The amount of stagnation temperature change is calculated as follows:

$$\frac{T_\infty - T_{o,2}}{T_\infty - T_{o,1}} = e^{-\left(\frac{P_h L}{\dot{m}c_p}U\right)}$$

where states 1 and 2 are the inlet and exit of the computing section, respectively. During iteration towards a converged solution, the mass flow rate is that which exists at the current solution state. Once the solution is converged, the correct mass flow rate will have been used.

Real Gas Properties

The real gas effects come into play in a couple ways. First, Eqns. 6 and 8 have terms which describe the change in compressibility factor, Z, over the computing section. There are also terms for change in γ, the specific heat ratio. The compressibility factor is calculated from one of two equation of state models.

These models employ the gas critical pressure and critical temperature to obtain density. Similar methods are used to obtain enthalpy from temperature and pressure data.

Computational Methods

To solve each pipe, the governing equations are iteratively solved over each computing section. The conditions at location 1 are all known. One parameter must be known at location 2, the target location. With the fixed length step method, Eqn. 7, the distance is known. This allows solution of the energy equation to obtain the stagnation enthalpy, which becomes the known parameter. At this point, the static enthalpy is calculated based on a velocity guess, and density can be obtained from the continuity equation. With density and enthalpy determined, static pressure and temperature are obtained from equation of state. These parameters are iterated upon until they converge over the computing section, then the converged parameters are used as the input to the next computing section.

Alternatively, using Eqn. 9 as the solution basis, the distance is not known, but the Mach number is known at location 2. Similar to the previous iterative method, the relevant fluid dynamic and thermodynamic parameters are iterated upon until convergence.

Each of the previous two methods relate the propagation of the solution down each pipe. If a pipe connects to another pipe, then the conditions at the exit of the upstream pipe are propagated to the inlet of the downstream pipe, taking into account any pressure losses (or increases, if a compressor) at the junction that connects the two pipes. Thermal changes may also exist such as a heat exchanger.

If a branch is the connector, then the mixing stagnation enthalpy is obtained for all pipes flowing into the branch based on Eqn. 11. This stagnation enthalpy is used as the inlet stagnation enthalpy for all pipes flowing out of the branch.

The previous methods all function as described until sonic choking occurs. After iteration, the Mach number is known at all computing sections, so that a check for sonic choking can be made. For example, in a particular pipe without flow restrictions, sonic choking can only occur at the pipe endpoint. If during iteration at the current mass flow rate the Mach number reaches sonic inside the pipe, then the solution method enters into a special iteration loop where the flow rate is lowered until sonic choking occurs right at the end point.

If sonic choking occurs because there is a flow restriction at the end of the pipe, then a similar special iteration loop is employed to determine the mass flow rate through the pipe and restriction based on the conditions at the restriction. This flow rate must also be iterated downward until sonic conditions are matched. Such a solution method requires extensive iteration, but also provides accurate and detailed solutions of a compressible flow system.

Software Implementation

Applied Flow Technology (AFT) has incorporated the described solution methodology into a commercial Microsoft Windows software product called *AFT Arrow*. All modeling with *AFT Arrow* is performed with drag-and-drop operations, which offers the side benefits of a short learning curve, rapid model setup, and straightforward verification of pipe and nodal connectivity.

AFT Arrow has been commercially available for two years. It has been successfully used on wide variety of gas system analyses including steam, natural gas, air, and high pressure nitrogen, oxygen, hydrogen and helium. Besides aerospace applications, *AFT Arrow* has been used heavily by engineers in power generation, gas transmission, and chemical and petrochemical processing. While the *Arrow* software product has been used to confirm the performance of the X-34 RCS design, *AFT* is not a direct participating member of the X-34 design team.

Model Description

The model of the X-34 nitrogen RCS was built using *AFT Arrow* is shown in Figure 4. Component data required for the model included information to represent the pressure loss and the geometry. Pressure loss data can be represented in a variety of formats including (but not limited to) K factors, discharge/flow coefficients, polynomial expressions, and lookup in built-in component databases.

The geometry of the component included the minimum flow area. This minimum flow area is required to calculate the sonic choking of the flow through the component. The geometry is represented by an equivalent orifice area with an associated discharge coefficient.

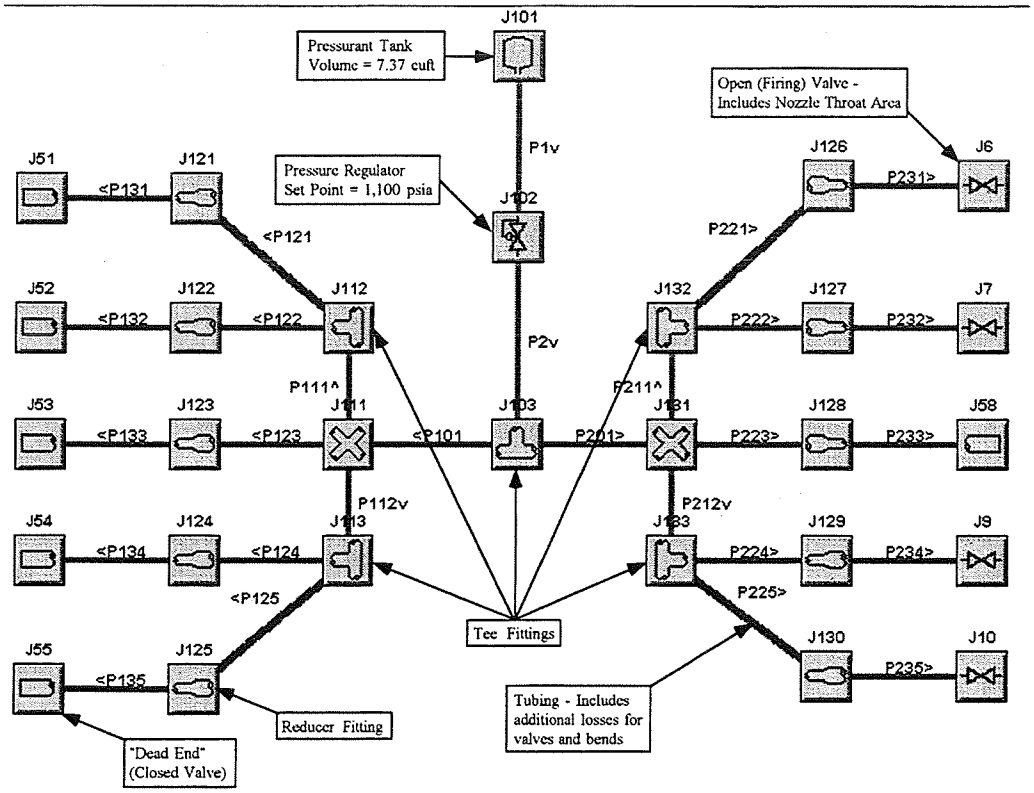

Figure 4 - X-34 RCS Arrow Model

The boundary conditions for the model included the definition of the propellant in the storage and the thrusters to be used in a particular case. The propellant storage was represented as a tank component at a specified pressure and temperature. The thrusters were represented by a valve component including the throat geometry of the nozzle.

Cases Examined

The cases to be studied were limited to the primary combinations of thrusters that would yield pure roll, pitch, or yaw maneuvers. This reduced the number of combinations from 100 to 34. In practice, the X-34 control system will fire thrusters in various coupled combinations as required. Disturbing moments will not be applied as ideal, single axis events. It is assumed the study of these 34 combinations will provide sufficient insight into the system. With this data, confidence will be gained to qualitatively assess the performance of the system under those conditions. The cases that were studied are shown in Table 1. Thruster numbers referenced in this table are defined in Figure 3.

For each of these firing combinations, two tank pressure/temperature conditions were examined. The first case represents the initial firing condition predicted in the tanks. The propellant is loaded on the ground to 5,000 psia and is chilled while the X-34 is carried to launch altitude. As the temperature in the tank drops, the pressure is reduced isochorically. The amount of pressure/temperature drop experienced in the tanks depends on the length of captive carry, atmospheric temperature conditions (hot or cold day), heat transfer characteristics of the hardware, and mass of propellant loaded. This case is represented by setting the pressure in the tanks to 4,000 psia and 460 R.

The second case depicts the propellant tanks at a reduced load later in flight. Pressure in the tanks is assumed to be 2,000 psia and the temperature has dropped as a result of expansion of the gas. As before, the assumed temperature is affected by the same influences noted in the first case. The temperature is assumed at 420 R.

Results

The 68 different conditions examined in this analysis provided each thruster different conditions to be simulated. Pressure and mass flow data were compiled for each thruster, pressure/temperature, and

Table 1 - Cases Studied

Case	Description	Thrusters Fired									
		1	2	3	4	5	6	7	8	9	10
1	Pos. Roll 1	X									X
2	Pos. Roll 2	X								X	
3	Pos. Roll 3		X								X
4	Pos. Roll 4		X							X	
5	Pos. Roll 5	X	X							X	X
6	Neg. Roll 1					X	X				
7	Neg. Roll 2					X		X			
8	Neg. Roll 3				X		X				
9	Neg. Roll 4				X			X			
10	Neg. Roll 5				X	X	X	X			
11	Pos. Pitch 1					X					X
12	Pos. Pitch 2					X				X	
13	Pos. Pitch 3				X						X
14	Pos. Pitch 4				X					X	
15	Pos. Pitch 5				X	X				X	X
16	Neg. Pitch 1	X					X				
17	Neg. Pitch 2	X						X			
18	Neg. Pitch 3		X				X				
19	Neg. Pitch 4		X					X			
20	Neg. Pitch 5	X	X				X	X			
21	Pos. Yaw 1			X							
22	Pos. Yaw 2	X				X					
23	Pos. Yaw 3	X			X						
24	Pos. Yaw 4		X			X					
25	Pos. Yaw 5		X		X						
26	Pos. Yaw 6	X	X		X	X					
27	Pos. Yaw 7	X	X	X	X	X					
28	Neg. Yaw 1								X		
29	Neg. Yaw 2						X				X
30	Neg. Yaw 3						X			X	
31	Neg. Yaw 4							X			X
32	Neg. Yaw 5							X		X	
33	Neg. Yaw 6						X	X		X	X
34	Neg. Yaw 7						X	X	X	X	X

firing combination. Mass flow was considered the primary parameter to examine since this is used in measuring the efficiency of the thruster. The efficiency is measured through the specific impulse, or ratio of thrust to mass flow as shown in the equation below. For a given design, this efficiency is relatively constant.

$$I_{sp} = \frac{F}{\dot{m}}$$

This relationship shows the thrust from the RCS is directly proportional to the mass flow into the nozzle.

Table 2 - Summary of Thruster Performance

Thruster	Mass Flow (lbm/sec)		
	Minimum	Maximum	Average
1	0.755	0.972	0.901
2	0.756	0.975	0.903
3	0.764	1.003	0.881
4	0.756	0.975	0.903
5	0.755	0.972	0.901
6	0.755	0.972	0.901
7	0.756	0.975	0.903
8	0.764	1.003	0.881
9	0.756	0.975	0.903
10	0.755	0.972	0.901

This information is readily available from the *Arrow* model. A summary of the thruster mass flow results is shown in Table 2. The data shown includes minimum, maximum, and average mass flow for the various firing combinations and propellant tank conditions.

These data show the system is capable of delivering the target mass flow of 0.92 lbm/sec. Examination of the detailed results indicates the primary factor influencing the mass flow for the system is the number of thrusters firing. This result is not surprising - the increased mass flow through the system drives up the pressure drop to the nozzles, reducing propellant density. The system delivers propellant at a mass flow within +9% and -18% of rated flow. The large difference seen for the reduced flow is for cases where 5 thrusters are firing simultaneously in yaw, an unlikely event.

The effect of different initial conditions is driven primarily by the temperature difference. The system is regulated to a set pressure upstream of the thruster nozzles. The density increase, nearly inversely proportional to the change in propellant storage temperature, causes the higher mass flow. If greater fidelity in thrust control is required, heaters can be added at various points in the system to reduce mass flow variations as propellant is depleted.

Verification

It is important in any computer-based analysis to confirm and verify the results. The first step in the process is simply to perform a reasonableness test on the numbers; do they make sense? If so, simplifications or non-complex cases can be examined and results estimated with hand calculations.

In the case of X-34 RCS, hand calculations were used to initially size most of the system components. Particularly, initial assumptions made in the conditions of the fluid at the thruster nozzle inlets were used to size the throats. This throat geometry was combined with a typical discharge coefficient for a conical nozzle (0.95) to determine the choking characteristics of the component. The mass flow at the nozzles is determined from the inlet conditions and the size of the throat. First estimates at the mass flow based on the desired thrust level (60 lbf.) and known performance of cold gas nitrogen systems (actual 65 lbf-sec/lbm) suggested a target mass flow of approximately 0.92 lbm/sec. The *Arrow* model confirmed the sizing of the throat for this flow rate as shown previously in the results.

The best confirmation of these analysis results is through operation of the system under flight conditions. These flight conditions can be simulated on the ground through component and subsystem (assembly) level testing. Reproducing flight conditions, particularly for a vehicle with high performance capability such as X-34, is difficult.

Component tests are being performed by the component suppliers as part of the qualification programs. Most of the procurements include flow tests that represent extreme flight conditions. The suppliers will test their components under these flight-like conditions and report the results to Orbital. This information will be used to refine the component data included in the *Arrow* model and update the performance analysis.

Subsystem level tests are also being planned to verify the performance of the integrated system. The current plan calls for one thruster panel assembly to be mounted in a vacuum chamber. Facility services would provide the nitrogen at conditions similar to flight operations. The performance of the thrusters will be measured and compared with results from the compressible flow model. The model will be updated to reflect the test data and rerun to generate predictions of upcoming flight trajectories. The model will continue to be used to investigate discrepancies in flight data from predicted performance.

Conclusions

The X-34 RCS is a vital system in a reusable vehicle that demonstrates high speed and altitude operation. The compressible network flow analysis performed using *AFT Arrow* confirmed system performance predicted through design efforts and hand calculations. The model also provided insight on the effect of various parameters such as tank temperature to make informed decisions on design trades. These results will continue to be verified and improved with continuing component and subsystem testing through model refinement. The ultimate validation of the system performance analysis will happen through the utilization of the X-34 RCS while successfully expanding the vehicle flight envelope.

Nomenclature

a	Sonic speed
A	Cross-sectional flow area of a pipe
c_p	Specific heat
D	Diameter of a pipe
f	Friction factor
F	Thrust
F_{To}	Parameter in Equation 9
F_f	Parameter in Equation 9
h	Enthalpy, static
h_o	Enthalpy, stagnation
I_{sp}	Specific impulse
L	Length of a pipe
$\dot{m}$	Mass flow rate
M	Mach Number
P	Pressure
P_h	Heated perimeter
P_o	Pressure, stagnation
R	Gas constant
T	Temperature, static
T_o	Temperature, stagnation
T_∞	Temperature, ambient
U	Overall heat transfer coefficient
V	Velocity
x	Length
Z	Compressibility factor
γ	Specific heat ratio
ρ	Density

Subscripts

1	Location 1 in pipe
2	Location 2 in pipe
i	Junction at which solution is sought
j	Junctions with pipes connecting to junction i

Acronyms

AFT	Applied Flow Technology
BFTP	Baseline flight test program
CG	Center of gravity
GN2	Gaseous nitrogen
LO2	Liquid oxygen
MSFC	Marshall Space Flight Center
NASA	National Aeronautics and Space Administration
OFTP	Optional flight test program
OML	Outer mold line
RLV	Reusable launch vehicle
RP-1	Rocket propellant (kerosene)
TPS	Thermal protection system

References

[1] Sgarlata, P., and Winters, B., "X-34 Propulsion System Design," AIAA-97-3304, Seattle, Washington, July 1997

THE EFFECT OF CATALYCITY ON THE HEATING OF THE X-38 SHAPE

S. Brück, W. Kordulla
DLR - Institut für Strömungsmechanik, Bunsenstr. 10, D-37073 Göttingen, Germany
T. Eggers, M. Orlowski, J.M.A. Longo
DLR - Institut für Entwurfsaerodynamik, Lilienthalplatz 7, D-38108 Braunschweig, Germany

Abstract: **The flow past the X-38 vehicle is numerically investigated for the trajectory point at 73 km altitude. At this regime the total temperature and the present length scale allow dissociation and vibrational excitation of the molecules in the air mixture. The equilibrium assumption of these processes is sometimes sufficient for aerodynamic purposes. The heating prediction of this simplified model produces an upper limit of the possible heat loads. The results of nonequilibrium flow simulation point out the influence of catalycity on the heating of the X-38 shape. A significant reduction of the surface heating is found for the finite catalytic behavior in comparison to that one of a fully catalytic wall.**

Nomenclature

c_p	pressure coefficient
L_{ref}	reference length (X-38: $1.19 \cdot 276\,inch$)
M_∞	freestream Mach number
$\dot{q}$	heat flux $[W/m^2]$
T_∞	freestream temperature $[K]$
T_{wall}	wall temperature $[K]$
Sc	Schmidt number
St	Stanton number
Z	altitude $[km]$
α	angle of attack $[^\circ]$
δ_{bf}	flap-deflection angle $[^\circ]$
ε	emission factor (0.85)
ρ_∞	freestream density $[kg/m^3]$
σ	Stefan-Boltzmann constant ($\sigma = 5.67 \cdot 10^{-8} W m^{-2} K^{-4}$)

Introduction

After the end of the european HERMES research programme the activities funded by ESA have been concentrated on the investigation of capsule type vehicles such as ARD "Aerothermal Reentry Demonstrator" and CTV "Crew Transport Vehicle". Since the middle of the year 1996 a limited effort has been focused on the study of a small reuseable space vehicle (X-24) originally designed in the US in the late sixties. This configuration is suggested with some modification as a rescue vehicle (CRV "Crew Rescue Vehicle") of the future space station. In a first attempt NASA/Houston and ESA collaborate in the design of an experimental vehicle X-38 derived from the X-24 shape (see Loomis et al.[1] and Chalot et al.[2]). A reentry flight experiment will be performed by releasing from the Shuttle payload bay and returning seperatly to the ground. Later on, it is planned to use the shape as well as for an experimental crew transport vehicle launched on top of ARIANE V. Fig. 1 shows the configurations suggested by ESA as possible crew transport vehicles.

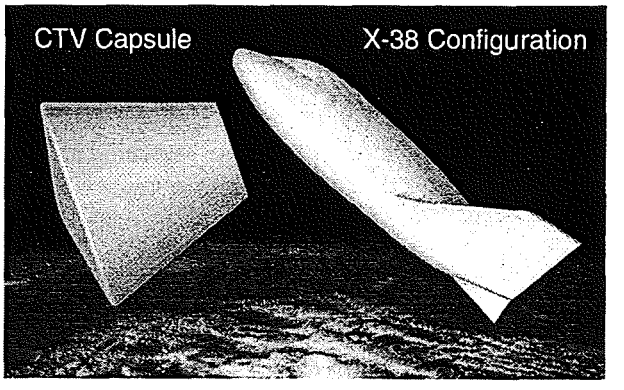

Fig. 1 CTV Capsule and X-38 Winged Reentry Vehicle.

At DLR, in a first numerical study the original X-24 shape has been investigated by Longo et al.[3] with respect to grid sensitivity and accuracy of aerodynamic and thermodynamic properties. Further investigations have been carried out to build up aerodynamic and aeroheating databases (see Brück et al.[4]). These work were done within a frame work of industrial partners and european research institutions.

In the following, the critical issue of surface heating is discussed with respect to the influence of flap deflection and wall catalysis effects. Therefore, different equilibrium and nonequilibrium simulations are performed to investigate the influence of catalycity on the heating of the X-38 shape. Beside the two extreme behaviors of a fully and a noncatalytic wall a detailed formulation of the recombination process along the surface are applied taking into account the material depending properties of the TPS material. In a first attempt the surface material was assumed to be the original Space-Shuttle TPS material RCG (Reaction Cured Glass).

Numerical Method

Flow Solver

The numerical method CEVCATS for the solution of the 3D Navier-Stokes equations for reacting flows is briefly described here (see Kroll et al.[5] and Brück et al.[6]). In order to stabilize the numerical scheme the chemical and thermodynamic source terms are treated point-implicitly. The solution is advanced in time by means of a five-stage Runge-Kutta scheme. Several acceleration techniques are used such as local time stepping, implicit residual averaging and full multigrid (see Radespiel et al.[7]).

The spatial discretization is done by means of a finite volume scheme which is implemented with the flow variables stored at the vertices of the cells. The residual is obtained by collecting the fluxes through the cell faces of a hexahedral control volume. The numerical scheme consists of a hybrid upstream flux vector splitting. In regions of strong flow expansions and/or strong shock waves van Leer's scheme is used, while for smooth flow regions, e.g. boundary layers, the AUSM scheme according to Liou and Steffen[8] is employed. Furthermore, a second order MUSCL extrapolation is applied to improve the capturing of strong shocks and contact discontinuities. The viscous terms are discretized centrally and the thin-layer approximation is introduced.

Physical Modelling

Chemistry and Thermodynamic State

The thermochemical model for air consists of five species, N_2, O_2, NO, N, O, which are assumed to behave as a mixture of perfect gases. It is assumed that the translational and rotational degrees of freedom are in equilibrium. The assumption of a harmonic oscillator is employed to calculate the energy of the internal degrees of freedom and for the present investigations the equilibrium formula is applied. The increase or decrease of the species' concentrations due to chemical reactions is given by the chemical source terms using the reaction rates of Park.[9]

Viscous Effects

The viscous effects such as shear stress, heat flux and diffusion are calculated according to the assumptions of Stokes, Fourier and Fick, respectively (see Hirschfelder et al.[10]). The species viscosities are calculated with the curve fits of Blottner et al.[11] and combined for the evaluation of the mixture viscosity by the rule of Wilke.[12] The Eucken correction is applied to evaluate the conductivities, and a constant Schmidt number $Sc = 0.84$ is assumed to calculate the diffusion coefficients.

Catalycity

The finite catalytic wall is covered with a single sort of chemically active sites S which are able to adsorb gas-phase particles. Two elementary surface reactions are considered. The first is the adsorption-desorption reaction of $N-$ or $O-$atoms which can be expressed as

$$AS \rightleftharpoons A + S \qquad (1)$$

where A stands for N or O (see Fig. 2). The adsorption of diatomic air species is unlikely and can be neglected.

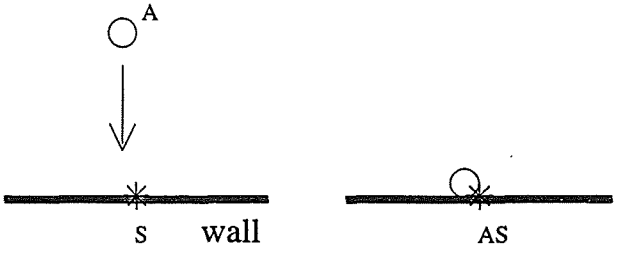

Fig. 2 Adsortion-desorption reaction (picture taken from Bergemann[13]).

The second surface reaction taken into account is the recombination-dissociation reaction according to the Eley-Rideal mechanism which can be written as

$$AB + S \rightleftharpoons AS + B. \qquad (2)$$

It describes the reaction of free atom B which extracts an adsorbed atom A out of the surface and recombine to the molecule AB (see Fig. 3). In the reverse reaction a molecule AB dissociates on the surface. The kinetics

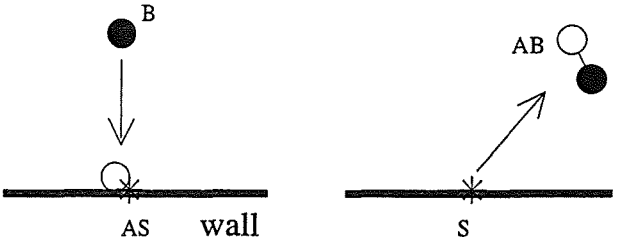

Fig. 3 Eley-Rideal mechanism (picture taken from Bergemann[13]).

of the heterogenous wall reactions are derived from the model of Willey[14] and are transformed in an appropriate form.

Wall Radiation

Beside a constant wall temperature a radiation-adiabatic wall is simulated as well

$$\sigma \varepsilon T^4 + \dot{q}_{con} + \dot{q}_{dif} = 0, \qquad (3)$$

where the heat flux due to conductivity and mass diffusion is in equilibrium with the energy reflected on the surface due to radiation. The emission factor is assumed to be $\varepsilon = 0.85$.

Validation

For the verification of the detailed catalysis model the flow past a hyperboloid is investigated. This geometry has been proposed as transfer model for the flow of the windward center line of the Space Shuttle. Fig. 4 shows the wall heat-flux distributions along the hyperboloid resulting from different catalysis assumptions for the flow at 85.7 km altitude. The given distributions are obtained by subtracting the heat-flux due to radiation cooling. In addition to the results of the continuum method the results obtained with a DSCM code given by Bergemann[13] are included as well as free flight measurements of the Space Shuttle given by Stewart et al.[15] Both numerical methods show a good agreement for the different wall-catalysis assumptions. Near the stagnation point the measurements follow the results of finite catalytic simulation. The free-flight data indicate that further downstream catalytic effects become more inportant. The measured heat fluxes are lying in the band between the fully and the non-catalytic wall. The same behavior is found in results of Shinn et al.[16] and for the threedimensional flow past the HALIS configuration presented by Brück et al.[6]

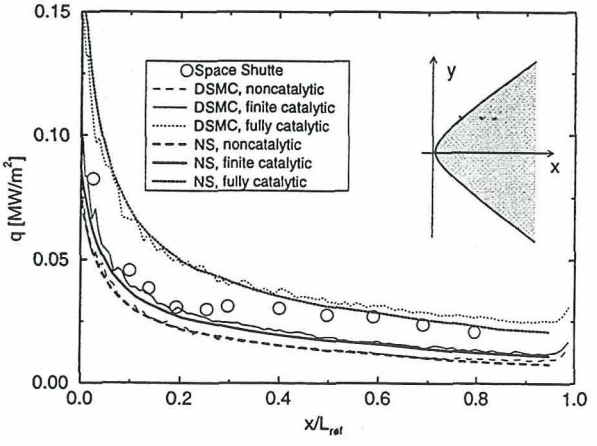

Fig. 4 Wall heat flux distribution along a hyperboloid as result of different catalysis modelling at 85.7 km altitude: $M_\infty = 27.35$, $T_\infty = 187\,K$, $\rho_\infty = 6.624 \cdot 10^{-6}\,kg/m^3$, $T_{wall} = 800\,K$.

Grid Generation

The basic multiblock grid is generated using the ICEM CFD package[17] while the smoothing of the volume grid is done with in-house tools. The grid in the boundary layer is introduced by means of an hyperbolic expansion of the grid lines between the configuration surface and first grid layer of the basic grid, and at the same time the grid lines are displaced away from the configuration contour to allow a monotonic stretching from the surface to the outer boundary. The resulting grid has 1982464 cells and consists of 10 blocks. The number of grid points in wall normal direction is 89 where about 40 points are located within the boundary layer. The minimum spacing for the first grid layer was prescribed as a linear variation from the body nose to the trailing edge of the configuration as well as from the symmetry plane to the leading edge of the configuration. Related to the reference length of the configuration, the minimum spacings are $1.3\,10^{-6}$ at the body nose and $2.7\,10^{-5}$ at the trailing edge. The inspection of the flow solutions revealed for the nondimensional boundary layer coordinate y^+ values smaller than 0.3 for the complete configuration. From the generated grid two coarser grids are obtained for the application of the multigrid method by removing every second grid point in all coordinate directions resulting in a medium and a coarse grid with 247808 and 30976 cells respectively. The medium surface grid is shown in Fig. 5 from the top, side and bottom. The grids for the X-24 and the X-38 configuration differ only in the scale. The X-38 configuration is scaled by the factor of 1.19 in relation to the X-24 shape.

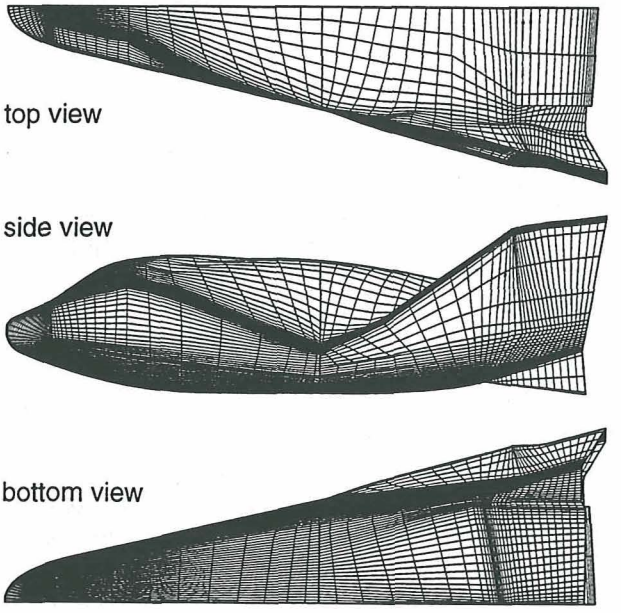

Fig. 5 Surface grid used for the computation of the flow past the X-24/X-38 configuration (medium grid: 247808 cells).

Results

Convergence and Accuracy

For the present study a 3-level full-multigrid V-cycle strategy is applied. The convergence histories are shown in Fig. 6 where the residual of the global-mass conservation equation is plotted over the number of multigrid cycles. The simulation starts on the coarsest grid. The full multigrid approach uses the coarse-grid results as starting solution for the next finer grid. This procedure is applied

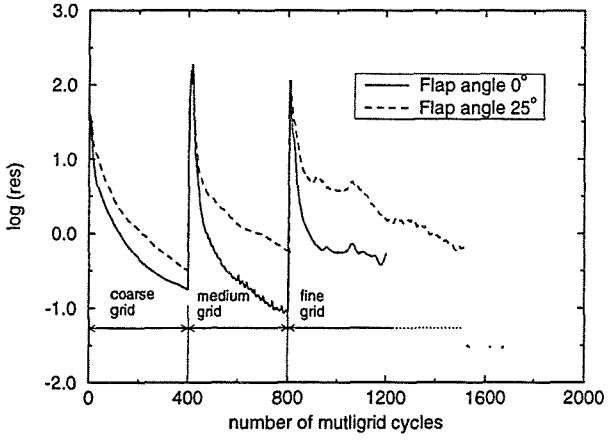

Fig. 6 Typical convergence histories for the simulations of the X-24 configuration with different flap deflections.

for the start on the medium and the fine grid which can be seen at the strong increase of the residual. For the computations on the medium and the fine grid the residual of the mass conservation equation decreases at about 3 orders of magnitude within 400 multigrid cycles which is sufficient to converge the aerodynamic coefficients and the wall properties. Differences in the convergence behaviour are found for the simulation with deflected body flap where a slower decrease of the rediuals is observed for all grids, which are due to the viscous dominated flow in the separation region at the hinge.

Computational performance of CEVCATS on a NEC SX4/8 super computer of the DLR is approximately 1.1 GFLOPS (single processor). The total CPU time for a complete computation results in $\approx 16\,h$ for a chemical nonequilibrium simulation. This results in a CPU time per grid point and multigrid cycle of $70\,\mu sec$ for the chemical nonequilibrium computations and $20\,\mu sec$ using a parallel version of the code running on 4 processors.

For grid-convergence studies the solutions on the medium (247808 cells) and the fine grid (1982464 cells) are compared with respect to pressure coefficient, Stanton number and flow structure (separation) on the windward side of the X-24 configuration.

The contour lines of the pressure coefficient are shown in Fig. 7 where a good agreement of the solution with different grid sizes can be observed. Here, small differences are only found in the hinge-line area which can be explained by the changing flow topology for the fine grid. The same holds for the Stanton-number contour lines in Fig. 8. Keeping in mind that the prediction of heat flux is more sensitive the results show a good agreement for the comparison between medium- and fine-grid solution. In addition to contour lines of wall values, the skin-friction lines have been generated to point out differences in the separation region. A secondary separation is found for the computation on the fine grid while the solution on the

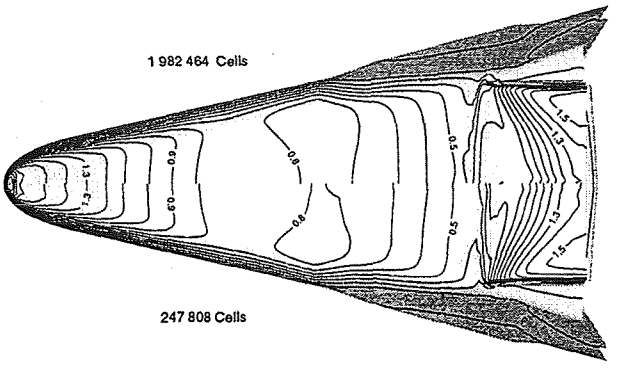

Fig. 7 Pressure coefficient on the windward side for different grid densities (top: fine grid, bottom: medium grid) at 75 km altitude: $M_\infty = 25$, $T_\infty = 208.4\,K$, $\rho_\infty = 3.99 \cdot 10^{-5}\,kg/m^3$, $T_{wall} = 1300\,K$, $\alpha = 40°$, $\delta_{bf} = 25°$.

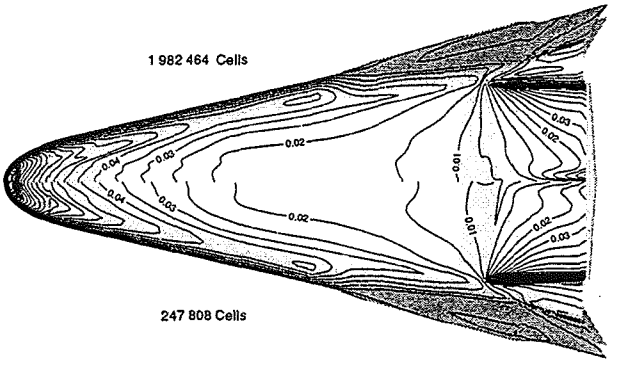

Fig. 8 Stanton-number distribution on the windward side for different grid densities (top: fine grid, bottom: medium grid) at 75 km altitude: $M_\infty = 25$, $T_\infty = 208.4\,K$, $\rho_\infty = 3.99 \cdot 10^{-5}\,kg/m^3$, $T_{wall} = 1300\,K$, $\alpha = 40°$, $\delta_{bf} = 25°$.

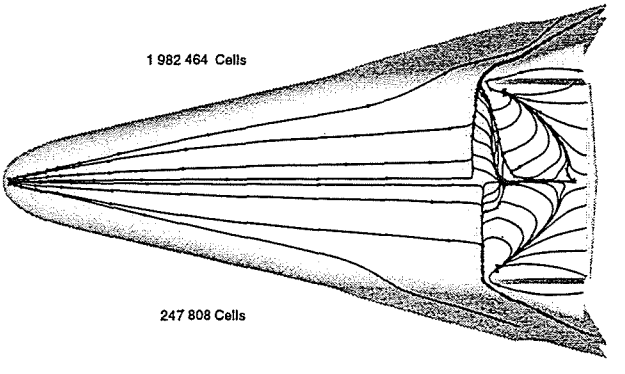

Fig. 9 Skin-friction lines on the windward side for different grid densities (top: fine grid, bottom: medium grid) at 75 km altitude: $M_\infty = 25$, $T_\infty = 208.4\,K$, $\rho_\infty = 3.99 \cdot 10^{-5}\,kg/m^3$, $T_{wall} = 1300\,K$, $\alpha = 40°$, $\delta_{bf} = 25°$.

medium grid shows a smaller separation region with only a single separation (Fig. 9). For further investigation the use of the medium grid is sufficient for parameter studies and qualitative investigations.

Heating of the Body Flap

In Fig. 10 the adiabatic wall temperatures of equilibrium flow simulation are plotted for different deflection angle of the body flap δ_{bf}. The highest wall temperatures are found in the stagnation point region at the nose of the configuration. Locally increased wall temperatures are observed further downstream at the shoulder in cross direction. With the increase of the flap deflection from $\delta_{bf} = 0°$ to $\delta_{bf} = 20°$ and $\delta_{bf} = 30°$ high wall temperatures on the flap are produced. For the highest investigated deflection angle the maximum wall temperature on the flap comes close to value at the nose region.

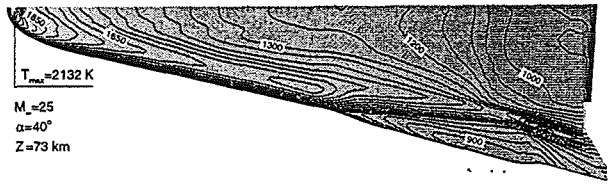

a) equilibrium flow, $\delta_{bf} = 0°$

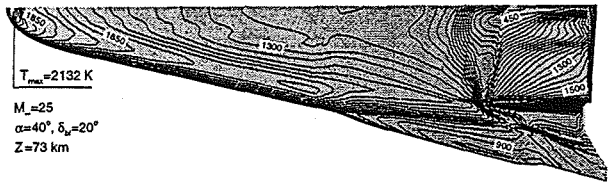

b) equilibrium flow, $\delta_{bf} = 20°$

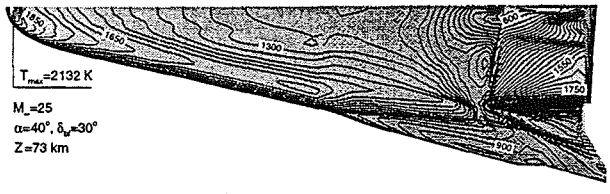

c) equilibrium flow, $\delta_{bf} = 30°$

Fig. 10 Wall-temperature distribution on the windward side for equilibrium flow at 73 km altitude with different flap deflections: $M_\infty = 25$, $T_\infty = 212.4\,K$, $\rho_\infty = 5.36 \cdot 10^{-5}\,kg/m^3$, $\alpha = 40°$, $\varepsilon = 0.85$.

Catalytic Effects

The radiation-adiabatic wall temperature as result of the nonequilibrium flow simulations with different catalysis models are presented in Fig 11. The temperature distribution with a fully catalytic wall shown in Fig. 11a) compare well in the nose region with to the equilibrium results in Fig. 10a). Further downstream larger differences are observed. The simulation considering a finite catalytic and a noncatalytic wall presented in Fig. 11b) and Fig. 11c) respectively produce significantly lower wall temperatures in the nose region in comparison to the results with a fully catalytic wall. Along the forebody the effect of catalycity decreases due to the lower dissociation level outside the boundary layer. Qualitatively similar results are presented by Loomis[1] for a different surface material. In fig. 12 the wall temperatures are shown

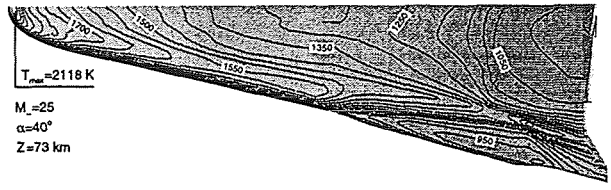

a) nonequilibrium flow, fully catalytic, $\delta_{bf} = 0°$

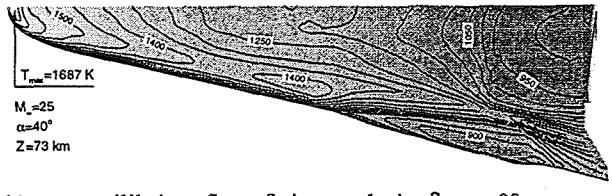

b) nonequilibrium flow, finite catalytic, $\delta_{bf} = 0°$

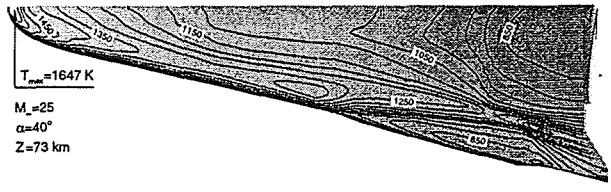

c) nonequilibrium flow, noncatalytic, $\delta_{bf} = 0°$

Fig. 11 Wall-temperature distribution on the windward side for different catalysis assumptions at 73 km altitude: $M_\infty = 25$, $T_\infty = 212.4\,K$, $\rho_\infty = 5.36 \cdot 10^{-5}\,kg/m^3$, $\alpha = 40°$, $\varepsilon = 0.85$.

in the front view. At the winglet leading edge the effect of wall catalysis is quite low in comparison to the differences in the stagnation point region. A localy increased heating is found at the winglet root.

Concluding Remarks

The results of the flow solver CEVCATS for a validation test case show good agreement with the results of a gaskinetic method (DSMC) and compare reasonably well with free-flight measurements. The accuracy of the code is investigated by grid convergence studies for the flow past the X-24 configuration where only small differences are found in the results of pressure coefficient, Stanton number and flow topology on the windward side. Therefore, the medium grid is applied for further investigations of flap heating and catalysis effects. For the equilibrium flow simulation the highest heat loads are found in the nose region of the configuration. For large flap deflections the maximum temperature values on the flap come quite close to the nose value. Catalysis effects are most important at the stagnation-point region at the nose while at the winglet the differences of the heat loads due to different catalysis assumptions are quite low.

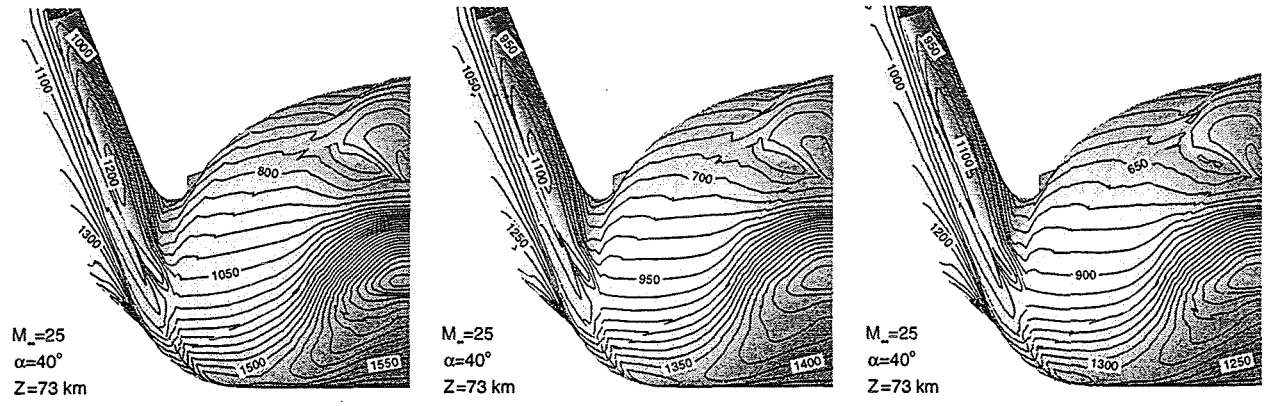

a) fully catalytic b) finite catalytic c) noncatalytic

Fig. 12 Wall-temperature distribution at front view for different catalysis assumptions at 73 km altitude: $M_\infty = 25$, $T_\infty = 212.4K$, $\rho_\infty = 5.36 \cdot 10^{-5}\, kg/m^3$, $\alpha = 40°$, $\varepsilon = 0.85$.

Acknowledgements

The work reported has been perfomed under an ESA contracts within the X-CRV 90-days study and within phase B of the CTV project monitored by G. Durand (ESA/CNES) and Ph. Rostand (Dassault Aviation) respectively.

References

[1]Loomis, M., Venkatapathy, E., Papadopoulos, P., Davies, C., Berry, S., Horvath, T., and Campbell, C., "Aeroheating and Aerodynamic CFD Validation and Prediction for the X-38 Program," *AIAA 32nd Thermophysics Conference*, AIAA 97-2478, Jun. 1997.

[2]Chalot, F., Hasholder, J., Mallet, M., Naïm, A., Perrier, P., Ravachol, M., Rostand, P., Stoufflet, B., Oskam, B., Hagmeijer, R., and de Cock, K., "Ground to flight transposition of the transonic characteristic of a proposed Crew Rescue/Crew Transfer Vehicle," *AIAA 32nd Thermophysics Conference*, AIAA 97-2305, Jun. 1997.

[3]Longo, J., Hermann, U., Brück, S., and Nickel, H., "DLR Contribution to ESA X-CRV 90 Days Study," DLR IB 129-96/37, 1996.

[4]Brück, s. Eggers, T., Longo, J., and Orlowski, M., "Investigation of Hypersonic Flows past the NASA X-24 Lifting Body Vehicle," DLR IB 129-97/7, 1997.

[5]Kroll, N. and Radespiel, R., "An Improved Flux Vector Split Discretization Scheme for Viscous Flows," DLR-FB 93-53, 1994.

[6]Brück, S., Radespiel, R., and Longo, J., "Comparison of Nonequilibrium Flows past a Simplified Space-Shuttle Configuration," *AIAA 35th Aerospace Sciences Meeting*, AIAA 97-0275, Jan. 1997.

[7]Radespiel, R. and Swanson, R., "Progress with Multigrid Schemes for Hypersonic Flow Problems," ICASE Report 91/89, 1991.

[8]Liou, M. and Steffen, C., "A New Flux Splitting Scheme," NASA Technical Memorandum 104404, May 1991.

[9]Park, C., "On Convergence of Computation of Chemically Reacting Flows," *AIAA 23rd Aerospace Science Meeting*, AIAA-85-0247, Jan. 1985.

[10]Hirschfelder, J., Curtiss, C., and Bird, R., *Molecular Theory of Gases and Liquids*, John Wiley & Sons, New York, 1954.

[11]Blottner, F., Johnson, M., and Ellis, M., "Chemically Reacting Viscous Flow Program for Multi-Component Gas Mixtures," Technical Report:SC-RR-70-754, SANDIA, 1971.

[12]Wilke, C., "A Viscosity Equation for Gas Mixtures," *Journal of Chemical Physics*, Vol. 18, Apr. 1950, pp. 517–519.

[13]Bergemann, F., "Gaskinetische Simulation von kontinuumsnahen Hyperschallströmungen unter Berücksichtigung von Wandkatalyse," DLR-FB 94-30, 1994.

[14]Willey, R., "Mechanistic Model for Catalytic Recombination During Aerobraking Maneuvers," NASA CR 185611, 1989.

[15]Stewart, D., Rakich, J., and Lanfranco, M., "Catalytic Surface on Space Shuttle Thermal Protection System during Earth Entry of Flights STS-2 through STS-5," *Shuttle Performance: Lessons Learned, NASA CP 2283*, edited by J. Arrington and J. Jones, Mar. 1983, pp. 827–845.

[16]Shinn, J., Moss, J., and Simmonds, A., "Viscous Shock-Layer Heating Analysis for the Shuttle Windward Symmetry Plane with Surface Finite Catalytic Recombination Rates," *Vehicle Heating and Thermal Protection Systems: Space Shuttle, Solar Probe, Jupiter Galileo Probe*, edited by P. Bauer and H. Collicott, No. 85 in Progess in Astronautics and Aeronautics, 1983, pp. 149–180.

[17]"ICEM^{TM} CFD/CAE Version 3.1.2 - Referenz Manuals Set," Control Data GmbH, 1993.

HEAT TRANSFER AND SHEAR STRESS PREDICTION IN 3D HYPERSONIC FLOWS BY APPROXIMATE METHODS

Irina Brykina, Vladimir Sakharov
Institute of Mechanics, Moscow State University, Russia

Abstract

The effective method for solving 3D viscous super- and hypersonic flows over blunted bodies is proposed. The method is based on combination of numerical algorithms for 2D equations and similarity method, which allows to obtain the solutions of 3D problems by calculating flows for equivalent axisymmetric bodies. Accuracy of the method is estimated by comparing heat flux and shear stress predictions, obtained with his help, with more accurate predictions, obtained from direct calculation of 3D governing equations set. The method is tested for various flow models: full and parabolized Navier-Stokes equations, viscous shock layer and boundary layer equations; for perfect gas and chemically reacting one; for different bodies and angles of attack. The approximate analytical solutions are obtained for heat flux to a surface relative to it's value at a stagnation point. The formulas for distribution of relative heat flux are obtained for infinite yawed wings, axisymmetric and 3D blunted bodies. Such formulas are obtained for various flow regimes. Accuracy of formulas is estimated by comparing with numerical solutions of corresponding 3D equations for boundary layer, hypersonic viscous shock layer and Navier-Stokes equations. Dependence of relative heat flux distribution on flow regime (altitude of flight), chemical reactions in a shock layer, wall catalytic properties is investigated.

Introduction

In spite of development the computational methods for calculating 3D hypersonic viscous gas flows in consideration of physical and chemical processes it is desirable to devise approximated methods for solving such problems, which could combine the advantage of minimum computational efforts with maximum accuracy of results. The most of approximate methods have been previously developed for the high Reynolds numbers, in the case of flowfield can be divided into inviscid one and thin boundary layer. For instance the method of axisymmetric analogy by Cooke[1] was widely employed to solving 3D viscous flow problems. This method reduces the 3D boundary layer equations along the streamline of the external inviscid flow to the boundary layer equations on some equivalent axisymmetric body, its shape is determined by the inviscid flow parameters on the surface. However the approximated methods for the low Reynolds numbers have not been essentially devised. To describe these flows it is necessary to use other models — viscous shock layer or Navier-Stokes equations. Such flow regimes are inherent in flight of space vehicles at hypersonic velocities in the upper atmosphere.

In this paper the method for solving 3D problems of supersonic viscous flows using 2D solutions is proposed. It can be applied for arbitrary Reynolds numbers (in the continuum regime) and in consideration of real gas effects. It is based on application of the similarity relations, expressing heat flux, shear stress and species fractions on the surface of 3D blunted body by their values on the surface of the equivalent axisymmetric body. Such bodies are constructed for each meridional plane in a wind-oriented coordinate system. These bodies depend only on the body geometry and the angle of attack and don't depend on values of gasdynamic flow parameters.

There is the essential difference between the present method and Cooke's axisymmetric analogy. Application of Cooke's analogy requires a 3D inviscid solution, i.e., reduction of 3D problem to 2D one is not complete. This analogy is applicable only for boundary layer model, for the high *Re* numbers. The using of analogy, presented in this paper, requires knowledge only the body geometry, and it can be applicable for arbitrary *Re* numbers and for different flow models. Notice that present method as applied to boundary layer problems is much simpler and does not require a 3D inviscid solution.

For hypersonic flows at Reynolds numbers $Re_\infty > 10^2$ the approximate analytical solutions are obtained for heat flux to a surface of 3D bodies relative to it's value at a stagnation point for various flow models. In case of using boundary layer model the formulas for relative heat flux depend on body geometry, wall temperature and inviscid flow parameters on a surface. The most simple solutions are obtained for hypersonic viscous shock layer: relative heat flux distribution depend only on body geometry and wall temperature and doesn't depend on gasdynamic flow parameters; for cool wall it doesn't depend also on wall temperature. However, these formulas can be applied only in flow regimes where the model of hypersonic viscous shock layer is applicable. In flow regimes where it's necessary to use Navier-Stokes equations analytical solutions for relative heat flux are also obtained. They are more exact and depend not only on body geometry, but also on pressure distribution on a surface.

The Similarity Method

The method for solving 3D problems of steady super- and hypersonic viscous flows over blunted bodies using 2D solutions is proposed. It is based on application of the similarity relations, expressing heat flux, shear stress and species fractions on the lateral surface of 3D body by their values on the surface of the axisymmetric body. The similarity relations have been obtained by analysis of the approximate analytical solution[2,3] of 3D hypersonic viscous shock layer equations which had been obtained by the integral method of successive approximations[4].

The similarity relations express heat flux q, shear stress τ and species fractions c_i along meridional plane of 3D body by their values q^s, τ^s and c_i^s on the corresponding equivalent axisymmetric body (EAB):

$$q(Re) = q^s(Re^*),\quad \tau(Re) = \tau^s(Re^*),\quad c_i(Re) = c_i^s(Re^*)$$

$$Re^* = \frac{H^s}{H} Re \qquad (1)$$

Here H is the average of the principal curvatures at a given point, H^s is the average of the principal curvatures of EAB at the point considered.

Let 3D body surface has been given in the cylindrical coordinate system by equation $r = r(z, \varphi)$. Then a shape $r^s(\varphi)$ of EAB constructed for meridional plane $\varphi = const$, is

$$r^s(z) = \int_0^z \frac{dr}{dz}\left[1 + \left(\frac{1}{r}\frac{dr}{d\varphi}\right)^2\right]^{-1/2} dz \qquad (2)$$

When we solve axisymmetric equations set for EAB to obtain q^s, τ^s, we must substitute instead usual constant Re number the variable Re^* dependent on surface geometry at a given point.

For a plane of symmetry of space body at zero or nonzero angle of attack the EAB is a body formed by rotation of the corresponding branch of the centerline around the axis z.

At a stagnation point the relation (1) for q is:

$$q^o(Re) = q^{so}(Re^*),\quad Re^* = \frac{2Re}{1+k} \qquad (3)$$

Here k is the ratio of the principal curvatures at the stagnation point, q^{so} is the heat flux to the stagnation point of an axisymmetric body, e.g., sphere.

For high Re numbers, when $q \sim Re^{-1/2}$ the asymptotic approximation for similarity relations (1) is:

$$q = \sqrt{H/H^s}\, q^s,\quad \tau = \sqrt{H/H^s}\, \tau^s \qquad (4)$$

Here q^s, τ^s are determined for EAB at the same constant Re number as q, τ for the real body.

The similarity relation (3) at a stagnation point for high Re numbers is reduced to

$$q^o = \sqrt{\frac{1+k}{2}}\, q^{so}. \qquad (5)$$

Note that equivalent bodies depend only on body geometry and angle of attack and don't depend on values of gasdynamic flow parameters and therefore can be easily constructed.

So, if we have 3D body, for each meridional plane we can construct EAB, solve axisymmetric equations for this body with variable, dependent on geometry Re number and thus obtain 3D solution.

The Numerical Method for Solving 2D Navier-Stokes Equations.

The finite-volume implicit numerical algorithm is developed to solve 2D full Navier-Stokes equations, which is an extension of the difference schemes[5,6].

The time-dependent Navier-Stokes equations set is written in a curvilinear coordinate system in conservative form, with separation of all the terms of equations into "viscous" and "inviscid". Discretization in the time and space variables is introduced and the resulting equations are linearized with respect to a temporal coordinate. A system of difference equations is written in delta form. Coordinate-oriented differences are used in the implicit part of the difference operator in accordance with signs of eigenvalues of Jacobi matrices in convective terms; this makes it possible to obtain a system of difference equations with diagonal dominance. "Viscous" terms are represented by adding to Jacobi matrices the special matrix which takes into account dependence of "viscous" terms only on derivatives. A system of difference equations is reduced to a form convenient for using Gauss-Zeidel iteration procedure along the lines normal to a surface; inversion of the implicit operator on each of these lines is carried out by vector three-point sweep method.

In conservative difference scheme the "inviscid" terms on the right, explicit side of the difference operator are calculated in terms of flux vectors on cell boundaries. The higher-accuracy Godunov scheme is used to calculate these vectors. It is based on the solution of Riemann problem and the parabolic distribution of parameters over network cells, satisfying the monotony conditions (TVD-scheme). All spatial derivatives in the "viscous" terms are approximated by central differences with second-order accuracy. The steady-state solution is obtained by time-iterative algorithm.

Computational Results.

The accuracy of the method is estimated by comparing heat flux, skin friction coefficient and species fractions predictions, obtained from numerical solution of 2D equations set with using similarity relations, with more accurate predictions, obtained from direct calculation of 3D governing equations set.

The method was tested for various flow models:

1. Hypersonic and full viscous shock layer - perfect gas and reactive flow.
2. Boundary layer - perfect gas and reactive flow.
3. Parabolized Navier-Stokes equations - perfect gas.
4. Full Navier-Stokes equations - perfect gas.

For testing method in the case of perfect gas flow in hypersonic viscous shock layer 3D governing equations set[2] and the finite-difference method[2] are used. Comparisons of approximate and exact solutions were made for ellipsoids, elliptical paraboloids and hyperboloids at angles of attack from 0 to 45° for wide variety of flow conditions: specific heats ratio γ = 1.1-1.67, the wall temperature T_w/T_o = 0.01-0.5, Re_o = 1-10^4. Here, $Re_o = \rho_\infty V_\infty R/\mu(T_o)$, T_o is a freestream adiabatic stagnation temperature, R is one of the radii of principal curvatures at a stagnation point. Some comparison results for the Stanton number St are presented in Fig. 1-2. Here and further solid lines — the solution of 3D equations, light dots — the solution of 2D equations using the relations (1), dark dots — the solution of 2D equations using the simplified relations (4); x, y — coordinates of a point at the surface in the Cartesian coordinate system x, y, z with origin at a stagnation point, the axis z is directed along V_∞, y = 0 — the plane of symmetry, $r = \sqrt{x^2 + y^2}$.

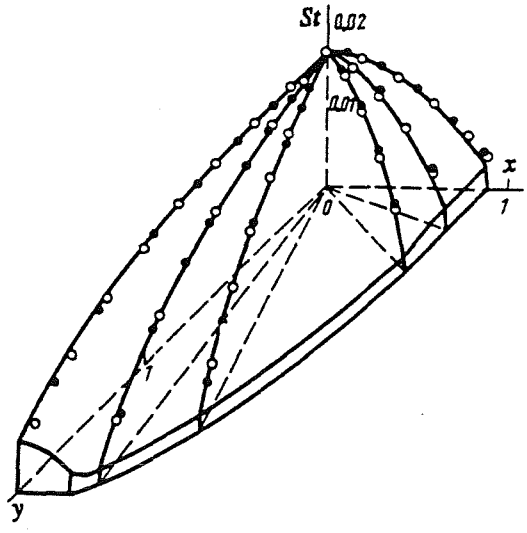

Figure 1. The Stanton number distribution on the surface of ellipsoid with axes ratio 1:1.6:1.3; Re_o = 10^4, T_w/T_o = 0.1, γ = 1.4.

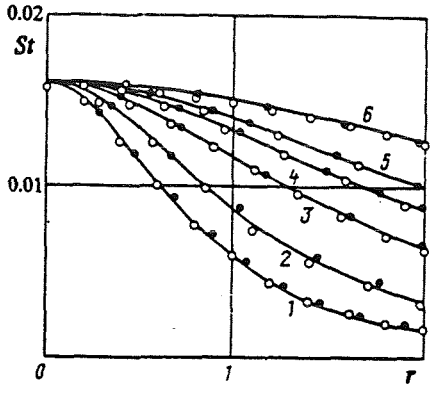

Figure 2. The Stanton number distributions in the different meridional planes of elliptical paraboloid with $k = 0.25$; lines 1-6 correspond $\varphi = 0$, 45°, 63.4°, 71.6°, 76°, 90°; $Re_o = 10^4$, $T_w/T_o = 0.1$, $\gamma = 1.4$.

The accuracy of relations (4), (5) has been verified for boundary layer model by using the numerical method[7]. The comparison of approximate and exact heat flux predictions showed, for instance, that for the elliptical paraboloid with $k = 0.25$ an error of using similarity relation (4) was less 5% for $z < 3$, $T_w/T_o = 0.01$-0.5, $\gamma = 1.15$-1.6.

The method proposed was also evaluated within the framework of the parabolic approximation of the Navier-Stokes equations including shock wave structure. The system of governing equations for perfect gas flow and method of solving are listed in[8]. Results of comparison showed that an error of using relation (3) did not exceed 2% for $Re_\infty = 10$-10^5, $T_w/T_o = 0.01$-1, $\gamma = 1.2$-1.6, $\omega = 0.5$-1 ($\mu \sim T^\omega$). The comparison of exact and approximate q values on elliptical paraboloid with $k = 0.4$ carried out for $Re_\infty = 367$, $T_w/T_o = 0.1$, $\gamma = 1.2$ has demonstrated applicability of the method for parabolized Navier-Stokes equations also on a lateral surface.

The method has also been verified for full Navier-Stokes equations. An example of comparing of approximate and exact solutions is presented in Fig. 3. Some disagreement between results for $Re_\infty = 333$ can be explained by the fact that 3D solution[9] was obtained for approximate Navier-Stokes equations and these equations are not so accurate for low Re numbers.

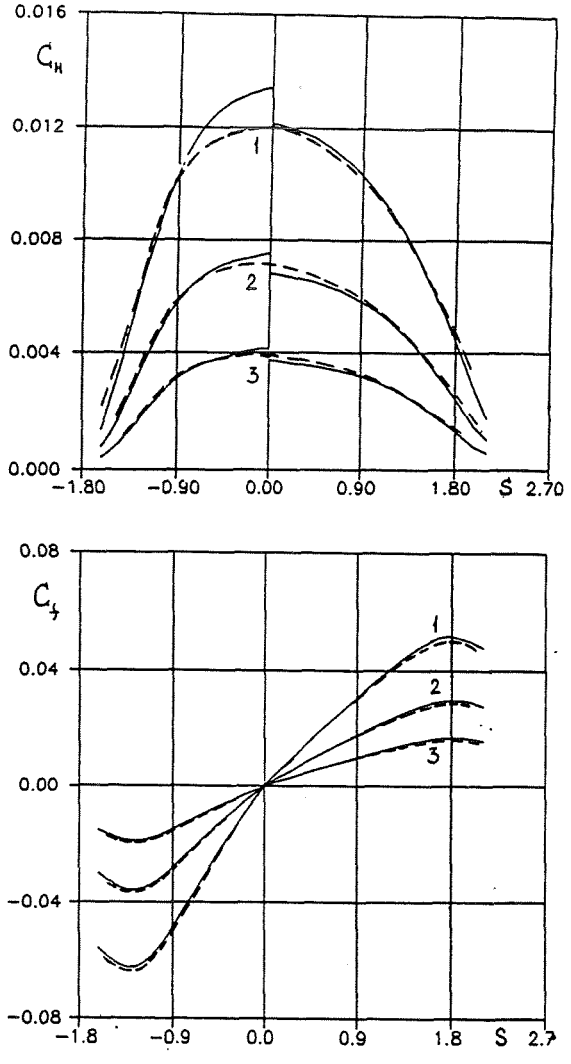

Figure 3. The Stanton number and skin friction coefficient distributions in the plane of symmetry of ellipsoid with axis ratio 1.5:1.5:1 at angle of attack 10°. Solid lines — numerical solution of 2D full Navier-Stokes equations with using the similarity relations, dashed — numerical solution of 3D Navier-Stokes equations[9]. $Re_\infty = 333$ (lines 1), 1000 (2), 3333 (3); the Mach number $M_\infty = 4$, $T_w/T_o = 0.8$.

In the case of application of the method for Navier-Stokes equations when there is an angle of attack, at a stagnation point different values for heat flux are obtained as it is seen in Fig. 3. Because stagnation point solutions of elliptical equations for equivalent axisymmetric bodies corresponding to different directions from a stagnation point depend not only

on radii of curvature at this point but on dimensions of these bodies. This discontinuity can be reduced and even eliminated by corresponding choose of linear parameter R in Re definition. But a value of discontinuity does not exceed an accuracy of the method and therefore we can use one of the radii of curvature as R and smooth away difference; as it is seen from Fig. 3, the exact solution lies between approximate ones.

Results of comparing showed good accuracy of the method for all test cases for perfect gas. For $Re_o > 10^2$ there is almost no difference between solutions using (1) and (4). The accuracy of relations (1), (4) is almost independent on values Re, γ, T_w, Pr.

To test the method for chemically nonequilibrium flows, the comparison was made between the numerical solutions of 2D (using (1) or (4)) and 3D hypersonic viscous shock layer equations accounting nonequilibrium chemical reactions and multicomponent diffusion for 5 species air. The details of chemical kinetics, thermodynamic, and transport properties are given in[10].

The wall temperature is assumed to be at the radiative equilibrium wall condition (or constant). Slip boundary conditions for nonequilibrium gas[11] were used at the wall. Different models of a surface catalytic activity were considered: noncatalytic, fully catalytic, first order heterogeneous reactions with the rates both constant and dependent on the temperature[12]. The modified Rankine-Hugoniot conditions taking account of the molecular transfer effects incorporating with the assumption of frozen chemical reactions in the front of the shock wave[13] were used at the shock.

The freestream conditions were corresponded to altitudes h from 100 to 50 km of the Earth atmosphere over the reentry trajectory of Space Shuttle[14] including frozen, nonequilibrium and closed to equilibrium flow regimes. The numerical method[2] for solving 2D and 3D equations was used. Some examples of comparing of approximated and exact solutions are given in Fig. 4-10. The values of c_f in Fig. 5, 10 are given only for fully catalytic wall as skin friction coefficient depend only slightly on the wall catalycity.

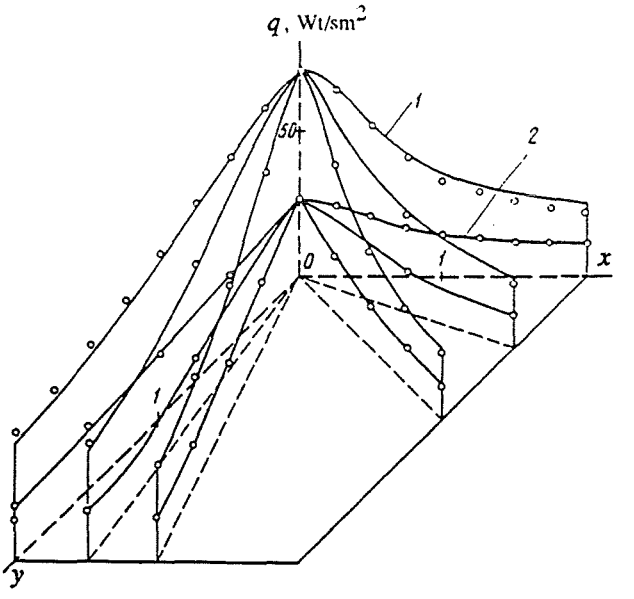

Figure 4. Heat flux distributions on the elliptical hyperboloid with $k = 0.4$ and angle 80° in the plane $y = 0$ for fully catalytic (lines 1) and noncatalytic (2) walls; $h = 70$ km.

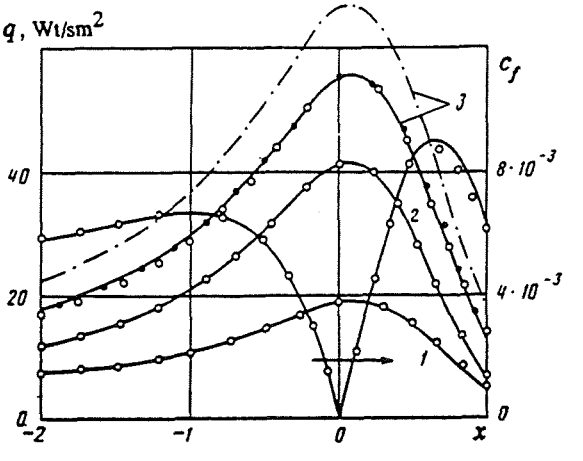

Figure 5. Heat flux and skin friction coefficient distributions in the plane of symmetry of paraboloid with $k = 0.4$ at angle of attack 15° for different surface catalycities: lines 1 — fully catalytic, 2 — model[12], 3 — noncatalytic wall; $h = 70$ km.

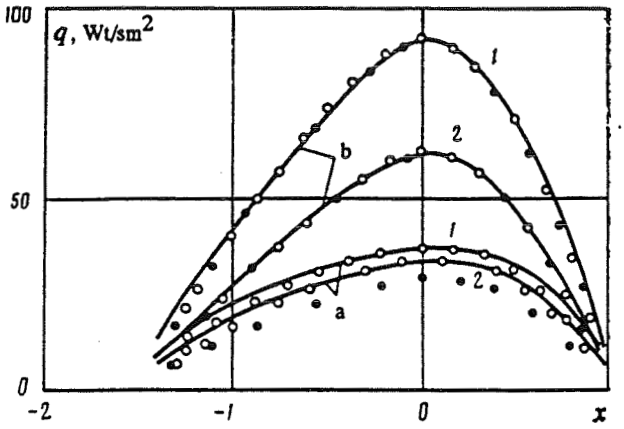

Figure 6. Heat flux in the plane of symmetry of ellipsoid with axes ratio 1.6:1:2.2 at angle of attack 15° at h = 70 km (lines 1) and h = 80 km (2) for noncatalytic (lines a) and fully catalytic (b) walls.

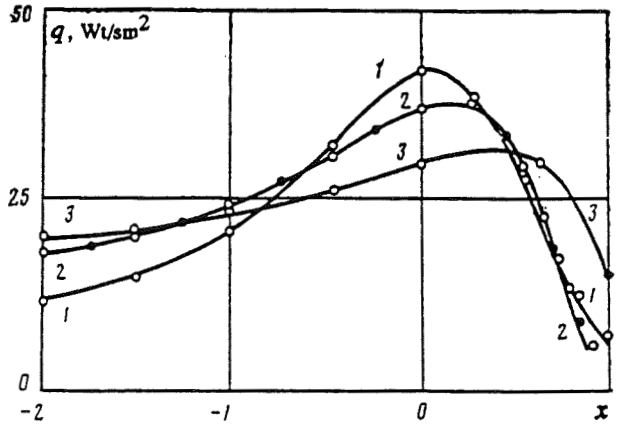

Figure 7. Heat flux in the plane of symmetry of paraboloid with k = 0.4 for angles of attack 15°, 30°, 45° — lines 1-3; h = 70 km, catalycity model[12].

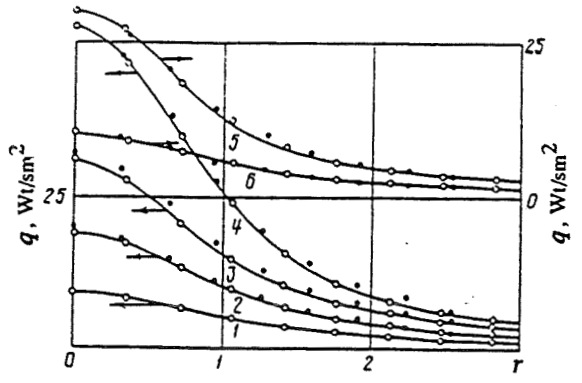

Figure 8. Heat flux in meridional plane φ = 45° of paraboloid with k = 0.5 for altitudes h = 100, 90, 80, 70, 60, 50 km — lines 1-6; catalycity model[12].

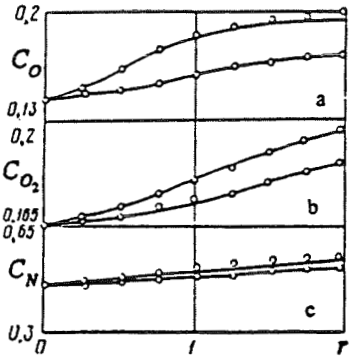

Figure 9. C_O (a) and C_N (b) distributions in planes of symmetry of hyperboloid with k = 0.5, a — h = 80 km, catalycity model[12], b — h = 70 km, noncatalytic wall; c — C_{O_2} distributions in planes of symmetry of paraboloid with k = 0.5, h = 100 km, noncatalytic wall.

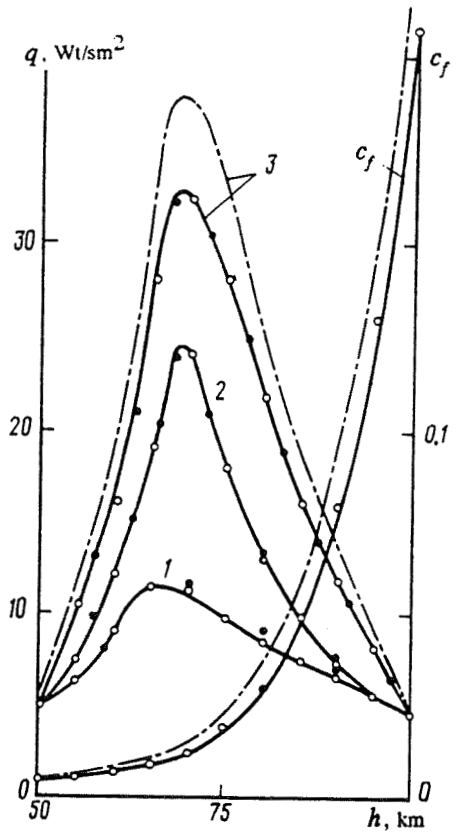

Figure 10. Heat flux and skin friction coefficient versus altitude over reentry trajectory[14] at the point x = 1, y = 0 of paraboloid with k = 0.4 at angle of attack 30° for different wall catalycities: lines 1 — noncatalytic, 2 — model[12], 3 — fully catalytic.

The testing of the proposed method for chemically nonequilibrium flows was made also for full viscous shock layer model. The governing equations set and numerical method are listed in[15]. Comparison of obtained by the method solutions with exact 3D ones were made for blunted cones at an angle of attack. Some examples of such comparing are shown in Fig. 11.

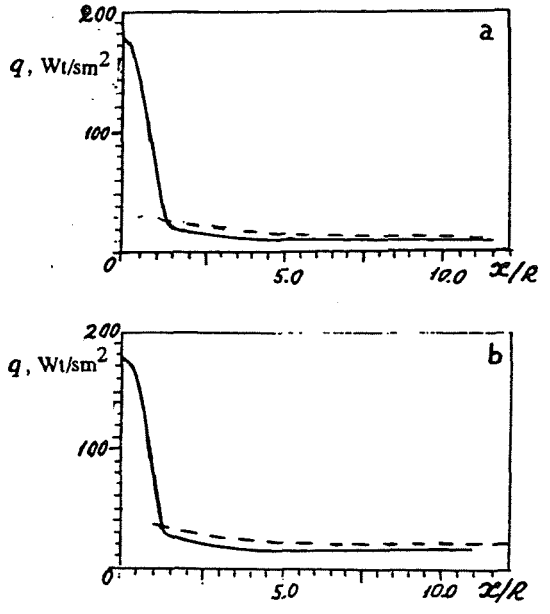

Figure 11. Heat flux distributions in the plane of symmetry of spherically blunted cone with half-angle 5.25° at angles of attack 6° (a) and 10° (b). Solid lines — approximate solution, dashed — exact solution[16]. R = 1.01 cm, T_w = 298°K, V_∞ =1.72 km/s, $Re_\infty = 3.3 \cdot 10^5$, M = 11.

Results of comparing for chemically reacting gas flow have shown that the similarity relations (1) allow us to predict wall heat flux, skin friction coefficient and species fractions on space bodies with good accuracy at all altitudes independently on wall catalytic properties, both for the constant wall temperature and for radiative equilibrium wall conditions. A range of applicability of simplified relations (4) essentially depends on the wall catalycity properties, as it is seen from Fig. 6, 8, 10 (dark dots); for instance, for noncatalytic wall they can be used at altitudes up to 65 km, for fully catalytic one — up to 90 km. It is connected with a range of applicability of boundary layer model.

Notice that for heat flux prediction in a plane of symmetry sometimes the usual axisymmetric solution for body formed by rotating a centerline around axis z, is used, i.e. without taking into account a real surface transverse curvature[17]. For comparison such axisymmetric solutions are shown in Fig. 5, 10, 12 by dashed-dotted lines. In Fig. 12 comparison of three solutions - exact, obtained by proposed method, and axisymmetric is presented. Five considered bodies have the same centerline, but different transverse curvature. The axisymmetric solution for all these bodies is the same while the real heat flux values differ a few times.

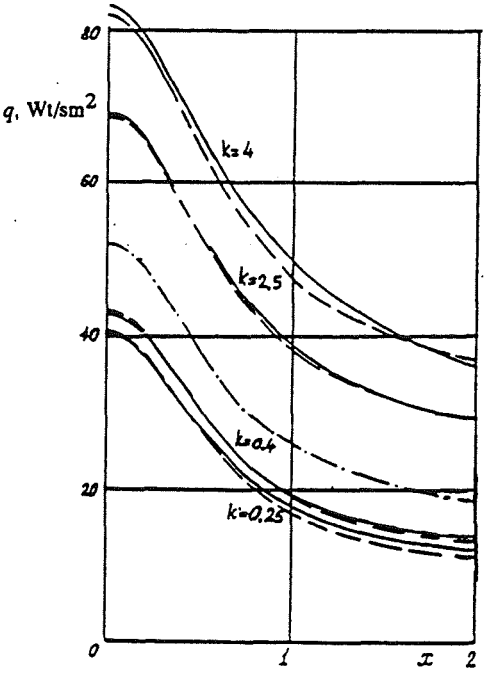

Figure 12. Heat flux distributions in the plane of symmetry for elliptical hyperboloids with different k. h = 70 km, V_∞ = 7.25 km/s, $Re_\infty = 1.33 \cdot 10^4$, catalycity model[12]. Solid lines - exact solution, dashed - by using similarity relations (4), dashed-dotted — axisymmetric one.

Thus the using of the usual axisymmetric solution can lead to great errors, because influence of transverse curvature on heat transfer is great. And these 3D effects are very well accounted by the similarity relations, introducing correction for the Reynolds number dependent on geometry.

Formulas for Relative Heat Flux

For hypersonic flows at Reynolds numbers $Re_\infty > 10^2$ the approximate analytical solutions are obtained for heat flux to a surface relative to it's value at a stagnation point. The formulas for distribution of relative heat flux are obtained by integral methods of successive approximations and other analytical methods for various flow regimes. Such formulas are obtained for infinite yawed wings at angle of attack, axisymmetric bodies, plane of symmetry and lateral surface of 3D blunted bodies.

The analytical solutions of boundary layer equations, obtained for relative heat flux depend on body geometry, wall temperature and inviscid flow parameters on the surface. Relative heat flux distribution q/q_o along infinite yawed wings is

$$\frac{q}{q_o} = \frac{(1-\alpha_1-\alpha_2)u_e\mu_e\rho_e}{[2\left(\frac{du_e}{ds}\right)_0(1-\alpha_2)\int_0^s(1-\alpha_1-\alpha_2)u_e\mu_e\rho_e ds]^{1/2}} \quad (6)$$

$$\alpha_1 = \frac{u_e^2(1-\sigma)}{2(H_e-H_w)}, \quad \alpha_2 = \frac{w_e^2(1-\sigma)}{2(H_e-H_w)}$$

Here s is a length of arc from a stagnation point along wing contour in a plane perpendicular to generatrix; subscripts o, e and w correspond to a stagnation point, to inviscid flow parameters on the surface, and to a wall; H - total enthalpy, σ is the Prandtl number; w_e , u_e are inviscid flow velocity components in the directions of generatrix and of tangent to wing contour in a plane perpendicular to generatrix.

In a plane of symmetry of 3D body q/q_o is

$$\frac{q}{q_o} = \frac{(1-\alpha_1)u_e\mu_e\rho_e F^{1/2}}{[2(1+c)\left(\frac{\partial u_e}{\partial s}\right)_0\int_0^s(1-\alpha_1)u_e\mu_e\rho_e F ds]^{1/2}} \quad (7)$$

$$F = \exp\int_0^s 2\frac{\partial w_e/\partial y}{u_e}ds, \quad c = \frac{(\partial w_e/\partial y)_0}{(\partial u_e/\partial s)_0}$$

Here s is a length of arc from a stagnation point along surface in a plane of symmetry; y is a length of arc from a centerline along surface in perpendicular direction; u_e , w_e are inviscid flow velocity components in directions of these coordinates. Formulas (8) can be used also for axisymmetric flows: in that case $c = 1$, $F = r^2$. It's interesting, that (7) written at a stagnation point exactly coincides with relation (5) obtained by quite another way.

For a lateral surface of 3D body q/q_o is

$$\frac{q}{q_o} = \frac{\alpha_3 u_e\mu_e\rho_e F^{1/2}}{[2\beta_0\left(\frac{\partial u_e}{\partial \xi}\right)_0\int_0^\xi \alpha_3 u_e\mu_e\rho_e F g_{11}^{1/2}d\xi]^{1/2}} \quad (8)$$

$$F = \frac{g}{g_{11}}\exp\int_0^\xi 2\frac{\partial}{\partial\eta}\left(\frac{w_e g_{11}^{1/2}}{u_e g_{22}^{1/2}}\right)d\xi$$

$$\alpha_3 = 1-\alpha_1-\alpha_2-\frac{2g_{12}(\alpha_1\alpha_2)^{1/2}}{(g_{11}g_{22})^{1/2}}, \quad g = g_{11}g_{22}-g_{12}^2$$

$$\beta = \frac{\xi}{2g_{11}^{1/2}}\frac{\partial\ln(u_e\mu_e\rho_e\xi g/g_{11})}{\partial\xi} + \frac{w_e\xi}{2u_e g_{22}^{1/2}}\frac{\partial\ln(w_e^2\mu_e\rho_e g/g_{22}u_e)}{\partial\eta}$$

Here ξ and η are curvilinear coordinates on a surface, g_{11} , g_{12} , g_{22} are metric coefficients. All integrals are along inviscid flow streamlines on a surface:

$$\frac{g_{11}^{1/2}d\xi}{g_{22}^{1/2}d\eta} = \frac{u_e}{w_e}$$

The most simple solutions are obtained for hypersonic viscous shock layer. In that case relative heat flux depends only on body geometry and wall temperature and doesn't depend on gasdynamic flow parameters; for cool wall it doesn't depend also on wall temperature. Distribution of relative heat flux along a cool wall of infinite wings ($\nu = 0$) at angles of yaw (φ) and attack and for axisymmetric body ($\nu = 1$) can be predicted from:

$$\frac{q}{q_o} = \frac{b\cos^2\alpha\sin\alpha\, r^\nu}{\lambda[2(1+\nu)b_o\int_0^s\lambda^{-1}b\cos^2\alpha\sin\alpha\, r^{2\nu}ds]^{1/2}} \quad (9)$$

$$\lambda = 1+\frac{8r\sin\alpha}{15R\cos^2\alpha(1+\nu)}, \quad \nu = 1: \quad b \equiv b_o \equiv 1$$

$\nu = 0$: $b = 1 - (\sin^2\varphi + \sin^2\alpha\cos^2\varphi)$, $b_o = 1 - \sin^2\varphi$

Here α is an angle between a normal to a surface and the freestream velocity ($\nu=1$) or a projection of the freestream velocity on the plane perpendicular to a generatrix ($\nu=0$); R is a radius of curvature of a generatrix ($\nu=1$) or a wing contour ($\nu=0$).

Distribution of q/q_o in a plane of symmetry of 3D body can be calculated from:

$$\frac{q}{q_o} = \frac{\cos^2\alpha\, F^{1/2}}{2\lambda}\left[H_0 \int_0^s \frac{F\cos\alpha}{\lambda\, tg\alpha} ds\right]^{-1/2} \qquad (10)$$

$$F = \exp\int_0^s \frac{4H}{tg\alpha} ds, \quad \lambda = 1 + \frac{4tg^2\alpha\, H^*}{15H}$$

H is the average of principal curvatures at a given point, H^* is a curvature of a centerline in the plane of symmetry, α is an angle between a normal to the surface and the freestream velocity.

For 3D blunted bodies using an axisymmetric solution incorporating with similarity relation (4) we can obtain a distribution of q/q_o along each meridional plane φ = *const*:

$$\frac{q}{q_o} = \frac{H^{1/2}\cos^2\alpha\sin\alpha\, r^s}{\lambda\left[2(1+k)H^s\int_0^s \lambda^{-1}\cos^2\alpha\sin\alpha\,(r^s)^2 ds\right]^{1/2}} \qquad (11)$$

$$\lambda = 1 + \frac{4tg^2\alpha}{15R^sH^s}$$

Here $r^s(z)$ is the shape of EAB given by relation (2) in cylindrical coordinate system, H^s and R^s are the average of principal curvatures and the radius of curvature of EAB, k is a ratio of principal curvatures at a stagnation point.

However, these simple formulas dependent only on body geometry can be applied only in flow regimes where the model of hypersonic viscous shock layer is applicable. In flow regimes where it's necessary to use Navier-Stokes equations analytical solutions for relative heat flux also are obtained. They are more exact and depend not only on body geometry, but also on pressure distribution on a surface. In that case q/q_o distribution along axisymmetric body for cool wall is:

$$\frac{q}{q_o} = \frac{\sin\alpha\, rp(s)}{2\left[\int_0^s \sin\alpha\, r^2 p(s) ds\right]^{1/2}} \qquad (12)$$

Here $p(s)$ is the pressure relative to it's value at a stagnation point. Relative heat flux distribution in a plane of symmetry of 3D body is:

$$\frac{q}{q_o} = \frac{F^{1/2}p(s)}{2}\left[H_0\int_0^s \frac{Fp(s)}{\sin\alpha} ds\right]^{-1/2} \qquad (13)$$

$$F = \exp\int_0^s \frac{4H}{tg\alpha} ds$$

Accuracy of formulas has been estimated by comparing with numerical solutions of corresponding 3D governing equations set for boundary layer, hypersonic viscous shock layer and Navier-Stokes equations. Some comparison examples for perfect gas flow are shown on Fig. 13-15.

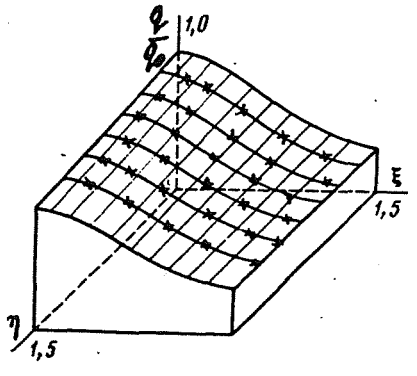

Figure 13. Relative heat flux distribution along elliptical paraboloid with $k = 0.25$, $T_w/T_o = 0.1$. Solid lines are numerical solution of 3D boundary layer equations, crosses - analytical solution (8).

Results of calculations for all flow regimes showed that relative heat flux is very conservative, it depends only slightly on Re, γ, ω, and in the case of cool wall ($T_w/T_o < 0.5$) on wall temperature. It is illustrated in Fig. 14.

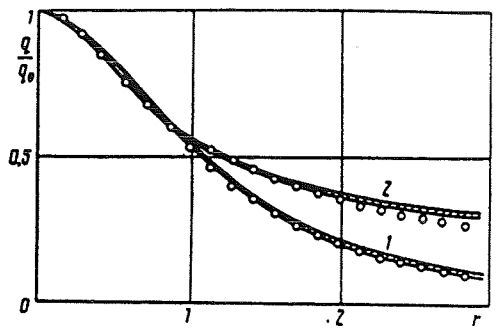

Figure 14. Relative heat flux distributions in meridional planes $\varphi = 45°$ of elliptical paraboloid with $k = 0.4$ (1) and hyperboloid with $k = 0.5$ and 80° angle in the plane $y = 0$. Strips contain all numerical solutions of 3D hypersonic viscous shock layer equations for $Re_o = 10^2$-10^5, $T_w/T_o = 0.01$-0.3, $\gamma = 1.15$-1.67; dots - analytical solution (11).

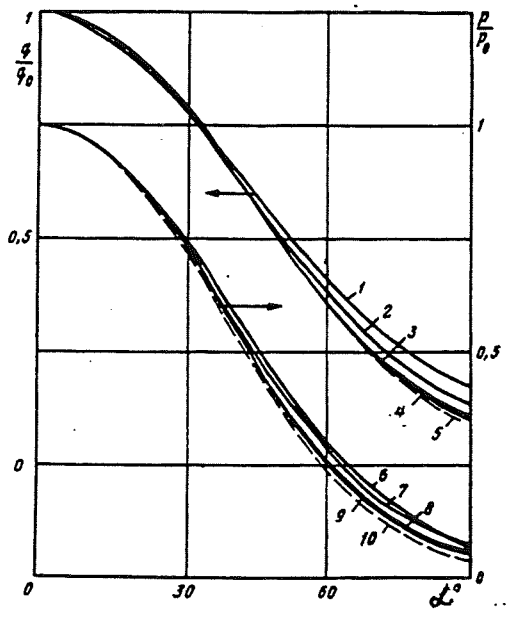

Figure 15. Relative heat flux and pressure distributions on sphere. Lines 1-4 and 6-9 correspond to $Re_\infty = 100$, 500, 3500 and the range $7 \cdot 10^3$-10^5. Solid lines are numerical solutions of Navier-Stokes equations, line 10 - numerical solution of inviscid flow Euler equations, line 5 - analytical solution (12) with using this inviscid pressure distribution.

Fig.15, where calculation results for Navier-Stokes equations are presented, also demonstrates that with *Re* number increasing relative heat flux no longer depend on *Re*. Similar conclusion can be done for relative pressure p/p_o distribution. As can be expected, for high *Re* relative pressure distribution obtained from Navier-Stokes equations and inviscid flow Euler equations are close and one can substitute the inviscid pressure p/p_o in analytical solutions (12) and (13). Navier-Stokes equations calculations have shown, that relative heat flux depend only slightly also on the Mach numbers *M*, and this dependence almost vanishes with *Re* increasing.

For reactive gas flow numerical solutions of boundary layer and viscous shock layer equations showed, that relative heat flux distribution on fully catalytic surface is almost independent on chemical reactions taking place within shock layer and differs very slightly from distribution obtained for perfect gas. It is seen from Fig. 16, 17 which show that q/q_o on fully catalytic wall is almost independent on flow regime (or flight altitude) and in good agreement with analytical solution.

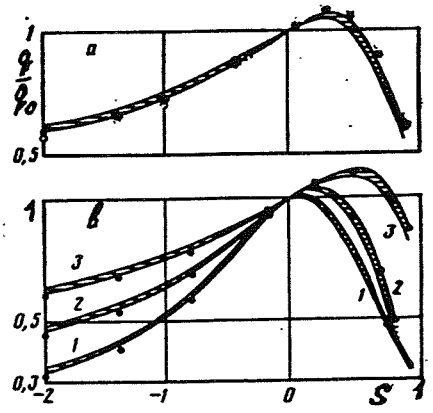

Figure 16. Relative heat flux distributions in planes of symmetry of 40° half-angle hyperboloid with $k = 2.5$ at angle of attack 30° (a) and of elliptical paraboloid with $k = 0.4$ (b) at angles of attack 15, 30, 45° (lines 1-3). Strips contain all numerical solutions of 3D hypersonic viscous shock layer equations in chemically nonequilibrium flow for altitudes from 50 to 90 km for two trajectories - Space Shuttle reentry trajectory[14] and with constant velocity 8 km/sec. Fully catalytic wall. Dots are analytical solution (10).

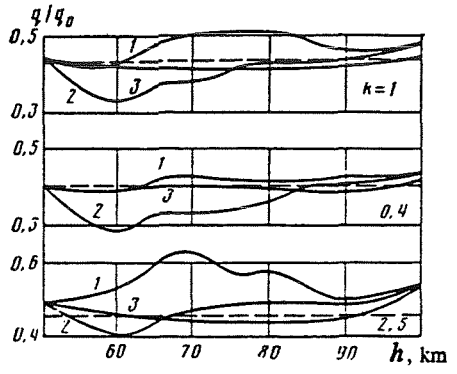

Figure 17. Dependence of relative heat flux on flight altitude for different wall catalycities: noncatalytic wall (lines 1), model[12] (2) and fully catalytic (3). Solid lines - numerical solutions of 3D hypersonic viscous shock layer equations for trajectory[14] in the point $x = 1$ in planes of symmetry of elliptical paraboloids with $k = 1$, 0.4 and 2.5. Dashed lines - analytical solution (10).

Fig. 17 shows how relative heat flux depends on flow conditions (flight altitude) for various wall catalycities. It is seen that for different wall catalycities an error of using formulas can reach in some cases 30-40% and only for fully catalytic wall q/q_o coincides with analytical solution.

Comparing showed a good agreement between numerical and analytical solutions for all flow conditions considered. Of course, absolute values of heat flux very differ for different flow regimes, but relative heat flux is very conservative, therefore, application of formulas obtained allow us to predict heat transfer with good accuracy both for a perfect gas and for chemically reacting one for fully catalytic surface. To predict absolute heat flux distribution on 3D body it's enough to know accurate heat flux prediction only at a stagnation point of axisymmetric body, for example, of sphere, and then to use formulas (6) - (13) and (5).

Conclusion

The proposed method, based on application of the similarity relations, allows to obtain accurate heat flux and skin friction coefficient predictions for space bodies regardless flow regimes, the flow model used, physical-chemical properties of gases, wall catalytic activity, etc. It is simple, easy to apply, and permits to use available axisymmetric methods and codes to solving 3D super- and hypersonic viscous flow problems. It represents significant reduction in computational efforts over fully 3D methods and has an essential advantage over the approximate methods which use Cooke's axisymmetric analogue and others.

The approximate analytical solutions for relative heat flux obtained for various flow models allow to predict heat transfer on 3D bodies for perfect gas and for chemically reacting one for fully catalytic wall at different altitudes of flight.

References

1. Cooke J.C., An axially symmetric analogue for general three-dimensional boundary layers, Aeronaut. Res. Council, Repts & Mem. 3200, 1959.

2. Brykina I.G., Rusakov V.V. and Shcherbak V.G., Analytical and numerical investigation of three-dimensional viscous shock layer on blunted bodies, Zh. Prikl. Mekh. Tekhn. Fiz. 4, 81, 1991.

3. Brykina I.G., Rusakov V.V. and Shcherbak V.G., Method of determining the heat fluxes and skin friction in the three-dimensional hypersonic flow problems using two-dimensional solutions", Dokl. AN SSSR, **316**, 1, 62, 1991.

4. Brykina I.G., Solving of hypersonic viscous shock layer equations by the method of successive approximations, Zh. Vych. Mat. Mat. Fiz. **18**, 1, 154, 1978.

5. Ivanov M.Ya., Krupa V.G., and Nigmatullin R.Z., Implicit higher-accuracy Godunov scheme for integrating the Navier-Stokes equations, Zh. Vych. Mat. Mat. Fiz., **29**, 888, 1989.

6. Polyansky V.A., Sakharov V.I., and Pankrat'eva I.L., Calculation of viscous compressible flows using higher-accuracy monotonic schemes, Institute of Mechanics, Moscow State University, Report No 4189, 1992.

7. Brykina I.G., Gershbein E.A. and Peigin S.V., Investigation of three-dimensional boundary layer on blunted bodies with penetrated surface, Izv. Akad. Nauk SSSR, Mekh. Zhid. Gasa, 3, 49, 1982.

8. Gershbein E.A. and Shcherbak V.G., Investigation of hypersonic three-dimensional flow within the framework of the parabolized Navier-Stokes equations, Izv. Akad. Nauk SSSR, Mekh. Zhid. Gasa, 4, 134, 1987.

9. Karjakin V.E., Popov F.D. Calculation of 3D supersonic viscous and heatconducting flow over blunted bodies, Zh. Vych. Mat. Mat. Fiz., **17**, 6, 1545, 1977.

10. Shcherbak V.G., Numerical investigation of the structure of nonequilibrium three-dimensional hypersonic flow past blunt bodies, Izv. Akad. Nauk SSSR, Mekh. Zhid. Gasa, 5, 143, 1987.

11. Scott C.D., Reacting shock layers with slip and catalytic boundary conditions, AIAA J. **13**, 1271, 1975.

12. Scott C.D., Catalytic recombination of nitrogen and oxygen on high-temperature reusable surface insulation, AIAA Paper 1477, 1980.

13. Shcherbak V.G., Boundary conditions at the shock in supersonic flows past bodies, Zh. Prikl. Mekh. Tekhn. Fiz. 1, 49, 1989.

14. Masek R.V., Hender D. and Forney J.A., Evaluation of aerodynamic uncertainties for space shuttle, AIAA Paper 737, 1973.

15. Brykina I.G., Kovalev V.L., Krupnov A.A., The effective method of solving 3D viscous flows over blunted bodies with real physical-chemical processes, Institute of Mechanics, Moscow State University, Report No 4278, 1993.

16. Hudson M. Evaluation of PNS-computed heating and hypersonic shock tunnel data on sharp and inclined blunt cones. AIAA Paper 310, 1989.

17. Gupta R.N., Moss J.N., Simmonds A.L., Shin J.L., and Zoby E.V., Space Shuttle heating analysis with variation in angle of attack and catalycity, J. Spacecraft and Rockets **21**, 217, 1984.

HYPERSONIC VISCOUS GAS MIXTURE FLOW OVER BLUNT BODIES USING CHEMICAL PARTIAL EQUILIBRIUM MODEL

Vladimir Sakharov, Elena Fateeva

Institute of Mechanics, Moscow State University, Russia
E—mail: sakharov@inmech.msu.su

Abstract

Hypersonic gas mixture flows over blunt bodies are often accompanied by chemical reactions whose rates essentially differ. The model of chemical partial equilibrium has been developed for flow problems under these conditions. In this model the part of differential diffusion equations is degenerated into algebraic relations of detailed chemical equilibrium. The number of such equations is equal to the number of high-rate independent chemical reactions. The component formation sources on the right-hand sides of the remaining diffusion equations of new unknown functions ('slow' combinations of mass fractions) do not contain fast stages. It permits to overcome the stiffness problem. It has been demonstrated that the chemical partial equilibrium model is applicable for determination of the hypersonic flow fields over blunt bodies with a nose radius of approx. 1 m on parts of their reentry trajectories in the Earth's and Martian atmospheres.

Introduction

Let us consider the dissociated and partially ionized gas flows past blunt-nosed bodies entering planetary atmospheres at hypersonic velocities with the nonequilibrium nature of the gas-phase chemical reactions taken into account. The analysis of dimensionless chemical reaction rates (the DamkOhler numbers) shows that such flows are often accompanied by reactions whose rates differ widely, i.e. chemical partial equilibrium sets in. For instance, as a reentry vehicle whose with 1 m characteristic radius enters the Earth's atmosphere at 5-8 km/sec velocities and 50-75 km altitudes, the gas-phase exchange reactions proceed quite fast in the disturbed region, while the dissociation rates are finite. The motion of a reentry vehicle with a blunted nose along a gliding trajectory in the Martian atmosphere is another example. At altitudes exceeding 35 km the ionized mixture flow past a landing module cannot be considered as chemical equilibrium. So the associative ionization reactions are close to equilibrium, while the O_2, N_2, and C_2 molecules dissociate either slowly or with finite rates.

Governing Equations

The Navier-Stokes equations (N-S) describe the flow of a multicomponent viscous heat-conducting gas mixture in the absence of external electromagnetic fields[1-2]. Here, we consider only the diffusion-thermal subsystem written in matrix form.

Let N be the number of mixture species, N_e the number of chemical elements, and R the total number of chemical reactions proceeding in the mixture simultaneously. Let us select a system from $r = N\text{-}N_e$ stoichiometrically independent reactions ($N\text{-}N_e$ is the number of reaction products).

Assuming that the mass fractions and diffusion fluxes of the reaction products, c_i and J_i (i=1,..,r), the mass fractions and diffusion fluxes of the chemical elements, c^*_k and J^*_k (k=r+1,..N), the mixture enthalpy h, and the heat flux J_q are unknown functions, we get

$$div\mathbf{J} + \rho\frac{\partial \mathbf{Z}}{\partial t} + \rho\mathbf{v}\nabla\mathbf{Z} = \mathbf{W}, \quad \nabla\mathbf{Z} = \boldsymbol{\varkappa}\mathbf{J} - \mathbf{K}_p\nabla ln p \qquad (1)$$

$$\mathbf{J} = (J_1,...,J_r,J^*_{r+1},...,J^*_{N-2},J_q)^T$$

$$div\mathbf{J} = (divJ_1,...,divJ_r,divJ^*_{r+1},...,divJ^*_{N-2},divJ_q)^T$$

$$\mathbf{Z} = (c_1,...,c_r,c^*_{r+1},...,c^*_{N-2},h)^T$$

$$\mathbf{W} = (w_1,...,w_r,0,...,0,w_q)^T$$

$$w_i = \frac{\rho m_i}{\tau m}\sum_{j=1}^{R}\Gamma_{ij}\frac{v_j}{\epsilon_{gj}}, \quad \Gamma_{ij} = \mu''_{ij} - \mu'_{ij} \qquad (2)$$

$$Dm_j = \frac{1}{\epsilon_{gj}} = \frac{\tau}{\tau_{gj}} = \tau k_j\left[\frac{p}{kT}\right]^{\mu''_j - 1}$$

$$v_j = K_{pj}p^{\mu'_j - \mu''_j}\sum_{k=1}^{N}x_k^{\mu'_{kj}} - \sum_{k=1}^{N}x_k^{\mu''_{kj}}$$

$$\mu'_j=\sum_{k=1}^{N}\mu'_{kj},\quad \mu''_j=\sum_{k=1}^{N}\mu''_{kj},\quad x_k=\frac{mc_k}{m_k}$$

$$w_q=\frac{dp}{dt}+\hat{\tau}:\hat{e}-divq_R$$

$$\sum_{k=r+1}^{N}c^*_k=1,\quad \sum_{k=r+1}^{N}J^*_k=0$$

$$c^*_E=0,\quad J^*_E=0,\quad p=\frac{\rho R_A T}{m} \qquad (3)$$

The equation set of the first order (1) incorporates r diffusion equations of the species adopted for "reaction products", N_e-2 diffusion equations of the elements, the equation of heat addition, the Stefan-Maxwell relations for the products and elements, and the heat transfer equation. The Stefan-Maxwell relations are not expressed in terms of fluxes **J** via gradients ∇Z. Three relations in (3) are the conditions of quasineutrality and absence of a current[1-2] and the equation of state.

Here ρ, p, T, **v**, and m are, respectively, the density, the pressure, the temperature, mean mass velocity, and mean molecular mass of the mixture, R_A and k are the universal gas and the Boltzmann's constants, w_i is the mass formation rate of the ith product in all the homogeneous chemical reactions, Γ is the stoichiometric matrix corresponding to the reaction products, τ_{gj} is the "chemical" time of the reverse reaction (characteristic chemical time), τ is the characteristic gasdynamic time, K_{pj}, $\bar{k}_j$, Dm_j, ϵ_{gj}, and v_j are, respectively, the equilibrium constant, the reverse reaction rate constant, the DamkOhler number, a parameter inversely proportional to the DamkOhler number, and the deviation from the equilibrium state (motive force) of the jth reaction, μ'_{kj} and μ''_{kj} are stoichiometric coefficients, $\hat{\tau}$, $\hat{e}$, and q_R are the viscous stress and deformation rate tensors and the specific radiation flux, m_i is the mass of the species i. The components of matrix π and vector K_P are connected to diffusion, thermal diffusion, and barodiffusion[1-3].

The free stream conditions for system (1) reduce to specifying v_∞, ρ_∞, T_∞, and $c_{1\infty},..,c_{N\infty}$. The wall is assumed to be impermeable and indestructible with possible heterogeneous catalytic reactions and radiation heat transfer:

$$J_{in}=\dot{s}_i,\quad J^*_{kn}=0,\quad J_{q_n}=\dot{s}_q=q_R-\epsilon\sigma_b(T_w)^4 \qquad (4)$$

$$\mathbf{v}=\mathbf{0}$$

where n is the normal to the surface; $\dot{s}_i$ $(i=1,..,r)$ is the surface formation rate of ith species owing to heterogeneous reactions; ϵ, σ_b, and T_w are, respectively, the emissivity, the Stefan-Boltzmann's constant and radiative surface temperature.

Chemical Partial Equilibrium Flows

Let the reactions proceed in the gas mixture with essentially different rates. Let's accept, that r_f and r_s are the numbers of high-rate (small values of ϵ_{gj} correspond to them) and slow ($\epsilon_{gj}\geq 1$) reactions, which are stoichiometrically independent ($r_f<r$, $r_f+r_s=r$). Note that system from r stoichiometrically independent reactions is selected so that the number of high-rate independent reactions r_f is maximal, and 'slow reactions' mean slow and finite-rate reactions. By R_f and $R_s=R-R_f$ we denote the total number of high-rate and slow reactions respectively.

Let's present ϵ_{gj} as $\epsilon_{gj}=\epsilon(\epsilon_{gj}/\epsilon)$ for $j\leq R_f$. Here $\epsilon<<1$ and $\epsilon_{gj}/\epsilon\simeq 1$. Then $w=(w_1,...,w_r)^T$ in (2) takes the form

$$w=\frac{\rho}{\tau m}M^o\Gamma U,\quad U=\left[\frac{1}{\epsilon}U^1,U^2\right]^T,\quad \Gamma=\begin{bmatrix}\Gamma_{11}&\Gamma_{12}\\ \Gamma_{21}&\Gamma_{22}\end{bmatrix}$$

$$rank\,\Gamma=r,\qquad M^o=diag(M^f,M^s)$$

$$M^f=diag(m_1,..,m_{r_f}),\quad M^s=diag(m_{r_f+1},..,m_r)$$

$$U^1_j=\frac{\epsilon}{\epsilon_{gj}}v_j\ (j=1,..,R_f),\quad U^2_j=\frac{1}{\epsilon_{gj}}v_j\ (j=R_f+1,..,R)$$

The first positions in U^1 are occupied by r_f components corresponding to the independent high-rate reactions. The blocks Γ_{11}, Γ_{12}, Γ_{21}, and Γ_{22} have dimensionalities $r_f\times R_f$, $r_f\times R_s$, $r_s\times R_f$, $r_s\times R_s$ respectively. The matrix of stoichiometric coefficients Γ is construsted so that $rank\,\Gamma_{11}=r_f$.

Then all rows Γ_{21} are linear combinations of rows Γ_{11}:

$$\Gamma_{21}=\mathbf{A}\Gamma_{11},\quad \mathbf{A}=\Gamma_{21}(\Gamma_{11})^T\left[\Gamma_{11}(\Gamma_{11})^T\right]^{-1}$$

$$det(\Gamma_{11}(\Gamma_{11})^T)\neq 0$$

Let's make transformations $\mathbf{Z}^4$ and $\mathbf{J}^{3,5}$ to introduce new unknown functions $\mathbf{u}$ and $\mathbf{I}$:

$$\mathbf{u}=\mathbf{TM}^{-1}\mathbf{Z},\quad \mathbf{I}=\mathbf{TM}^{-1}\mathbf{J}$$

$$\mathbf{M}=diag(\boldsymbol{M}^o,\boldsymbol{M}^*,1),\quad \boldsymbol{M}^*=diag(m_{r+1},..,m_{N-2})$$

$$\mathbf{T}=\begin{bmatrix} E_1 & 0 & 0\\ -A & E_2 & 0\\ 0 & 0 & E_3\end{bmatrix},\quad \mathbf{u}=\begin{bmatrix}\boldsymbol{u}^f\\ \boldsymbol{u}^s\\ \boldsymbol{u}^z\end{bmatrix},\quad \mathbf{I}=\begin{bmatrix}\boldsymbol{I}^f\\ \boldsymbol{I}^s\\ \boldsymbol{I}^z\end{bmatrix}$$

$$u_i^f=\frac{c_i}{m_i},\quad I_i^f=\frac{J_i}{m_i}$$

$$u_l^s=-\sum_{i=1}^{r_f}\alpha_{li}c_i+\frac{c_l}{m_l},\quad I_l^s=-\sum_{i=1}^{r_f}\alpha_{li}J_i+\frac{J_l}{m_l}\qquad (5)$$

$$u_k^z=\frac{c_k^*}{m_k},\quad I_k^z=\frac{J_k^*}{m_k}$$

$$u_{N-1}^z=h,\quad I_{N-1}^z=J_q,\quad \boldsymbol{\alpha}=(\alpha_{li})=\mathbf{A}(\boldsymbol{M}^f)^{-1}$$

$$i=1,...,r_f,\quad l=r_f+1,...,r,\quad k=r+1,...,N-2$$

Here the identity matrices E_1, E_2, and E_3 have dimensionalities $r_f\times r_f$, $r_s\times r_s$ and $(N_e-1)\times(N_e-1)$ accordingly. Functions u_l^s represented the linear combinations of mass fractions are designated as the 'slow' combinations. Then Eqs.(1) become

$$\epsilon\rho\frac{\partial \boldsymbol{u}^f}{\partial t}+\epsilon\rho\mathbf{v}\nabla\boldsymbol{u}^f+\epsilon div\boldsymbol{I}^f=\frac{\rho}{\tau m}\mathbf{W}^f \qquad (6)$$

$$\mathbf{W}^f=\Gamma_{11}U^1+\epsilon\Gamma_{12}U^2$$

$$\rho\frac{\partial \boldsymbol{u}^s}{\partial t}+\rho\mathbf{v}\nabla u^s+div\boldsymbol{I}^s=\frac{\rho}{\tau m}\mathbf{W}^s \qquad (7)$$

$$\mathbf{W}^s=(\Gamma_{22}-\mathbf{A}\Gamma_{12})U^2$$

$$\rho\frac{\partial \boldsymbol{u}^z}{\partial t}+\rho\mathbf{v}\nabla u^z+div\boldsymbol{I}^z=\frac{\rho}{\tau m}\mathbf{W}^z \qquad (8)$$

$$\mathbf{W}^z=\left[0,\frac{\tau m}{\rho}w_q\right]^T$$

$$\nabla\mathbf{u}=\mathbf{III}-\mathbf{K}_p^{(u)}\nabla lnp \qquad (9)$$

$$\mathbf{II}=\mathbf{TM}^{-1}\boldsymbol{\pi}\mathbf{MT}^{-1},\qquad \mathbf{K}_p^{(u)}=\mathbf{TM}^{-1}\mathbf{K}_p$$

Note that $\mathbf{W}^s$ depends only on mass formation rates in the slow and finite-rate chemical reactions. It permits to overcome the stiffness problem in this case. At $\epsilon\to 0$ Eqs.(6) are degenerated into the algebraic equation set of the chemical detailed equilibrium for r_f high-rate independent reactions (the chemical partial equilibrium):

$$v_i=0,\quad (i=1,..,r_f) \qquad (10)$$

Let's mark that it is possible to consider instead of (10) quasi-equilibrium conditions[3]:

$$\Gamma_{11}U^1=0$$

In order to find the partial-equilibrium chemical composition in any point of the medium from (10), it is necessary to know the temperature T, pressure p, N_e-2 mass fractions of elements c_k^*, and r_s 'slow' combinations u_l^s from the solutions of the differential equations and to use expressions u_l^s and c_k^* in terms of c_i and $\sum_{i=1}^{N}c_i=1$. To express the 'fast' fluxes $\boldsymbol{I}^f$ in terms of $\boldsymbol{I}^s$ and $\boldsymbol{I}^z$ it is necessary to write the Stefan-Maxwell relations for the deviations from the equilibrium v_i and to equate appropriate r_f deviations to zero. Then obtained relations are substituted in Eqs.(9) and the transfer equations for 'slow' combinations are derived. These equations close the appropriate diffusion equations for the 'slow' combinations (7) and (8) with wall boundary conditions following from (4)

$$\boldsymbol{I}_n^s=-A(\boldsymbol{M}^f)^{-1}\dot{\boldsymbol{s}}^f+(\boldsymbol{M}^s)^{-1}\dot{\boldsymbol{s}}^s,\quad \boldsymbol{I}_n^z=\dot{\boldsymbol{s}}^z \qquad (11)$$

$$\dot{\boldsymbol{s}}^f=(\dot{s}_1,...,\dot{s}_{r_f})^T,\quad \dot{\boldsymbol{s}}^s=(\dot{s}_{r_f+1},...,\dot{s}_r)^T$$

$$\dot{\boldsymbol{s}}^z=(0,...,0,\dot{s}_q)^T$$

Results for the Earth's and Martian Atmospheres

The model of chemical partial equilibrium has been used for the numerical simulation of hypersonic viscous multicomponent gas flows past a blunt bodies in the framework of the boundary layer model[6] and the full nonequilibrium 2-D N-S. The flow conditions correspond to proceeding along the part of the reentry trajectory of the "Space Shuttle" (5th flight,

H= 50-70 km). 11-species air model with 49 chemical reactions is considered.

At the beginning, the hypersonic flows over the axisymmetric blunt body are calculated using the boundary layer equations on the stagnation streamline. The implicit finite difference scheme of the fourth order of an accuracy on the normal coordinate[7] is applied to the numerical solution. The preliminary analysis of the DamkOhler numbers has shown that it is enough to enter only one 'slow' combination of mass fractions (and diffusion fluxes accordingly) in the considered case:

$$u_1^s = \frac{c(O)}{m(O)} + \frac{c(N)}{m(N)} + 2\left[\frac{c(NO^+)}{m(NO^+)} + \frac{c(O_2^+)}{m(O_2^+)} + \right.$$

$$\left. + \frac{c(N_2^+)}{m(N_2^+)}\right] + 3\left[\frac{c(O^+)}{m(O^+)} + \frac{c(N^+)}{m(N^+)}\right]$$

As an example, the results of calculations for the trajectory point on 54 km altitude (ρ_∞=0.411 · 10^{-3} kg/m^3, v_∞=4.56 km/sec) are submitted for a body with 1 m bluntness radius. The surface temperature is assumed fixed (T_W=1350°K). The profiles of species mass fractions c_i plotted against the Lees-Dorodnitsyn coordinate η are represented in fig.1,2 (noncatalytic surface) and fig.3 (full catalytic surface): symbols, solid and dashed lines correspond, respectively, to the profiles of the solutions of the full diffusion-thermal problem (full model), the partial-equilibrium model and the full equilibrium model. Value of $c(NO^+)$ is increased in 10^3 times in fig.2.

Further the N-S are used for flow calculations past a sphere. A finite-volume implicit numerical algorithm (TVD-scheme) is developed to solve the 2-D time-dependent N-S in conservation form[8]. It is assumed that the flux vector can be split into inviscid and viscous parts. The convective fluxes are descretized by the procedure based on Godunov's method using second-order monotonic scheme. The used scheme is based on a second-order 'minmod' limited extrapolation of the physical variables. The diffusive numerical fluxes are calculated using interpolation and central differences of the conservative variables. The steady-state solution of the discretized equations is obtained by implicit local time stepping. The technique utilizes the line Gauss-Seidel relaxation in the marching direction and the sweep in the normal direction to the surface.

Note, that the numerical simulation of the hypersonic flow in the framework of the full N-S assumes deriving the solution in a whole disturbed region over the body including the shock wave structure. An analysis of the DamkOhler numbers for such conditions does not permit to limit by one 'slow' combination. It is connected with the strong chemical nonequilibrium in the relaxation zone near the fuzzy shock wave. In this case the whole group of chemical reactions being high-rate in the boundary layer passes into category 'slow' ones, and the maximal number of independent high-rate reactions decreases by unit. Because of this, the second 'slow' combination linearly independent with the first one is introduced:

$$u_2^s = \frac{c(N)}{m(N)} + \frac{c(NO)}{m(NO)} + \frac{c(NO^+)}{m(NO^+)} + \frac{c(N^+)}{m(N^+)} +$$

$$+ 2\left[\frac{c(O^+)}{m(O^+)} + \frac{c(N_2^+)}{m(N_2^+)}\right]$$

Fig.4 shows the flow calculation results for 0.5 m radius sphere at the following free stream conditions: ρ_∞=0.392 · 10^{-4} kg/m^3, and v_∞=7.17 km/s (altitude H=74.9 km). Wall is assumed to be noncatalytic with T_W=1350°K. The resultant profiles plotted against the dimensionless normal to the surface coordinate y are represented by symbols for the full model, by dashed lines for the model using one 'slow' combination, and by solid lines for the model using two 'slow' combinations. Data in fig.4-9 correspond, respectively, to the stagnation streamline θ= 0° (a) and the line with θ= 80° (b). Let's remark that the distributions of the gasdynamic parameters (p, ρ, T, **v**) agree very closely for all considered models (see fig.5-7). Some results of similar calculations for the full catalytic surface are submitted in fig.8. The similar comparisons for another trajectory point (ρ_∞=0.998 · 10^{-4} kg/m^3, v_∞=6.19 km/s, H=61.9 km) are shown in fig.9 in the case of noncatalytic wall.

It is necessary to note that with the increase of the sphere radius the solutions of a problem obtained using the full model and the approach of the chemical partial equilibrium are brought closer together still further. As size of a body is about several centimeters, the distributions of the gasdynamic parameters remain close to each other for all three models, while in the values of mass fractions the distinctions are observed.

In the paper[9] the problem of chemically nonequilibrium flow past blunt body (bluntness

radius is 0.425 m) entering in the Martian atmosphere has been numerically resolved in the framework of the N-S. The flow conditions H=41.7 km, $\rho_\infty=0.269\cdot10^{-3}$ kg/m^3, v_∞=6.16 km/s, and T_W=2250°K simulate the most heat-intensive point of the trajectory. 16-species CO_2-N_2 mixture is used. For reaction system considered in the paper[9] we introduce one 'slow' combination:

$$u_1^s=\frac{c(C)}{m(C)}+\frac{c(O)}{m(O)}+\frac{c(N)}{m(N)}-\frac{c(CO_2)}{m(CO_2)}+2\left[\frac{c(O_2^+)}{m(O_2^+)}+\right.$$

$$\left.+\frac{c(CO^+)}{m(CO^+)}+\frac{c(NO^+)}{m(NO^+)}\right]+3\left[\frac{c(C^+)}{m(C^+)}+\frac{c(O^+)}{m(O^+)}\right]$$

The partial-equilibrium composition is calculated along the stagnation streamline using values T and u_1^s from the paper[9] for comparison between the solutions of the full model and the model using one 'slow' combination (see fig.10). The notations are similar to fig.1-3. Some distinctions of mass fractions are observed in the relaxation zone near the fuzzy shock wave, that indicates necessity of introduction of an additional 'slow' combination, as it has been made above for the air flow fields.

In fig.1-3,10 the equilibrium values are shown by the dashed lines. Their strong difference from the exact values (full model) and the values obtained in the framework of the chemical partial equilibrium model is evident.

Conclusion

Finally, it should be stated that the above-proposed method for the describing partial-equilibrium flows of viscous heat-conducting multicomponent gas mixture permits a substantial simplification of the diffusion-thermal component of the problem. The approach may be used over wide ranges of temperatures and pressures, including flows past reentry modules on parts of their reentry trajectories in the Earth's and Martian atmospheres.

References

[1]Suslov,O.N., Tirskiy,G.A., and Schennikov, V.V., "Description of the Chemical Equilibrium Flows of Multicomponent Ionized Mixtures in the Framework of the Navier-Stokes and Prandtl Equations," *PMTF*, N1, 1971, pp.73-89, (in Russian).

[2]Piluygin,N.N., and Tirskiy,G.A., *Dynamics of an Ionized Radiating Gas*, Moscow State University, 1989, 310p.,(in Russian).

[3]Suslov,O.N., and Fateeva,E.I.,"Application of the Methods of the Chemical Partial Equilibrium and Quasistationary Concentrations for the Description of the multicomponent diffusion in the moving, viscous. heat-conducting mixtures," Institute of Mechanics, Moscow State University, *Report* N4325, 1993, 59p., (in Russian).

[4]Gorskiy,V.G., Katsman,E.A., and Shvetsova-Shilovskaya,T.N., "Mathematical Aspects of Quasi-Equilibrium of Reactions in Chemical Kinetics," in collection *Matematicheskie Metodu v Himicheskoi Kinetike*, Novosibirsk: Nauka, 1990, pp.136-152, (in Russian).

[5]Suslov,O.N., and Fateeva,E.I.,"Analysis of Multicomponent Gas Mixture flows with Partial Chemical Equilibrium," *J. of Fluid Dynamics*, vol.31, N1, 1996, pp.97-106.

[6]Sakharov,V.I., Suslov,O.N., and Fateeva,E.I., "Investigation of the Flow past Blunt Bodies under Chemical Partial Equilibrium Conditions in the Framework of the Boundary Layer Equations," *J. of Fluid Dynamics*, vol.32, N2, 1997.

[7]Kovalev,V.L., and Suslov,O.N., "High-Accuracy Differential Method for Integration of Chemically Nonequilibrium Multicomponent Viscous Shock Layer Equations," in collection *Giperzvukovye Prostranstvennye Techeniya pri Nalichii Fiziko-Himicheskih Prevraszheniy*, Moscow State University, pp.113-138, 1981, (in Russian).

[8]Polyansky,V.A., Sakharov,V.I., and Pankrat'eva,I.L., "Calculation of viscous compressible flows using higher-accuracy monotonic schemes," Institute of Mechanics, Moscow State University, *Report* N4189, 1992, 43p., (in Russian).

[9]Chen,Y.K., Henline,W.D., Stewart,D.A., and Candler,G.V., "Navier-Stokes Solutions with Surface Catalysis for Martian Atmospheric Entry," *J. of Spacecraft and Rockets*, vol.30, N1, 1993, pp.32-42.

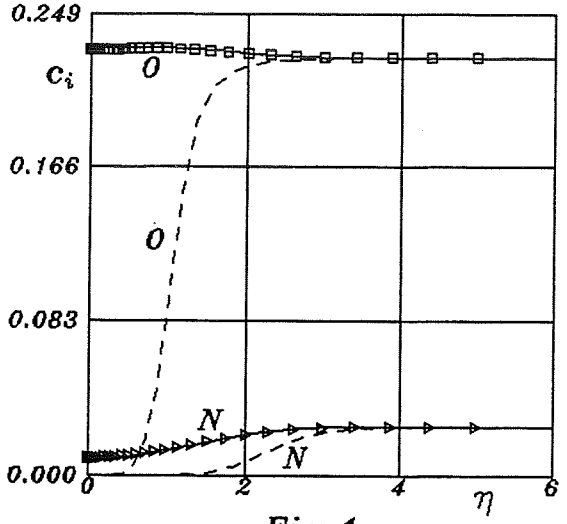

Fig.1

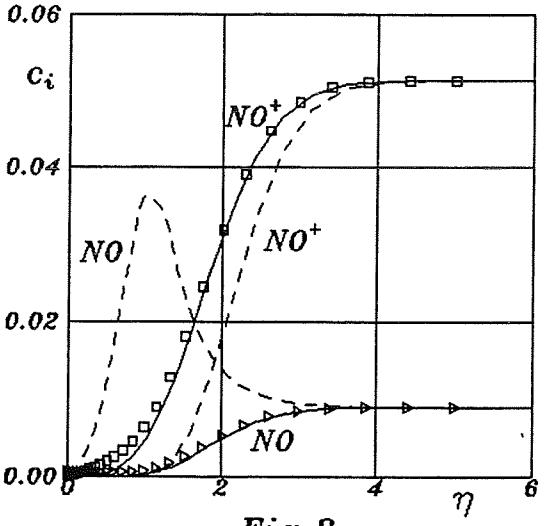

Fig.2

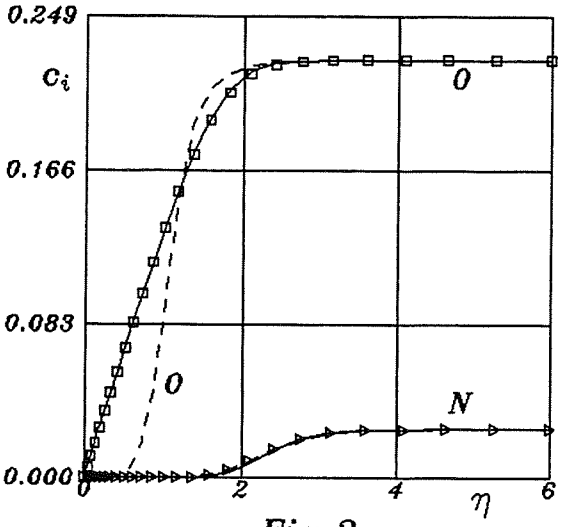

Fig.3

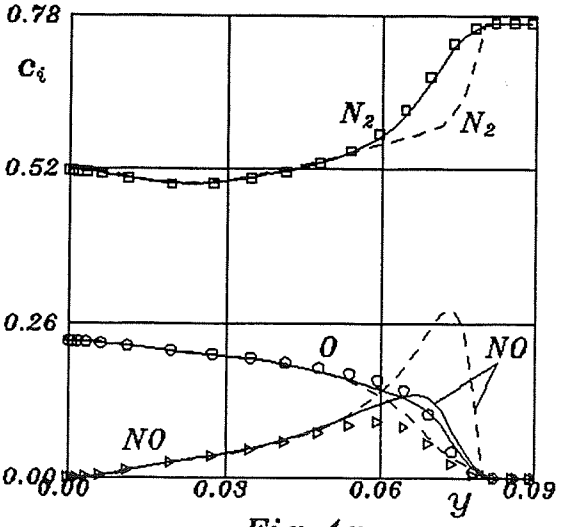

Fig.4a

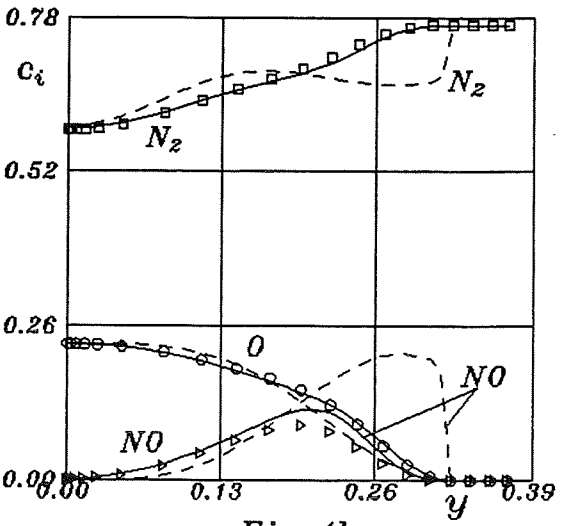

Fig.4b

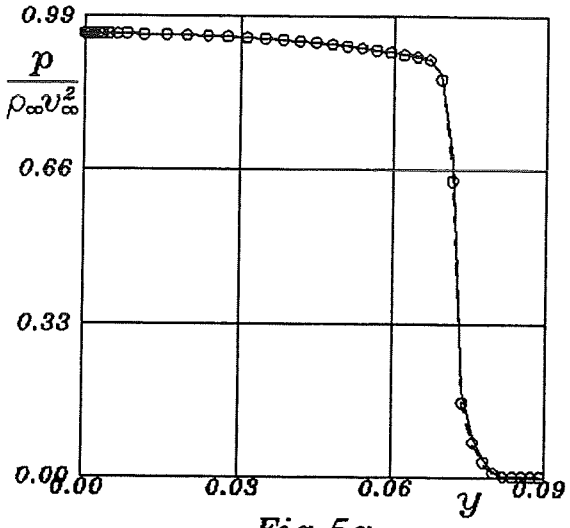

Fig.5a

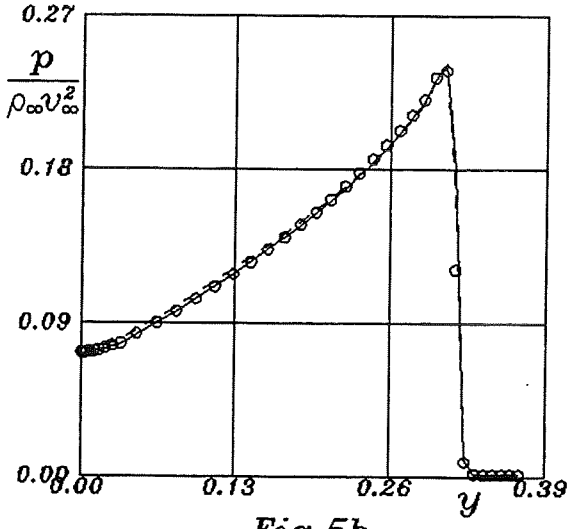

Fig.5b

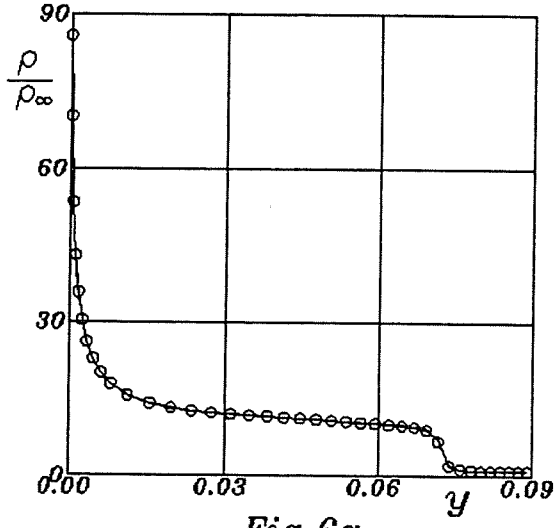

Fig.6a

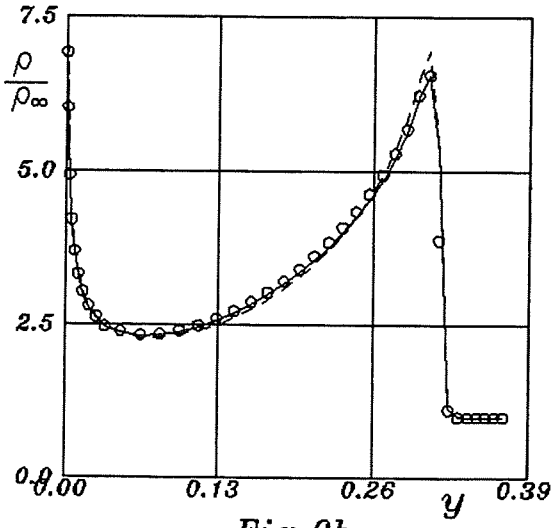

Fig.6b

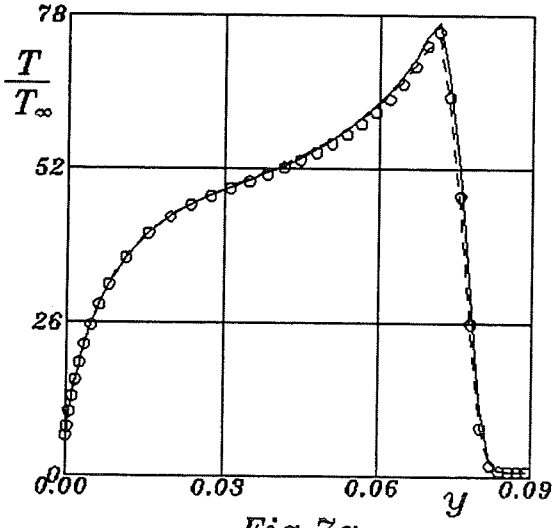

Fig.7a

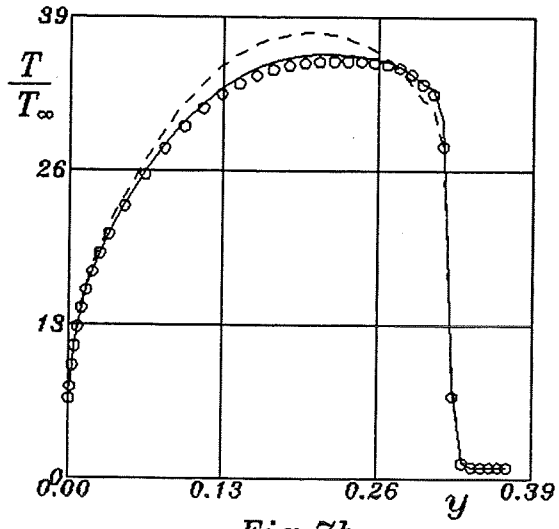

Fig.7b

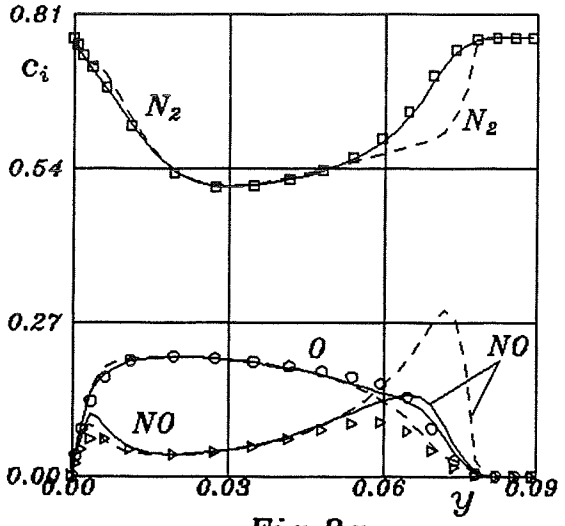

Fig.8a

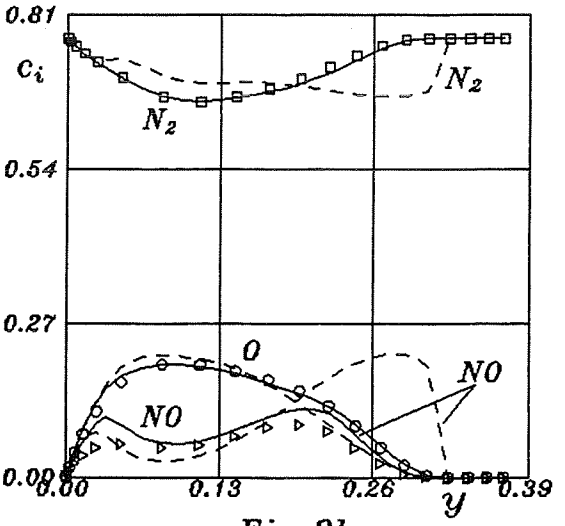

Fig.8b

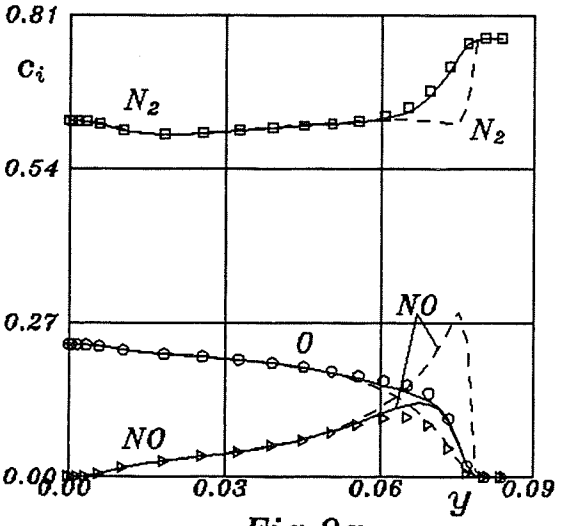

Fig.9a

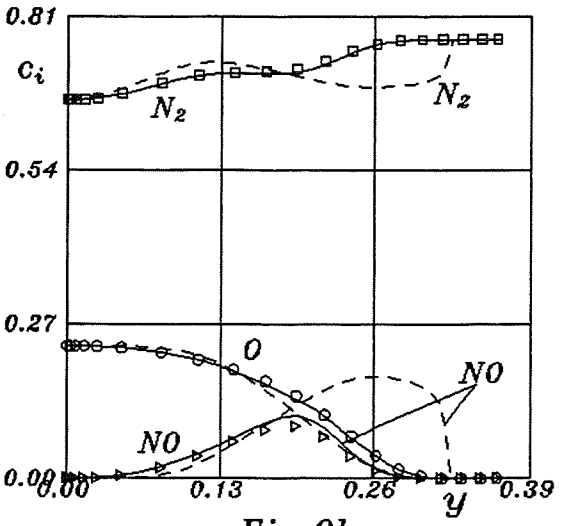

Fig.9b

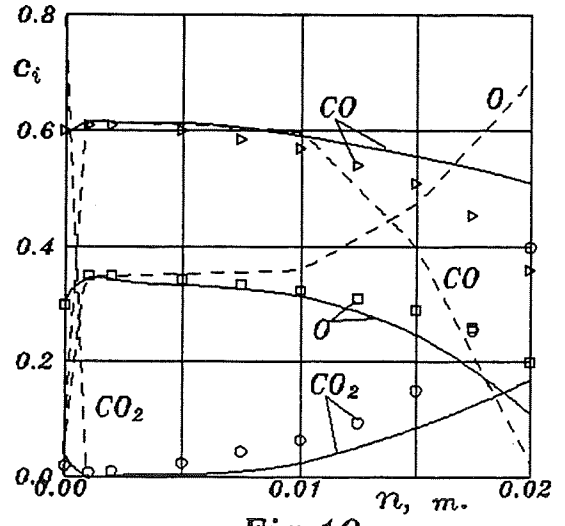

Fig.10

MULTIPHYSICS SIMULATION FOR COUPLED FLUIDS, THERMAL AND STRUCTURAL ANALYSIS ON HIGH-PERFORMANCE PARALLEL COMPUTING PLATFORMS.

Steven M. Rifai
Centric Engineering Systems, Inc.
Sunnyvale, California

Abstract

This article describes some of the theoretical foundations and applications of the Spectrum™ Solver. Spectrum, a multiphysics simulation software based on the finite element method, addresses compressible and incompressible fluid flow, structural, and thermal modeling as well as the interaction between these disciplines. Multiphysics simulation is based on a single computational framework for the modeling of multiple interacting physical phenomena. Interaction constraints are enforced in a fully-coupled manner using the augmented-Lagrangian method. Within the multiphysics framework, the finite element treatment of fluids is based on the Galerkin-Least-Squares (GLS) method with discontinuity capturing operators. The arbitrary-Lagrangian-Eulerian method is utilized to account for deformable fluid domains. The finite element treatment of solids and structures is based on the Hu-Washizu variational principle. The multiphysics architecture lends itself naturally to high-performance parallel computing. Several industrial applications are presented.

1. Introduction

Many of the current directions in product design and analysis are driven by competitive and regulatory constraints, such as the need to shorten design cycles, reduce cost, meet increasingly stringent government regulations, improve quality and safety, and reduce environmental impact. These directions have increased the need for accurate product and component simulation and pressed analysts for simulations of unprecedented scale and complexity. Many of today's computations require simulation of coupled physical phenomena, modeling of more product details, resolution of finer time scales, and investigation of larger design spaces. Typically, these simulations are 3-dimensional, mathematically nonlinear, and often transient.

While single processor computers improve every year, the quantum increase in computational needs requires a quantum increase in computational power. The hardware industry is answering this increased need with affordable high-performance parallel architectures which are built on commodity parts and compatible with workstation systems. These architectures offer the level of computational performance and increased memory capacity needed for large-scale computing. Because the underlying architecture is different than traditional uniprocessor or vector computers, this increased performance is most fully available to codes designed to take advantage of the new design.

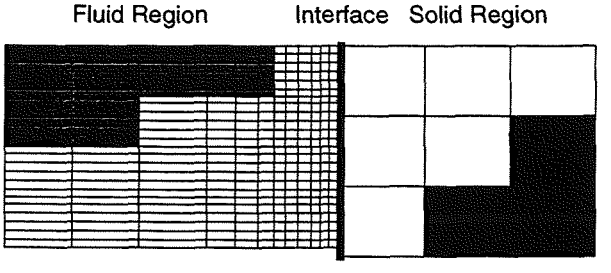

Figure 1. Multiphysics problem domain.

Multiphysics simulation is based on a single computational framework for the modeling of multiple interacting physical phenomena. In this model, the problem domain is decomposed into spatial regions (as illustrated in Figure 1), each simulating a different physical discipline. By using the finite element formulation, (automatically generated) unstructured meshes are admitted. The different disciplines interact at the shared region boundaries through general purpose interfaces. Because of the varying discretization requirements of the different physical phenomena, this approach is designed to allow variable mesh densities and element topologies at the region interfaces. The generality of the interface treatment permits a variety of interaction constraints to be used independently on the mechanical, thermal and mesh field variables. The slave-master algorithm is used to impose continuity relations between two sides of an interface. These interaction constraints are enforced in a fully-coupled manner using the augmented-Lagrangian method with the Uzawa algorithm. Penalty-enforcement of these constraints is a special case of the method.

The multiphysics architecture lends itself naturally to high-performance parallel computing. Coarse grain parallel processing is utilized through the SPMD paradigm

with domain decomposition. Within each problem subdomain, data-parallelism, vector processing and cache efficiency is leveraged with element blocking schemes.

Within the multiphysics framework, the finite element treatment of fluids is based on the Galerkin-Least-Squares (GLS) method with discontinuity capturing operators. The compressible flow formulation is expressed in a symmetric, conservative form, employing physical entropy variables. Rigorous proofs of the mathematical properties of this method are available in the literature. Reynolds-averaged and Large-Eddy-Simulation models are utilized for turbulence simulation. The arbitrary-Lagrangian-Eulerian method is utilized to account for deformable fluid domains. The finite element treatment of solids and structures is based on the Hu-Washizu variational principle. These methods are well documented in the literature to address numerical locking phenomena. The kinematic description admits small and finite deformations and strains. The structural formulations (beams and shells) are expressed in resultant form. The exponential map is employed for rotational updates which are geometrically exact and singularity free. Linear and nonlinear material models are used for the constitutive relations with thermo-mechanical coupling. The structural elements are coupled to all the material models in the constitutive library.

2. The Multiphysics Problem Model

The multiphysics architecture supports multiple physical interactions through a data model defined as a hierarchical tree of regions and interfaces[1]. Regions of a problem are used to separate the different physics being analyzed over the spatial domain. For example, in a fluid-structure interaction (FSI) problem, the fluid domain is one region and the solid structure is another (Figure 1). Interfaces are used to enforce the coupling constraints between the different regions.

Because of the varying discretization requirements of the different physical phenomena, this approach is designed to allow variable mesh densities and element topologies at the region interfaces. The finite element formulation admits (automatically generated) unstructured meshes. For example, in a typical FSI problem, a highly refined tetrahedral mesh may be used to model the fluid domain with a relatively coarse hexahedral discretization representing the solid region. These discretizations do not, in general, coincide at the shared region boundaries.

To support various element types, each region contains multiple element sets. Each element set is uniform in material model, element topology and element formulation. As described in section 7 below, this decomposition organization is not only useful for user model management, but is also utilized to leverage dataparallel, vector and cache-sensitive hardware architectures.

3. Fluids

The finite element treatment of fluid regions within this framework is based on the Galerkin-Least-Squares (GLS) method with discontinuity capturing operators[2-5]. Reynolds-averaged and Large-Eddy-Simulation models are utilized for turbulence simulation[6]. In this treatment, the compressible flow formulation makes use of the *physical entropy variables*

$$V^c = \frac{1}{T^c}\begin{pmatrix} \tilde{\mu} - |u|^2/2 \\ u_1 \\ u_2 \\ u_3 \\ -1 \end{pmatrix}^c , \tag{1}$$

where the superscript c denotes compressible flow variables, T is the fluid temperature and u is the fluid velocity. The chemical potential $\tilde{\mu}$ is defined as

$$\tilde{\mu} = e + p/\rho - Ts , \tag{2}$$

with e, s, ρ and p being the specific internal energy, specific entropy, density and pressure, respectively.

With these variables, the fluid conservation laws are expressed in symmetric form which intrinsically expresses the mathematical and physical stability provided by the second law of thermodynamics. In turn, the finite element techniques employed herein inherit this fundamental stability and convergence proofs are available[7].

Entropy variables, however, do not yield the most efficient form of the incompressible equations. In practice, the advantages of the entropy variable formulation are not significant without the presence of the shocks and discontinuities of compressible flows[4]. Hence, the state variables used in the incompressible flow formulation are defined as

$$V^i = \begin{pmatrix} p/\rho \\ u_1 \\ u_2 \\ u_3 \\ T \end{pmatrix}^i , \tag{3}$$

where the superscript i denotes incompressible flow variables.

With the definitions above, the Navier-Stokes equation system can be expressed as follows: A solution V is sought for the symmetric convective-diffusive system

$$\tilde{A}_0 V_{,t} + \tilde{A}_i V_{,i} = (\tilde{K}_{ij} V_{,j})_{,i} + \tilde{F}^{src} \tag{4}$$

where

$$\tilde{A}_0 = U_{,V}, \tag{5}$$

$$\tilde{A}_i = F^{conv}_{i,V}, \tag{6}$$

$$\tilde{K}_{ij} V_i = F^{diff}_i, \tag{7}$$

and

$$\tilde{F}^{src} = F^{src}(U(V)). \tag{8}$$

Here U is the vector of conservation variables, V is the vector of entropy variables, and $U = U(V)$ is the appropriate transformation of variables leading to the *symmetric* system. The matrices $\tilde{A}_0$, $\tilde{A}_i$, and $\tilde{K}_{ij}$ and the vector $\tilde{F}^{src}$ are nonlinear functions of V. For convenience, the vector $\tilde{C}$ is introduced such that the source vector may be written as $\tilde{F}^{src} \equiv -\tilde{C}V$.

3.1. The Galerkin-Least Squares Formulation

The finite element weighted residual formulation is as follows: given the definition of the above vectors and matrices, find solution vector V^h such that for all admissible weighting functions, W^h, the vector V^h satisfies the variational equation

$$\begin{aligned}
&\int_\Omega \Big(W^h \cdot \tilde{A}_0 \dot{V}^h - W^h_{,i} \cdot F^{conv}_i\Big(V^h\Big) \\
&\quad + W^h_{,i} \cdot \tilde{K}_{ij} V^h_{,j} - W^h \cdot \tilde{F}^{src}\Big(V^h\Big)\Big) d\Omega \\
&+ \sum_{e=1}^{n_{elem}} \int_{\Omega^e} \Big(LW^h + \tilde{C}W^h\Big) \cdot \tau \Big(L_t V^h - \tilde{F}^{src}\Big) d\Omega \\
&+ \sum_{e=1}^{n_{elem}} \int_{\Omega^e} \nu\ W^h_{,\xi_i} \cdot \tilde{A}_0 V^h_{,\xi_i} d\Omega \\
&= \int_\Gamma W^h \cdot \Big(-F^{conv}_i\Big(V^h\Big) + F^{diff}_i\Big(V^h\Big)\Big) n_i d\Gamma
\end{aligned} \tag{9}$$

where Ω is the computational domain with boundary Γ; Ω^e is the domain of element e, $e = 1, \ldots, n_{elem}$; and n_{elem} is the total number of elements. The vectors V^h and W^h are the usual finite element functions; they are piecewise polynomials within each element domain Ω^e and C^0 continuous over the entire domain Ω. The vector $\dot{V}^h$ is the time derivative of V^h; ξ is a generalized vector of local coordinates for each element domain Ω^e; and n is the outward normal to the boundary Γ.

In equation (9), the first integral on the left-hand side and the integral on the right-hand side constitute the usual Galerkin formulation as applied to the symmetric convective-diffusive system. The convective and diffusive fluxes, F^{conv}_i and F^{diff}_i, are formulated in an integrated-by-parts form. This results in the conservation of fluxes under all quadrature rules. In addition, the boundary integrals (right-hand side of equation (9)) lead to a set of natural (or Neumann) boundary conditions.

In equation (9), the second integral on the left-hand side is the *least-squares* operator. The time dependent quasi-linear differential operator for the symmetric convective-diffusive system is

$$L_t V^h \equiv \tilde{A}_0 \dot{V}^h + L V^h \text{ where} \tag{10}$$

$$L V^h \equiv \tilde{A}_i \frac{\partial}{\partial x_i} V^h - \frac{\partial}{\partial x_i} \tilde{K}_{ij} \frac{\partial}{\partial x_j} V^h \tag{11}$$

The metric τ is the *least-squares matrix* and is a symmetric positive-semidefinite matrix of intrinsic time scales. The design of τ crucially influences the behavior of the numerical solutions; therefore, considerable care is required here.

In equation (9), the third integral on the left-hand side is the *discontinuity-capturing* operator. The scalar discontinuity-capturing factor ν has dimension of reciprocal time and is a function of the residual of the differential equation, $L_t V^h - \tilde{F}^{src}$. The operator satisfies three fundamental properties:

- It acts in the direction of the gradient to control oscillations.
- It is proportional to the residual $L_t V^h - \tilde{F}^{src}$ for consistency.
- It vanishes quickly in smooth regions of the solution to ensure accuracy.

These properties are achieved through the proper choice of ν.

3.2. The Arbitrary Lagrangian-Eulerian Formulation

Multiphysics problems often require the movement of the computational fluid domain in response to the defor-

mation of the common solid region boundaries. The arbitrary-Lagrangian-Eulerian (ALE) method is utilized to account for the deformations in fluid domains[8].

ALE boundary conditions ensure that the deforming mesh conforms to both the stationary and moving boundaries. Within the interior of the fluid domain, mesh movement is modeled by the equations of large deformation elasticity. In effect, this model computes the position of the interior nodes as if all nearest nodal neighbors were coupled by an elastic medium and sets the positions and velocities of the boundary nodes to exactly match the boundary motions. Note that this model is a purely mathematical construct; it is a method for updating the mesh in a way that has a reasonable chance of maintaining mesh integrity. Thus, terms such as Cauchy stresses, elastic moduli, and so forth do not have the usual physical interpretation within this context.

To take mesh movement into account, the convective or Euler flux in equations (4),(6) is replaced by the ALE convective flux. The ALE convective flux is related to the Euler flux by the equation

$$\boldsymbol{F}_i^{ALE} = \boldsymbol{F}_i^{conv} - u_i^{ALE}\boldsymbol{U} \tag{12}$$

where $\boldsymbol{u}^{ALE}$ is the velocity field of the mesh. The Euler Jacobians of equation (4) become

$$\tilde{\boldsymbol{A}}_i^{ALE} = \tilde{\boldsymbol{A}}_i - u_i^{ALE}\tilde{\boldsymbol{A}}_0 \tag{13}$$

where the $\tilde{\boldsymbol{A}}_0$ and $\tilde{\boldsymbol{A}}_i$ are defined in equations (5) and (6), respectively. This substitution is equivalent to transforming the material derivatives of field variables using

$$\frac{Dw}{Dt} = w_{,t} + \left(u_i - u_i^{ALE}\right)w_{,i} \tag{14}$$

where w represents any of the field variables.

Note the following special cases:

Eulerian
$$\tilde{\boldsymbol{A}}_i^{ALE} = \tilde{\boldsymbol{A}}_i\,, \qquad \boldsymbol{u}^{ALE} = \boldsymbol{0}$$
$$\boldsymbol{F}_i^{ALE} = \boldsymbol{F}_i^{conv} \tag{15}$$

Lagrangian
$$\tilde{\boldsymbol{A}}_i^{ALE} = \tilde{\boldsymbol{A}}_i - u_i\tilde{\boldsymbol{A}}_0\,, \qquad \boldsymbol{u}^{ALE} = \boldsymbol{u}$$
$$\boldsymbol{F}_i^{ALE} = \boldsymbol{F}_i^{conv} - u_i\boldsymbol{U} \tag{16}$$

4. Structures

The finite element treatment of solid regions within this framework employs a 3-field formulation based on the Hu-Washizu variational principle. This method is well documented in the literature to address numerical locking phenomena[10,11]. The kinematic description admits small and finite deformations and strains. Linear and nonlinear material models are used for the constitutive relations with thermo-mechanical coupling.

The balance of linear momentum in a solid continuum can be expressed for the current and reference configurations in terms of the Cauchy stress, σ and the first Piola-Kirchhoff stress, $\boldsymbol{P}$, respectively.

$$\begin{aligned} \mathrm{div}\sigma + \rho\mathbf{b}_m &= \rho\dot{\boldsymbol{v}} \\ \mathrm{Div}\boldsymbol{P} + \rho_0\boldsymbol{b}_m &= \rho_0\dot{\boldsymbol{v}} \end{aligned} \tag{17}$$

where ρ is the mass density, $\mathbf{b}_m$ is the body force, $\boldsymbol{v}$ is the particle velocity and the 0 subscript denotes a quantity in the reference configuration.

The balance of angular momentum leads to the symmetry requirement on the Cauchy stress tensor, $\sigma = \sigma^T$. This result also leads to a requirement on the first Piola-Kirchhoff stress tensor, $\boldsymbol{F}\boldsymbol{P}^T = \boldsymbol{P}\boldsymbol{F}^T$, and subsequently to the symmetry of the second Piola-Kirchhoff stress tensor, $\boldsymbol{S} = \boldsymbol{S}^T$.

4.1. Three-field Variational Formulation

In order to address incompressibility locking, a mixed method which modifies the interpolation of the deformation gradient is used[10]. The modified deformation gradient is based on a separation of the deformation gradient $\boldsymbol{F}$ into volumetric and deviatoric parts.

$$\boldsymbol{F} = \boldsymbol{F}_{\mathrm{vol}}\boldsymbol{F}_{\mathrm{dev}} \tag{18}$$

The determinant, J, of the deformation gradient measures the volumetric part of the deformation.

$$J = \det\boldsymbol{F} = \det\boldsymbol{F}_{\mathrm{vol}}\det\boldsymbol{F}_{\mathrm{dev}}. \tag{19}$$

This leads to

$$\det\boldsymbol{F}_{\mathrm{vol}} = J \text{ and } \det\boldsymbol{F}_{\mathrm{dev}} = 1\,. \tag{20}$$

In constructing the modified deformation gradient, a mixed treatment replaces the volumetric part. The modified deformation tensor, $\tilde{\boldsymbol{F}}$, is defined using a mixed representation, θ, for the determinant of the deformation gradient.

$$\tilde{\boldsymbol{F}} = (\theta/J)^{1/3}\boldsymbol{F} \tag{21}$$

The virtual modified deformation gradient, $\delta\tilde{\boldsymbol{F}}$, is

$$\delta\tilde{\boldsymbol{F}} = \left[\frac{\delta\theta}{3\theta}\mathbf{1}_t + \left(\nabla\delta\boldsymbol{u} - \frac{1}{3}\mathrm{div}\delta\boldsymbol{u}\mathbf{1}_t\right)\right]\tilde{\boldsymbol{F}} \tag{22}$$

where $\boldsymbol{u}$ is the solid displacement. Here, the rank two identity tensor, $\mathbf{1}_t$, with respect to the current configuration basis vectors $\mathbf{e}_i$, is given by

$$\mathbf{1}_t = \delta_{ij}\mathbf{e}_i \otimes \mathbf{e}_j. \tag{23}$$

Adding the mixed pressure, p, to the motion, ϕ, and the mixed determinant, θ, of the modified deformation gradient completes a three-field variational statement of the problem. Variational equations can be written for the linear momentum, the relationship between the mixed pressure and the trace of the stress, and the relationship between the mixed pressure and the determinant of the deformation gradient.

$$\int_\Omega \delta\boldsymbol{u} \cdot (\rho\dot{\boldsymbol{v}})\, dv + \int_\Omega \mathrm{tr}\,[\nabla\delta\boldsymbol{u}\,(\tilde{\sigma}_{\mathrm{dev}} + p\mathbf{1}_t)]\, dv = \int_\Omega \delta\boldsymbol{u} \cdot (\rho\dot{\boldsymbol{v}})\, dv + \int_\Gamma \delta\boldsymbol{u} \cdot \boldsymbol{t} ds \tag{24}$$

$$\int_\Omega \delta\theta\left(\frac{\mathrm{tr}\tilde{\sigma}}{3\theta} - \frac{p}{J}\right) dv = 0 \tag{25}$$

$$\int_\Omega \delta p\left(1 - \frac{\theta}{J}\right) dv = 0 \tag{26}$$

In this variational statement, the modified Cauchy stress, $\tilde{\sigma}$, in equation (25) is related to the modified Kirchhoff stress, $\tilde{\tau}$, and to the modified second Piola-Kirchhoff stress, $\tilde{S}$, by $J\tilde{\sigma} = \tilde{\tau} = \tilde{F}\tilde{S}\tilde{F}^T$. The spherical part of the stress is given by the mixed pressure, p, not by the trace of the modified Cauchy stress, $\mathrm{tr}\tilde{\sigma}$. The mixed pressure, p, is computed from $\mathrm{tr}\tilde{\sigma}$ using variational relation (25). Thus, the stress in this approach is computed using

$$\sigma = p\mathbf{1}_t + \tilde{\sigma}_{\mathrm{dev}} \tag{27}$$

4.2. Structural Elements

The structural formulations (beams and shells) are expressed in resultant form[12-14]. The exponential map is employed for rotational updates which are geometrically exact and singularity free. The structural elements are coupled to general material models using numerical integration of the constitutive relations through the thickness direction. For brevity of exposition, these formulations will not be described herein.

5. Heat Transfer

The energy balance equation for heat transfer gives temperature rates in terms of heat flux, $\boldsymbol{q}$, and a volumetric heat source, r. Because thermal energy is a conserved quantity, the energy balance for a point in a solid body has the form

$$\rho c_v \frac{\partial T}{\partial t} = -\mathrm{div}\boldsymbol{q} + r \tag{28}$$

For isotropic heat conduction using Fourier's Law in a solid material with constant properties, this reduces to

$$\frac{\partial T}{\partial t} = k\ \mathrm{div}\,(\mathbf{grad}T) + r \tag{29}$$

Density, ρ, specific heat, c_v, and thermal conductivity, k, are material-dependent variables. The origin of the volumetric heat source, r, differs depending on the type of analysis, e.g.,

- In a Joule heating problem, the heat source takes the form of electrical dissipation derived from voltage gradients and the electrical conductivity of the material.
- In a thermomechanical problem, the heat source can take the form of either heat dissipation from inelastic deformations of the body, or structural heating from thermal strains and temperature variations in the material properties.

Convective heat flux boundary conditions are applied to element surfaces on a boundary Γ_h. A convective heat flux describes the heat flow from a solid body to a surrounding fluid using Newton's Law of cooling. Here, the sign convention is reversed, and a positive value indicates a flow of energy out of the body.

$$q_n = h\,(T_{\mathrm{surf}} - T_{\mathrm{ref}}) \tag{30}$$

The heat transfer coefficient, $h = h(\boldsymbol{x}, t)$, can be a function of both space and time.

The weak form of the heat transfer problem is

$$\int_\Omega \left(\rho C_p W\dot{T} - (\mathbf{grad}W) \cdot \boldsymbol{q}\right) d\Omega = \int_\Omega W r d\Omega + \int_{\Gamma_h} W h d\Gamma_h \tag{31}$$

The heat flux, h, is prescribed on the boundary, Γ_h, of the body of domain Ω, and the temperature field, $T(x, t)$, must satisfy the boundary conditions at these points.

6. Multiphysics Interfaces

Interactions between regions are enforced through variable unstructured mesh *interfaces* (Figure 1). A slave-master algorithm is used to define the discrete interface constraints of multiphysics problems[9]. These constraints are enforced with the augmented Lagrangian formulation. Full exposition of these algorithms is beyond the

scope of this presentation, however, the basic concepts can be illustrated with simple examples.

6.1. Slave-Master Algorithm

Interfaces are defined on surfaces between two regions labeled as a *master* and a *slave* surface. In FSI applications, the solid surface is chosen as the master surface. A search/projection algorithm identifies the master element facet which contains each slave node. This algorithm supports contact with separation, tied and sliding interfaces.

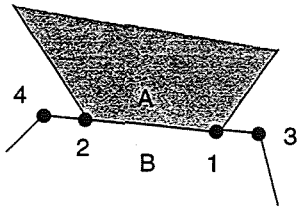

Figure 2. Interface illustration.

The interface constraints which couple the physics between two regions are enforced as a relationship between *state variables* at the slave nodes and the master element facets. This is illustrated in two dimensions in Figure 2, where slave nodes 1 and 2 are tied to master facet B with nodes 3 and 4.

6.2. Augmented-Lagrangian Formulation

To illustrate the augmented Lagrangian formulation, consider the case of thermally and mechanically coupled compressible flow at a fluid slave node, s, with a solid master facet, m. The coupling constraints γ_s for the slave node s in this case are

$$\gamma_s = \left\{ \begin{array}{c} u_1|_s - u_1|_m \\ u_2|_s - u_2|_m \\ u_3|_s - u_3|_m \\ T|_s - T|_m \end{array} \right\} = 0, \qquad s = 1, n_{sn}, \tag{32}$$

where the subscripts s and m denote a quantity at the slave and master surfaces, respectively and n_{sn} is the number of slave nodes on the interface. Recall that u and T are the displacement components and temperature at either side of the interface, respectively. These constraints are enforced through an augmented Lagrangian formulation with penalty regularization. In the Uzawa implementation of this method, two sets of decoupled equation systems are solved in an iteration to determine the physical simulation variables, V, and a set of Lagrange multipliers, λ, associated with the interface constraints. These equation systems can be represented as

$$\begin{aligned} &\left[\frac{dr}{dV} + \frac{d\gamma}{dV} \cdot K \frac{d\gamma}{dV}\right] \Delta V = f \quad , \\ &K \Delta\lambda = \gamma \end{aligned} \tag{33}$$

where r is the equation system associated with the physical simulation variables, f is the residual force associated with that system, γ is the set of interface constraints, ΔV and $\Delta\lambda$ are solution increments, and the matrix K is a diagonal matrix of penalties for regularizing the interface constraints.

For computational efficiency, equation (33) contains some approximations to the rigorous derivation of the augmented Lagrangian formulation. In equation (33)-a, second derivative terms of the interface constraints are omitted from the linearization. In practice, these terms have shown a destabilizing effect on nonlinear iterations for large time steps. In equation (33)-b, the matrix K is an approximation of the linearization of the Lagrangian equations. This approximation is valid for large values of the penalty terms. Both of these approximations are typical in augmented Lagrangian implementations.

The derivatives $d\gamma/dV$ in equation (33) can be obtained from equation (32) by using the chain rule

$$\frac{d\gamma}{dV} = \frac{d\gamma}{dp}\frac{dp}{dV} + \frac{d\gamma}{du}\frac{du}{dV} + \frac{d\gamma}{dT}\frac{dT}{dV}. \tag{34}$$

7. Parallel Processing

The same architecture that supports multiple physics simulation naturally and cleanly supports independent and parallel computation. For each problem, we maintain the concept of multiple subdomains. A subdomain is a collection of regions which are uniform with respect to linear solution technology (e.g., iterative, direct, etc.).

While early research in parallel processing focused on hardware architectures (e.g. SIMD vs. MIMD), the debate is now more appropriately on programming models. Two parallel programming models have emerged as popular and supported approaches: dataparallel and Same-Program Multiple Data (SPMD). The multiphysics architecture provides the support and underlying data structures for efficient parallel processing (as illustrated in Figure 3). At the higher-level, the coarse-grained subdomains map well to the SPMD programming model[1]. At the lower-level, the fine-grained element sets map well to the dataparallel model[15].

Therefore, the multiphysics architecture maps well to either (or both) parallel programming models.

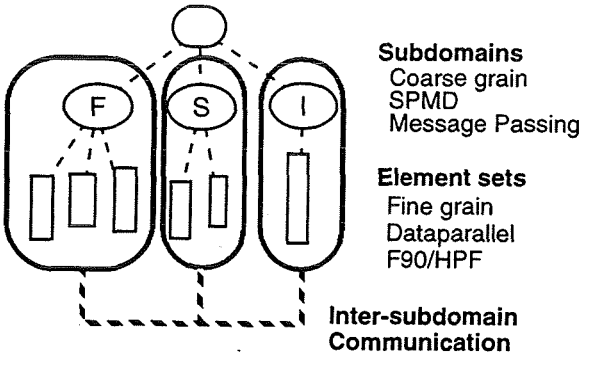

Figure 3. Parallel processing models under the multiphysics architecture.

The dataparallel approach has been investigated on the Thinking Machines CM-5. Dataparallel programming requires significant re-coding in a dataparallel language such as Fortran-90 (F90) or High-Performance Fortran (HPF). Along with these emerging and competing dialects, proprietary languages also exist. Thus no dataparallel language standard exists. In addition, the programmer is expected to specify explicit, and often system dependent, data layout. It was also observed that the unified program view simplifies debugging and the investigation showed good speedup in many cases. However, the program development and support costs are significant and the resulting source code is generally not portable.

By comparison, the alternate approach of SPMD is implemented via message-processing. In this case, there is support for a wide range of hardware platforms with the standard and readily available message-passing interface of PVM and the evolutionary standard MPI. This programming model has the advantage of allowing the reuse of large portions of code from the uniprocessor version. Excellent performance has been demonstrated on a number of different parallel systems for large, multiphysics simulations. The relative ease of programming and support as well as the portability, scalability and wide availability of systems supporting SPMD make it the preferred model for our applications.

In the coarse-grain model, each processor of the parallel machine runs a copy of the application to solve one subdomain of the partitioned grid. Conceptually, this approach attempts to parallelize computation at the newly created subdomain level (i.e., at the outermost loop level). For example, the pseudo-code below shows the outer subdomain loop implicit in the computation.

```
doacross (subdomains)
    perform local subdomain computations
enddo

communicate non-local data

doacross (subdomains)
    ...
enddo
```

In the multiphysics domain, this code structure already exists in the uniprocessor simulator. The translation and communication of data between the physically derived subdomains required a "serial messaging" service. During the initial design of the serial application, the future parallelization of the code was also considered. Consequently, control of the subdomains and communication between them is carefully choreographed in order to create a so-called "shared none" execution from the subdomain viewpoint. For example, the computation of global values for points along an interface is accomplished in a master-slave fashion as shown below:

```
foreach (shared point)
    all slaves post update to master

masters create global values

foreach (shared point)
    all masters post final value to slaves
```

In the serial implementation, updates to boundary nodes are placed in a memory buffer for use by the master. Under the coarse-grain parallel model, updates are passed along via send/receive pairs.

The separation of control from computation in uniprocessor code proved to be a significant design decision. This separation by design, facilitated the straightforward conversion to parallel execution. Fundamentally, the changes are limited to the dispatch operation of the global choreographer and the data exchange mechanism. A schematic description of the coarse-grain parallel architecture is presented in Figure 4.

The decomposition of the computational domain is an active area of research which has produced many algorithms and general purpose tools[16-19]. Many decomposition methods commonly use the recursive spectral bisection (RSB) approach[16]. A significant cost of the RSB method is associated with the computation of eigenvectors of a Laplacian matrix constructed from the adjacency structure of the mesh. Hendrickson and Leland introduced a multi-level implementation for the construction of the Laplacian matrix, resulting in significant CPU performance improvement[18]. Karypis and

Kumar present a rigorous analysis of multilevel methods and demonstrate analytically their effectiveness[19].

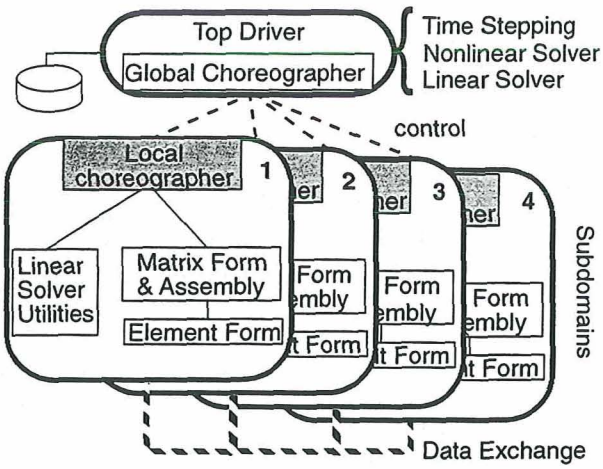

Figure 4. Multi-subdomain architecture for coarse-grain parallel processing.

A common feature of most domain decomposition research is the focus on single homogeneous grid applications. In order to support multiphysics simulations, algorithms which extend the multilevel method of Karypis and Kumar to heterogeneous interfaced discretizations are used in the present approach.

8. Multi-subdomain Equation Solver

To take full advantage of the architecture described above, a multi-subdomain solver is employed to solve the matrix set of equations which result from the discrete finite element problem. In this context, the solver is composed of one global solver and a set of local subdomain solvers. At the subdomain level, the local solver may be explicit, implicit iterative or implicit direct. The local subdomain solver may vary from subdomain to subdomain. The global solver must be implicit iterative.

Two iterative solvers are used for multiphysics problems: the preconditioned conjugate gradient (CG) and generalized minimum residual (GMRES) methods[20-22]. CG is used for symmetric systems which arise, e.g., from solid linear momentum, heat transfer and mesh movement equations. GMRES is used for non-symmetric systems which arise, e.g., from the fluid linear momentum, thermal, scalar transport, and turbulence equations.

The example shown in Figure 5 can be used to demonstrate how the interior nodes of certain subdomains are "removed" from the global solver. The general structure of the equation systems of domain decomposition is also illustrated by the example.

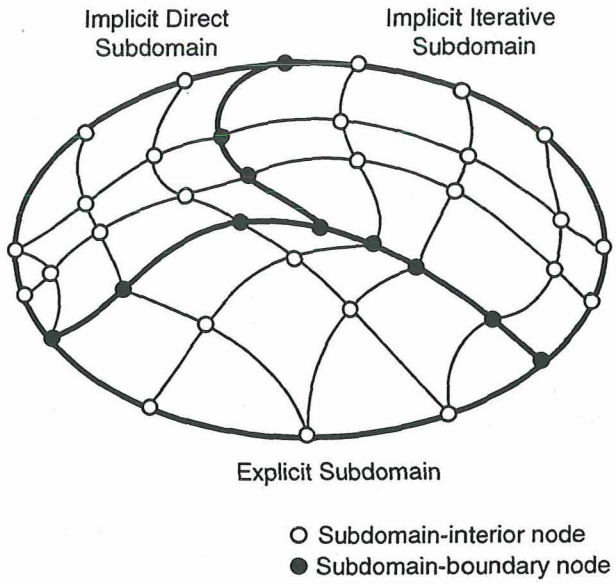

Figure 5. Subdomain partitioning example.

Two sets of nodes are distinguished: subdomain boundary nodes and subdomain interior nodes. Boundary nodes are shared by elements belonging to different subdomains. All other nodes are interior nodes. Arrays associated with interior nodes and boundary nodes are denoted by subscripts 1 and 2, respectively. In solving the global system $\boldsymbol{Ax} = \boldsymbol{b}$, contributions to $\boldsymbol{A}$ are assembled from $\boldsymbol{A}^{exp}$ of the explicit subdomain, $\boldsymbol{A}^{dir}$ of the implicit direct subdomain, and $\boldsymbol{A}^{iter}$ of the implicit iterative subdomain.

These contributions can be written as

$$\boldsymbol{A}^{exp} = \begin{bmatrix} \boldsymbol{A}_{11}^{exp} & \boldsymbol{0} \\ \boldsymbol{0} & \boldsymbol{A}_{22}^{exp} \end{bmatrix} \tag{35}$$

$$\boldsymbol{A}^{dir} = \begin{bmatrix} \boldsymbol{A}_{11}^{dir} & \boldsymbol{A}_{12}^{dir} \\ \boldsymbol{A}_{21}^{dir} & \boldsymbol{A}_{22}^{dir} \end{bmatrix} \tag{36}$$

$$\boldsymbol{A}^{iter} = \begin{bmatrix} \boldsymbol{A}_{11}^{iter} & \boldsymbol{A}_{12}^{iter} \\ \boldsymbol{A}_{21}^{iter} & \boldsymbol{A}_{22}^{iter} \end{bmatrix} \tag{37}$$

where $\boldsymbol{A}^{exp}$ is a block diagonal matrix and both $\boldsymbol{A}^{dir}$ and $\boldsymbol{A}^{iter}$ are potentially nonsymmetric matrices with symmetric profiles.

Figures 6, 7, and 8 graphically represent the structure of these matrices. Note the symmetric skyline structure of A^{dir} and the fact that A^{iter} is stored in the form of unassembled element matrix files.

With these representations, the global system $Ax = b$ is

$$A = \begin{bmatrix} A_{11}^{exp} & 0 & 0 & 0 \\ 0 & A_{11}^{dir} & 0 & A_{12}^{dir} \\ 0 & 0 & A_{11}^{iter} & A_{12}^{iter} \\ 0 & A_{21}^{dir} & A_{21}^{iter} & \left(A_{22}^{exp} + A_{22}^{dir} + A_{22}^{iter}\right) \end{bmatrix} \tag{38}$$

$$x = \begin{Bmatrix} x^{exp} \\ x^{dir} \\ x^{iter} \\ x^{bndy} \end{Bmatrix} \tag{39}$$

$$b = \begin{Bmatrix} b_1^{exp} \\ b_1^{dir} \\ b_1^{iter} \\ \left(b_2^{exp} + b_2^{dir} + b_2^{iter}\right) \end{Bmatrix} \tag{40}$$

where x^{exp}, x^{dir}, and x^{iter} are the solution subvectors for the interior nodes of the three subdomains and x^{bndy} is the solution subvector for the shared boundary nodes. The right-hand side vectors b_1^{exp}, b_1^{dir}, and b_1^{iter} are stored with their respective element subdomain data; whereas $b_2^{exp} + b_2^{dir} + b_2^{iter}$ is stored with the global data.

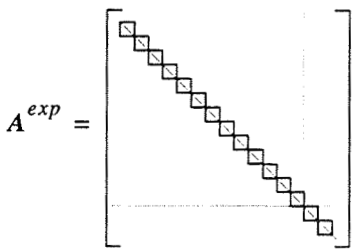

Figure 6. Explicit matrix structure.

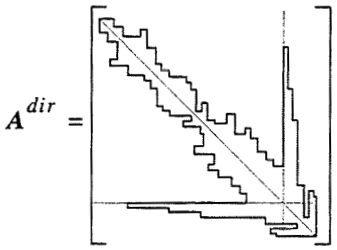

Figure 7. Implicit direct matrix structure.

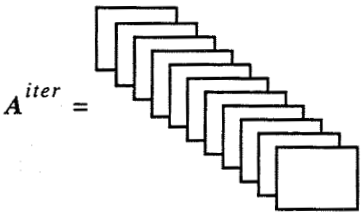

Figure 8. Implicit iterative matrix structure.

Direct solution techniques are used to eliminate x^{exp} and x^{dir}. The solution of

$$A_{11}^{exp} x^{exp} = b_1^{exp} \tag{41}$$

involves the triangularization of uncoupled, symmetric, positive-definite matrices. A static condensation is used to eliminate x^{dir}. The reduced system has the form

$$A^{red} x^{red} = b^{red} \tag{42}$$

where

$$A^{red} = \begin{bmatrix} A_{11}^{iter} & A_{12}^{iter} \\ A_{21}^{iter} & \left(A_{22}^{exp} + \hat{A}_{22}^{dir} + A_{22}^{iter}\right) \end{bmatrix} \tag{43}$$

$$x^{red} = \begin{Bmatrix} x^{iter} \\ x^{bndy} \end{Bmatrix} \tag{44}$$

$$b^{red} = \begin{Bmatrix} b_1^{iter} \\ \left(b_2^{exp} + \hat{b}_2^{dir} + b_2^{iter}\right) \end{Bmatrix} \tag{45}$$

where

$$\hat{A}_{22}^{dir} \equiv A_{22}^{dir} - A_{21}^{dir}\left(A_{11}^{dir}\right)^{-1} A_{12}^{dir} \tag{46}$$

and

$$\hat{b}_2^{dir} \equiv b_2^{dir} - A_{21}^{dir}\left(A_{11}^{dir}\right)^{-1} b_1^{dir} \tag{47}$$

The reduced system contains only the interior nodes of the implicit-iterative elements and the boundary nodes. This is the desired result. Once equation (42) is solved, x^{dir} is determined from

$$x^{dir} = \left(A_{11}^{dir}\right)^{-1}\left(b_1^{dir} - A_{12}^{dir} x^{bndy}\right) \tag{48}$$

The global system has been replaced by equations (41), (42), and (48).

9. Multiphysics Applications

Four applications are presented here to demonstrate the applicability of multiphysics simulation in thermal management and fluid-structure interaction problems. The scalability of the method on parallel computers is also illustrated.

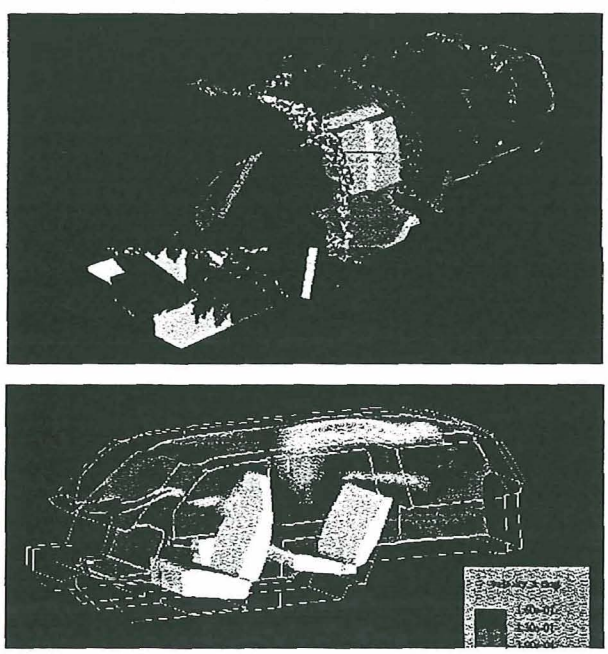

Figure 9. Interior cooling simulation of a sports-utility vehicle. Domain decomposition and velocity contour plane.

9.1. Sport Utility Vehicle

This method has been applied to the simulation of heating and cooling systems in automotive interior comfort analyses[23]. These analyses involve flow simulation through the interior of the vehicle (see Figure 9) and coupled solution of the fluid and solid equations. The computations are performed with automatically generated tetrahedral meshes on high-performance parallel processing platforms. The coupled thermal simulations are transient and involve physical time scales of 15-30 minutes. Excellent agreement has been observed with wind-tunnel experimental data in these simulations[23].

9.2. Exhaust Manifold

Another multiphysics application from the automotive industry is the coupled simulation of flow and thermal deformation within exhaust manifolds (Figure 10). These simulations include the evaluation of fluid flow features such as pressure drop and velocity profiles, and mechanical characteristics such as thermal stresses and vibration amplitudes. The computations are necessarily transient to model the firing sequence of internal combustion engines.

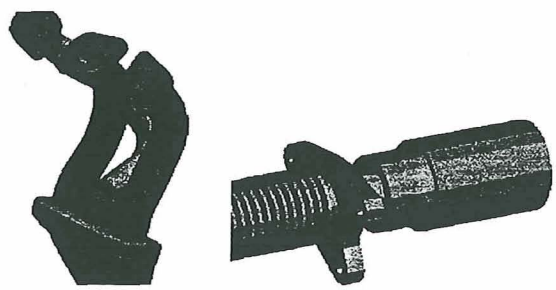

Figure 10. Exhaust manifold partial geometry.

9.3. Wing Aeroelasticity

This method is being utilized to address fixed-wing aeroelasticity at NASA Ames and ONERA[24]. This approach simulates the fully-coupled compressible flow-wing structure interaction problem using "high-fidelity" transient simulations. Each simulation models the oscillation of wing structures at a particular frequency and a set of flight conditions. Good agreement has been shown with experimental results[24].

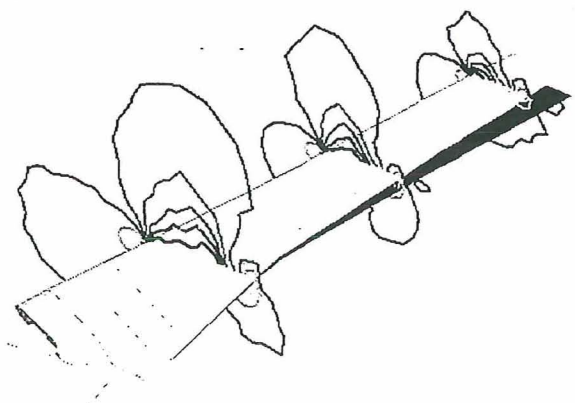

Figure 11. Pressure contours on a deformed wing configuration during an aeroelastic simulation.

9.4. Cowl Lip

The high aerothermodynamic loading on the leading edges of hypersonic flight vehicles leads to a clear example of thermal FSI. This problem class encompasses external hypersonic (compressible) flow with high heating rates near stagnation points, internal coolant (incompressible) flow through the leading edge with heat conduction and convection, and thermal conduction and thermal stresses in the leading edge structure. A study by Melis, et.al. is underway using this method for the simulation of an impingement-cooled cowl lip for hypersonic flight[25].

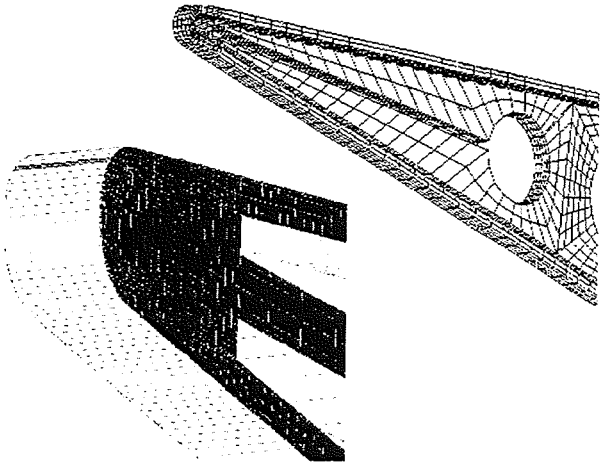

Figure 12. Solid and interior fluid grids for the impingement cooled cowl lip.

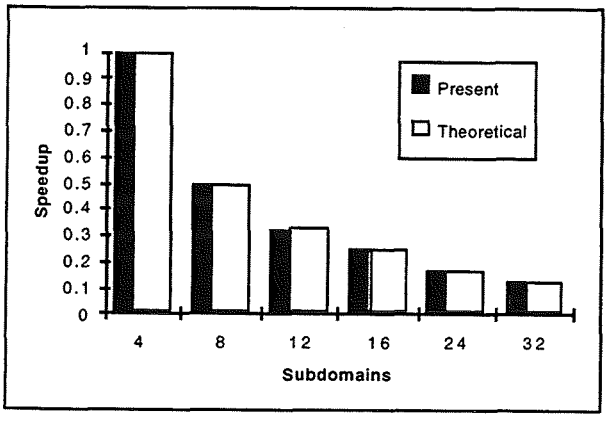

Figure 13. Scalability illustration.

9.5. Scalability

An internal flow computation from a socket instability analysis is used to illustrate the scalability of this method on parallel processing computers. The simulation involved the computation of steady state flow on a 250,000 hexahedral element mesh using the IBM/SP2 testbed at NASA/Ames. The computations were repeated for subdomain decompositions of 4, 8, 12, 16, 24 and 32. The scalability results are illustrated in Figure 13. Excellent scalability was obtained in the entire range in comparison with the theoretical limit. Note that for decompositions of 12 and 16, super-linear scalability is obtained. This phenomenon (achieving higher scalability than the theoretical limit) is explained by the hardware architecture. Many of the current parallel processing hardware platforms use cache-sensitive workstation CPUs. As the number of subdomains increases, the memory usage within each subdomain decreases and at some decompositions, this results in increased cache efficiency which improves the scalability results beyond the theoretical limit.

Conclusions

A multiphysics simulation approach based on the finite element method has been described. This work addresses compressible and incompressible fluid flow, structural, and thermal modeling as well as the interaction between these disciplines. The approach is based on a single computational framework for the modeling of multiple interacting physical phenomena. The augmented-Lagrangian method is used to enforce interaction constraints among all field variables in a fully-coupled manner. Consistent finite element treatments of uniform region balance laws were described within the multiphysics framework. The arbitrary-Lagrangian-Eulerian method is utilized to account for deformable fluid domains.

The efficacy of this method in simulating coupled fluid-solid-thermal interaction was demonstrated with thermal management and flow-induced vibration problems. These applications were derived from industrial models in the automotive and aerospace sectors. The multiphysics architecture lends itself naturally to high-performance parallel computing. The excellent scalability of this approach was illustrated on parallel processing hardware platforms.

References

[1] Eldredge, M., Hughes, T.J.R., Raefsky, R., Ferencz, R., Rifai, S., and Herndon, B., "High-Performance Parallel Computing in Industry," *Parallel Computing*, Special issue on High Performance Computing in Flow Simulations, Eds., Tezduyar, T. and Hughes, T.J.R., to appear.

[2] Hughes, T.J.R., "Recent Progress in the Development and Understanding of SUPG Methods with Special Reference to the Compressible Euler and

Navier-Stokes Equations," *Int. J. Num. Meth. Fluids*, Vol. 7, pp.1261-1275, 1987.

[3] Shakib, F., Hughes, T.J.R., and Johan, Z., "A New Finite Element Formulation for Computational Fluid Dynamics: X. The Compressible Euler and Navier-Stokes Equations," *Comp. Meth. App. Mech. and Eng.*, Vol. 89, pp. 141-219, 1991.

[4] Hauke, G. and Hughes, T.J.R., "A Unified Approach to Compressible and Incompressible Flows," *Comp. Meth. App. Mech. and Eng.*, Vol. 113, pp. 3849-396, 1994.

[5] Chalot, F. and Hughes, T.J.R., "A Consistent Equilibrium Chemistry Algorithm for Hypersonic Flows," *Comp. Meth. App. Mech. and Eng.*, Vol. 112, pp. 25-40, 1994.

[6] Jansen, K. Johan, Z. and Hughes, T.J.R., "Implementation of a One-Equation Turbulence Model within a Stabilized Finite Element Formulation of a Symmetric Advective-Diffusive System," *Comp. Meth. App. Mech. and Eng.*, Vol. 105, pp. 405-433, 1993.

[7] Johnson, C, Szepessy, A. and Hansbo, P., "On the Convergence of Shock-Capturing Streamline Diffusion Finite Element Methods for Hyperbolic Conservation Laws," *Mathematics of Computation*, Vol. 54, pp. 107-129, 1990.

[8] Hughes, T.J.R., Liu, W.K., and Zimmerman, T.K., "Lagrangian-Eulerian Finite Element Formulation for Incompressible Viscous Flows," *Comp. Meth. App. Mech. and Eng.*, Vol. 29, pp. 329-349, 1981.

[9] Doghri, I., Muller, A., and Taylor, R.L., "A General Three-Dimensional Contact Procedure for Implicit Finite Element Codes," *Eng Comp.*, to appear.

[10] Simo, J.C., Taylor, R.L., and Pister, K.S., "Variational and Projection Methods for the Volume Constraint in Finite Deformation Elastoplasticity," *Comp. Meth. App. Mech. and Eng.*, Vol. 51, pp. 177-28, 1985.

[11] Simo, J.C. and Rifai, M.S., "A Class of Mixed Assumed-Strain Methods and the Method of Incompatible Modes," *Int. J. Num. Meth. Eng.*, Vol. 29, pp. 1595-1638, 1990.

[12] Simo, J.C. and Vu-Quoc, L., "A 3-Dimensional Finite Strain Rod Model. Part II: Computational Aspects," *Comp. Meth. App. Mech. and Eng.*, Vol. 58, pp. 79-116, 1986.

[13] Simo, J.C., Fox, D.D. and Rifai, M.S., "On a Stress Resultant Geometrically Exact Shell Model. Part III: Computational Aspects of the Nonlinear Theory," *Comp. Meth. App. Mech. and Eng.*, Vol. 79, pp. 21-70, 1990.

[14] Simo, J.C., Rifai, M.S. and Fox, D.D., "On a Stress Resultant Geometrically Exact Shell Model. Part VI: Dynamic Analysis," *Int. J. Num. Meth. Eng.*, Vol. 34, pp. 117-164, 1992.

[15] Johan, Z., "Data-Parallel Finite Element Techniques for Large-Scale Computational Fluid Dynamics," Ph.D. Thesis, Stanford University, Stanford, 1992.

[16] Simon, H.D., "Partitioning of Unstructured Problems for Parallel Processing," *Comp. Sys. Eng.*, Vol. 2, pp. 135-148, 1991.

[17] Farhat, C. and Lesionne, M., "Automatic Partitioning of Unstructured Meshes for the Parallel Solution of Problems in Computational Mechanics," *Int. J. Num. Meth. Eng.*, Vol. 36, pp. 745-764, 1993.

[18] Hendrickson, B. and Leland, R., "A Multi-level Algorithm for Partitioning Graphs," Sandia National Labs Rep., Albuquerque, NM 87185-1110.

[19] Karypis, G. and Kumar, V., "Analysis of Multilevel Graph Partitioning," Report 95-037, University of Minnesota, Department of Computer Science, Minneapolis, MN 55455, 1995.

[20] Saad, Y. and Schultz, M.H., "GMRES: A Generalized Minimum Residual Algorithm for Solving Nonsymmetric Linear Systems," *SIAM J. Sci. Statist. Comp.*, Vol. 7, pp. 856-869, 1986.

[21] Winget, J.M. and Hughes, T.J.R., "Solution Algorithms for Nonlinear Transient Heat Conduction Analysis Employing Element-by-Element Iterative Strategies," *Comp. Meth. App. Mech. and Eng.*, Vol. 52, pp. 711-815, 1985.

[22] Ferencz, R.M., "Element-by-Element Preconditioning Techniques for Large Scale Vectorized Finite Element Analysis in Nonlinear Solid and Structural Mechanics," Ph.D. Thesis, Stanford University, Stanford, 1989.

[23] Gielda, T.P., Webster, B.E., Hesse, M.E. and Halt, D.W., "The Impact of Computational Fluid Dynamics on Automotive Interior Comfort Engineering," AIAA paper 96-0794, 1996.

[24] Grisval, J.P., Sauvignet, C. and Johan, Z., "Application of the Finite Element Method to Aeroelasticity," Euromech Colloquium 96, Germany, 1996.

[25] Melis, M.E., Gladden, H.J., Schubert, J.F., Westfall, L.J. and Trimarchi, P.A., "A Unique Interdisciplinary Research Effort to Support Cowl Lip Technology Development for Hypersonic Applications," NASA Technical Paper 2876, 1989.

CFD Analysis of Hypersonic Flowfields with Surface Thermochemistry and Ablation

W. D. Henline *
NASA Ames Research Center, MS 230-2,
Moffett Field, CA 94035-1000

September 9, 1997

Abstract

In the past forty years much progress has been made in computational methods applied to the solution of problems in spacecraft hypervelocity flow and heat transfer. Although the basic thermochemical and physical modeling techniques have changed little in this time, several orders of magnitude increase in the speed of numerically solving the Navier-Stokes and associated energy equations have been achieved. The extent to which this computational power can be applied to the design of spacecraft heat shields is dependent on the proper coupling of the external flow equations to the boundary conditions and governing equations representing the thermal protection system in-depth conduction, pyrolysis and surface ablation phenomena. A discussion of the techniques used to do this in past problems as well as the current state-of-art is provided. Specific examples, including past missions such as Galileo, together with the more recent case studies of ESA/Rosetta Sample Comet Return, Mars Pathfinder and X-33 will be discussed. Modeling assumptions, design approach and computational methods and results are presented.

Nomenclature

$\tilde{D}_\alpha$	=	diffusivity for species α against the mean
$\underline{F}$	=	local body function (e.f. acceleration of gravity) for momentum eq.
h_1, h_2, h_3	=	flowfield metrics for body fixed coordinate system
h	=	static enthalpy
H_T	=	total flowfield enthalpy (static and kinetic energy)
$\underline{J}$	=	diffusive mass flux vector
k_T	=	thermal conductivity
P	=	local total pressure
$\underline{q}$	=	total heat flux vector
$\underline{q}^R$	=	total radiative heat flux vector
r	=	local radial distance to flowfield point (axisymmetric flow)
R	=	universal gas constant (equation of state)
R_α	=	gas phase volumetric reaction rate source term for species, α
s, n, t	=	streamwise, normal and tangential body fixed coordinate variables
T	=	temperature
$\underline{V}$	=	flowfield velocity vector
$\underline{v}$	=	flowfield velocity vector in body fixed coordinates
W	=	volumetric source term for total energy equation
u, v, w	=	velcity components along s,n,t coordinate directions in body fixed coordinate system
x, y, z	=	general rectangular cartesian coordinates
x_α	=	mass fraction for species α

Greek Symbols

κ	=	local surface metric or surface curvature function
μ	=	coefficient of viscosity
ρ	=	fluid mass density
τ	=	time variable
$\underline{\underline{\tau}}$	=	total stress tensor

Subscripts and Superscripts

α	=	reference to species "α"
g	=	gas phase
n	=	direction normal to wall
s	=	solid phase
ave	=	average

Introduction and Background

Whenever any spacecraft is placed in an orbit with a high enough energy state, its ultimate return to rest on the surface of a planetary body will result in the rapid dissipation of kinetic energy through either release of stored chemical energy (retro-rockets) or compressive and frictional drag forces due to an atmosphere. This latter situation is the object of the current discussion and

*Research Scientist, Reacting Flow Environments Branch, Senior Member AIAA.

represents the usual hypersonic re-entry physics problems prevalent in modern spacecraft heatshield design. This design issue has been with us since World War II when the German V-2 missile program first encountered pre-mature, in-flight warhead detonations which, after some head scratching, was correctly traced to aerothermodynamic heating of the nosecone during the high dynamic pressure portion of the V-2 trajectory. The solution at the time was to use readily available plywood as an ablative heatshield covering for the warhead. Obviously it worked! Things have progressed somewhat since then, but none of the underlying principles or problems have changed.

With the onset of the Cold War, development of ballistic missile technology provided a boost to activities in the theoretical aspects of hypersonic flight and heat transfer. Re-entry vehicles for these military missions experienced flight environments where peak dynamic pressures exceeded several tens of atmospheres and stagnation heat fluxes in the kilowatt range. To properly shape nosecones, to choose heat shield materials and to determine their thicknesses, adequate theoretical methods needed to be developed. The classic works of Lees[1], Fay and Riddell[2], Kemp, Rose and Detra[3] and Goulard[4] were the response to these analytical needs. These very early hypersonic flow and heat transfer methods were the initial basis for todays' modern real gas theoretical and flowfield solution techniques.

From the above discussion it is obvious that it is impossible to refer in any way to the issue of hypersonic flight and associated vehicle surface heating without reference to the specific re-entry trajectory and flight domain. The choice of theoretical modeling methods for the underlying fluids and thermophysics, as well as the analytical or numerical solution methods (including the proper CFD technique) are intimately related to the specific flight corridor under consideration. The entire approach is mission dependent. An example of the rather extreme variation in conditions and resultant phenomena which are thus generated can be ascertained from Figure 1. This composite plot of flight velocity, altitude and normal shock density ratio encompasses some of the primary missions NASA has flown within the Earth's atmosphere. As Earth entry velocities increase from 5 km/sec. up to orbital values of 7-8 km/sec, most flight bodies, e.g. Shuttle, NASP (as originally proposed) and the current proposed RLV (Re-usable Launch Vehicle) experience strong bow shock waves which, initially excite the vibrational modes of the constituent N_2 and O_2 molecules, and ultimately dissociate them into N and O to varying degrees depending on velocity and altitude. This, of course, is the source of the so-called "real gas" effects an accounting of which is necessary in the Navier-Stokes, energy and constituent species governing equations. The existence of dissociated gas species in the vehicle shock layer flow for these flights can also (depending on the specific heat shield material used) give rise to exothermic surface catalytic recombination reactions which further add to the surface heat transfer. Further increases in entry speed continue to excite additional energy exchange modes among the flowfield species including electronic state excitation, ionization and radiation events. In the range of 7-10 km/sec, such proposed missions as the Aeroassist Flight Experiment (AFE) and cargo carrying GEO to LEO return aerobraking missions begin to encounter these additional phenomena. At higher velocities, beyond 10 km/sec. past missions like Apollo and proposed Mars, Earth return entries result in increased levels of flowfield generated radiation and thermochemical ablative heating. The computation of these effects adds an additional element of complexity to both the thermophysical modeling as well as the numerical complexity of solving the necessary governing equations. Discussion of these latter issues is a main topic of this paper.

Finally, at the far end of the energy spectrum lie the very high speed comet and asteroid entry scenarios typified in Fig. 1 by the Pribram Meteor with entry velocities in excess of 20-30 km/sec. Very few attempts have been made to accurately simulate the flowfield and associated fluid physics for such severe entry problems. This is true regardless of the level of fidelity of the modeling. High speed asteroid entries involve radiation dominated flows at extreme enthalpy and pressure levels. Radiation events result from multiple levels of electronic exitation and several levels of ionization. Knowledge of the radiation cross-sections for these events do not yet exist. Pressure levels, although high, are not high enough to allow the usual radiation diffusion approximations possible with stellar radiation problems. Therefore a complete spectral treatment is required. To make matters worse, the resultant heat transfer and ablative response of the entry bolide is so severe that the induced thermal and mechanical stresses tend to cause deformation and breakup of the body. Modeling of such tightly coupled solid/flowfield behavior has not yet been attempted. To perform a first principles Navier-Stokes type CFD/radiation/ablation computation of this type amounts to one of the most difficult problems that can occur in both physics and computational science. Future research is obviously required to accurately solve such complex interactions.

The range of flight velocities experienced in hypersonic re-entry is very large and therefore results in a wide range of induced energy exchange phenomena. To accurately compute surface heating thus requires examination of the range of differences in flowfield behavior, transport phenomena, chemical reaction mechanisms and radiation physics which occur over these flight regimes. This is discussed in the following.

Flight Regimes and Flow Physics

In the above discussion surrounding Fig. 1, it is implicit that the proper governing equations are available

to solve the various problems possible in each flight regime. This is not actually the case, and some assumptions and restrictions are applied to constrain the problem. Figure 2 depicts the typical flight regimes which can occur under hypervelocity conditions. This plot also includes a density ratio for air (i.e. Earth entry) at the various velocity-altitudes encountered. As a re-ntry vehicle (RV) descends in altitude, the fluid mechanical behavior of the body's external flowfield will dramatically change. At the highest altitudes, densities are low enough such that only free molecular flow (no particle interaction) occurs. At slightly lower altitudes, atomic and molecular collisions are occurring but do not significantly affect the fluid dynamics (free collision regime). These flight regimes are called the "non-continuum" domain and require radically different mathematical techniques, such as direct simulation Monte Carlo (DSMC) and molecular dynamics methods to compute aerodynamics and heat transfer. From the standpoint of surface heat transfer, this regime is of little interest to the designer and will not be dealt with further in this review.

Further descent (with attendent reduction in flight velocity) brings the RV into the so-called "continuum" flight regime where increasing compressive and frictional forces cause a bow shock wave (a standing or stationary pressure wave) to envelop the vehicle. At the top of this continuum region is located what is termed the viscous or merged shock layer domain. This terminology refers to a state whereby the flowfield between the body surface and bow shock experiences a continuous set of velocity, temperature and species concentration profiles. The shock layer is in effect a very thick boundary layer terminating at the bow shock. Once inside this flight regime, the full suite of Navier-Stokes, energy and species governing equations can be applied. The viscous layer regime is the area where the well known "viscous shock layer (VSL)" subset of the N-S equations is applied. These approximation equations are discussed below. Continuing with the re-entry, at lower altitudes the Reynolds number increases dramatically (along with an associateds rapid fall in Knudsen number) and the shock layer flow separates into a thinner viscous layer underlying a semi-inviscid region with a high degree of vorticity.

Finally at the highest Reynolds numbers, the external flowfield separates into the well known inviscid/boundary layer flow. Returning to Fig. 2, the region of the plot delineated for radiation coupling at the highest entry velocities and dynamic pressures corresponds to an important flight regime encountered (as discussed above) for high speed Earth entry and outer planet entry missions. At the lower end of this region, incident surface sensible heat fluxes are high enough to induce pyrolytic breakdown of most thermal protection system (TPS) materials followed, in most cases, by vaporization (thermochemical ablation) of the material surface. This process injects significant amounts of mass into the shock layer, and in the process, absorbs large amounts of energy to protect the vehicle, but also is self correcting by directly convecting energy downstream. Unfortunately as the flight velocity increases, shock layer exitation with associated production of gas cap radiation directly impinges on the TPS surface. This radiative heat flux directly determines the shock layer temperature distributions and rate of surface ablation. Ablative mass injection can act to absorb some of this incident radiation, but the effect is less than for convective blocking. This latter situation is termed the "radiation/ablation regime". In this case the dominant factor in the flowfield governing equations is the radiation source term, and this must be accurately modeled. The mathematical coupling of the fluid mechanics and radiation becomes paramount. In the discussion to follow, the various phenomenological modeling techniques as well as governing equations (including full CFD techniques) which apply to each of these regions will be outlined. Particular attention will be focused on the induced surface effects of catalytic recombination, ablation and pyrolysis.

Governing Equations, Thermophysical Modeling and Mission Profiles

General

Each of the above described flight regimes and their related chemistry and physics requires a different set of modeling equations. Many past and current flight missions have encountered some or all of the flowfield thermophysical phenomena typified by each of these flight regimes. The discussion below focuses on sub-categories of these, and reference to the important computational issues of the various re-entry mission profiles is made. First, however, a general starting point for the computational science is needed. In any 3-dimensional reference frame, the invariant-vector representation of the Navier-Stokes equations, the constituent species conservation and total energy conservation equations take on the following forms.

Total Mass Conservation

$$\frac{\partial \rho}{\partial \tau} + \nabla \cdot (\rho \underline{V}) = 0 \qquad (1)$$

Species,α, Conservation:

$$\frac{\partial \rho_\alpha}{\partial \tau} + \nabla \cdot (\rho_\alpha \underline{V}) = \nabla \cdot (\rho \mathcal{D}_\alpha \nabla x_\alpha) + \mathcal{R}_\alpha \qquad (2)$$

Navier-Stokes Momentum Conservation:

$$\frac{\partial \underline{V}}{\partial \tau} + (\underline{V} \cdot \nabla)\underline{V} = -\frac{1}{\rho}\nabla P + \frac{\underline{F}}{\rho} + \frac{1}{\rho}\nabla \cdot \underline{\underline{\tau}} \qquad (3)$$

Total Energy Conservation:

$$\rho \frac{\partial H_T}{\partial \tau} + \rho(\underline{V} \cdot \nabla) H_T = \frac{\partial P}{\partial \tau} - \nabla \cdot \underline{q} + \nabla \cdot (\underline{\underline{\tau}} \cdot \underline{V}) + \underline{F} \cdot \underline{V} + W \qquad (4)$$

These equations represent and encompass any and all of the fluid physics, chemistry and radiation transport phenomena that can occur in continuum flight regime of interest for hypervelocity flight. Their solution in any particular flight case or entry mission requires an appropriate set of initial and boundary conditions to form a well posed problem. In hypersonic flight the following conditions are required for any flight domain.

1) Freestream conditions: Thermodynamic state variables (temperature, pressure, composition,e.g.)and velocity.

2) In-flow and Out-flow conditions: characteristic velocity, pressures constraints, Extrapolation of flow conditions.(Also, surface hydrodynamic conditions such as, slip, no slip or tangency would be included.)

3) Surface boundary conditions: von Neumann or Dirichlet conditions; i.e. surface heat flux and mass flux (either specified or via instantaneous surface mass and energy balance), specified surface concentration and temperature.

Although conditions 1) and 2) are somewhat obvious and, in most cases, are imbedded in the N-S solution algorithm, the surface boundary condition 3) invokes a full range of surface hydrodynamic, surface chemistry and thermophysical phenomena which need further elucidation. As outlined in Ref.8, these are generally expressible as;

Species, α, Surface Mass Conservation:

$$(\rho_\alpha \underline{v})_g + \underline{J}^g_\alpha = (\rho_\alpha \underline{v})_s + \underline{J}^s_\alpha + (\underline{R}_\alpha + \underline{S}_\alpha)(1-\epsilon_s) \quad (5)$$

where
$\underline{R}_\alpha$ = the mass rate of production of species α by heterogeneous (surface)reactions,
$\underline{S}_\alpha$ = the mass rate of injection (thermochemical ablation) of species α via surface vaporization and in-depth pyrolysis,
and,
ϵ_s = the volumetric porosity of the solid surface material (TPS).

Surface Momentum Conservation:

$$P_s = P_g + [(\rho \underline{v})_g + \frac{4}{3}\kappa\mu_{ave}\hat{s}] \cdot (\underline{v}_g - \underline{v}_s) + \frac{4}{3}(\mu \nabla \cdot \underline{v})|_g - \frac{4}{3}(\mu \nabla \cdot \underline{v})|_s . \quad (6)$$

Once having established the surface mass and momentum conditions, the total surface energy conservation can be written down.

Total Surface Energy Conservation:

$$(h_1 h_3)[-k_T \nabla T|_g - \sum_\alpha h_\alpha \underline{J}^g_\alpha + \underline{q}_R|_{net}] = \sum_\alpha h_\alpha (\rho_\alpha \underline{v}|_g - \rho_\alpha \underline{v}|_s) - (h_1 h_3) k_T \nabla T|_s \quad (7)$$

Equations (1)-(7), although completely general, are extremely compact and contain a multitude of information. To further understand the behavior of this equation set, specific subsets representing the three separate hypervelocity flight regimes discussed above are delineated. The governing equations for the Viscous Shock Layer, High Reynolds Number (Boundary Layer) and the Coupled Radiation/Ablation flow regimes are discussed in the following sections.

Viscous Shock Layer Region:

To properly represent the viscous shock layer behavior the N-S equations need to be written down in a form general enough to include the bow shock behavior, the full range of viscous effects in a viscous shock layer and be constrained by an appropriate set of boundary conditions appropriate for this flight regime. For this case (and all of the subsequent cases and discussion) the N-S set will be written in a specific body oriented, 3-D, coordinate system typically used in most CFD and other solution algorithms. Also, these equations will be simplified to an appropriate level accurate enough to describe most mass, momentum and heat transfer phenomena encountered and still eliminate extraneous details of complex 3-D flowfields. These simplifications result in the so-called "thin layer Navier- Stokes" equations which basically eliminate the cross-flow derivative terms. These terms are only necessary when such details of vortical flow, unsteady vortices and detailed wake flows are to be studied accurately. Most problems involving surface heating and TPS design for hypervelocity flight are computationally intensive enough that the numerical grid densities cannot be high enough to justify inclusion of the cross-derivatives in any case. Thus the Thin Layer Navier-Stokes equations are written as;

Total Continuity:

$$(h_1 h_3)\frac{\partial \rho}{\partial \tau} + \frac{\partial}{\partial s}(h_3 \rho u) + \frac{\partial}{\partial n}(h_1 h_3 \rho v) + \frac{\partial}{\partial t}(h_1 \rho w) = 0 \quad (8)$$

Species,α,Continuity:

$$(h_1 h_3)\frac{\partial \rho_\alpha}{\partial \tau} + \frac{\partial}{\partial s}(h_3 \rho_\alpha u) + \frac{\partial}{\partial n}(h_1 h_3 \rho_\alpha v) + \frac{\partial}{\partial t}(h_1 \rho_\alpha w) = \frac{h_3}{h_1}\frac{\partial}{\partial s}(\rho \mathcal{D}_\alpha \frac{\partial x_\alpha}{\partial s}) + h_1 h_3 \frac{\partial}{\partial n}(\rho \mathcal{D}_\alpha \frac{\partial x_\alpha}{\partial n}) + \frac{h_3}{h_1}\frac{\partial}{\partial t}(\rho \mathcal{D}_\alpha \frac{\partial x_\alpha}{\partial t}) + \mathcal{R}_\alpha \quad (9)$$

s-Momentum:

$$(h_1h_3)\frac{\partial \rho u}{\partial \tau}+\frac{\partial}{\partial s}(h_3\rho u^2)+\frac{\partial}{\partial n}(h_1h_3\rho uv)+\frac{\partial}{\partial t}(h_1\rho uw)+ h_3\rho uv\frac{\partial h_1}{\partial n}+\rho uw\frac{\partial h_1}{\partial t}-\rho w^2\frac{\partial h_3}{\partial s}=-h_3\frac{\partial P}{\partial s}+ \frac{4}{3}\frac{h_3}{h_1}\frac{\partial}{\partial s}(\mu\frac{\partial u}{\partial s})+h_1h_3\frac{\partial}{\partial n}(\mu\frac{\partial u}{\partial n})+\frac{h_1}{h_3}\frac{\partial}{\partial t}(\mu\frac{\partial u}{\partial t}) \quad (10)$$

n-Momentum:

$$(h_1h_3)\frac{\partial \rho v}{\partial \tau}+\frac{\partial}{\partial s}(h_3\rho uv)+\frac{\partial}{\partial n}(h_1h_3\rho v^2)+\frac{\partial}{\partial t}(h_1\rho wv) -h_3\rho u^2\frac{\partial h_1}{\partial n}-\rho w^2\frac{\partial h_3}{\partial n}=-h_1h_3\frac{\partial P}{\partial n} +\frac{h_3}{h_1}\frac{\partial}{\partial s}(\mu\frac{\partial v}{\partial s})+\frac{4}{3}h_1h_3\frac{\partial}{\partial n}(\mu\frac{\partial v}{\partial n})+\frac{h_1}{h_3}\frac{\partial}{\partial t}(\mu\frac{\partial v}{\partial t}) \quad (11)$$

t-Momentum:

$$(h_1h_3)\frac{\partial \rho w}{\partial \tau}+\frac{\partial}{\partial s}(h_3\rho uw)+\frac{\partial}{\partial n}(h_1h_3\rho vw)+\frac{\partial}{\partial t}(h_1\rho w^2) +\rho uw\frac{\partial h_3}{\partial s}+\rho vwh_1\frac{\partial h_3}{\partial n}-\rho u^2\frac{\partial h_1}{\partial t}=-h_1\frac{\partial P}{\partial t}+ \frac{h_3}{h_1}\frac{\partial}{\partial s}(\mu\frac{\partial w}{\partial s})+h_1h_3\frac{\partial}{\partial n}(\mu\frac{\partial w}{\partial n})+\frac{4}{3}\frac{h_1}{h_3}\frac{\partial}{\partial t}(\mu\frac{\partial w}{\partial t}) \quad (12)$$

Total Energy (Enthalpy) Conservation:

$$(h_1h_3)\beta_H\frac{\partial \rho H_T}{\partial \tau}+\frac{\partial}{\partial s}(h_3\rho uH_T)+\frac{\partial}{\partial n}(h_1h_3\rho vH_T)+ \frac{\partial}{\partial t}(h_1\rho wH_T)=\frac{h_3}{h_1}[\frac{\partial}{\partial s}(Pr\frac{\partial(\rho H_T)}{\partial s}+q_s^R) +\mu(\frac{4}{3}u\frac{\partial u}{\partial s}+v\frac{\partial v}{\partial s}+w\frac{\partial w}{\partial s})]+h_1h_3[\frac{\partial}{\partial n}(Pr\frac{\partial(\rho H_T)}{\partial n} +q_n^R)+\mu(u\frac{\partial u}{\partial n}+\frac{4}{3}v\frac{\partial v}{\partial n}+w\frac{\partial w}{\partial n})] +\frac{h_1}{h_3}[\frac{\partial}{\partial t}(Pr\frac{\partial(\rho H_T)}{\partial t}+q_t^R) +\mu(u\frac{\partial u}{\partial t}+\frac{4}{3}v\frac{\partial v}{\partial t}+\frac{4}{3}w\frac{\partial w}{\partial t})] \quad (13)$$

where,

$$\beta_H=1-(\frac{H_T}{RT}+\rho\frac{\partial h}{\partial P})^{-1}. \quad (14)$$

In the reduction process from equations (1) - (4) to the above, not only have cross derivatives associated with viscous effects been eliminated, but also those second order terms involving derivatives of metrics (i.e. h_1, h_2 and h_3) have been dropped for both clarity and because such higher order geometric effects are inconsequential for most hypervelocity flight bodies of interest. Consistent with these reduced equations the surface boundary conditions (equations (5) - (7)) can be written in terms appropriate to a body fixed coordinate system. namely;

Species, α, Surface Mass Conservation:

$$(\rho_\alpha v)_g+J^g_{\alpha,n}=(\rho_\alpha v)_s+J^s_{\alpha,n}+(R^n_\alpha+S^n_\alpha)(1-\epsilon_s) \quad (15)$$

Surface Momentum Conservation:

$$P_s=P_g \quad (16)$$

and,

Total Surface Energy Conservation:

$$(h_1h_3)[-k_T\frac{\partial T}{\partial n}|_g-\sum_\alpha h_\alpha J^g_{\alpha,n}+q^R_n|_{net}]= \sum_\alpha h_\alpha(\rho_\alpha v|_g-\rho_\alpha v|_s)-(h_1h_3)k_T\frac{\partial T}{\partial n}|_s. \quad (17)$$

Vehicle surface metrics have been defined as,

$$h_1=\sqrt{(\frac{\partial x}{\partial s})^2+(\frac{\partial y}{\partial s})^2+(\frac{\partial z}{\partial s})^2} \quad (18)$$

$$h_2=1 \quad (19)$$

$$h_3=\sqrt{(\frac{\partial x}{\partial t})^2+(\frac{\partial y}{\partial t})^2+(\frac{\partial z}{\partial t})^2}\ . \quad (20)$$

The above set of thin-layer Navier-Stokes equations is general enough to apply to any of the continuum flight regimes, including the viscous shock case being considered in this section. As a general 3-D set they can be solved along any entry trajectory (continuum) from the entry interface to the ground using modern CFD numerical techniques. Discussion of these methods and associated issues is deferred to the following section on high Reynolds number flow, since that region is the most widely studied area from the standpoint of TPS design. However, there is a class of re-entry problems for which the specific aspects of merged and viscous shock behavior is important. For mission profiles which require a spacecraft to return from high Earth orbit, e.g. geosynchronous orbit (GEO) to low Earth orbit (LEO), the entry problem usually consists of the use of an aerobraking pass followed by return to LEO. These missions are relegated to higher altitude perigees, during which a significant portion of the flight will be in the viscous shock region. Depending on the vehicle ballistic coefficient and entry velocity, such missions may experience high Reynolds number flow (e.g. boundary layer flow) during the peak heating portion of the flight. In spite of this, solution techniques which depend on the lower Reynolds number for a viscous shock flow have been succesfully applied to these problems. To date these solution methods have been restricted to the 2-D axisymetric limit of the governing equations, either by the nature of the vehicle geometry and zero angle-of-attack mission profile or by virtue of a lack of interest in investing further computational resources for this problem. The 2-D axisymmetric set of equations is a subset of equations (8)- (17) whereby the vehicle/flow metrics take on the

following limits;

$$h_1 \longrightarrow 1 + \kappa y \tag{21}$$

$$h_2 = 1 \tag{22}$$

$$h_3 \longrightarrow r \tag{23}$$

Examples of the so-called "Viscous-Shock" or VSL methods come from the classic works of Davis[9], Miner and Lewis[10], Moss[11] and Gupta[12]. Briefly, without a long discourse on the method, the general VSL numerical algorithmic approach is to treat the above subset of 2-D axisymmetric N-S equations, in the steady state limit, as a parabolic set of partial differential equations, with known conditions at the origin of the computational domain. By providing an estimate of the funtional form of the surface pressure distribution along the body at, and in the vicinity of the stagnation point, the N-S equations and associated species mass and total energy conservation equations can be numerically differenced and solved via an appropriate downstream marching technique. In this process the complete shock-layer, including the bow shock can be numerically constructed and all field variables obtained throughout the computational domain. For more in-depth study and details, the reader is referred to the above references. The VSL methodology has been applied to several actual NASA flight missions and proposed flight experiments. A few example results will be discussed next.

Shown in Fig. 3 (Ref. 14) is a sketch of the flight geometry and flowfield of a previously proposed major NASA flight test mission known as AFE. This flight was planned to perform an aerobraking pass from LEO (launch from orbit by shuttle orbiter) to LEO under the impetus of a solid rocket. The altitude vs. time history of the flight is plotted in Fig. 4. Figure 5 provides a plot of Reynolds number (behind a normal shock and based on body diameter) as a function of time for this trajectory and shows that the primary period of peak heating will be in the full continuum regime. However, significant portions of the flight are in the VSL region. Various computational methods have been applied to this flight, including full N-S, VSL and boundary layer techniques. Stewart, etal[14] have presented a comparison of the pertinent heat transfer effects for AFE based on these three different techniques. These computations were performed with the following simplified subset of surface boundary conditions as stated in equations (15)-(17);

Species,α,Surface Mass Conservation:

$$J^g_{\alpha,n} = R^n_\alpha \tag{24}$$

Surface Momentum Conservation:

$$P_s = P_g \tag{25}$$

and,

Total Surface Energy Conservation:

$$-k_T \frac{\partial T}{\partial n}|_g - \sum_\alpha h_\alpha J^g_{\alpha,n} + q^R_n|_{net} = 0. \tag{26}$$

Surface heterogeneous reactions embodied in the terms, R^n_α, consist of the irreversible surface recombination reactions of nitrogen and oxygen (i.e. N + N = N_2 and O + O = O_2) using surface kinetics expressions emprically determined for Shuttle tiles with RCG (Reaction Cured Glass) coating. As shown in Figure 6, computed surface temperatures using the reacting, non-similar boundary layer code BLIMPK[15] have similar magnitudes and distributions when using non-equilibrium boundary layer edge conditions taken from full N-S (LAURA code) (Gnoffo[16]) and VSL (Gupta[12]) solutions for the AFE configuration. Obviously at altitudes of 75 km and above, the use of equilibrium boundary layer edge conditions will not give adequate results. Figure 7 shows a comparison of edge conditions taken from equilibrium, from non-equilibrium VSL and LAURA N-S solutons for AFE. There is a vast departure from equilibrium and even significant differences between N-S and VSL edge conditions at 75 km. These kinds of non-equilibrium effects are typical of shock-layer behavior in the viscous shock flow regime and indicate the necessity of accounting for this unique behavior in these higher altitude heat transfer computations.

Finally, the VSL technique has, in the past, been successfully applied to analysis of Shuttle Orbiter centerline heat transfer computations and compared with Orbiter flight data. Thompson[15] has performed VSL centerline hypersonic flow computations for the Orbiter at altitudes above 60 km. Figure 8 shows a comparison of Shuttle centerline heat transfer at 75 and 64 km (Mach 25 and Mach 18) using the same surface boundary (finite rate catalysis) conditions as in equations (24)-(26). To within the variation in surface catalysis models the agreement is excellent.

High Reynolds Number (Boundary Layer) Flow Regime

At lower altitudes for re-entry trajectories (e.g. less than 65 km in air), most RV's will experience peak heating under conditions of high Reynolds number flow where the shock layer separates into a well defined inviscid outer layer and a contiguous, near surface boundary layer. Since this is a most important flow regime from the standpoint of aerothermodynamics and TPS design, some discussion will be focused on the applicable state-of-the-art Navier-Stokes solution techniques. Certainly the traditional two-layer inviscid/ boundary layer techniques, and even Fay and Riddell stagnation heat transfer simplified relations can be used here for engineering level heat transfer estimates using simplified geometry assumptions. (i.e. axisymmetric flow, tangent

cone, tangent wedge and flat plate approximation methods, cf. Ref. 16). However, in this paper the focus will be on the more recent applications of 2-D and 3-D CFD Navier-Stokes solution techniques with some examples of applications.

Equations (8)-(14) along with surface boundary conditions (15)-(17), the necessary gas phase reaction rate kinetics, and thermal and caloric equations of state comprise the complete set of real gas governing equations which most current CFD N-S solvers address. If the reentry velocity is high enough then this equation set must be supplemented with transport relations for shock layer gas spectral radiative fluxes and TPS material and surface ablation thermophysical models. These latter effects will be the subject of the next section. Although there are many different and varied numerical techniques currently being used to solve these N-S equations for real gas flows (including algorithms for massively parallel processors), the author is most familiar with three algorithms which have been most widely applied to problems within NASA, and this discussion will be limited to this group. For 2-D axisymmetric problems, without coupled radiation heat transfer, the fully implicit Gauss-Seidel method of Candler and MacCormack[17] has found wide application to real gas, high Reynolds number flows. As with other CFD numerical N-S solvers, this method is based on the time-hyperbolic nature of the N-S set. Hypersonic flowfields are comprised of mixed sub-sonic and supersonic domains, the mathematical characteristics of which are different. Fully steady state sub-sonic domains possess characteristics of elliptic PDE's, while the supersonic domains are hyperbolic. Numerical techniques which can handle both computational domains within the same problem are very cumbersome and can be ill-behaved (i.e. difficult to converge and unstable). If the time derivative terms are retained, then the entire computational domain is hyperbolic in time and time accurate and pseudo-time accurate time marching algorithms can be applied. This mathematical feature is universal in current CFD N-S Solvers. The Gauss-Seidel implicit method is based on a spatial discretezation of the governing equations using upwind biased, modified Steger-Warming flux functions (or flux splitting method). All terms are forward differenced in time to result in a fully implicit, time updated scheme. The set of resulting matrix, difference equations is solved at each time update across the computational domain via the line-by-line Gauss-Seidel direct matrix inversion scheme. This method is extremely efficient computationally because of the relatively non-sparse matrices which are generated. Courant-Friederichs-Lewy numbers (CFL) as high as 500 have been routinely achieved with this method. However, its drawback is that, with modern supercomputers (at least using a single processor), memory restrictions will, practically speaking, only permit its application to 2-D axisymmetric problems. Three-D problems will generate extremely large matrices, particularly for problems involving even a modest number of chemical species and reactions. For 2-D axisymmetric problems, the Gauss-Seidel N-S solver technique has been successfully applied to a number of NASA mission scenarios. Among these is the Mars Pathfinder entry vehicle that landed on Mars on July 4,1997. This set of computations involves coupled ablation from the heat shield and will be discussed in the next Section. However, an example of a non-ablating system is given in Fig. 9 (Ref. 13) and shows the computed behavior for the temperature excursion expected in the previously proposed AFE wall catalysis experiment. A specific ceramic tile located near the flowfield centerline is coated with a highly reactive (or catalytic) catalytic overcoat. As shown in the plot a temperature increase of at least 150 K can be expected. This result was obtained using a 2-D axisymmetric shape approximation for the AFE flowfield and the Gauss-Seidel algorithm was employed with the reacting wall boundary conditions of equations (24)-(26). The solution was obtained at the expected peak heating point for AFE.

A second widely employed 3-D CFD real gas method is the point-implicit, TVD (Total Variation Diminishing) algorithm, most successfully embodied in the Langley Research Center LAURA code by Gnoffo[18]. The LAURA code employs a numerical scheme originally developed by Coakley[19] which employs upwind biased spatial differencing for a given set of cell face flux functions. Forward (implicit) time differencing is invoked on a point-by-point basis in the domain. This technique generates a series of compact matrix equations for the cell averaged field variables for each sweep through the computational domain. When employed with a selected residual or solution variation reduction scheme, this results in very efficient solution iteration. However, the limited degree of implicitization limits the advancement of CFL numbers in the range of one (1) to five (5). Readers are very much encouraged to consult Ref. 18 for more numerical details. The LAURA code currently employs Roe flux difference splitting for flux function evaluation. Cell average solution variables can be reconstructed to cell faces with accuracies of up to one and one half (1.5) orders. The code is a complete reacting, real gas, N-S solver and includes air and Mars atmosphere gas reaction kinetics. Finite rate surface catalysis boundary conditions and a modified Baldwin-Lomax algebraic turbulence model are installed. The code can be run with finite volume grids subdivided into multiple grid blocks and a form of grid mesh density sequencing can be accomplished. For problems requiring a very large number of grid points (e.g. the complete flowfield of the Shuttle Orbiter) supercomputer memory limitations will require the multi-block approach with LAURA. Solutions are obtained for individual sub-blocks and then reconstructed to yield the full domain solution. An example of the application of LAURA and of the use of the multi-block approach is given by Weilmuenster,et al[20] and Gnoffo,et al[21]. These two studies have pro-

vided detailed LAURA results for both aerodynamics and aerothermodynamic heating of the Shuttle Orbiter at selected critical points along the Orbiter re-entry trajectory. Figure 10 (Ref. 20) shows a schematic of the general grid layout for these Orbiter computations and is fairly typical of a LAURA finite volume grid. Using the multiblock approach mentioned above, the results from Gnoffo's[21] study can be typified by the normalized heat transfer distribution plots shown in Figs. 11 -14. Figure 11 shows the heating distribution along the windward centerline along with comparisons with alternate engineering techniques and with flight data. As is typical with most 3-D CFD results, agreement with flight is excellent for this portion of the flowfield. A similar plot is provided in Fig. 12 for the leeward centerline heating, and, where flight data is available, agreement is either adequate (where heating is low) or quite poor. These discrepancies are usually due to inadequate grid resolution in regions of rapidly accelarating or deccelarating flow (or for shock-shock interactions). The remaining plots (Figs. 13 -14) show the off-centerline predictive capability of LAURA, and the results are generally quite good. These computations were performed using a seven species gas reaction kinetics model, temperature dependent transport properties and a two-temperature nonequilibrium thermal model.

A final example of high Reynolds number real gas flow computations with surface catalysis is discussed here from the standpoint of a slightly different computational approach for the 3-D CFD algorithm. Recently NASA has embarked on a series of studies and flight test programs (e.g. X33 and X34) to develop reusable launch systems to drastically reduce the cost of payload insertion into LEO. A NASA Access-to-Space study[22] presented several alernate launch system scenarios, including an airbreathing NASP single-stage-to-orbit (SSTO) option, a hybrid airbreathing/rocket two-stage-to-orbit (TSTO) case as well as a separate single-stage-to-orbit pure rocket (SSTOR) configuration. Weight statements, required technologies, fixed and variable costs and space launch infrastructure impacts of each of option were reported. It is well known by now that the SSTOR option was selected, and is being pursued in the form of the X33 flight test vehicle program. As a part of the NASA reusable launch vehicle (RLV) technology development program which followed the Access-to-Space Report, NASA Ames Research Center developed a more systematic approach to the design process for TPS selection and sizing. The method involves solving the 3-D real gas CFD flowfield solutions to obtain detailed surface heat transfer rates for the actual SSTOR vehicle configuration at selected "anchor points" along the TPS design limiting trajectory. These heating environments are then interpolated in time along the trajectory, thus forming an input database for time dependent in-depth conduction and TPS sizing computations for each surface body location. In this manner a detailed 3-D surface material and thickness map can be obtained, and more accurate estimates of TPS mass distributions can be realized. An example of the CFD heat transfer results obtained in this study is given in this discussion. A more detailed accounting is provided in the last Section of this paper. TPS heating environments have been obtained for a generic winged-body SSTO rocket configuration developed by the Langley Research Center (LaRC). A computational surface grid which defines the geometric configuration is depicted in Fig. 15. Henline,et al[23] have employed the numerical methods an real gas modeling contained in the GASP (version 2.2) CFD N-S solver to compute the heating environments on this vehicle.

The GASP code, developed by Aerosoft, Inc.[24], is a general purpose, finite volume based, 3-D real gas Navier-Stokes solver. It contains a variety of gas phase chemical kinetics, thermal and thermodynamic and transport property models. These include models for air, H_2-He and (at Ames Research Center) CO_2 atmospheres. The code is unique in that a variety of finite volume, spatial differencing schemes can be applied to a given problem through the use of optionally available flux functions. These include full flux, Steger Warming, Van Leer, Roe and Roe/Harten flux and flux diference split functions. If the user determines that the individual characteristics of each of these flux functions has a unique advantage in any particular coordinate direction, then that flux splitting method can be so applied. GASP 2.2 uses first, second or third order MUSCL variable reconstruction stencils based on user choice. In addition to the above features, GASP employs a variety of time integration strategies which can be used according to the nature of the problem. These schemes can be used to perform time integration in either a global or space marching manner (if flow characteristics warrant it). These include 3-factor AF (approximate factorization), 2-factor AF with line relaxation, LU-decomposition-for 2-D space marching and m-stage Runge-Kutta time accurate methods. Finite volume computational grids can be constructed in a zonal manner so that different time integration strategies can be used in each zone where appropriate. Convergence acceleration schemes such as mesh sequencing, CFL ramping and (in more recent version) multi-grid techniques can be used. In all of the implicit schemes used for GASP, the full implicit matrix is not used, but only approximations of the inverse are applied to the right-hand side of the matrix equations (e.g. 3-factor and 2-factor AF). Because of this, the ultimate upper limit of possible CFL numbers for any given problem is somewhat restricted. In large 3-D reacting flow hypersonic problems, the author has experienced CFL values limited to the range of 5 to 10. Finally, the GASP code architecture has been designed to be very memory efficient and can be run in both plane and zonal parallel modes on multi-processor Cray machines.

As discussed in Ref. 23, for the LaRC SSTOR Access-to-Space vehicle shown in Fig. 15, the GASP (Version

2.2) code has been used to perform full 3-D flowfield reacting, real gas aerothermodynamic heating computations at several points along the TPS design limiting entry trajectory for this configuration. These have been performed using a 5-species air gas kinetics model, single temperature thermal model, constant Schmidt number based mass diffusion coefficients and temperature dependent thermal conductivity and viscosities. Both laminar and Baldwin-Lomax algebraic turbulence model results have been obtained using finite rate surface catalysis and surface radiative equilibrium boundary conditions. The surface boundary conditions have been implemented for a variety of possible TPS material mappings. Solutions have been obtained using the full Navier-Stokes set of momentum equations with van Leer inviscid flux functions. First order differencing was found to be adequate in the streamwise and circumferential directions, while is was necessary to resort to third order reconstruction in the normal direction to obtain accurate estimates of surface heat transfer. The 2-factor AF algorithm with streamwise relaxation was used for time integration. The maximum CFL number reached for these cases was five (5). Approximately 30 hrs. of Cray C-90 CPU time was required to converge a solution to $4\frac{1}{2}$ levels of L2-Norm residual reduction for a grid density of approximately 400,000 nodes. All of this was accomplished with less than 18 megawords of Cray run time memory.

Typical results from these simulations are presented in the folowing sequence of figures. Figure 16 shows the full 3-D finite volume flow grid at a sequence level of 161 X 65 X 38 cells. In such cases, usually at least three grid sequence levels are employed. In the case studied here, two levels of grid density were used for the streamwise and normal coordinate directions and found to be sufficient for grid independence. Figure 17 depicts the TPS material mapping used for this vehicle, which is in accordance with that proposed in the Access-to-Space Study Report[22]. RCG coated Carbon-Carbon or TUFI tiles (Toughened Unipiece Insulation) are used for higher temperature regions (nosecap and leading edges) while TABI (Tailorable Advanced Blanket Insulation) and AFRSI (Alumina Flexible Reusable Surface Insulation) blankets are used elsewhere. Surface kinetics for oxygen and nitrogen recombination reactions on each of these materials were obtained from Stewart, etal[25]. The resultant GASP computational results for the radiative equilibrium surface temperature are shown in Fig. 18 for fully laminar flow and in Fig. 19 for turbulent flow. These simulations were performed near the peak heat transfer rate portion of the LaRC SSTOR trajectory (1300 sec from entry interface, at 58 km altitude and 32° angle-of-attack). Although it is hard to see in the grayscale plots, near the division between the Carbon-Carbon (C-C) nosecap and the windward TABI blankets, there is a substantial jump in temperature due to the highly catalytic nature of TABI in comparison to the C-C. Finally, in Fig. 20 a larger scale view of the wing/winglet region is shown to detail the effect of impingement of the bow shock wave on the leading edge surface. The shock-shock interaction results in the highest temperatures on the vehicle, reaching nearly 2000 K.

The Coupled Radiation and Ablation Flow Regime

In Fig. 2 the region in the lower right portion of the plot at the highest velocities and lowest altitudes corresponds the the flight regime where the kinetic energy levels are high enough, that when dissipated via a shock layer will exite the radiation exchange mechanisms in the gas to high enough rates to produce substantial gas cap radiation fluxes. In this flight regime these radiative fluxes will be high enough to penetrate the optical interference (absorption) of the shock layer gases and impinge directly on the TPS. This will begin to happen in air (Fig. 2) at velocities above (25,000 ft/sec) 8 km/sec. For almost all mission scenarios, entries into the Venusian atmosphere and into Jupiter or Saturn will result in flow regimes in this so-call "radiation/ablation coupled" domain. The term "radiation coupled" or "radiation dominated" is used to refer to dominance of the gas phase radiative flux terms appearing in the total energy (enthalpy) conservation equation(Eq. (13)). When this term is the overwhelming factor in the shock layer energy balance, both enthalpy (temperature), species concentration and velocity profiles will be fully governed by the radiation processes. Obviously, accurate determination of the radiation flux terms in analytical forms compatible with Eq. (13) is a critical factor when attempting to compute both the flowfield and surface heat fluxes on vehicles operating at these high energies.

When solving the governing equations for these cases, in principle the complete set of terms in equations (8)-(14) and boundary conditions (15)-(17) are required. Since the extremely high incident radiative heat flux at the surface will inevitably cause massive TPS ablation which injects mass into the shock layer at high rates, significant additional coupling of this ablation hydrodynamics and the external flowfield will occur. This fact will have a significant impact on the mathematical characteristics of the resultant shock layer flow. Figure 21 is a sketch of this general type of behavior for such a massive ablation condition. Ablation species exit the wall at high enough velocities so that a blowing sub-layer which has nearly inviscid flow properties, forms near the wall. The thickness of this layer depends on the blowing rate. The sub-layer flow then intercepts the incoming inviscid flow from the bow shock, forming a viscous mixing layer at the intersection. The various different material layers present in the ablative TPS are also shown in Fig. 21. Also shown are representations of the general behavior of the radiation processes in the different shock layer flow regions. Emission is dominant in the usually optically thin inviscid layer, while the denser (cooler) layer of ablation products will cause absorption to dominate near

the wall. As a consequence of these very large coupling effects any numerical N-S solution technique will have to be quite different and more robust than those currently in use for non-ablating situations. For this reason, there are currently no fully developed 2-D or 3-D Navier-Stokes solution techniques which completely include all of the radiation and ablation (mass injection) effects for coupled radiation/ablation problems. There are two extremely difficult issues needing resolution to allow such a fully coupled algorithm. The first is centered around the inclusion of very high mass injection rates into the surface mass and energy balance boundary conditions. These high rates will, in any time accurate or pseudo time accurate transient solution method, result in very massive (almost discontinuous) surface cell updates, which in turn will cause massive instabilities unless handled by some type of implicit formulation. This means that the full set of ablation/ radiation boundary conditions must be incorporated into the numerical Jacobians of the difference equations. For any real gas problem with a large number of species and radiation, this is an algebraically daunting task and has not yet been done and is certainly a subject of future research.

The second difficult numerical issue is the coupling of the radiation source terms, q_s^R, q_n^R and q_t^R. Computation of the individual radiative flux terms at any given point in the flowfield requires an integration over all of the radiative, species and temperature profiles throughout the entire computational domain. This must be repeated for each numerical computational point in the flowfield. Such an elliptic problem is currently beyond the capabilities of today's most powerful supercomputers. Approximations must, have been and will be made to simplify this situation. The remaining portion of this section is thus devoted to a brief description of the current simplified techniques for solving this coupled radiation/massive ablation problem. Some examples of past design results will be given.

Prior to this, however, an example of a partial exception to the above conclusion will be discussed. In a case where there is minimal radiation and incident convective heat fluxes are high enough to cause only modest ablation and mass injection, it has been possible to obtain CFD solutions with coupled ablation. This has been done in the design phase of the recent NASA Mars Pathfinder mission entry probe forebody heat shield. Chen, etal[26] has used the 2-D axisymmetric Gauss-Seidel algorithm to perform full Navier-Stokes solutions at selected points along the design entry trajectory for Mars Pathfinder. These solutions (for the predominantly CO_2 Mars atmosphere) were loosely coupled to time dependent, in-depth conduction/pyrolysis/ablation solutions for the surface blowing rates, surface temperatures and in-depth TPS temperatures of the Pathfinder SLA-561V heat shield ablative material. Several iterations, at each trajectory point, between the CFD N-S solver and the in-depth conduction code were required to converge on resultant matching surface temperatures, blowing rates and heat fluxes. Figures 22 and 23 show the surface heat flux distributions and components for this 70-deg. sphere-cone shaped flight body.Figures 24 and 25 give the results for in-depth TPS material temperatures at the stagnation point and one downstream location. To the author's knowledge, this is the only fully coupled CFD/ablation solution thus far obtained.

In the past, fully coupled radiation/ablation solutions have been limited to 2-D axisymmetric configurations with severe restrictions on the fidelity of the flowfield modeling. Solutions have been based exclusively on steady state, algebraic algorithms. The governing set of equations (which are a subset of equations (8)-(14)) have, in most situations, taken the following forms.

Total Continuity:

$$\frac{\partial}{\partial s}(h_3\rho u) + \frac{\partial}{\partial n}(h_1 h_3 \rho v) = 0 \tag{27}$$

Species,α,Continuity:

$$\frac{\partial}{\partial s}(h_3\rho_\alpha u) + \frac{\partial}{\partial n}(h_1 h_3 \rho_\alpha v) = h_1 h_3 \frac{\partial}{\partial n}(\rho \mathcal{D}_\alpha \frac{\partial x_\alpha}{\partial n}) \tag{28}$$

s-Momentum:

$$\frac{\partial}{\partial s}(h_3\rho u^2) + \frac{\partial}{\partial n}(h_1 h_3 \rho u v) = -h_3\frac{\partial P}{\partial s} + h_1 h_3 \frac{\partial}{\partial n}(\mu \frac{\partial u}{\partial n}) \tag{29}$$

Total Energy (Enthalpy) Conservation:

$$\frac{\partial}{\partial s}(h_3\rho u H_T) + \frac{\partial}{\partial n}(h_1 h_3 \rho v H_T) = h_1 h_3[\frac{\partial}{\partial n}(Pr\frac{\partial(\rho H_T)}{\partial n} + q_n^R) + \mu(u\frac{\partial u}{\partial n} + \frac{4}{3}v\frac{\partial v}{\partial n} + w\frac{\partial w}{\partial n})], \tag{30}$$

with the following set of simplified surface boundary conditions.

Species α Surface Mass Conservation:

$$(\rho_\alpha v)_g + J^g_{\alpha,n} = (\rho_\alpha v)_s + S^n_\alpha(1-\epsilon_s) \tag{31}$$

and,

Total Surface Energy Conservation:

$$(h_1 h_3)[-k_T\frac{\partial T}{\partial n}|_g - \sum_\alpha h_\alpha J_{\alpha,n} + q_n^R|_{net}] = \sum_\alpha h_\alpha(\rho_\alpha v|_g - \rho_\alpha v|_s). \tag{32}$$

The in-depth solid (TPS) conduction terms have not been included, since these effects having been lumped

into an apriori empirical determination of the thermochemical ablation rate. This is usually done through the use of a correlation for the TPS material "effective heat of ablation". The algorithm most often used to solve this so-called "thin viscous shock" set of geoverning equations is that used in the RASLE[27] code used to design the Galileo probe forebody heat shield. This algorithm integrates the coupled equations by means of a parabolic marching technique reminiscent of integral boundary layer methods. It is an inverse, shock fitting technique in which the shock standoff distance and streamwise shape are estimated by a correlation developed by Falanga and Olstad[28]. The governing equations are discretized across the shock layer using polynomial expansions which encorporate a matching parameter to match expansions from the surface and shock boundaries at the inviscid/blowing layer interface. Radiative fluxes are computed using a "tangent slab" or plane-parallel approximation. In this model the radiation view factor in the shock layer is assumed to exist only along a line of sight normal to the body surface. It is a good approximation for thin shock layers and near stagnation streamlines. In all solutions to date, all radiation processes have been assumed to in equilibrium, i.e. whereby emission is equal to absorption at each point in the flow. Scattering and reflection have been neglected. A full suite of radiation exchange events and processes have been modelled. These include line radiation, molecular continuum radiation, as well as photo-ionization events. As outlined in Ref. 27, line radiation has been accounted for by using a lumped band approach, with up to twenty (20) bands possible in the RASLE code. Radiation property models have been developed for this method which can be applied to air, the Jovian atmosphere ($H_2 - He$) and the CO_2 system (Venusian atmosphere).

As a brief example of the types of solutions possible with an algorithm like RASLE, some results from the preliminary design of the proposed ESA/Rosetta Comet return mission probe will be given. Henline and Tauber[29] have used the RASLE methodology to compute net surface heat fluxes, surface temperatures and TPS surface ablation and recession rates by coupling the RASLE code to the in-depth conduction/pyrolysis/ablation code CMA[30] along the proposed ESA/Rosseta probe entry trajectory. Figure 26 shows a simple sketch of the probe's forebody geometry, while the entry trajectory is shown in Fig. 27. The probe returns to Earth with an entry speed of 16 km/sec resulting in very high radiative fluxes. As can be seen from Fig. 28, the stagnation point radiation pulse (accounting for ablation) peaks at 1.2 kw/cm^2, which is about 60% of the total. Figure 29 shows the surface heat flux and tempertures (from a coupled solution with CMA) along the entry trajectory. Substantial ablation rates occur for the carbon-phenolic heat shield material selected for this mission. These, along with the computed recession rates are shown in Figs. 30.

The NASA Galileo probe to Jupiter represents one of the most severe entry problems ever attempted and analyzed via the thin VSL/radiation/ablation techniques discussed above. This probe entered the Jovian atmosphere at a relative velocity of 48 km/sec. The resultant flowfield is radiation dominated and the probe was predicted to lose about 50% of its' carbon-phenolic heat shield mass in the first 10 sec of the heating pulse. The as designed probe is shown in Fig. 31 and the RASLE code computed peak radiative and convective surface heat fluxes are shown in Fig. 32. Approximately 95% of the net surface heat flux is incident radiation.

A Case Study in CFD Based TPS Design

During the technology development phase of the Access-to-Space reusable launch vehicle program in NASA, CFD based techniques were developed to make it possible to obtain a higher degree of accuracy or fidelity in the selection and thickness determination of TPS materials for RLV type vehicle concepts. The philosophy taken here was that with 3-D real gas Navier-Stokes solvers like GASP, there is enough computational efficiency to allow the determination of full 3-D body surface heat transfer distributions over any general 3-D RLV shape, and that this can be done at enough trajectory points to allow coupling of these surface heat transfer rates to a transient 1-D conduction TPS design code. As detailed in Ref. 23, this is in fact true.

A test design case was selected which focused on the TPS design for the LaRC winged-body SSTOR concept and its' associated entry trajectory. This configuration and some selected results for surface temperatures was discussed previously (see Figs. 18 and 19). The re-entry trajectory plot for this mission is given in Fig. 33. Shown here are discrete points which have been selected as so-called "CFD anchor points" to characterize the heating pulse experienced by the RLV. In Fig. 34, the rational for the selection of these point should be clear. It can be seen that each point anchors a given heating rate-time curve distinct feature. Between these features the heat transfer profile is relatively linear (or flat) and it is assumed that the full 3-D surface heat transfer rates obtained from CFD at these points can be linearly interpolated in time to provide an input database for a trajectory based transient conduction code. Figure 34 also shows the final CFD stagnation results for the anchor points. Although the magnitudes are different (as expected), the general shape of the distribution is similar to the initial engineering estimates. Using GASP (Version 2.2) winged-body RLV solutions were obtained with a specified TPS material mapping at each anchor point. Partial catalytic, radiative equilibrium surface boundary conditions were applied. From these solutions a database of recovery temperatures and associated heat transfer coefficients was constructed at each trajectory time point. These data were then used as input database for an implicit transient conduction code (OMLITS[23]) which sim-

ulated the surface energy balance and in-depth temperature profiles thru the proper TPS stack-up for each of 10,500 vehicle body points. By constraining the conduction code material interface and backface boundary conditions to the proper material maximum temperature limits, minimum TPS material thicknesses could be estimated for each RLV body point location. This result was achieved with only one iteration between the CFD trajectory solutions and the conduction solver. As reported in a study by Chen and Milos[31], even with very high in-depth conduction heat transfer rates, approximately converged flowfield/transient conduction solutions can be obtained to within 5% in a single iteration provided there is no ablation or mass injection. A conclusion such as this is a result of the relative insensitivity of surface heat and mass transfer coefficients to surface temperature. In principle the near surface hydrodynamic state and thermophysics determines these coefficients. The CFD solution determine the near surface hydrodynamics and thermophysics. Results of this design/sizing analysis for the LaRC RLV mission are given in Figs. 35 and 36. Figure 35 displays the full 3-D vehicle distribution of top layer TPS thicknesses, and Fig. 36 includes a centerline line plot of these values. Since, as part of the TPS material stack-up, lumped structural thickness were included, the effect of these structural "thermal masses" is quite evident in Fig. 36.

In closing, a brief reference is made here to the current application of this CFD/trajectory based TPS design to the now on-going NASA/Lockheed Martin X33 prototype flight test vehicle project. A full spectrum of GASP and LAURA 3-D real gas CFD solutions are being developed to construct a comprehensive aerothermodynamic database for TPS design. Figure 37 shows one GASP (Version 3) solution for the X33 configuration near the peak Mach 15 in its' design trajectory. This plot shows the general nature of the surface temperature distribution, and in addition, reveals important features of the external flowfield. In particular the effects of a shock-shock-surface impingement can be seen near the root of the canted fin. Solutions of this type to examine many TPS heating and design details are now continuing. The approach being taken in development of the X33 aerothermal design database has gravitated away from focus on given trajectories to that of performing CFD solutions at carefully selected design points which cover the entire possible flight envelope for the X33 mission. In this manner, a database (which can be accurately interpolated) can be developed independently of any specific trajectory. This permits TPS designs which can be rapidly revised during the vehicle design cycle. Thus a minimum number of somewhat expensive CFD solutions can be used for the entire design process. Figure 38 shows a plot of the current database space for X33 aerothermodynamic solutions which spans several design trajectories and a flight envelope which encompasses the proposed flight design space.

Summary and Conclusions

The above review of hypersonic re-entry flowfield analysis techniques when applied to problems with surface thermochemistry (e.g. surface catalysis), radiation and ablation indicates that, if the modern implicit and partially implicit 2-D and 3-D Navier-Stokes codes are properly utilized, then flowfield solutions, surface heat transfer, and TPS design can be performed at the final design level with CFD/trajectory based techniques. This conclusion is, however, restricted to the TPS design for missions which do not experience radiative heating and ablation coupling. Major research is needed to extend the methodology to this flight regime. As such, this design process is now being applied to the current NASA X33 and RLV flight projects. This has never been done before and represents a significant advancement in design tool development.

References

[1] Lees, L., "Laminar Heat Transfer Over Blunt Nosed Bodies at Hypersonic Speeds," *Jet Propulsion*,Vol. 26, No.4, pp. 259-269, 1956.

[2] Fay, J.A. and Riddell, F.R.,"Theory of Stagnation Point Heat Transfer in Dissociated Air," *Journal of the Aerospace Sciences*, Vol. 25,No. 2, pp. 54-67,1958.

[3] Kemp. N.H., Rose, P.H. and Detra, R.W.,"Laminar Heat Transfer Around Blunt Bodies in Dissociated Air," *Journal of the Aerospace Sciences*,pp. 421-430, July 1959.

[4] Goulard, R.,"On Catalytic Recombination Rates in Hypersonic Stagnation Heat Transfer," *Jet Propulsion*,Vol. 28, pp.737-745, November 1958.

[5] Howe, J.T.,"Hypervelocity Atmospheric Flight:Real Gas Flowfields," NASA TM 101055, June 1989.

[6] Probstein, R.F.,"Shock Wave and Flow Field Development in Hypersonic Reentry," *American Rocket Society Journal*,31,pp. 184-194, Feb. 1961.

[7] Edelman, R.K. and Fortune, D.,"Mixing and Combustion in the Exhaust Plumes of Rocket Engines Burning RP1 and Liquid Oxygen," TR-631 General Applied Science Laboratories, Inc., Nov. 1966.

[8] Engel,C.D.,"Ablation and Radiation Coupled Viscous Hypersonic Shock Layers," Volume I, Ph.D. Thesis, Dept. of Chem. Eng., Louisiana State University, Baton Rouge, La., NASA Grant NGR 19-001-059, Langley Research Center, October 1971.

[9] Davis, R.T.,"Numerical Solution of the Hypersonic Viscous Shock-Layer Equations," *AIAA Journal*,Vol. 8, No. 5, pp. 843-851, May 1970.

[10] Miner,E.W. and Lewis,C.H.,"Hpersonic Ionizing Air Viscous Shock-Layer Flows over Non-Analytic Blunt Bodies," NASA CR-2550, May 1975.

[11] Moss, J.N.,"Reacting Viscous-Shock-Layer Solutions with Multicomponent Diffusion and Mass Injection," NASA TR R-411, 1974. [12] Gupta, R.N. and Simmonds, A.L.,"Hypersonic Low-Density Solutions of the Navier-Stokes Equations with Chemical Nonequilibrium and

Multicomponent Surface Slip," AIAA Paper 86-1349, June 1986.

[13] Stewart, D.A. and Kolodziej, P.,"Wall Catalysis Experiment on AFE," AIAA 88-2674, AIAA Thermophysics, Plasma Dynamics and Lasers Conference, June 27-29,1988, San Antonio, TX.

[14] Stewart, D.A., Chen,Y-K. and Henline, W.D., "Effect of Non-Equilibrium Flow Chemistry and Surface Catalysis on Surface Heating to AFE," AIAA 91-1373, AIAA 26th Thermophysics Conference, June 24-26,1991, Honolulu, HI.

[15] Thompson, R.A.,"Three-Dimensional Viscous Shock-Layer Applications for the Space Shuttle Orbiter," *Thermophysical Aspects of Re-Entry Flows*,edited by J. N. Moss and C. D. Scott, Vol. 103 of Progress in Astronautics and Aeronautics, 1986, pp. 541-570.

[16] Tauber, M.E.,"A Review of High-Speed Convective, Heat Transfer Computation Methods," NASA TP 2914, July 1989.

[17] Candler, G.V. and MacCormack, R.W.,"The Computation of Hypersonic Ionized Flows in Chemical and Thermal Nonequilbrium," AIAA Paper 88-0511, 1988.

[18] Gnoffo,P.A.,"Point-Implicit Relaxation Strategies for Viscous, Hypersonic Flows," *Computational Methods in Hypersonic Aerodynamics*, edited by T.K.S. Murthy, Computational Mechanics Publications, Kluwer Academic Publishers, Hingham, MA,1991,pp. 115-151.

[19] Coakley, T.B.,"Implicit Upwind Method for the Compressible Navier-Stokes Equations," AIAA Paper 83-1958, July 1983.

[20] Weilmuenster, K.J., Gnoffo, P.A. and Greene, F.A.,"Navier-Stokes Simulations of Orbiter Aerodynamic Characteristics Including Pitch Trim and Bodyflap," *Journal of Spacecraft and Rockets*, Vol. 31, No. 3, May-June 1994, pp. 365-366.

[21] Gnoffo, P.A., Weilmuenster, K.J. and Alter, S.J.,"Multiblock Analysis for Shuttle Orbiter Re-entry Heating from Mach 24 to Mach 12," *Journal of Spacecraft and Rockets*, Vol. 31, No. 3, May-June 1994, pp. 367-377.

[22] Anon.,Access to Space, Advanced Technology Team, Final Report, Volumes 1-4, NASA, July 1993.

[23] Henline, W.D., Palmer, G.E., Milos, F.S., Olynick, D.R. and Chen, Y.-K.,"Aerothermodynamic Heating Analysis and Heatshield Design of an SSTO Rocket Vehicle for Access-to-Space," AIAA Paper 95-2079, 30th AIAA Thermophysics Confernce, June 19-22,1995, San Diego, CA.

[24] McGrory, W.D., Slack, D.C., Applebaum, M.P. and Walters, R.W., GASP Version 2.2, User's Guide, Aerosogt, Inc., 1872 Pratt Dr. Suite 1275, Blacksburg, VA 24060, 1993.

[25] Stewart, D.A.,Pallix, J. and Esfahani, L.,"Surface Catalytic Efficiency of Candidate Ceramic Thermal Protection Materials," NASA CDTM-20007, March 1995.

[26] Chen. Y.-K.,Henline, W.D. and Tauber, M.E.,"Mars Pathfinder Trajectory Based Heating and Ablation Calculations," *Journal of Spacecraft and Rockets*,Vol. 32, No. 2, pp. 225-230, MArch-April 1995.

[27] Nicolet, W.E. and Balakrishnan, A.,"Radiating Shock Layer Environment, RASLE, (User's Manual), Acurex Rept. UM-79-10/AS, Mountain View, CA, July 1979.

[28] Falanga, R.A. and Olstad, W.B.,"An Approximate Inviscid Radiation Flowfield Analysis for Sphere Cone Venusian Entry Vehicles," AIAA Paper 74-758, July 1974.

[29] Henline, W.D. and Tauber, M.E.,"Trajectory-Based Heating Analysis for the European Space Agency/Rosetta Earth Return Vehicle," *Journal of Spacecraft and Roclets*, Vol. 31, No.3, pp. 421-428, May-June 1994.

[30] Anon.,"Aerotherm Charring Material Thermal Response and Ablation Program, (CMA87S)," Acurex Report UM-87-13/ATD, Mountain View ,CA, Nov. 30,1987.

[31] Chen, Y.-K. and Milos, F.S.,"Solution Strategy for Thermal Response of Nonablating Thermal Protection System Materials at Hypersonic Speeds," AIAA 34th Aerospace Sciences Meeting , Reno,NV, January 1996.

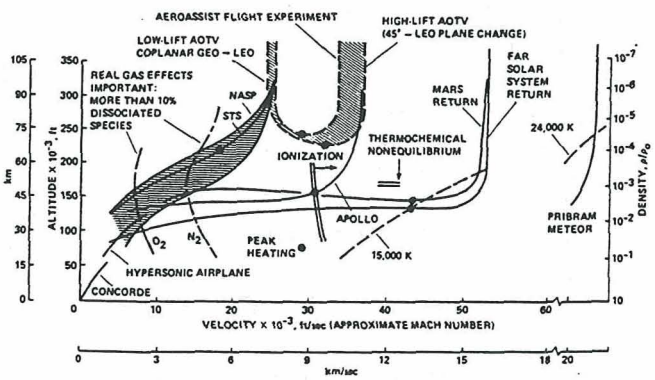

Figure 1. Comparison of vehicle flight regimes in Earth's atmosphere. (Ref.–5)

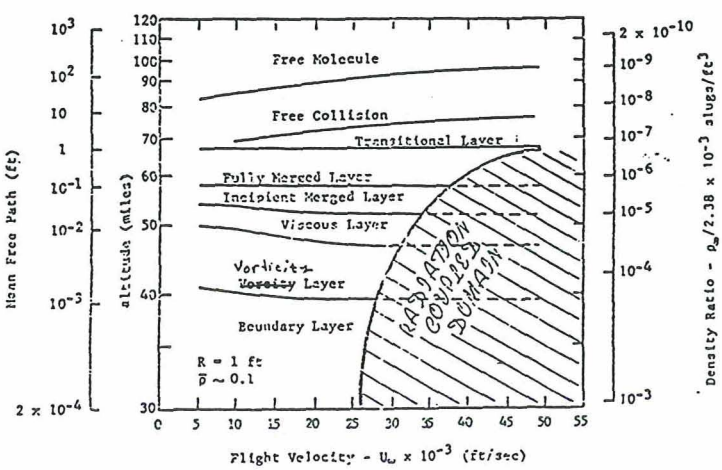

Figure 2. Flight regimes (based on Ref.–6 and modified from Ref.–7).

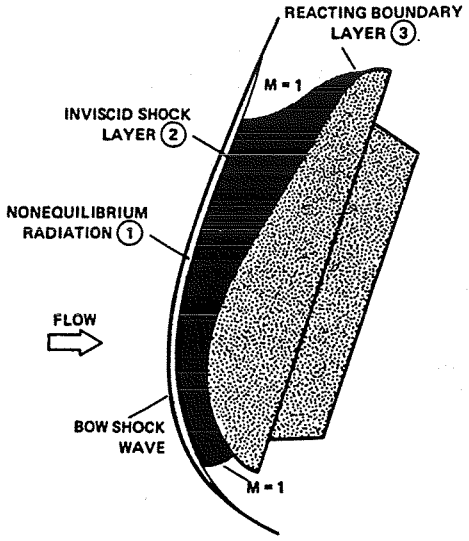

Figure 3. Vehicle geometry and flowfield characteristics of the AFE. (Ref.-14)

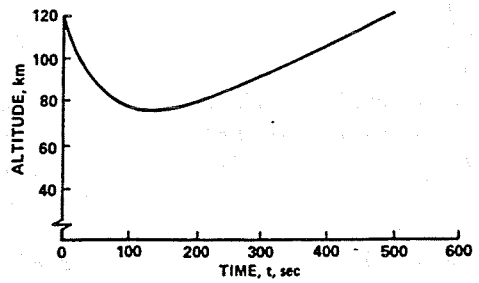

Figure 4. AFE trajectory. (Ref. 14)

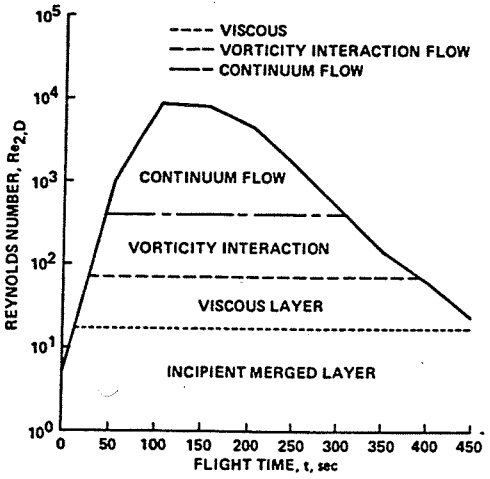

Figure 5. Reynolds number history and flight regimes for AFE. (Ref. 14)

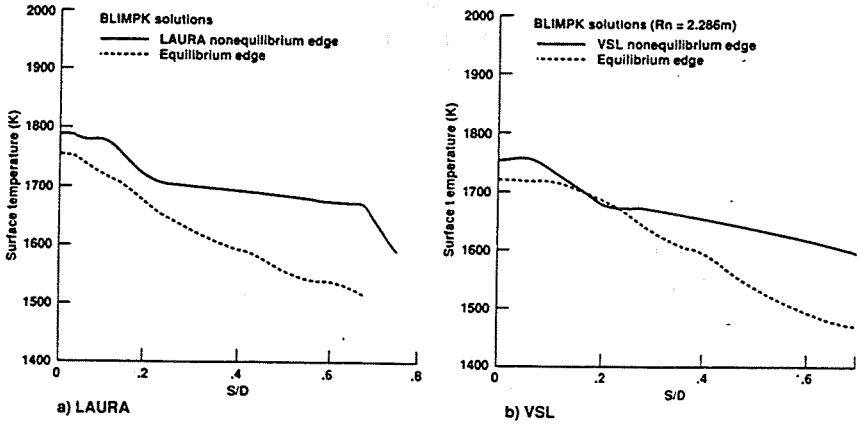

Figure 6. AFE surface temperature distribution showing effects of boundary layer edge conditions. (Ref. 14)

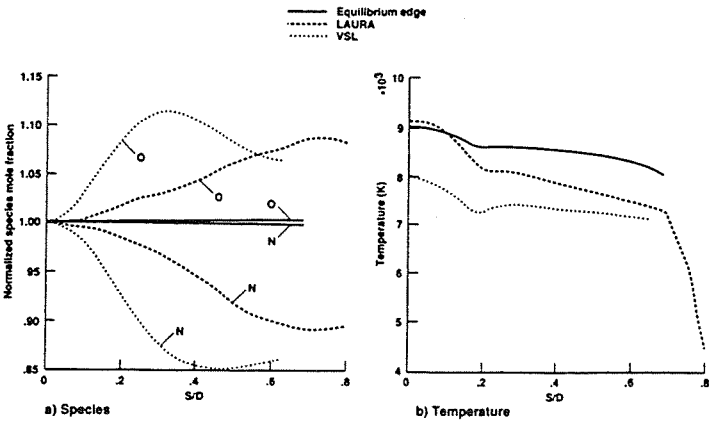

Figure 7. Comparison of boundary layer edge conditions for different computational methods applied to AFE. (Ref. 14)

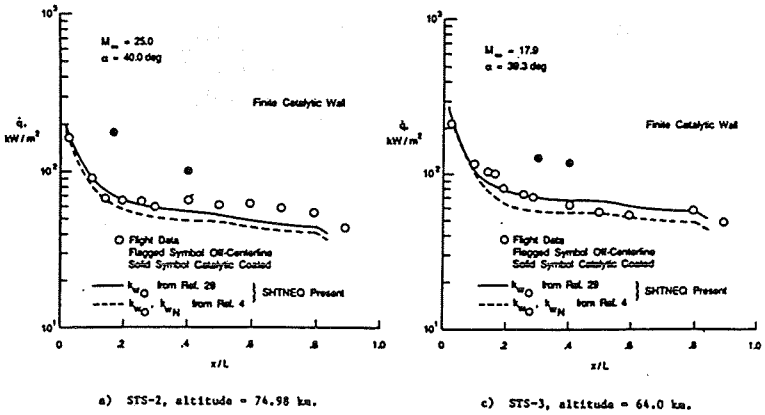

Figure 8. Viscous shock layer non-equilibrium heat transfer predictions for the Shuttle Orbiter windward centerline. (Ref. 15)

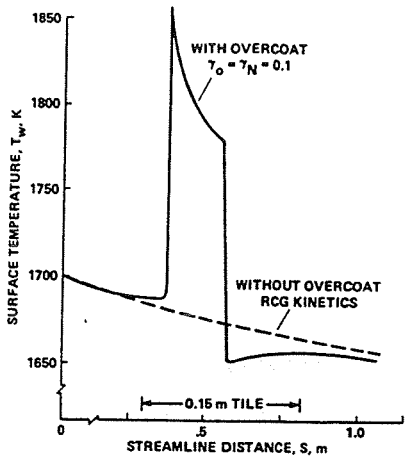

Figure 9. Surface temperature profile for the Wall Catalyis Experiment on AFE. (Ref. 13)

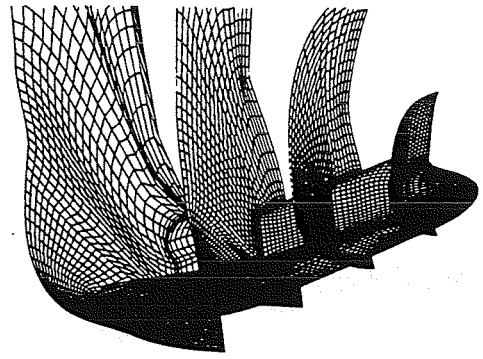

Figure 10. Shuttle Orbiter surface and volume grid (LAURA Code). (Ref. 20)

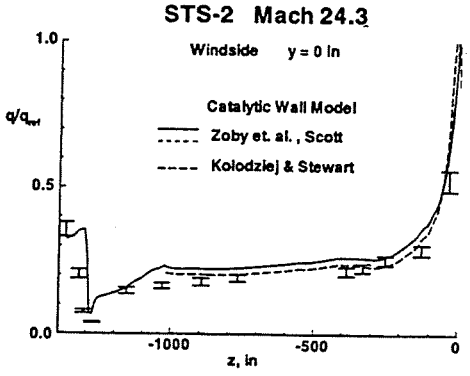

Figure 11. Surface heat transfer distribution for Shuttle windward centerline with surface catalysis. (Ref. 21)

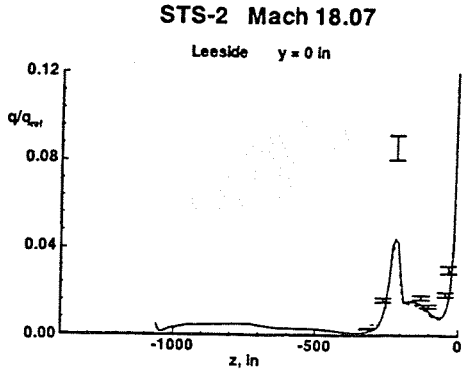

Figure 12. Leeward centerline surface heat transfer distribution for Shuttle. (Ref. 21)

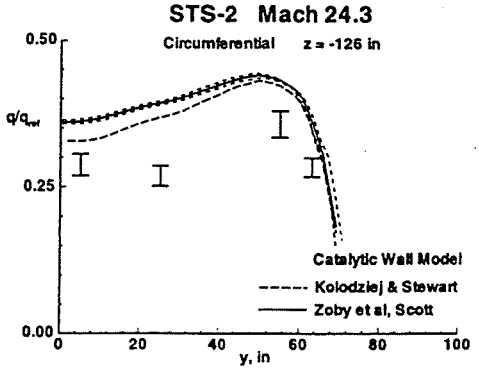

Figure 13. Windward circumferential heating distribution for Shuttle, 126 in. aft of nose. (Ref. 21)

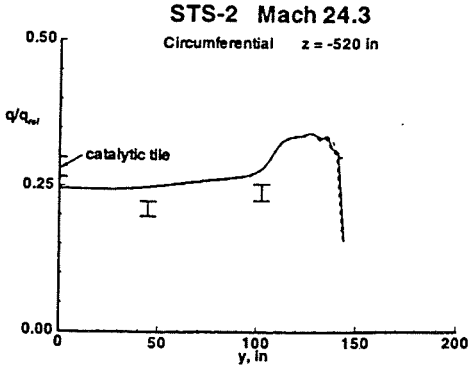

Figure 14. Windward circumferential heating distribution for Shuttle, 520 in. aft of nose. (Ref. 21)

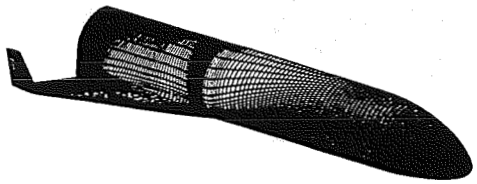

Figure 15. Langley Research Center SSTO(R) configureation and surface grid. (Ref. 23)

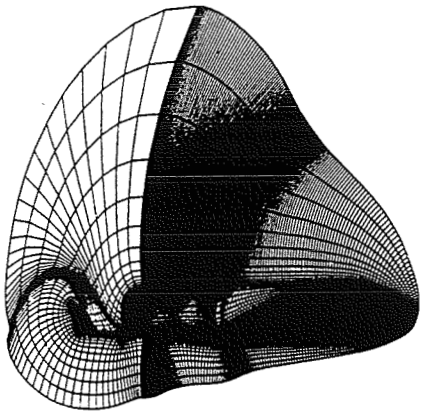

Figure 16. LaRC SSTO(R) finite volume flow grid (161 X 65 X 38) cells. (Ref. 23)

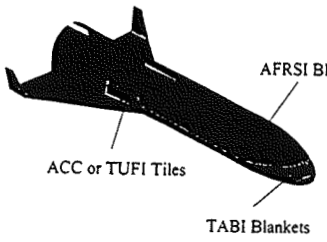

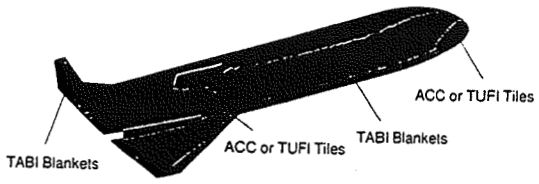

Figure 17. TPS material mapping for SSTO(R). (Ref. 23)

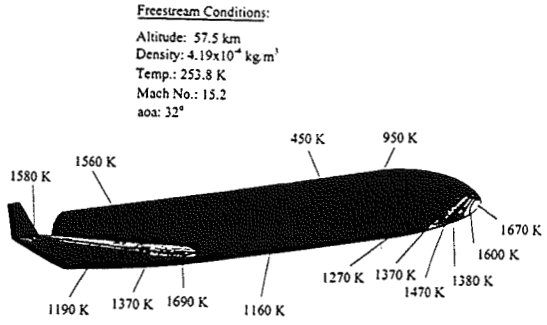

Figure 18. Adiabatic surface equilibrium temperatures for SSTO(R) at peak heating-laminar flow. (Ref. 23)

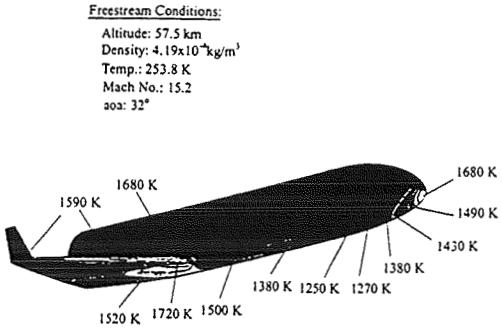

Figure 19. Adiabatic surface equilibrium temperatures for SSTO(R) at peak heating-turbulent flow. (Ref. 23)

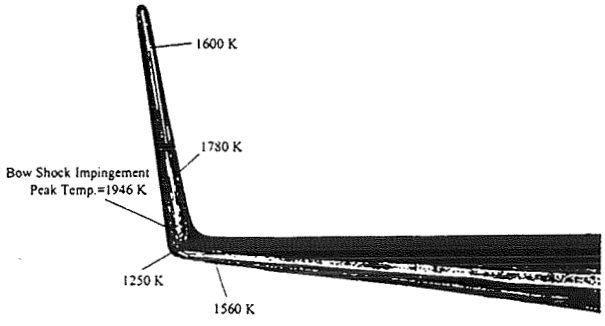

Figure 20. SSTO(R) winglet detail of maximum vehicle surface temperatures. (Ref. 23)

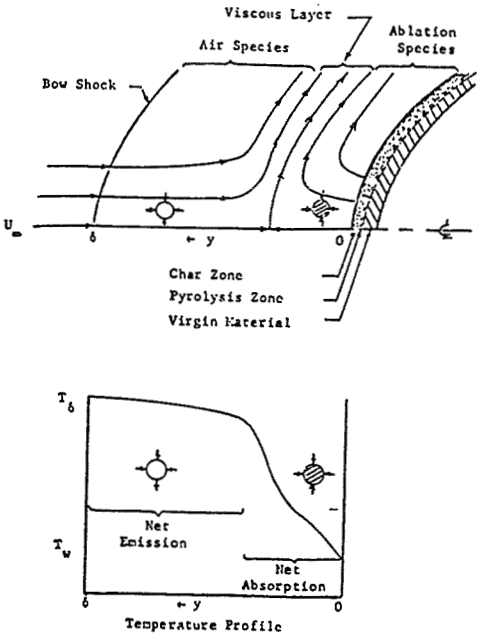

Figure 21. Schematic of various regions in a radiation/ablation coupled shock layer. (Ref. 8)

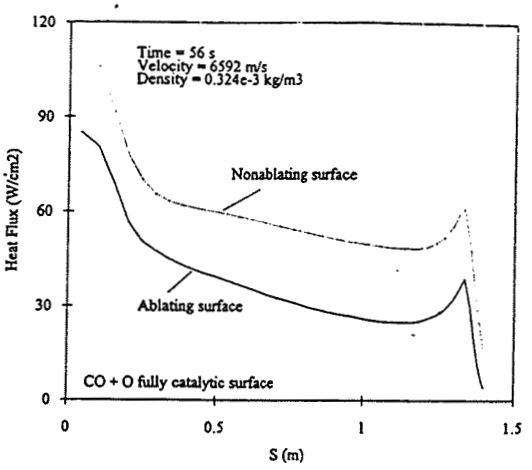

Figure 22. Surface convective heat transfer distribution for Mars Pathfinder forebody. (Ref. 26)

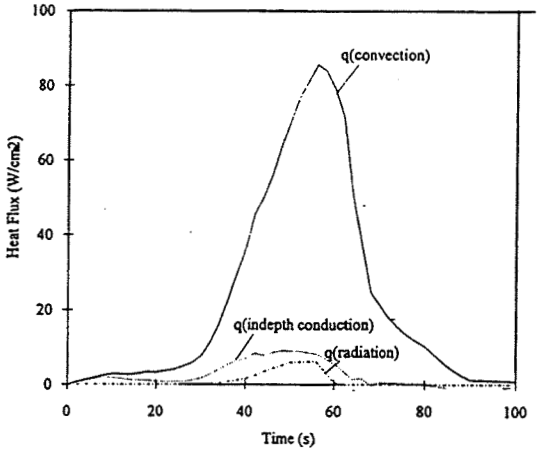

Figure 23. Mars Pathfinder stagnation point surface heat flux history. (Ref. 26)

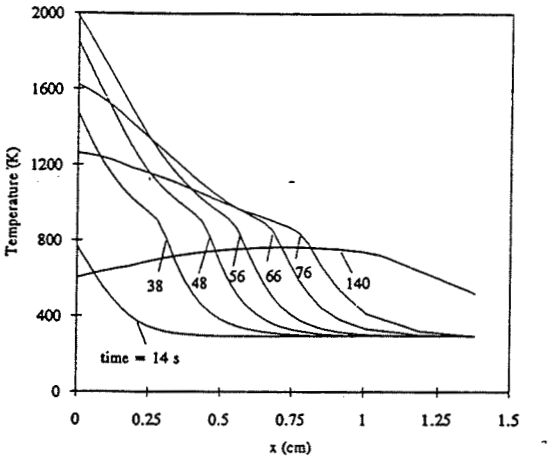

Figure 24. Mars Pathfinder stagnation point in-depth temperature histories. (Ref. 26)

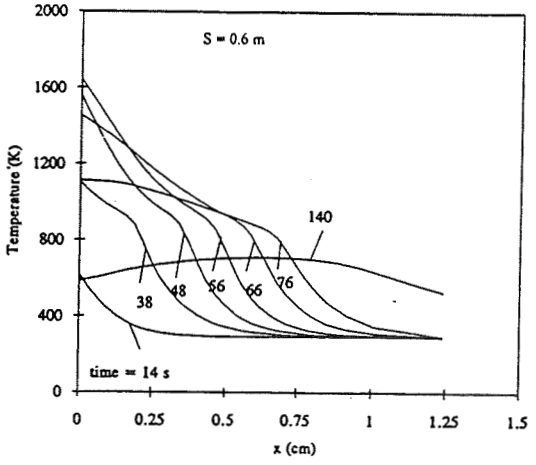

Figure 25. Mars Pathfinder downstream in-depth temperature histories. (Ref. 26)

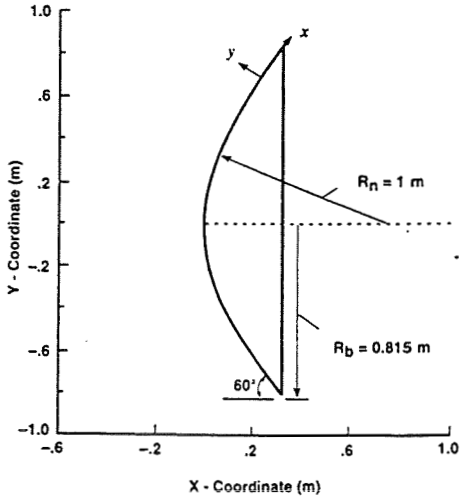

Figure 26. ESA/Rosett comet nucleus sample return probe forebody geometry. (Ref. 29)

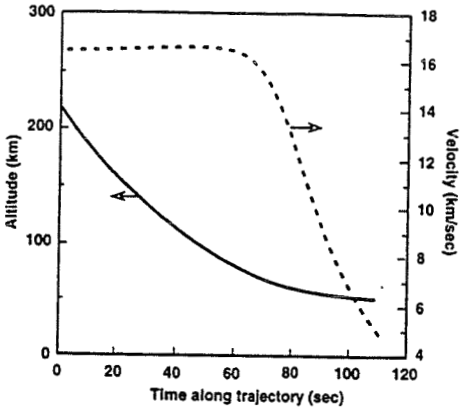

Figure 27. ESA/Rosetta entry trajectory. (Ref. 29)

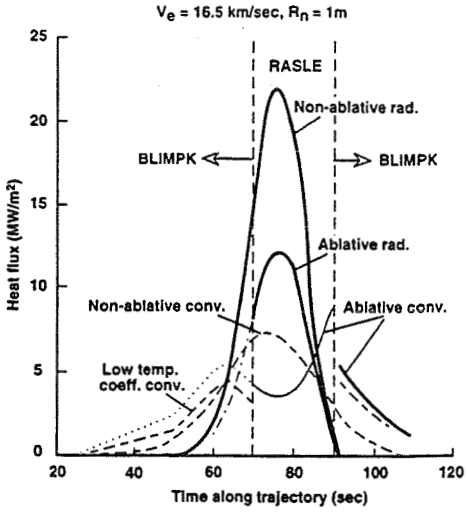

Figure 28. ESA/Rosetta stagnation heating. (Ref. 29)

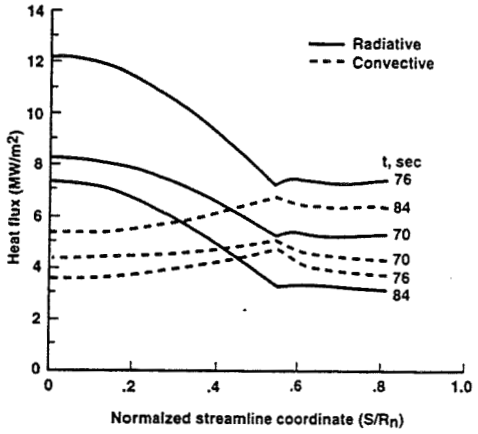

Figure 29. ESA/Rosetta probe forebody heating rate distributions. (Ref. 29)

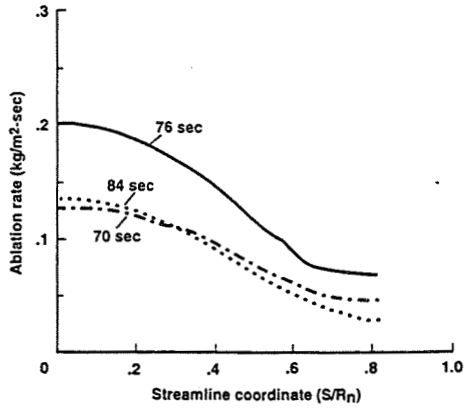

Figure 30. Forebody ablation rates for the ESA/Rosetta probe. (Ref. 29)

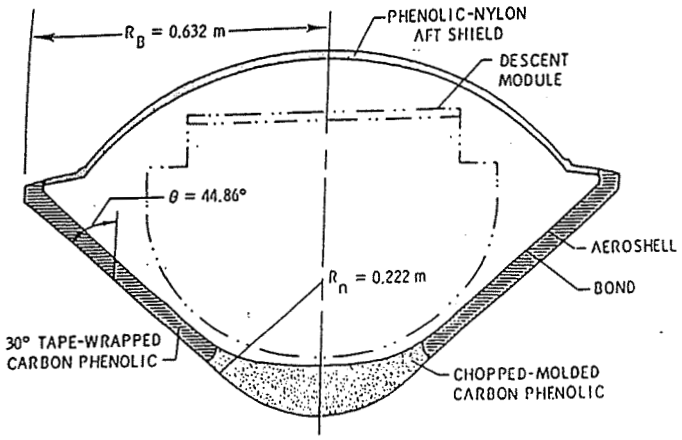

Figure 31. Galileo entry probe geometry.

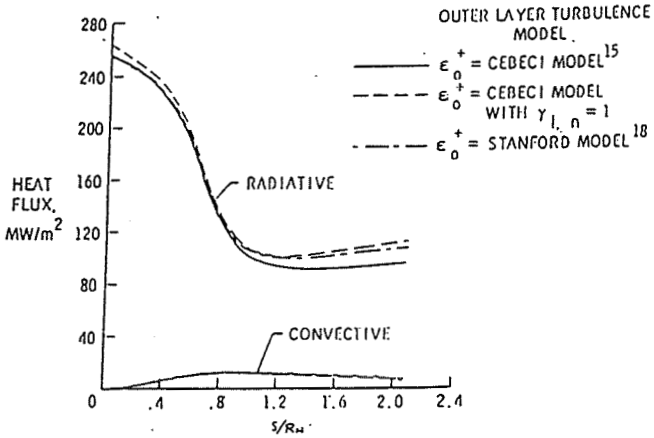

Figure 32. Galileo probe forebody heat transfer distributions.

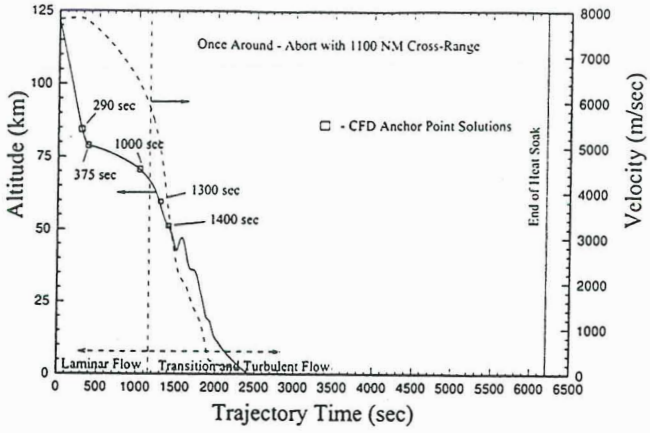

Figure 33. SSTO(R) entry trajectory and CFD anchor points. (Ref. 23)

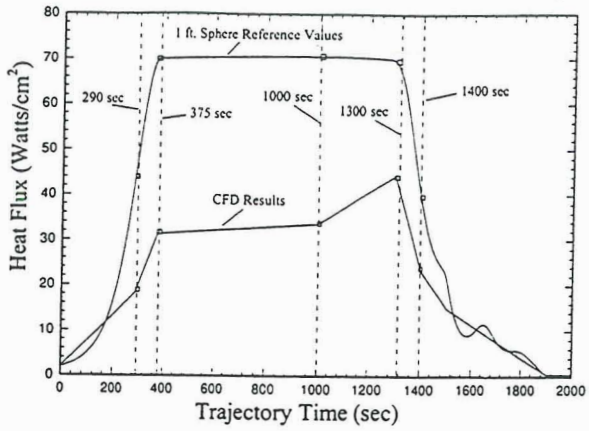

Figure 34. SSTO(R) stagnation point heat fluxes. (Ref. 23)

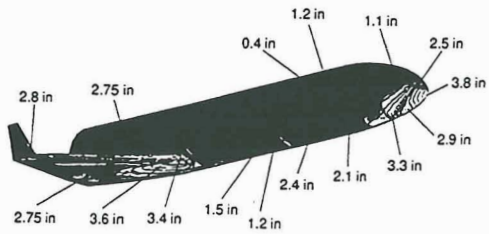

Figure 35. Contour plot of TPS thicknesses for SSTO(R) (Ref. 23)

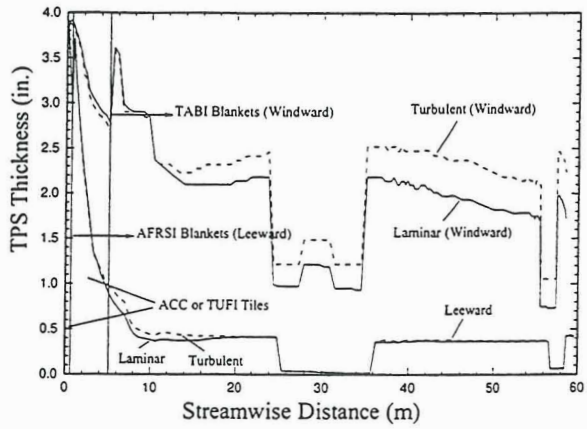

Figure 36. SSTO(R) centerline TPS thicknesses. (Ref. 23)

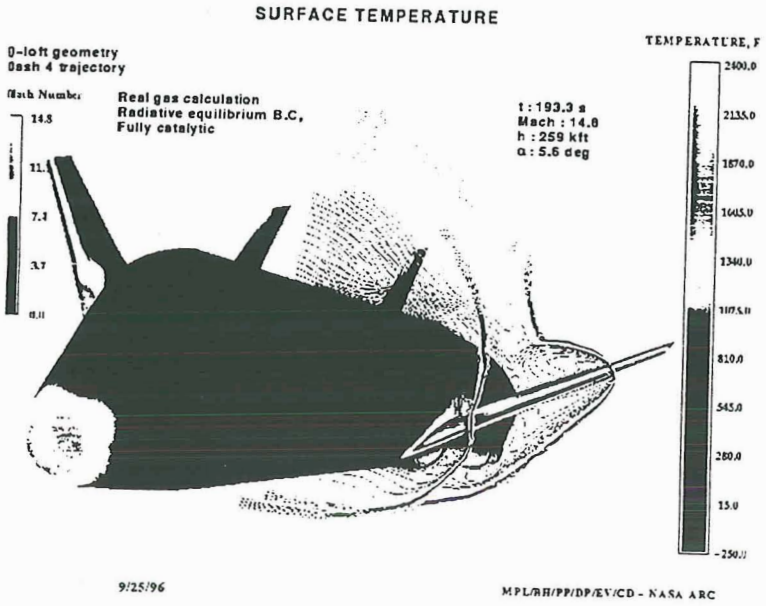

Figure 37. GASP solution for X33.

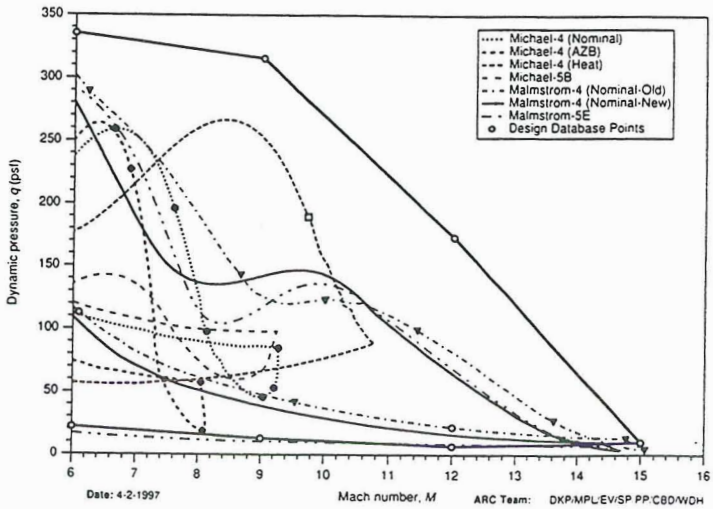

Figure 38. X33 CFD database/trajectory plot.

REPORT DOCUMENTATION PAGE

Form Approved
OMB No. 0704-0188

1. AGENCY USE ONLY *(Leave Blank)*	2. REPORT DATE	3. REPORT TYPE AND DATES COVERED
	September 1997	Conference Publication

4. TITLE AND SUBTITLE
Eighth Annual Thermal and Fluids Analysis Workshop on Spacecraft Analysis and Design

5. FUNDING NUMBERS

6. AUTHOR(S)
Editors and Co-chairs: Todd Peters, John Saiz, Dr. Carl Scott and Dr. Eugene Ungar, NASA/JSC

7. PERFORMING ORGANIZATION NAME(S) AND ADDRESS(ES)
Lyndon B. Johnson Space Center
Houston, TX 77058

8. PERFORMING ORGANIZATION REPORT NUMBERS
S-831

9. SPONSORING/MONITORING AGENCY NAME(S) AND ADDRESS(ES)
National Aeronautics and Space Administration; Washington, D. C. 20546

10. SPONSORING/MONITORING AGENCY REPORT NUMBER
NASA CP 3359

11. SUPPLEMENTARY NOTES

12a. DISTRIBUTION/AVAILABILITY STATEMENT
Available from the
NASA Center for Aerospace Information
800 Elkridge Landing Road
Linthicum Heights, MD 21090
Subject Category: 34

12b. DISTRIBUTION CODE

13. ABSTRACT *(Maximum 200 words)*

This document contains papers presented at the Eighth Annual Thermal and Fluids Analysis Workshop (TFAWS) on Spacecraft Analysis and Design hosted by the NASA/Johnson Space Center (JSC) on September 8-11, 1997, and held at the University of Houston - Clear Lake (UHCL) in the Bayou Building. The Workshop was sponsored by NASA/JSC. Seminars were hosted and technical papers were provided in fluid and thermal dynamics. Seminars were given in GASP, SINDA, SINAPS Plus, TSS, and PHOENICS. Seventeen papers were presented.

14. SUBJECT TERMS	15. NUMBER OF PAGES	16. PRICE CODE
cyogenics; environment, orbital thermal; flow fields, plume; catalycity; flow, hypersonic; radiation, thermal; analysis, aerothermal, thermal, structural, fluid	175	

17. SECURITY CLASSIFICATION OF REPORT	18. SECURITY CLASSIFICATION OF THIS PAGE	19. SECURITY CLASSIFICATION OF ABSTRACT	20. LIMITATION OF ABSTRACT
Unclassified	Unclassified	Unclassified	Unlimited